LARGE-SCALE GROWTH, FLUORINATION, CLEAN TRANSFER, AND LAYERING OF GRAPHENE AND RELATED NANOMATERIALS

BY

JOSHUA D. WOOD

DISSERTATION

Submitted in partial fulfillment of the requirements
for the degree of Doctor of Philosophy in Electrical and Computer Engineering
in the Graduate College of the
University of Illinois at Urbana-Champaign, 2013

Urbana, Illinois

Doctoral Committee:

Professor Joseph W. Lyding, Chair
Associate Professor Eric Pop, Co-Chair
Professor Rashid Bashir
Professor Martin Gruebele
Professor Umberto Ravaioli

ABSTRACT

This dissertation improves the synthesis, functionalization (i.e., fluorination), and transfer of graphene and hexagonal boron nitride (h-BN). Further, this document explores new avenues in the large-area, heterogeneous layering of graphene, h-BN, and related nanomaterials like nanoscale water and biomolecules.

It is determined that monolayer, high-quality graphene growth by chemical vapor deposition (CVD) on Cu depends on the substrate's crystallography, with few-defect, monolayer graphene growing on Cu(111). Functionalizing CVD graphene with XeF_2 produces fluorinated graphene (FG) with C_4F and CF stoichiometries. FG films seed high-κ HfO_2 films better than pristine graphene. An atomically clean nanomaterial transfer method using poly(bisphenol A carbonate) (PC) is developed and benchmarked against alternative transfer scaffolds. A transferred CVD graphene overlayer encapsulates one to three nanoscale water layers on mica. The graphene shrink wrapped water is highly viscous and robust, withstanding ultra-high vacuum and high-temperature treatments.

The PC transfer process is then used to shrink wrap heterogeneous combinations of graphene, h-BN, FG, water, CNTs, and biomolecules like tobacco mosaic viruses, proteins, and DNA. Biomolecules under graphene shrink wrap undergo pressure denaturation, affecting vicinal hydration. The water crystallizes at MBD-DNA complexes and spinodally dewets at pressure-denatured NA proteins on mica. Finally, the CVD growth of h-BN progresses from planar, large-grain films to amorphous, polymeric films as surface catalysis is suppressed and the growth pressure is increased. Also, the CVD h-BN films are thicker and more defective on high-index Cu facets versus low-index Cu(100).

To Julia, whose love made this possible

ACKNOWLEDGMENTS

First, I would like acknowledge my graduate advisers Prof. Joseph Lyding and Prof. Eric Pop. It was my great privilege to have worked under you both simultaneously. The intellectual freedom, curiosity, and advice you provided me allowed me to become a creative scientist and independent thinker. Your combined attention to detail and constructive feedback will serve me well in my future work in nanotechnology as well as my other academic endeavors. The level of camaraderie in your groups was admirable, which certainly increased collaboration and made work more enjoyable. Further, I would like to thank Dr. Kurt Gaskill at the U.S. Naval Research Laboratory for his research advice, financial support, and jovial conversations during my research experience there in the summer of 2012.

I would like to thank my dissertation committee members: Prof. Rashid Bashir, Prof. Martin Gruebele, and Prof. Umberto Ravaioli. I appreciate the helpful comments you have provided and the time commitment that you have levied for this body of work. I hope that I have the pleasure to collaborate closely with you all in the future. I am exceptionally grateful for the varied funding sources that have financed my graduate work: the National Defense Science and Engineering (NDSEG) graduate fellowship, issued through the Army Research Office (ARO); the Department of Electrical and Computer Engineering (ECE) Distinguished Fellowship; the Beckman Graduate Student Fellowship through the Beckman Foundation; the Naval Research Enterprise Intern Program (NREIP) through the American Society for Engineering Education (ASEE); the National Science Foundation (NSF) through grant CHE 10-38015; and finally, the Office of Naval Research (ONR) through grant N00014-06-10120.

I am especially appreciative to the former Pop and Lyding lab students who collaborated with me closely, provided me untold amounts of advice and stories, and shared great times with

me at conferences and around the grill: Dr. David Estrada, Dr. Kevin He (aka He-Man), Dr. Albert Liao, Dr. Zhun-Yong Ong, and Dr. Scott Schmucker. Equally great things can be said about my friends in the lab who made life always more interesting: Dr. Sumit Ashtekar, Dr. Myung-Ho Bae, Dr. Ashkan Behnam, Dr. Greg Scott, Dr. Thierry Tsafack, Dr. Wei Ye, Basil Aruin, Enrique Carrion, Yaofeng Chen, Sumit Dutta, Jae-Won Do, Vince Dorgan, Chris English, Kyle Grosse, Sungduk Hong, Sharnali Islam, Torin Kilpatrick, Justin Koepke, Zuanyi Li, Feifei Lian, Ximeng Liu, Austin Lyons, Pam Peña Martin, Lea Nienhaus, Christopher Neumann, Duc Nguyen, Adrian Radocea, Sundar Rajarajan, Balaji Ramasubramanian, Aniruddh Rangarajan, Andrey Serov, Ning Wang, Feng Xiong, and Fan Zhang. I know that we all will cross paths in the future, and I look forward to then. I would like to note for the record that the Simpsons, Dr. Strangelove, and Futurama references made by Basil Aruin, Kevin He, and Justin Koepke were far too infrequent. I charge them to make more in the future, as these references assuredly increased lab productivity ten or even one-hundred fold.

I would like to thank my great collaborators, as it has been my utmost honor to work with you: Prof. Narayana Aluru, Prof. Gregory Girolami, Prof. Prashant Jain, Dr. Jiwook Shim, Dr. Parsian Mohseni, Dr. Salvador Barraza-Lopez, Dr. Rick Haasch, Dr. Marina Timmermans, Dr. Yang Xu, Dr. Nelson Garces, Dr. Virginia Wheeler, Dr. Boris Feigelson, Dr. Travis Anderson, Dr. Brent Walling, Dr. Tim Spila, Dr. Dennis Nordlund, Omar Khatib, Greg Damhorst, Josh Kaitz, Houssam Daoud, Yanbin Wu, Anindya Nath, Shouvik Banerjee, Sarah White, Justin Oberst, and Eric Salm.

Additional thanks go to the undergraduate students that worked with me, as I could not have done it without you. Thank you for your unwavering dedication, and I wish you nothing but great things in the future: Rushabh Mehta, Isha Datye, Jayan Hewaparakrama, Greg Doidge, Jose

Matamoros, Thaddeus Krawczyk, Charishma Puliyanda, Vineet Nazareth, Yehan Liu, and Roshan Choxi.

Further thanks go to the supporting research staff who made this research possible: Kelly Young, Karen Driscoll, Scott Robinson, Cate Wallace, Kriss Eisenhauer, Hal Romans, Edmond Chow, Yaguang Lian, Mike Hansen, Glennys Mensing, Kathy Motsegood, Dianwen Zhang, Scott MacLaren, Jim Mabon, and Stephanie Schneider.

Thanks go to my friends and family for their unconditional support of this undertaking. While my intentions might have been unclear, you assuredly backed me, every step of the way. Nothing but my warmest love and gratitude goes to you all. We will share war stories in the future, sooner rather than later. To my fiancée, Julia, I cannot wait to begin our next journey together. Your love has been a constant bulwark—through thick and thin—and words do not do justice to express how thankful I am for that. Finally, I want to thank God for all of the gifts He has given me. I humbly hope that I am fulfilling Your will, whatever it may be. Soli Deo Gloria.

TABLE OF CONTENTS

CHAPTER 1. ADVENTURES IN THE FLATLAND: AN INTRODUCTION TO TWO-DIMENSIONAL NANOMATERIALS

1.1. Moore's Law Scaling: The Ultimate Benchmark

History is demarcated by ages: the Stone Age, the Bronze Age, the Iron Age, and, more recently, the Silicon Age. Each age was ultimately replaced by a better material. Stone tools and weapons were ousted by more robust bronze. Still, bronze was soft, and so harder iron eventually won out in sword-making, utensils, and tools. And, in the late 1940s and early 1950s [1], bulky, hot vacuum tubes came up against compact, low-power, solid-state germanium and silicon transistors. There was no contest material-wise—the "Silicon Age" was born.

For almost fifty years [2], Intel and related semiconductor companies have aggressively pushed this Silicon Age forward. The Si-based transistor switch, the bedrock of the Silicon Age, has been scaled continuously in its dimensions and operating power. As a result, companies have and continue to place twice as many metal oxide semiconductor field-effect transistors (MOSFETs) in the same unit area every 18-24 months, a scaling rate eponymously dubbed "Moore's law" [2]. Companies benchmark their scaling against "technology nodes," the physical distance between the centers of two dynamic random access memory (DRAM) transistors [3]. With techniques like straining Si with Ge [4, 5], double patterning [6], and FinFET geometries [7], semiconductor companies have entered the world of nanotechnology, scaling to the 32 nm technology node and beyond [3]. The immense computational power unleashed by this Moore law's scaling has thoroughly advanced information dissemination, medicine, biology, physical sciences, predictive modeling, and countless other fields.

Thus, it appears that all is well in the Silicon Age. Regardless, all of that switching power comes at price. Si-based FETs are energy hungry devices; to operate, they require a power

density of ~100 W/cm^2 [8], equivalent to a light bulb being concentrated into a fingernail. These power densities have forced semiconductor companies to increase the area footprint for their central processing units (CPUs), lest their chips melt. Overall, the varied forms of Si-based computing—at home, at work, in data centers, and in the cloud—require over 22 GW per year in the United States alone [8]. Computing's ubiquitous nature assuredly will make this energy burden more severe in the future. Moreover, at technology nodes below 45 nm, Si-based FETs suffer from severe short channel parasitics [9], increasing the switching power and consequently limiting scaling.

Moore's law scaling below the 22 nm node might be slowed by technological issues like extreme-UV lithography [10], but semiconductor companies are tenacious, innovative, and will continue the Moore's law march. Nevertheless, the fundamental power dissipation and short channel concerns still will plague the Si material. Further, worldwide energy concerns beg the question on the longevity of Si-based computing technology. Better materials supplanted each of the Stone, Bronze, and Iron Ages and harkened in a new era of technology. But what material—or nanomaterial—can usurp the Silicon Age?

1.2. Carbon Nanotubes (CNTs)

1.2.1. The Carbon Family

For thirty years [11-14], researchers have looked to a family of carbon-based allotropes as novel nanomaterials and possible Si successors. This family is composed of buckminsterfullerenes (predominantly C_{60}, also known as fullerenes or "buckyballs"), carbon nanotubes (CNTs), graphite, and the mother material, graphene [15]. All of these allotropes differ in their "electronic dimensionality". While they are spatially three-dimensional objects, charged carriers in the materials experience electronic effects as if they were confined in one,

two, or three dimensions. Fullerenes are 0-dimensional ("0D") compounds [16], CNTs are 1D compounds [17], graphene films are 2D compounds [14], and graphite stacks are 3D compounds [18] of ten or more graphene layers [15]. The remainder of this dissertation will refer to 1D, 2D, and 3D materials in the electronic context, despite 0D and 1D nanomaterials having finite diameters and 2D materials having a finite, atomic thickness.

1.2.2. Band Structure of CNTs and Graphene

The electronic band structure of nanomaterials ultimately decides their electronic, optical, and vibrational properties. Therefore, it is important to discuss the band structure of 1D CNTs and 2D graphene before fully addressing their innate properties. Iijima discovered CNTs in 1991 [11, 12], further catalyzing the carbon nanomaterial research field. CNTs are made up of a sheet of graphene, an atomically thin, honeycomb-structured, hexagonal carbon lattice [19]. Research teams have highlighted this 1D-2D connection by unraveling grown CNTs into narrow graphene ribbons [20, 21]. Figure 1.1a shows the two C atom unit cell basis [22] for graphene, and Fig. 1.1b gives a diagram of a graphene sheet. The two atom basis also applies to the band structure of CNTs [23]. Rolling the graphene monolayer into a cylinder of diameter d and length L gives a CNT, as shown in Fig. 1.1c. Graphene has two primary edges, the "zigzag" and "armchair"

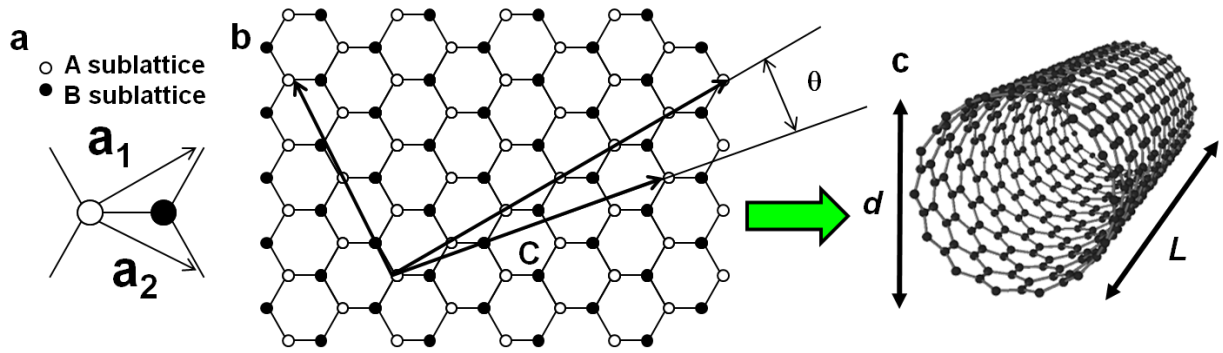

Figure 1.1. (a) The two independent A and B carbon sublattices that describe graphene and CNTs. **(b)** A prototypical graphene sheet. CNTs are created by rolling along the circumferential vector **C** with a chiral angle θ versus the primary zigzag and armchair graphene directions. **(c)** Schematic of a fully rolled CNT of diameter d and length L. Figure modified in part from [19] with permission.

edges, indicated in Fig. 1.2 [22, 23]. CNTs all have a unique chiral angle θ (Fig. 1.1b) determined by how the CNT is rolled relative to the zigzag direction. The rolling vector **C** is represented by a superposition of the two sublattice basis vectors by $\mathbf{C} = n\mathbf{a_1} + m\mathbf{a_2}$. These integers n and m are related to the chiral angle θ by $\cos\theta = (2n+m)\cdot\left(2\sqrt{n^2+nm+m^2}\right)^{-1}$, and consequently the ($n$, m) indices define a CNT's chirality. CNTs with rolled at angles of 0°, 30°, and 0° ≤ θ ≤ 30° are zigzag, armchair, and chiral CNTs, respectively. Combining this information with graphene's band structure will allow us to determine the CNT band structure.

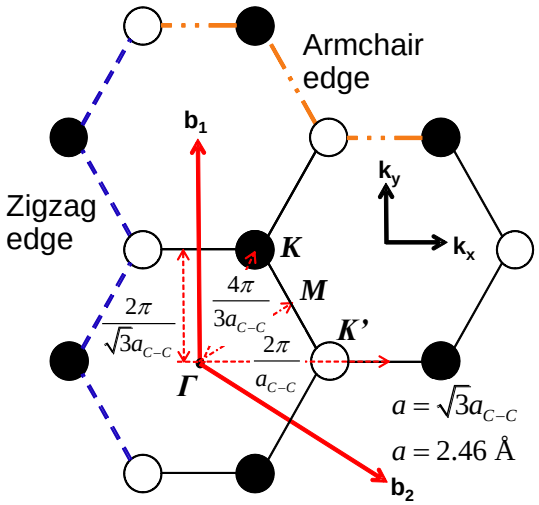

Figure 1.2. Zigzag (blue dashed), armchair (orange dot-dashed), and high symmetry (*Γ*, *K*, *M*, *K*') directions in the graphene *k*-space (i.e., the Brillouin zone). Graphene's lattice constant is 2.46 Å [19].

Graphene possesses a linear band structure at low energy, expressed as $E(k) = \hbar v_F|\mathbf{k}|$, where $\hbar$ is Planck's constant over 2π, v_F is the Fermi velocity in graphene (ca. 1×10^6 m/s [22, 24]), and $|\mathbf{k}|$ is a wavevector in momentum space [25]. The high energy band structure of graphene has been explored theoretically [22], but it is out-of-scope here. Using angle-resolved photoemission spectroscopy (ARPES), many groups have verified the linear valence band structure [26, 27] of graphene. With "doped" samples (see Section 1.3.1) [28], the linear nature of the conduction band has also been confirmed with ARPES. Thus, the above expression is valid for our consideration. Two immediate consequences of the graphene band structure are the symmetry of the conduction and valence bands and the lack of a band gap between them.

Perfect CNT edge terminations force electronic quantization along the transverse direction (the "diameter" direction, see Fig. 1.1c). This changes the electronic dimensionality

from 2D to 1D. Graphene's linear band structure must be modified to accommodate and then the tight-binding approximation can be used to get

$$E_{\text{q-zz}}(k_{\text{x}}) = \pm t_{\text{A-B}}\left[1 \pm 4\cos\left(\frac{ak_{\text{x}}}{2\sqrt{3}}\right)\cos\left(\frac{q\pi}{n}\right) + \left(\cos\left(\frac{q\pi}{n}\right)\right)^2\right] \quad (1.1)$$

$$E_{\text{q-a}}(k_{\text{x}}) = \pm t_{\text{A-B}}\left[1 \pm 4\cos\left(\frac{ak_{\text{x}}}{2}\right)\cos\left(\frac{q\pi}{n}\right) + \left(\cos\left(\frac{ak_{\text{x}}}{2}\right)\right)^2\right] \quad (1.2)$$

where $E_{\text{q-zz}}(k_{\text{x}})$ is the band structure of a zigzag CNT, $E_{\text{q-a}}(k_{\text{x}})$ is the band structure of an armchair CNT, $t_{\text{A-B}}$ is the tight-binding energy term, a is the graphene lattice constant (2.46 Å), q is an integer, n is a chiral index, and k_{x} is a vector in momentum space along the CNT axis [29]. The dispersions in Equations 1.1 and 1.2 are subject to the constraints $-\pi < k_{\text{x}} \cdot a < \pi$ for zigzag CNTs and $-\pi/\sqrt{3} < k_x \cdot a < -\pi/\sqrt{3}$ for armchair CNTs, respectively. Furthermore, if the axial wavevector $\mathbf{k}_{\text{x}}$ crosses the high symmetry points K and K' (Fig. 1.2) in the first Brillouin zone (BZ), then carrier conduction can occur through the delocalized π electron cloud. This is akin to the CNT band structure in Equations 1.1 and 1.2 simplifying to the metallic, linear graphene band structure. The high conduction condition occurs when $k_x = 2\pi/\left(a\sqrt{3}\right)$ [29], reducing Equations 1.1 and 1.2 to two CNT electronic types: semiconducting and metallic. Semiconducting CNTs occur when the difference of CNT chiral indices $n - m$ is not divisible by three, and that statement's negation is true for metallic CNTs. Therefore, a large, random group of CNTs will be electronically polydisperse, having 2/3 semiconducting and 1/3 metallic CNTs.

1.2.3. Issues in CNT-Based Applications

1.2.3.1. CNT Field Effect Transistors (FETs)

In saturation, the drive current in Si-based FETs is defined by the expression

$$I_{DS} = \frac{\mu C_{ox} W}{L}\left(V_{GS} - V_T\right)^2 \tag{1.3}$$

where C_{ox} is the gate oxide capacitance, W is the transistor channel width, L is the transistor channel length, V_{GS} is the gate-source voltage, V_T is the threshold voltage (when the transistor exits the subthreshold region and turns "ON"), and μ is a constant defined as the carrier mobility [9]. When advancing to the next technology node (see Section 1.1), device designers want to scale W, L, and $V_{GS} - V_T$ while maintaining a constant mobility. For Si-based devices, the mobility often decreases with smaller device dimensions due to incidences of ionized impurity scattering and optical phonon scattering [30]. While these concerns are troublesome but not insurmountable, the solid-state semiconductor community is continually looking for high-mobility materials. For decades, group III–V compound semiconductors provided high-mobility materials for high-electron mobility transistors (HEMTs) and heterojunction bipolar transistors (HBTs) [30]. Still, high hole mobility III–V compounds did not exist, preventing III–V entry in Si-based complementary MOSFET (CMOS) logic. CNTs and graphene are both high-mobility materials with symmetric band structures, thereby garnering great interest for their use in CMOS-type applications.

Therefore, using high-mobility, semiconducting single-walled CNTs (SWNTs) seemed like an obvious choice for next-generation, post-Si CMOS logic. Soon after CNT isolation, high-performance single CNTFETs were reported, with measured field-effect mobilities as high as 79,000 $cm^2V^{-1}s^{-1}$ (>300 μm long semiconducting SWNTs) [31]. While one CNTFET is great for demonstrating fundamental device physics, millions of devices are needed to drive substantial currents and make complex circuitry. Large-scale, cheap growth methods are required to produce the CNTs necessary for higher level device construction. Advances have been made in CNT synthesis, and large quantities of CNTs are now produced by processes like arc discharge [32,

33], laser ablation [34], high-pressure carbon monoxide (HiPco) [35], and chemical vapor deposition (CVD) [36-40].

1.2.3.2. Chirality Control

There are further issues for SWNTs in typical CNTFET applications. Approximately a third of a random group of SWNTs will be metallic, and these metallic SWNTs will prevent the CNTFET from turning off. Groups have made advances in controlling chirality during SWNT CVD growth [36, 38] on a substrate, but perfect chirality control remains to be seen, limiting large-scale device work. Electronically [41] and chirally [42] pure SWNTs solutions have been made via the density gradient ultracentrifugation (DGU) technique from polydisperse, raw SWNT materials. The DGU method is solution-based, employing anionic surfactants like sodium dodecyl sulfate (SDS) and sodium cholate (SC) [41] and non-ionic surfactants like Pluronic [43]. Nevertheless, any CNTFET application will require SWNTs to be deposited on a substrate from a purified solution. Often, these deposition processes randomly align the SWNTs and introduce hard-to-remove, hysteretic surfactants, both of which degrade CNTFET performance.

1.2.3.3. CNT-CNT Junctions and Alignment

Electronic carriers percolating [44] through two randomly crossing SWNTs will experience a higher resistance at the SWNT junction from two factors: the SWNT electronic type (Fig. 1.3a) and the overlap junction area (Fig. 1.3b). Figure 1.3c shows the ideal case, wherein the two SWNTs do not cross from perfect alignment. The junction resistance for metallic-semiconducting and metallic-metallic SWNT junctions was ~600 kΩ [45] and ~100 kΩ [46], respectively. These high junction resistances lead to local Joule heating at the SWNT junctions [37, 47]. For CNT network (CNN) devices [37, 48], junction heating ultimately leads to thermal runaway, resulting in intriguing CNN fissures and device failure.

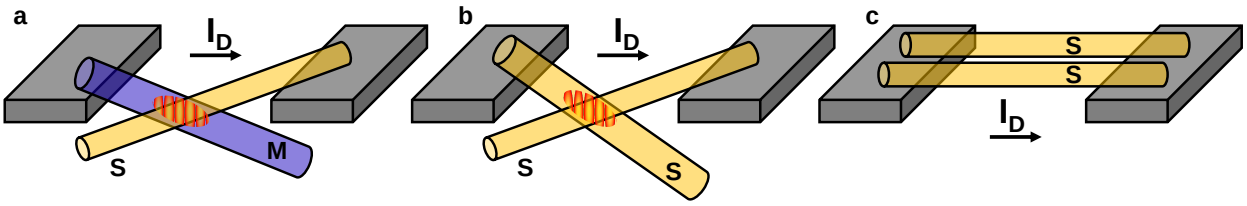

Figure 1.3. Different CNT-CNT junction types. **(a)** Schottky-barrier (SB) junction formed between a metallic (M) and a semiconducting (S) SWNT. M-S junction resistance is highest. **(b)** Junction formed between two S SWNTs. Junction resistance is lower than (a). **(c)** No junction between perfectly aligned S SWNTs.

When SWNTs are solution-deposited onto surfaces, random networks can result, giving a high density of resistive SWNT junctions. Solution-based SWNT alignment using techniques like meniscus alignment [19, 49], layer-by-layer combing [50], and stick-slip dewetting [51] can produce quasi-aligned SWNT networks with low junction density. In addition to the aforementioned Joule heating effects, high resistance SWNT junctions lower the mobility in a CNN device. A recent report showed quasi-aligned CNNs being deposited by thermal precipitation [52]. Thermally precipitated CNNs possessed increased I_{ON}/I_{OFF} ratios—a general metric for transistor performance—and higher mobilities than the other, more misaligned deposition techniques explored [52].

On the other hand, nearly perfect CNT alignment results for catalyst-assisted, CVD-grown SWNTs on ST-cut quartz [39]. Nevertheless, CVD growth does not yet have chirality control, though advances have been made by metallic shell/SWNT burn out [53] and metallic SWNT etching through a thermoplastic polymer mask [54]. Problematic SWNT junctions—resulting from growth, CNN transfer, or deposition—can have metal deposits placed on them by SWNT junction-induced thermolysis of metallic precursors [47]. These "nanosoldered" SWNT devices have higher I_{ON}/I_{OFF} ratios and better CNTFET performance [47].

1.2.4. Other CNT Concerns

All transistors require source and drain contacts and a gate over the channel region, separated from the channel by a thin gate dielectric. It is still challenging to making ohmic

contacts to CNT devices [55], and lowering drive current and causing a voltage drop at the contacts. Unlike inert graphene [56], thin gate dielectric ($t_{ox} \leq 8$ nm) placement via atomic layer deposition (ALD) on the CNT channel is feasible [57], eliminating that possible concern. Also, CNTs can be covered with sputtered overlayers like phase change memory (i.e., $Ge_2Sb_2Te_5$, GST). A recent report conformally placed GST on CNTs and also within a CNT "nanogap," demonstrating small footprint, low power memory bits [58]. These findings suggest that deposition on CNTs is a non-issue.

A more pressing concern involves the use of large quantities of grown and dispersed SWNTs. During the handling and dispersal of these nanomaterials, known carcinogenic solvents are employed [59, 60], necessitating increased precaution with nanomaterial manipulation. More importantly, there is risk for SWNT and SWNT bundles to become airborne during these manipulations. CNTs have been shown to cause lung granulomas [61], to increase risk of contracting mesothelioma [62], and to suppress phagocytosis of common pulmonary infections like *Pseudomonas aeruginosa* [63]. Still, there is debate as to the overall pulmonary toxicity of CNTs [64]. Therefore, any prominent future use of CNTs will require consensus on CNT toxicity before leading to a new set of safety standards.

1.3. Graphene

1.3.1. Graphene's Structure and Isolation

As detailed in Section 1.2.2, graphene is a 2D, atomically thin, carbon sheet with a low-energy, linear band structure. For nearly eighty years [65], the prevailing wisdom claimed that such atomically thin sheets could not exist, as energetically they should segregate into few layer sheets [66] to minimize thermal fluctuation. However, in 2004 and early 2005, researchers Andre Geim and Kostantin Novoselov disputed Peirels [65], Landau, and others [66] by isolating few-

layer graphene [67] and monolayer graphene [14] using Scotch tape and natural graphite. They placed their "exfoliated" graphene (and graphite) samples on SiO_2 of a proper thickness (ca. 300 nm or 90 nm [14, 68]), producing strong optical contrast and allowing them to modulate graphene's Fermi level by the electric field effect [14, 67, 69]. Geim and Novoselov's work in isolating graphene ultimately started the field of graphene science, winning them the Nobel Prize in Physics in 2010. After isolation, researchers discovered the high intrinsic (i.e., suspended) mobility [70], high thermal conductivity [71-73], and superior mechanical flexibility [74-76] of graphene. All of these characteristics—and many others—have caused an explosion of research in fundamental graphene science and applications.

1.3.2. Large-Area Production of Graphene

1.3.2.1. Techniques

While nanomaterial mechanical exfoliation [14, 67, 77] from bulk crystals is useful for studying fundamental nanomaterial properties, it is a stochastic process that produces small, micron-sized flakes. Hence, it is a not technologically scalable procedure. Conversely, large-area graphene production proceeds in two disparate ways. Kilogram amounts of graphene flakes can be made by solvent exfoliation [78, 79], reduction of graphene oxide [80], and DGU separation [81, 82]. A large-area film composed of misoriented, thick, stacked graphene flakes occurs when these solutions are spun cast onto substrates [83]. Alternatively, the second approach produces large-area graphene with layer number control. These methods include molecular beam epitaxy (MBE) of graphene [84], electron-beam heating from a carbon source in ultra-high vacuum (UHV) [85], epitaxial growth on expensive Ru [86], Ir [87], Co [88], and Rh [89] substrates, epitaxial growth on SiC [90-92], and CVD growth on Ni [93-95], Pt [96], and Cu [94, 97-104]. We will only discuss large-area, layer-controlled graphene growth via the last two methods.

1.3.2.2. Epitaxial Graphene Growth on SiC

The facial terminations used for SiC-based epitaxial graphene (EG) growth are the so-called Si-face, SiC(0001), and the C-face, SiC(000$\bar{1}$). At temperatures above ~1200 °C [105], Si sublimes off SiC, giving graphene and, on the SiC(0001) surface, an interfacial, carbon-rich $\left(6\sqrt{3}\times 6\sqrt{3}\right)R30°$ reconstruction [106]. For SiC(0001), the Si atom removal is fastest at the step edges, giving thicker graphene layers in their vicinity [107]. Figure 1.4a depicts growth on SiC(0001). Since the growth proceeds by Si sublimation, the graphene epitaxially matches the underlying SiC, at least within the SiC terraces. On SiC(0001), EG growth gives graphene domains (single grains) that are on the order of the terrace width [107] and one to two layers thick [108]. Still, the epitaxy between the graphene and SiC makes morphological artifacts and substrate defects [109] problematic for producing large-grain graphene samples with high mobility. Graphene growth rate and layer number can also be controlled by an overpressure of Ar [110] or disilane [111] for SiC(0001).

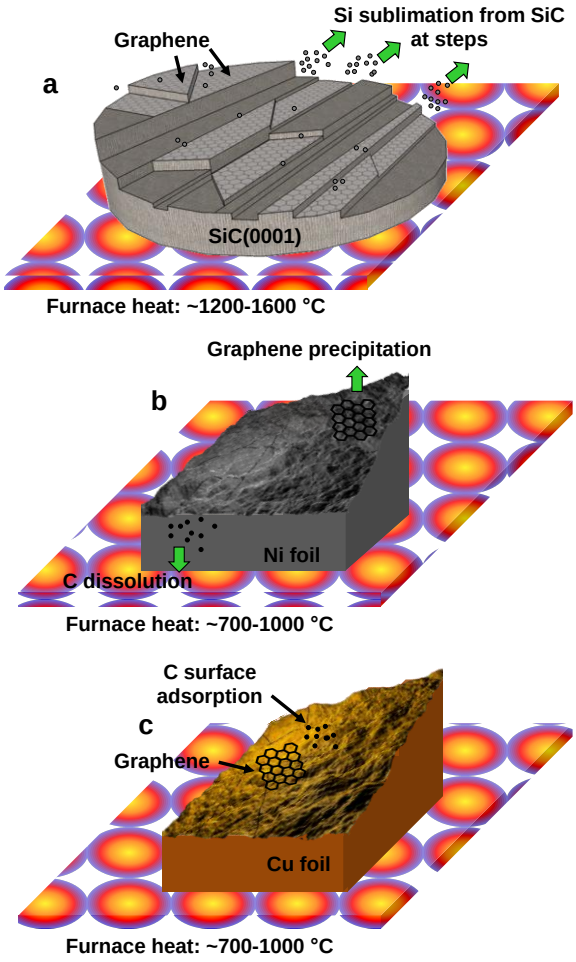

Figure 1.4. (a) Cartoon of graphene growth on SiC(0001) (Si-face). At high temperature, Si sublimes from SiC step edges and terraces, leaving graphene regions behind. **(b)** Cartoon of graphene growth on polycrystalline Ni foil. Carbon dissolves into the Ni bulk and precipitates past the C solubility point or during cooling, giving graphene. **(c)** Cartoon of graphene growth on polycrystalline Cu foil. Carbon has low solubility in Cu, forcing surface adsorption of C species. Graphene growth ends when the Cu catalytic source is covered.

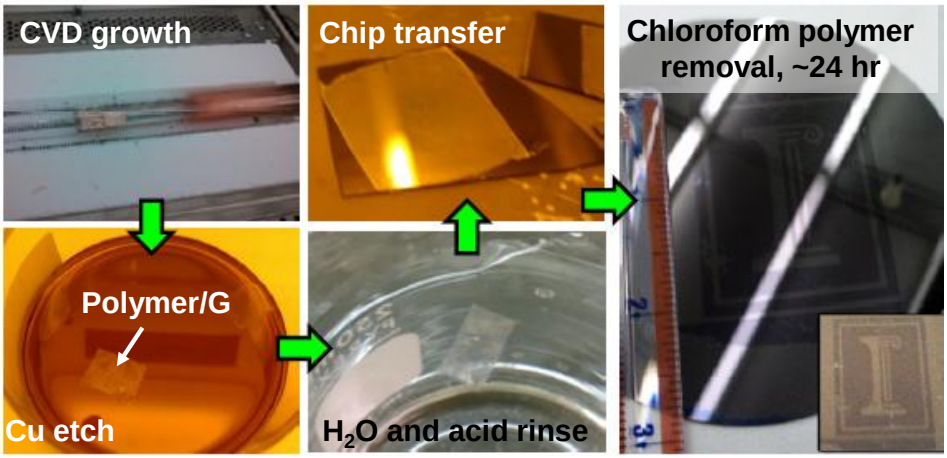

Figure 1.5. Photographic images representing each step in the graphene growth and transfer process. Note that the process would be the same if graphene growth substrate were switched from Cu to Ni.

Conversely, graphene grown on SiC(000$\bar{1}$) is multilayer and turbostratic [112], but with few defects and no sp^3 interfacial reconstruction. EG has been produced on other SiC polytypes like 4H–SiC(0001) [113], 6H–SiC(0001) [114], and 4H–SiC(000$\bar{1}$) [91], but a full treatment of the effect of the different polytypes is out of scope here.

We note that high growth temperature is out of the range of most conventional benchtop furnaces, requiring a significant capital outlay to grow EG. Moreover, technological-grade SiC wafers are expensive (about ~$1,000 per wafer [115]), and these as-received wafers often have a high defect density (e.g. screw dislocations, pits, etc.) [109]. To date, no one has transferred graphene off SiC(0001), though groups have transferred graphene layers off SiC(000$\bar{1}$) [116, 117]. Despite these cost considerations, EG on SiC is quite useful for high-performance applications not requiring graphene transfer, like high speed radio frequency (RF) mixing [92, 118].

1.3.2.3. Graphene Growth on Ni and Cu

Graphene has been grown on more inexpensive substrates like Ni [119, 120], as diagrammed in Fig. 1.4b. Compared to EG on SiC, CVD growth on Ni substrates is cost-effective, as the growth temperatures are more modest, typically at 1000°C. Further, the low cost

of Ni means that the substrates can be chemically etched, allowing the graphene to be transferred via the process shown in Fig. 1.5 to arbitrary substrates (see also Section 1.3.4). Ni-based growth proceeds by dissolution and segregation [121] of soluble C (ca. ~2 atomic percent at 1000 °C [122]) into the Ni bulk. Then, graphene precipitates when the solubility limit is exceeded or the sample is cooled. Thus, the graphene growth is mediated by the cooling rate [123] and the Ni morphology [124], and control of the graphene layer number [119] and defect density is challenging.

In 2009, Li et al. rediscovered [125, 126] CVD growth of graphene on Cu foils [127]. Figure 1.4c shows a cartoon of the graphene growth mechanism on Cu. Cu-based growth proceeds by surface adsorption [128] and Cu-induced catalysis [100] of a hydrocarbon feedstock. This feedstock is normally CH_4, but C_2H_4 [103, 129], solid [104, 130], liquid [131], and waste-based [132] precursors have been employed. Graphene on Cu shares some of the same qualities as Ni with its easily realizable growth conditions and common transfer process (Fig. 1.5). However, carbon is practically insoluble in Cu at ~1000 °C [127], forcing all hydrocarbon adsorption and dehydrogenation steps to be Cu surface-mediated. Consequently, growth on Cu allegedly terminates when the Cu catalyst is quenched, resulting in greater than 95% monolayer graphene [100]. Monolayer graphene is advantageous for many applications, and thus the self-limiting nature of graphene growth on Cu is appealing. Still, we caution the reader against thinking that CVD graphene on Cu always results in monolayer films, as will be apparent in Sections 1.3.2.4 and 1.3.2.5, Chapter 2, and Chapter 5. Growing graphene on Cu foils in roll-to-roll processes, companies have produced up to 0.76 m (30”) wide by 100 m long graphene sheets [133, 134]. Thus, technological processes involving CVD graphene on Cu are becoming viable.

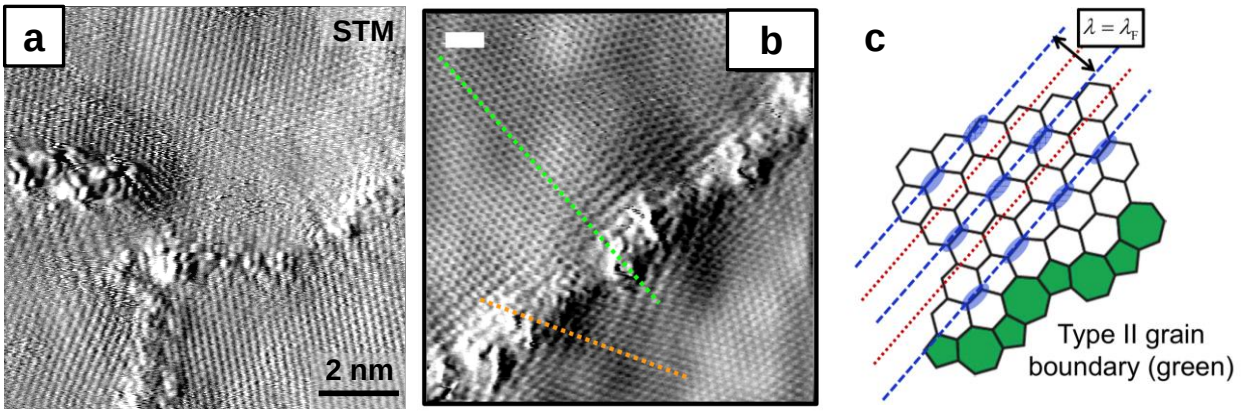

Figure 1.6. Graphene grain boundaries (GBs) and scattering. **(a)** Scanning tunneling microscopy (STM) derivative image of three merged, aperiodic graphene GBs. **(b)** Strong linear superstructures present at the GB, indicative of carrier interference and scattering. **(c)** Cartoon diagram of a GB (green) showing the C–C bonds where the superstructure in (b) would localize. Modified with permission from [139].

We will therefore focus our efforts on understanding and optimizing CVD graphene growth on Cu for a considerable remainder of this dissertation.

1.3.2.4. Graphene Grain Boundaries (GBs)

Graphene grown on Ni or Cu is rarely epitaxial [129, 135], especially if grown on polycrystalline foils. Graphene can nucleate on substrate sites where the hydrocarbon desorption probability is low and chemisorption is energetically favored. Such sites include Ni or Cu grain boundaries (GBs) [103, 124], rough sites [98], annealing twins, and vacancies. Nucleating graphene grains ultimately grow together in a complete CVD graphene film. The lack of epitaxy between the graphene overlayer and foil substrate causes these grains to be at angles with respect to each other, giving graphene GBs. These GBs can enhance the mechanical strength of the CVD film [136] and improve sensor response [137], but their electrical effects are more pernicious.

Figure 1.6a shows a scanning tunneling microscopy (STM) derivative image of three merged graphene GBs after film transfer to SiO_2/Si [138]. The GBs meander and deviate from theoretically predicted pentagon-heptagon (5-7) GB arrangements [139]. They also produce strong electronic carrier scattering [138], as evident from the linear superstructures in Figs. 1.6b-

c. Groups have identified GBs as a major limiting factor for high mobility samples [99, 140], as incident carriers undergo substantial intervalley scattering [104]. To get better graphene electronic devices, considerable effort has been made to increase graphene grain size. Some methods include using "seeds" for predetermined graphene nucleation [104], growing in Cu enclosures [101], and maintaining a high graphene growth rate through the partial pressure ratio carbon feedstock to H_2 [102]. Alternatively, films riddled with reactive GBs could be "passivated" by metallic overlayers that will readily adsorb on the defects. Preliminary work growing highly doped InAs on graphene showed island formation on GBs, resulting in a two-fold mobility improvement. This suggests the possibility of GB passivation. Still, that study's primary goal was to look at the epitaxial growth relationship between InAs and $In_xGa_{1-x}As$ and a graphene substrate [141]; further work is necessary to see if GBs can be passivated by III–V compounds.

1.3.2.5. Additional Graphene Growth on Cu Issues

Thus, graphene GBs are problematic for CVD graphene growth on non-epitaxial metals like Ni and Cu. In Section 1.3.2.4, we briefly mentioned some ways to mitigate graphene GB formation by nucleation suppression. Regardless, there are further issues in lowering defect density and also controlling spurious graphene layer growth. Bilayer and multilayer graphene growth occur if the CVD growth pressure is not carefully maintained [97]. Depending on the growth conditions, these multilayer growths can be Bernal (i.e., AB) stacked [142] or turbostratic [138, 143] and twisted [144-146]. Further, growth at low carbon feedstock partial pressure and high temperature (~1000 °C) has a slow growth rate [147]. These growth conditions can give monocrystalline graphene samples [102, 104], if growing at atmospheric pressure with an excess of H_2 [102, 148]. That notwithstanding, a slow growth rate gives poor film stitching and

discontinuities. Another factor is substrate roughness, which increases graphene nucleation [98, 124]. This necessitates growth on smoother, evaporated Cu thin films [149] or on chemically mechanically polished (CMP) Cu foils [150]. Successful graphene growth on Cu thin films (ca. ~250 nm) is challenging, as Cu readily evaporates and dewets at 1000 °C and low pressure [151]. The Cu dewetting process gives more defective graphene films. Nonetheless, groups have recently grown graphene on molten Cu thin films on refractory Mo substrates at ~1090 °C [152], suggesting a route to circumvent these roughness issues. Finally, we must consider the polycrystalline nature of the Cu growth substrate itself [103]; we will discuss this in detail in Chapter 2.

1.3.3. Band Gap Opening in Graphene

1.3.3.1. Graphene Nanoribbons (GNRs)

CMOS-based switching electronics require a band gap. Graphene's linear band structure (Section 1.2.2) makes manifest bizarre physics like Klein tunneling [153], Veselago lenses [154], and excitonic condensation [155, 156]. Still, this linear band structure means that graphene has no band gap, precluding it from conventional, CMOS-based electronics. Currently, three methods exist for opening a band gap in graphene: patterning graphene into graphene nanoribbons (GNRs) to get quantum confinement [157]; applying transverse electric fields to AB-stacked bilayer graphene [158]; and covalent, chemical functionalization of graphene [159-161]. Quantum confinement in GNRs can open a band gap of up to ~0.8 eV [157]. There have been many reports of GNR-based electronic devices [20, 162-164], all which suffer from metallic edge states [157, 165], edge roughness [166, 167], or small band gaps. Recent progress with GNR growth by bottom-up molecular assembly and cyclodehydrogenation [168, 169] is promising. This technique can achieve atomically precise, armchair (see Section 1.2.2) GNR

edges. Regardless, it remains to be seen how this method will be scalable and how it will circumvent the issues intrinsic to CNTs (Section 1.2.3 and following subsections). Hence, we will dismiss top-down or bottom-up GNR fabrication as a possible route for band gap opening in graphene.

1.3.3.2. Transverse Electric Fields

The band structure of AB-stacked, bilayer graphene differs from monolayer graphene from an interlayer potential term in the Hamiltonian [170]. By applying a transverse electric field to AB-stacked graphene, a ~0.25 eV band gap can be opened [142, 158]. While vapor-assisted CVD growth [171] can produce AB-stacked graphene [142], large-scale stacking order varies dramatically based on the growth conditions [138, 143, 145]. To open the band gap, the fabrication requires top and bottom gates. This eliminates the ability to address individual devices on a wafer and conjures problems with top-gate dielectric deposition on graphene (vide infra). Furthermore, the large transverse electric fields required to open the gap can cause unwanted parasitics. We thus dismiss bilayer graphene as a route to band gap opening.

1.3.3.3. Covalent Functionalization

Graphene can be functionalized by hydrogen [160], oxygen [172], chlorine [173], bromine [174], and fluorine [161, 175], scalable processes that open band gaps from 0 to 3 eV [176]. The most prevalent graphene functionalization is by the oxidation of graphite through the so-called Hummers method [177]. The subsequent water stabilization gives graphene oxide (GO) [80, 178]. However, non-uniform epoxy and hydroxyl groups occur in GO production [159, 172]. Houssain et al. recently reported more uniform oxygenation of graphene [172], but scalability remains to be seen. Despite theoretical reports [179], graphane, a fully hydrogenated version of graphene [160], appears unstable at room temperature, dehydrogenating to graphene.

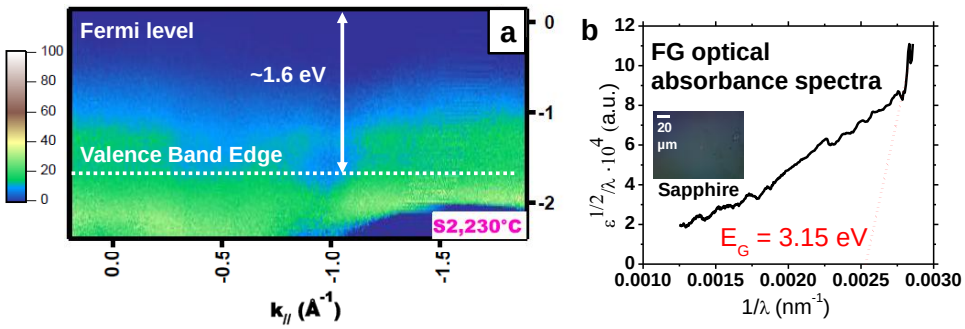

Figure 1.7. (a) ARPES valence band structure for single-sided FG on Cu (~C_4F stoichiometry), revealing a 1.6 eV band offset to the valence band edge from the Fermi level. If the Fermi level is mid-gap in the FG film, the band gap will be ~3.2 eV, consistent with predictions [161]. **(b)** Optical absorbance measurement for a FG film on sapphire. Optical image shown inset. Optical band gap is ~3.2 eV by the Tauc equation [176], also consistent with theory [161].

The fluorination of graphene gives two major stoichiometries, single-sided (C_4F) [161] and dual-sided (perfluorographene, CF) fluorinated graphene (FG) [175]. These functionalized derviatives are easy to produce, have high stability (relative to graphane), and give a ~3 eV band gap, as shown in Fig. 1.7 for single-sided FG. FG films are more sp^3 in character, breaking the delocalized π network. For dilute fluorinations (C_xF, $x > 10$), the fluorine gathers in islands, and electrical conduction in the film proceeds by variable range hopping (VRH) [180]. Higher fluorine contents open a band gap and give heightened reactivity, as discussed in Chapter 3. Also, our preliminary data show that the fluorine coverage depends critically on the graphene's surface charge (i.e., "doping") [181]. Using polycrystalline Cu, mica, SiO_2, and quartz substrates, we can change the covalent C–F bonding and therefore the band gap, based solely on the graphene doping. Fluorination appears to be most viable way to open a gap in graphene.

1.3.4. Transferring Graphene

1.3.4.1. Conventional Transfer Process

Most graphene and related nanomaterial applications require the films to be removed from its growth substrate (Cu, Ni, SiC, Pt, et al.) and placed on another arbitrary surface. As shown in Fig. 1.8, the standard method by which graphene is transferred from its growth surface

involves a poly(methyl methacrylate) (PMMA) support [95, 119, 182-187]. Further PMMA residues are purportedly removed by Ar/H_2 gas annealing [188]. Moreover, in these wet transfers, water layers are trapped between the graphene and the receiving substrate [182]. Also, Cu, Fe, and organic residues from the transfer can physisorb on the underside of graphene and dope it. Using a modified RCA clean [189] during the graphene transfer removes some—but not necessarily all—of the metallic and organic contaminants. This process somewhat addresses the graphene underside, but the topside graphene, despite the Ar/H_2 cleaning, still possesses considerable PMMA contamination [184]. The contamination is disconcerting for graphene applications that have low thermal budgets or require atomic cleanliness. Alternative polymers like poly(bisphenol A carbonate) (PC) appear to come off more cleanly than PMMA [183, 190]. Nevertheless, the mechanism for why PC comes off graphene cleanly is unknown. Also, no one has thoroughly explored the use of PC and other graphene transfer polymers in devices, layered structures, and in atomic-level STM experiments. We answer these PC-related questions in more detail in Chapter 4. Finally, we note that manipulating the polymer/graphene stack from etchant to substrate requires a careful touch [182, 191]. This high sample-to-sample variation raises the question for a more industrially compatible nanomaterial transfer approach.

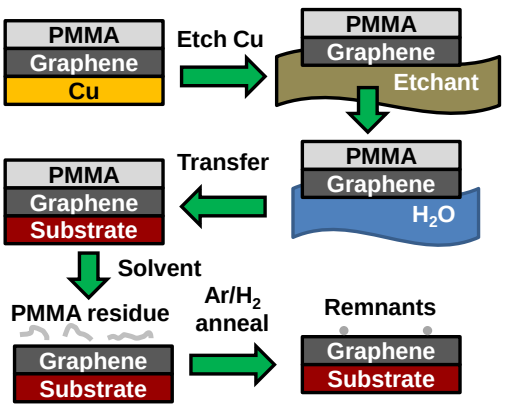

Figure 1.8. Conventional graphene and related nanomaterial transfer process using poly(methyl methacrylate) (PMMA). PMMA introduces hard-to-remove residues on the graphene top-side.

1.3.4.2. Industrial Processes

Companies like Samsung and Sony have developed roll-to-roll processes to transfer 0.76 m by 100 m graphene sheets off Cu [133, 134]. These techniques support the graphene during transfer with thermal release tape (TRT) [116, 133, 192]. After the

Cu is removed from the TRT/graphene, the TRT is released by exceeding the thermal release temperature (~90-120 °C for most TRTs). However, just like PMMA, the TRT introduces adhesive residues that are hard to remove [116]. Furthermore, the TRT transfer process introduces many holes within the graphene sheet. Industries circumvent this by transferring graphene several times, as their applications are not layer number sensitive [133]. This problem has recently been partially solved by transferring the graphene onto a hot substrate [193]. By using a bilayer support—such as bonded TRT with an interfacial PC layer—concerns with adhesion and cleanliness can be mitigated. We discuss these methods in more detail in Chapter 4.

Another industrial process is the electrochemical delamination of graphene from its metallic growth substrate. This process was shown for graphene on Pt [96] and Cu [194, 195]. In this process, a support (PMMA, PET [194], etc.) is placed on graphene on Cu (or Ni, Pt, etc.) with part of the graphene on Cu still exposed. The supported film is a cathode in an electrolyte of NaOH [96, 194] or $K_2S_2O_8$ [195]. The anode can be another piece of Cu, Pt [96, 194], or a glassy carbon rod [195]. By biasing the electrochemical cell, H_2 is evolved and intercalates between the supported graphene and the Cu. Eventually, the film is removed from the Cu, allowing the catalyst to be recycled and the supported film to be transferred. Avoiding Cu etching assuredly lowers the amount of backside graphene contamination [97, 196]. Further, catalyst recycling is cost-effective and practical for carefully prepared substrates (e.g. single crystals).

1.3.5. Top Gate Dielectrics on Graphene

Original graphene experiments [14, 67, 197] demonstrated the field-effect through a thick (ca. 90–300 nm) oxide on a highly doped (n^{++} or p^{++}) Si back gate. This global back gate prevents one from individually addressing graphene FET devices on a wafer. The capacitance—and also the induced carrier density *n*—in the graphene FET are determined by

$$C_{ox} = \frac{\kappa_r \kappa_0}{t_{ox}} \tag{1.4}$$

$$n = -\frac{C_{ox}\left(V_{GS} - V_D\right)}{q} \tag{1.5}$$

where C_{ox} is the capacitance per area from the SiO_2, κ_r is the dielectric constant of SiO_2 (~3.9), κ_0 is the permittivity of free space (8.854×10^{-14} F/cm), t_{ox} is the SiO_2 thickness, q is the elemental charge (1.6×10^{-19} C), V_{GS} is the gate–source voltage, and V_D is the voltage at the conductivity minimum in graphene, termed the "Dirac point" [24, 197]. The obvious consequence of Equations 1.4 and 1.5 is that the induced carrier density n decreases with thicker t_{ox}. High carrier densities are required to get current saturation in graphene [198], necessary for the graphene FET to depend less on the drain–source bias V_{DS} and be truly "ON". Therefore, t_{ox} needs to be lower for high-field graphene FET operation [24, 199]. Top-gate dielectric deposition is the only way to individually address the graphene FETs and reach current saturation simultaneously.

The conventional top-gate dielectric deposition method is by ALD. Regardless, graphene's sp^2 structure is chemically inert [56] and somewhat hydrophobic [200]. As ALD proceeds by successive H_2O and metalorganic precursor (e.g. trimethylaluminum and tetrakis(ethylmethylamino)hafnium) cycles, hydrophobic surfaces [201, 202] can be problematic. For graphene, the usual trick is to add interfacial layers between graphene and the ALD overlayer. These ALD seeding layers include evaporated Al [203], perylene-3,4,9,10-tetracarboxylic dianhydride (PTCDA) [204], O_3 [205, 206], polyhydroxystyrene derivatives [207], and surface fluorine [108]. Nonetheless, defects often are induced in this seeding process during metal evaporation, O_3 exposure, and fluorination (see Section 1.3.3.3). These defects lower the mobility in graphene and reduce performance of the top-gated devices. Therefore,

many issues still persist in successfully placing and scaling ultra-thin, uniform dielectrics on graphene. We will discuss approaches to better dielectric deposition using FG in Chapter 3.

1.4. Hexagonal Boron Nitride (h-BN)

1.4.1. Initial Study and Isolation

Like graphite, there is nearly a century of research on hexagonal boron nitride (h-BN) [208-226]. Also like graphite, h-BN is a layered, two-dimensional material, possessing a resonant, honeycomb structure of B–N bonds. However, unlike graphite, h-BN is a synthetic crystal [208-210, 213, 222] and is insulating, with a 3.8–6 eV optical and electronic band gap [213, 222, 224]. By pressurizing and heating h-BN powders in the presence of a Ba–B–N solvent, large h-BN single crystals have been fabricated [222, 223]. Groups used these single crystals as exfoliation sources [225, 227, 228], vis-à-vis what was done with graphene and other 2D crystals [229]. Monolayer exfoliated graphene flakes were then dry transferred with poly(vinyl alcohol) (PVA) onto exfoliated h-BN (several layers thick), and graphene FETs were fabricated. As a result, several groups observed exceptional improvement in the mobility, charge inhomogeneity, and cleanliness of graphene on h-BN [225, 228, 230]. Via additional exfoliations and dry transfers, groups have manifested complex van der Waals heterostructures [231] using graphene, h-BN, and other 2D lamellae [77, 232-234]. Therefore, h-BN is becoming the insulating spacer and substrate of choice for graphene and related nanomaterials.

1.4.2. Large-Area Synthesis

To date, most of the high-performance applications using h-BN have been with exfoliated flakes. As was true with graphene, technological scalability requires the ability to synthesize h-BN in large-area. While large-area h-BN synthesis on single crystals like Pt(111) [235], Ni(111) [236, 237], Rh(111) [238], and Ru(0001) [239] was reported long ago, it was only recently that

h-BN was grown by CVD on more technologically relevant substrates like Cu [224, 240, 241], Ni [226, 242], and sapphire [243]. The single crystal and Ni growth studies all used borazine ($B_3N_3H_6$), an expensive, volatile h-BN precursor. Conversely, demonstrated CVD work on Cu [224, 240, 241] used ammonia borane ($H_3B–NH_3$), an inexpensive, inert, and non-toxic precursor whose pyrolysis ultimately gives the same by-products as borazine [244]. Ammonia borane has lower volatility than borazine, and to achieve growth, the material must be sublimed. Ultimately, this sublimation process increases the growth-to-growth variability. Still, this is a concern which can be easily mitigated with proper vacuum hardware and temperature control.

h-BN growth on inexpensive Cu and Ni substrates is appealing, as the process is subject to many of the same methods and knowledge gained for CVD graphene growth and transfer (Chapters 2 and 4). As a result, some of the prevailing issues for CVD graphene growth—growth pressure [97], substrate roughness [150, 245], and substrate crystallography [103]—are also applicable to h-BN growth. Electronic applications require h-BN films with large grain size and precise control over layer number. To the end of producing high-quality h-BN, we explore the effects of CVD growth pressure and Cu crystallography in Chapter 7.

1.5. Nanoscale Water

Transfer of CVD grown nanomaterials often requires water as a solvent and support, as indicated in Figs. 1.5 and 1.8. Still, dry transfer approaches have been reported [187, 246], with relatively low-yield in the area of graphene transferred. For wet nanomaterial transfers, the vestigial water is worth considering as a related nanomaterial. Understanding nanoscale fluids is important for applications in bionanotechnology [247, 248], protein folding [249], and water desalination [250]. Fluid encapsulation is one area where low-dimensional nanomaterials are well suited, as the encapsulation allows new nanoscale imaging techniques [251, 252].

Furthermore, nanoscale interactions between the solid, liquid, and vapor phases are still points of contention [253-255]. To that end, CVD nanomaterials can explore and elucidate fundamental fluid dynamics phenomena.

1.6. Motivation and Grand Challenges

Major concerns face the world in the fields of medicine, energy, and information technology. Great headway has been on these issues through the computing might of the Silicon Age. But the world's growing, aging population demands better health care, more energy, and faster information dissemination. More affordable, more sophisticated, and more integrated materials can help in undertaking the grand challenges.

Will the Carbon Age succeed the Silicon Age? Silicon has a forty-year head start, and semiconductor manufacturers are not slowing down. Thus, considerable work in carbon-based material science, physics, chemistry, and electrical engineering is still necessary to catch up to silicon. The electronic, thermal, and mechanical properties of carbon-based nanomaterials are without equal, and as such, they have niche technological applications like those in solar cells, touch screens, and RF transceivers. Regardless, as made apparent in this chapter, there are major problems with synthesizing, manipulating, contacting, and chemically modifying these carbon-based nanomaterials. Without making headway on these concerns, carbon-based nanomaterials do not stand a chance in ushering the new Carbon Age. Thus, the remainder of the dissertation will broach these problems in nanomaterial synthesis, manipulation, and chemical modification, and provide scalable solutions to those concerns. Further, this body of work will examine alternative uses for low-dimensional nanomaterials, such as heterogeneous integration with biomaterials. Heterogeneous nanomaterial layering is a burgeoning field in which silicon cannot compete. Still, that level of control requires mastery in nanomaterial synthesis and manipulation.

1.7. Dissertation Organization

In this dissertation, we investigate and solve materials problems facing the technological scalability of nanomaterials like graphene and h-BN. To that end, we use multi-scale characterization methods to examine the large-area synthesis, functionalization, and manipulation of graphene, h-BN, and related low-dimensional nanomaterials. Our studies are predominantly experimental and fundamental in nature, with simulations, devices, and other applications used to bolster our conclusions elucidating the science of these nanomaterials. This chapter has served to motivate this dissertation and to cover the background supporting literature.

In Chapter 2, we determine that graphene grown by CVD on Cu depends critically on the underlying Cu crystallography. In particular, we discover that lattice-templated graphene on low-index Cu(111) is monolayer and contains few defects. With scanning electron microscopy (SEM), electron-backscatter diffraction (EBSD), and Raman spectroscopy, we find that graphene on high-index Cu and Cu(100) is more multilayer and defective than graphene on Cu(111). Finally, we ascertain that graphene grows fastest on Cu(111).

In Chapter 3, we place high-κ HfO_2 by ALD onto CVD graphene on Cu, fluorinated graphene (FG) on Cu, and highly FG ($x < 4$ for C_xF) on transferred graphene on SiO_2/Si. For Cu substrates, we transfer the HfO_2 films to SiO_2/Si. Fluorinating graphene prior to ALD improves the HfO_2 coverage on CVD graphene on Cu and on SiO_2/Si. Dual-side fluorinated, sp^3 graphene films give pinhole and crack free HfO_2 films. We correlate the degree of fluorination to the uniformity and morphology of the ALD HfO_2 dielectrics. With the highly FG films, we achieve ultra-thin HfO_2 scaling, down to 2.0 nm.

In Chapter 4, we examine the transfer of CVD graphene off Cu using polymer scaffolds of poly(methyl methacrylate) (PMMA), poly(lactic acid) (PLA), poly(phthalaldehyde) (PPA),

and poly(bisphenol A carbonate) (PC). With optimally reactive PC scaffolds, we get the cleanest graphene transfers without any annealing, after extensive comparison with optical microscopy, SEM, XPS, AFM, STM, and device transport. Comparatively, films transferred with PLA, PPA, PMMA/PC, and PMMA have a twofold higher roughness and a fivefold higher chemical doping. We then cleanly layer nanomaterials like multilayer graphene, FG, and h-BN.

In Chapter 5, interfacial water is trapped between a cleaved mica surface and sheet of CVD graphene. We confirm the existence of trapped water with Fourier transform infrared (FTIR) and Raman spectroscopies. Using ultra-high vacuum STM (UHV-STM) at room temperature, we atomically resolve the graphene-water interface with atomic resolution. Under the graphene sheet, there are one to three layers of amorphous, trapped water. We also nanomanipulate the higher water layers at greater electron energies via the STM tip.

In Chapter 6, we examine vicinal (e.g. "interfacial") water between two seemingly hydrophobic graphene layers. We then shrink wrap water and tobacco mosaic viruses (TMV), methyl-binded domain (MBD) protein-DNA complexes, and NeutrAvidin (NA) proteins under a cleanly transferred graphene overlayer, producing highly viscous water at those graphene-biomolecule interfaces. The graphene shrink wrap exerts up to 2 GPa hydrostatic pressures, as evident from deformations in the TMV capsid and detailed molecular dynamics simulations. Such hydrostatic pressures denature the biomolecules, inserting water into the hydrophobic core. Via UHV-STM and AFM, we also produce the first observation of nanoscale water at graphene-biomolecule interfaces. The shrink wrapped water crystallizes near MBD-DNA complexes and spinodally dewets around pressure denatured NA protein residues.

In Chapter 7, we investigate the different growth regimes of large-area hexagonal boron nitride (h-BN) on Cu grown by CVD. Growing with low pressure CVD gives us high-quality,

large-grain, thin h-BN films. As we progress to atmospheric pressure CVD, the film quality degrades, giving an inhomogeneous mixture of h-BN, polyaminoborane, and polyiminoborane. This growth change occurs from a switch from Cu-mediated surface catalysis to an ammonia–borane mass transport regime. We find that our h-BN growth films are thicker and more defective on high-index Cu facets versus low-index Cu.

Chapter 8 provides some final remarks and conclusions about this dissertation. We then list some additional considerations for future studies and experiments.

1.8. References

[1] L. Hoddeson and V. Daitch, *True Genius: The Life and Science of John Bardeen*. Washington, D.C.: Joseph Henry Press, 2002.

[2] G. E. Moore, "Cramming more components onto integrated circuits," *Electronic Magazine,* vol. 38, no. 8, pp. 1-4, 1965.

[3] International Technology Roadmap for Semiconductors (July 31, 2013). 2011 Edition. [Online]. Available: http://www.itrs.net/Links/2011ITRS/Home2011.htm

[4] M. V. Fischetti and S. E. Laux, "Band structure, deformation potentials, and carrier mobility in strained Si, Ge, and SiGe alloys," *Journal of Applied Physics,* vol. 80, no. 4, pp. 2234-2252, 1996.

[5] J. L. Hoyt, H. M. Nayfeh, S. Eguchi, I. Aberg, G. Xia, T. Drake, E. A. Fitzgerald, and D. A. Antoniadis, "Strained silicon MOSFET technology," in *International Electron Devices Meeting*, 2002, pp. 23-26.

[6] C. Auth, A. Cappellani, J. S. Chun, A. Dalis, A. Davis, T. Ghani, G. Glass, T. Glassman, M. Harper, M. Hattendorf, P. Hentges, S. Jaloviar, S. Joshi, J. Klaus, K. Kuhn, D. Lavric, M. Lu, H. Mariappan, K. Mistry, B. Norris, N. Rahhal-orabi, P. Ranade, J. Sandford, L. Shifren, V. Souw, K. Tone, F. Tambwe, A. Thompson, D. Towner, T. Troeger, P. Vandervoorn, C. Wallace, J. Wiedemer, and C. Wiegand, "45 nm high-K + metal gate strain-enhanced transistors," in *Symposium on VLSI Technology*, 2008, pp. 128-129.

[7] D. Hisamoto, L. Wen-Chin, J. Kedzierski, H. Takeuchi, K. Asano, C. Kuo, E. Anderson, K. Tsu-Jae, J. Bokor, and C. Hu, "FinFET - A self-aligned double-gate MOSFET scalable to 20 nm," *IEEE Transactions on Electron Devices,* vol. 47, no. 12, pp. 2320-2325, 2000.

[8] E. Pop, "Energy dissipation and transport in nanoscale devices," *Nano Research,* vol. 3, no. 3, pp. 147-169, 2010.

[9] Y. Taur and T. H. Ning, *Fundamentals of Modern VLSI Devices*, 2nd ed. Cambridge, UK: Cambridge University Press, 2009.

[10] T. Ito and S. Okazaki, "Pushing the limits of lithography," *Nature,* vol. 406, no. 6799, pp. 1027-1031, 2000.

[11] S. Iijima, "Helical microtubules of graphitic carbon," *Nature,* vol. 354, no. 6348, pp. 56-58, 1991.

[12] S. Iijima and T. Ichihashi, "Single-shell carbon nanotubes of 1-nm diameter," *Nature,* vol. 363, no. 6430, pp. 603-605, 1993.

[13] H. W. Kroto, J. R. Heath, S. C. O'Brien, R. F. Curl, and R. E. Smalley, "C60: Buckminsterfullerene," *Nature,* vol. 318, no. 6042, pp. 162-163, 1985.

[14] K. S. Novoselov, A. K. Geim, S. V. Morozov, D. Jiang, M. I. Katsnelson, I. V. Grigorieva, S. V. Dubonos, and A. A. Firsov, "Two-dimensional gas of massless Dirac fermions in graphene," *Nature,* vol. 438, no. 7065, pp. 197-200, 2005.

[15] A. K. Geim and K. S. Novoselov, "The rise of graphene," *Nature Materials,* vol. 6, no. 3, pp. 183-191, 2007.

[16] S. Saito and A. Oshiyama, "Cohesive mechanism and energy bands of solid C_{60}," *Physical Review Letters,* vol. 66, no. 20, pp. 2637-2640, 1991.

[17] R. Saito, M. Fujita, G. Dresselhaus, and M. S. Dresselhaus, "Electronic structure of chiral graphene tubules," *Applied Physics Letters,* vol. 60, no. 18, pp. 2204-2206, 1992.

[18] J. C. Slonczewski and P. R. Weiss, "Band structure of graphite," *Physical Review,* vol. 109, no. 2, pp. 272-279, 1958.

[19] J. D. Wood, "Single-walled carbon nanotube alignment and placement by mechanical meniscus action," M.S. thesis, University of Illinois at Urbana-Champaign, Urbana, IL, 2009.

[20] L. Jiao, L. Zhang, X. Wang, G. Diankov, and H. Dai, "Narrow graphene nanoribbons from carbon nanotubes," *Nature,* vol. 458, no. 7240, pp. 877-880, 2009.

[21] D. V. Kosynkin, A. L. Higginbotham, A. Sinitskii, J. R. Lomeda, A. Dimiev, B. K. Price, and J. M. Tour, "Longitudinal unzipping of carbon nanotubes to form graphene nanoribbons," *Nature,* vol. 458, no. 7240, pp. 872-876, 2009.

[22] A. H. Castro Neto, F. Guinea, N. M. R. Peres, K. S. Novoselov, and A. K. Geim, "The electronic properties of graphene," *Reviews of Modern Physics,* vol. 81, no. 1, pp. 109-162, 2009.

[23] R. Saito, G. Dresselhaus, and M. S. Dresselhaus, *Physical Properties of Carbon Nanotubes*. London: Imperial College Press, 1998.

[24] V. E. Dorgan, M. H. Bae, and E. Pop, "Mobility and saturation velocity in graphene on SiO_2," *Applied Physics Letters,* vol. 97, no. 8, pp. 082112-082112-3, 2010.

[25] P. R. Wallace, "The band theory of graphite," *Physical Review,* vol. 71, no. 9, pp. 622-634, 1947.

[26] A. Bostwick, T. Ohta, T. Seyller, K. Horn, and E. Rotenberg, "Quasiparticle dynamics in graphene," *Nature Physics,* vol. 3, no. 1, pp. 36-40, 2007.

[27] M. Sprinkle, D. Siegel, Y. Hu, J. Hicks, A. Tejeda, A. Taleb-Ibrahimi, P. Le Fèvre, F. Bertran, S. Vizzini, H. Enriquez, S. Chiang, P. Soukiassian, C. Berger, W. A. de Heer, A. Lanzara, and E. H. Conrad, "First direct observation of a nearly ideal graphene band structure," *Physical Review Letters,* vol. 103, no. 22, pp. 226803-226803-4, 2009.

[28] A. Grüneis, C. Attaccalite, A. Rubio, D. V. Vyalikh, S. L. Molodtsov, J. Fink, R. Follath, W. Eberhardt, B. Büchner, and T. Pichler, "Angle-resolved photoemission study of the graphite intercalation compound KC_8: A key to graphene," *Physical Review B,* vol. 80, no. 7, p. 075431, 2009.

[29] M. S. Dresselhaus, A. Jorio, A. G. Souza, and R. Saito, "Defect characterization in graphene and carbon nanotubes using Raman spectroscopy," *Philosophical Transactions of the Royal Society A-Mathematical Physical and Engineering Sciences,* vol. 368, no. 1932, pp. 5355-5377, 2010.

[30] K. Hess, *Advanced Theory of Semiconductor Devices*. Hoboken, NJ: Wiley-IEEE Press, 1999.

[31] T. Dürkop, S. A. Getty, E. Cobas, and M. S. Fuhrer, "Extraordinary mobility in semiconducting carbon nanotubes," *Nano Letters,* vol. 4, no. 1, pp. 35-39, 2003.

[32] Z. Shi, Y. Lian, X. Zhou, Z. Gu, Y. Zhang, S. Iijima, L. Zhou, K. T. Yue, and S. Zhang, "Mass-production of single-wall carbon nanotubes by arc discharge method," *Carbon,* vol. 37, no. 9, pp. 1449-1453, 1999.

[33] T. Sugai, H. Yoshida, T. Shimada, T. Okazaki, H. Shinohara, and S. Bandow, "New synthesis of high-quality double-walled carbon nanotubes by high-temperature pulsed arc discharge," *Nano Letters,* vol. 3, no. 6, pp. 769-773, 2003.

[34] M. Yudasaka, T. Komatsu, T. Ichihashi, and S. Iijima, "Single-wall carbon nanotube formation by laser ablation using double-targets of carbon and metal," *Chemical Physics Letters,* vol. 278, no. 1-3, pp. 102-106, 1997.

[35] P. Nikolaev, M. J. Bronikowski, R. K. Bradley, F. Rohmund, D. T. Colbert, K. A. Smith, and R. E. Smalley, "Gas-phase catalytic growth of single-walled carbon nanotubes from carbon monoxide," *Chemical Physics Letters,* vol. 313, no. 1-2, pp. 91-97, 1999.

[36] W.-H. Chiang and R. Mohan Sankaran, "Linking catalyst composition to chirality distributions of as-grown single-walled carbon nanotubes by tuning Ni_xFe_{1-x} nanoparticles," *Nature Materials,* vol. 8, no. 11, pp. 882-886, 2009.

[37] D. Estrada and E. Pop, "Imaging dissipation and hot spots in carbon nanotube network transistors," *Applied Physics Letters,* vol. 98, no. 7, pp. 073102-073102-3, 2011.

[38] A. R. Harutyunyan, G. Chen, T. M. Paronyan, E. M. Pigos, O. A. Kuznetsov, K. Hewaparakrama, S. M. Kim, D. Zakharov, E. A. Stach, and G. U. Sumanasekera, "Preferential growth of single-walled carbon nanotubes with metallic conductivity," *Science,* vol. 326, no. 5949, pp. 116-120, 2009.

[39] S. J. Kang, C. Kocabas, T. Ozel, M. Shim, N. Pimparkar, M. A. Alam, S. V. Rotkin, and J. A. Rogers, "High-performance electronics using dense, perfectly aligned arrays of single-walled carbon nanotubes," *Nature Nanotechnology,* vol. 2, no. 4, pp. 230-236, 2007.

[40] A. Liao, Y. Zhao, and E. Pop, "Avalanche-induced current enhancement in semiconducting carbon nanotubes," *Physical Review Letters,* vol. 101, no. 25, pp. 256804-256804-4, 2008.

[41] M. S. Arnold, A. A. Green, J. F. Hulvat, S. I. Stupp, and M. C. Hersam, "Sorting carbon nanotubes by electronic structure using density differentiation," *Nature Nanotechnology,* vol. 1, no. 1, pp. 60-65, 2006.

[42] A. Green, M. Duch, and M. Hersam, "Isolation of single-walled carbon nanotube enantiomers by density differentiation," *Nano Research,* vol. 2, no. 1, pp. 69-77, 2009.

[43] A. L. Antaris, J.-W. T. Seo, A. A. Green, and M. C. Hersam, "Sorting single-walled carbon nanotubes by electronic type using nonionic, biocompatible block copolymers," *ACS Nano,* vol. 4, no. 8, pp. 4725-4732, 2010.

[44] N. Pimparkar, C. Kocabas, K. Seong Jun, J. Rogers, and M. A. Alam, "Limits of performance gain of aligned CNT over randomized network: Theoretical predictions and experimental validation," *IEEE Electron Device Letters,* vol. 28, no. 7, pp. 593-595, 2007.

[45] Z. Yao, H. W. C. Postma, L. Balents, and C. Dekker, "Carbon nanotube intramolecular junctions," *Nature,* vol. 402, no. 6759, pp. 273-276, 1999.

[46] P. N. Nirmalraj, P. E. Lyons, S. De, J. N. Coleman, and J. J. Boland, "Electrical connectivity in single-walled carbon nanotube networks," *Nano Letters*, vol. 9, no. 11, pp. 3890-3895, 2009.

[47] J.-W. Do, D. Estrada, X. Xu, N. N. Chang, G. S. Girolami, J. A. Rogers, E. Pop, and J. W. Lyding, "Nanosoldering carbon nanotube junctions with metal via local chemical vapor deposition for improved device performance," in *IEEE Conference on Nanotechnology (IEEE-NANO)*, 2012, pp. 1-5.

[48] A. Behnam, V. K. Sangwan, X. Zhong, F. Lian, D. Estrada, D. Jariwala, A. J. Hoag, L. J. Lauhon, T. J. Marks, M. C. Hersam, and E. Pop, "High-field transport and thermal reliability of sorted carbon nanotube network devices," *ACS Nano*, vol. 7, no. 1, pp. 482-490, 2013.

[49] J. D. Wood and J. W. Lyding, "Carbon nanotube alignment using meniscus action," in *IEEE Conference on Nanotechnology*, 2009, pp. 475-476.

[50] B. S. Shim and N. A. Kotov, "Single-walled carbon nanotube combing during layer-by-layer assembly: From random adsorption to aligned composites," *Langmuir*, vol. 21, no. 21, pp. 9381-9385, 2005.

[51] M. Engel, J. P. Small, M. Steiner, M. Freitag, A. A. Green, M. C. Hersam, and P. Avouris, "Thin film nanotube transistors based on self-assembled, aligned, semiconducting carbon nanotube arrays," *ACS Nano*, vol. 2, no. 12, pp. 2445-2452, 2008.

[52] M. Y. Timmermans, D. Estrada, A. G. Nasibulin, J. D. Wood, A. Behnam, D.-M. Sun, Y. Ohno, J. W. Lyding, A. Hassanien, E. Pop, and E. Kauppinen, "Effect of carbon nanotube network morphology on thin film transistor performance," *Nano Research*, vol. 5, no. 5, pp. 307-319, 2012.

[53] P. G. Collins, M. S. Arnold, and P. Avouris, "Engineering carbon nanotubes and nanotube circuits using electrical breakdown," *Science*, vol. 292, no. 5517, pp. 706-709, 2001.

[54] S. H. Jin, S. N. Dunham, J. Song, X. Xie, J.-H. Kim, C. Lu, A. Islam, F. Du, J. Kim, J. Felts, Y. Li, F. Xiong, M. A. Wahab, M. Menon, E. Cho, K. L. Grosse, D. J. Lee, H. U. Chung, E. Pop, M. A. Alam, W. P. King, Y. Huang, and J. A. Rogers, "Using nanoscale thermocapillary flows to create arrays of purely semiconducting single-walled carbon nanotubes," *Nature Nanotechnology*, vol. 8, no. 5, pp. 347-355, 2013.

[55] S. C. Lim, J. H. Jang, D. J. Bae, G. H. Han, S. Lee, I.-S. Yeo, and Y. H. Lee, "Contact resistance between metal and carbon nanotube interconnects: Effect of work function and wettability," *Applied Physics Letters*, vol. 95, no. 26, pp. 264103-264103-3, 2009.

[56] Q. H. Wang, Z. Jin, K. K. Kim, A. J. Hilmer, G. L. C. Paulus, C.-J. Shih, M.-H. Ham, J. D. Sanchez-Yamagishi, K. Watanabe, T. Taniguchi, J. Kong, P. Jarillo-Herrero, and M.

S. Strano, "Understanding and controlling the substrate effect on graphene electron-transfer chemistry via reactivity imprint lithography," *Nature Chemistry,* vol. 4, no. 9, pp. 724-732, 2012.

[57] A. Javey, H. Kim, M. Brink, Q. Wang, A. Ural, J. Guo, P. McIntyre, P. McEuen, M. Lundstrom, and H. Dai, "High-K dielectrics for advanced carbon-nanotube transistors and logic gates," *Nature Materials,* vol. 1, no. 4, pp. 241-246, 2002.

[58] F. Xiong, A. D. Liao, D. Estrada, and E. Pop, "Low-power switching of phase-change materials with carbon nanotube electrodes," *Science,* vol. 332, no. 6029, pp. 568-570, 2011.

[59] J. L. Bahr, E. T. Mickelson, M. J. Bronikowski, R. E. Smalley, and J. M. Tour, "Dissolution of small diameter single-wall carbon nanotubes in organic solvents?," *Chemical Communications,* vol. 2001, no. 2, pp. 193-194, 2001.

[60] S. D. Bergin, Z. Sun, P. Streich, J. Hamilton, and J. N. Coleman, "New solvents for nanotubes: Approaching the dispersibility of surfactants," *The Journal of Physical Chemistry C,* vol. 114, no. 1, pp. 231-237, 2009.

[61] C.-W. Lam, J. T. James, R. McCluskey, and R. L. Hunter, "Pulmonary toxicity of single-wall carbon nanotubes in mice 7 and 90 days after intratracheal instillation," *Toxicological Sciences,* vol. 77, no. 1, pp. 126-134, 2004.

[62] C. A. Poland, R. Duffin, I. Kinloch, A. Maynard, W. A. H. Wallace, A. Seaton, V. Stone, S. Brown, W. MacNee, and K. Donaldson, "Carbon nanotubes introduced into the abdominal cavity of mice show asbestos-like pathogenicity in a pilot study," *Nature Nanotechnology,* vol. 3, no. 7, pp. 423-428, 2008.

[63] B. E. Walling, Z. Kuang, Y. Hao, D. Estrada, J. D. Wood, F. Lian, R. T. Haasch, J. W. Lyding, A. B. Shah, J. L. Jeffries, E. Pop, and G. W. Lau, "Helical carbon nanotubes inhibit macrophage-mediated phagocytosis of Pseudomonas aeruginosa," *PLOS One,* to be published, 2013.

[64] D. B. Warheit, "Long-term inhalation toxicity studies with multiwalled carbon nanotubes: Closing the gaps or initiating the debate?," *Toxicological Sciences,* vol. 112, no. 2, pp. 273-275, 2009.

[65] R. Peierls, "Quelques propriétés typiques des corps solides," *Annales de l'institut Henri Poincaré,* vol. 5, no. 3, pp. 177-222, 1935.

[66] J. A. Venables, G. D. T. Spiller, and M. Hanbucken, "Nucleation and growth of thin films," *Reports on Progress in Physics,* vol. 47, no. 4, pp. 399-459, 1984.

[67] K. S. Novoselov, A. K. Geim, S. V. Morozov, D. Jiang, Y. Zhang, S. V. Dubonos, I. V. Grigorieva, and A. A. Firsov, "Electric field effect in atomically thin carbon films," *Science,* vol. 306, no. 5696, pp. 666-669, 2004.

[68] P. Blake, E. W. Hill, A. H. C. Neto, K. S. Novoselov, D. Jiang, R. Yang, T. J. Booth, and A. K. Geim, "Making graphene visible," *Applied Physics Letters,* vol. 91, no. 6, pp. 063124-063124-3, 2007.

[69] Y.-J. Yu, Y. Zhao, S. Ryu, L. E. Brus, K. S. Kim, and P. Kim, "Tuning the graphene work function by electric field effect," *Nano Letters,* vol. 9, no. 10, pp. 3430-3434, 2009.

[70] K. I. Bolotin, K. J. Sikes, Z. Jiang, M. Klima, G. Fudenberg, J. Hone, P. Kim, and H. L. Stormer, "Ultrahigh electron mobility in suspended graphene," *Solid State Communications,* vol. 146, no. 9-10, pp. 351-355, 2008.

[71] A. A. Balandin, S. Ghosh, W. Bao, I. Calizo, D. Teweldebrhan, F. Miao, and C. N. Lau, "Superior thermal conductivity of single-layer graphene," *Nano Letters,* vol. 8, no. 3, pp. 902-907, 2008.

[72] E. Pop, V. Varshney, and A. K. Roy, "Thermal properties of graphene: Fundamentals and applications," *MRS Bulletin,* vol. 37, no. 12, pp. 1273-1281, 2012.

[73] J. H. Seol, I. Jo, A. L. Moore, L. Lindsay, Z. H. Aitken, M. T. Pettes, X. Li, Z. Yao, R. Huang, D. Broido, N. Mingo, R. S. Ruoff, and L. Shi, "Two-dimensional phonon transport in supported graphene," *Science,* vol. 328, no. 5975, pp. 213-216, 2010.

[74] J. S. Bunch, S. S. Verbridge, J. S. Alden, A. M. van der Zande, J. M. Parpia, H. G. Craighead, and P. L. McEuen, "Impermeable atomic membranes from graphene sheets," *Nano Letters,* vol. 8, no. 8, pp. 2458-2462, 2008.

[75] C. Lee, X. Wei, J. W. Kysar, and J. Hone, "Measurement of the elastic properties and intrinsic strength of monolayer graphene," *Science,* vol. 321, no. 5887, pp. 385-388, 2008.

[76] C. S. Ruiz-Vargas, H. L. Zhuang, P. Y. Huang, A. M. van der Zande, S. Garg, P. L. McEuen, D. A. Muller, R. G. Hennig, and J. Park, "Softened elastic response and unzipping in chemical vapor deposition graphene membranes," *Nano Letters,* vol. 11, no. 6, pp. 2259-2263, 2011.

[77] L. Britnell, R. V. Gorbachev, R. Jalil, B. D. Belle, F. Schedin, M. I. Katsnelson, L. Eaves, S. V. Morozov, A. S. Mayorov, N. M. R. Peres, A. H. Castro Neto, J. Leist, A. K. Geim, L. A. Ponomarenko, and K. S. Novoselov, "Electron tunneling through ultrathin boron nitride crystalline barriers," *Nano Letters,* vol. 12, no. 3, pp. 1707-1710, 2012.

[78] J. N. Coleman, M. Lotya, A. O'Neill, S. D. Bergin, P. J. King, U. Khan, K. Young, A. Gaucher, S. De, R. J. Smith, I. V. Shvets, S. K. Arora, G. Stanton, H.-Y. Kim, K. Lee, G.

T. Kim, G. S. Duesberg, T. Hallam, J. J. Boland, J. J. Wang, J. F. Donegan, J. C. Grunlan, G. Moriarty, A. Shmeliov, R. J. Nicholls, J. M. Perkins, E. M. Grieveson, K. Theuwissen, D. W. McComb, P. D. Nellist, and V. Nicolosi, "Two-dimensional nanosheets produced by liquid exfoliation of layered materials," *Science*, vol. 331, no. 6017, pp. 568-571, 2011.

[79] A. Salehi-Khojin, D. Estrada, K. Y. Lin, K. Ran, R. T. Haasch, J.-M. Zuo, E. Pop, and R. I. Masel, "Chemical sensors based on randomly stacked graphene flakes," *Applied Physics Letters*, vol. 100, no. 3, pp. 033111-033111-4, 2012.

[80] S. Stankovich, D. A. Dikin, R. D. Piner, K. A. Kohlhaas, A. Kleinhammes, Y. Jia, Y. Wu, S. T. Nguyen, and R. S. Ruoff, "Synthesis of graphene-based nanosheets via chemical reduction of exfoliated graphite oxide," *Carbon*, vol. 45, no. 7, pp. 1558-1565, 2007.

[81] A. A. Green and M. C. Hersam, "Solution phase production of graphene with controlled thickness via density differentiation," *Nano Letters*, vol. 9, no. 12, pp. 4031-4036, 2009.

[82] A. A. Green and M. C. Hersam, "Emerging methods for producing monodisperse graphene dispersions," *The Journal of Physical Chemistry Letters*, vol. 1, no. 2, pp. 544-549, 2009.

[83] J. Kim, L. J. Cote, F. Kim, and J. Huang, "Visualizing graphene based sheets by fluorescence quenching microscopy," *Journal of the American Chemical Society*, vol. 132, no. 1, pp. 260-267, 2009.

[84] C. Mohapatra, "Growth and characterization of epitaxial graphene films by molecular beam epitaxy," Ph.D. dissertation, University of Illinois at Urbana-Champaign, Urbana, IL, 2012.

[85] J. M. Wofford, S. Nie, K. F. McCarty, N. C. Bartelt, and O. D. Dubon, "Graphene islands on Cu foils: The interplay between shape, orientation, and defects," *Nano Letters*, vol. 10, no. 12, pp. 4890-4896, 2010.

[86] P. W. Sutter, J. I. Flege, and E. A. Sutter, "Epitaxial graphene on ruthenium," *Nature Materials*, vol. 7, no. 5, pp. 406-411, 2008.

[87] J. Coraux, A. T. N'Diaye, C. Busse, and T. Michely, "Structural coherency of graphene on Ir(111)," *Nano Letters*, vol. 8, no. 2, pp. 565-570, 2008.

[88] H. Ago, Y. Ito, N. Mizuta, K. Yoshida, B. Hu, C. M. Orofeo, M. Tsuji, K.-I. Ikeda, and S. Mizuno, "Epitaxial chemical vapor deposition growth of single-layer graphene over cobalt film crystallized on sapphire," *ACS Nano*, vol. 4, no. 12, pp. 7407-7414, 2010.

[89] S. Roth, J. Osterwalder, and T. Greber, "Synthesis of epitaxial graphene on rhodium from 3-pentanone," *Surface Science*, vol. 605, no. 9-10, pp. L17-L19, 2011.

[90] C. Berger, Z. Song, T. Li, X. Li, A. Y. Ogbazghi, R. Feng, Z. Dai, A. N. Marchenkov, E. H. Conrad, P. N. First, and W. A. de Heer, "Ultrathin epitaxial graphite: 2D electron gas properties and a route toward graphene-based nanoelectronics," *The Journal of Physical Chemistry B,* vol. 108, no. 52, pp. 19912-19916, 2004.

[91] C. Berger, Z. M. Song, X. B. Li, X. S. Wu, N. Brown, C. Naud, D. Mayou, T. B. Li, J. Hass, A. N. Marchenkov, E. H. Conrad, P. N. First, and W. A. de Heer, "Electronic confinement and coherence in patterned epitaxial graphene," *Science,* vol. 312, no. 5777, pp. 1191-1196, 2006.

[92] J. S. Moon, D. Curtis, M. Hu, D. Wong, C. McGuire, P. M. Campbell, G. Jernigan, J. L. Tedesco, B. VanMil, R. Myers-Ward, C. Eddy, and D. K. Gaskill, "Epitaxial-graphene RF field-effect transistors on Si-face 6H-SiC substrates," *IEEE Electron Device Letters,* vol. 30, no. 6, pp. 650-652, 2009.

[93] A. Reina, X. Jia, J. Ho, D. Nezich, H. Son, V. Bulovic, M. S. Dresselhaus, and J. Kong, "Large area, few-layer graphene films on arbitrary substrates by chemical vapor deposition," *Nano Letters,* vol. 9, no. 1, pp. 30-35, 2008.

[94] X. Li, W. Cai, L. Colombo, and R. S. Ruoff, "Evolution of graphene growth on Ni and Cu by carbon isotope labeling," *Nano Letters,* vol. 9, no. 12, pp. 4268-4272, 2009.

[95] X. Li, Y. Zhu, W. Cai, M. Borysiak, B. Han, D. Chen, R. D. Piner, L. Colombo, and R. S. Ruoff, "Transfer of large-area graphene films for high-performance transparent conductive electrodes," *Nano Letters,* vol. 9, no. 12, pp. 4359-4363, 2009.

[96] L. Gao, W. Ren, H. Xu, L. Jin, Z. Wang, T. Ma, L.-P. Ma, Z. Zhang, Q. Fu, L.-M. Peng, X. Bao, and H.-M. Cheng, "Repeated growth and bubbling transfer of graphene with millimetre-size single-crystal grains using platinum," *Nature Communications,* vol. 3, no. 699, pp. 1-7, 2012.

[97] S. Bhaviripudi, X. Jia, M. S. Dresselhaus, and J. Kong, "Role of kinetic factors in chemical vapor deposition synthesis of uniform large area graphene using copper catalyst," *Nano Letters,* vol. 10, no. 10, pp. 4128-4133, 2010.

[98] G. H. Han, F. Güneş, J. J. Bae, E. S. Kim, S. J. Chae, H.-J. Shin, J.-Y. Choi, D. Pribat, and Y. H. Lee, "Influence of copper morphology in forming nucleation seeds for graphene growth," *Nano Letters,* vol. 11, no. 10, pp. 4144-4148, 2011.

[99] P. Y. Huang, C. S. Ruiz-Vargas, A. M. van der Zande, W. S. Whitney, M. P. Levendorf, J. W. Kevek, S. Garg, J. S. Alden, C. J. Hustedt, Y. Zhu, J. Park, P. L. McEuen, and D. A. Muller, "Grains and grain boundaries in single-layer graphene atomic patchwork quilts," *Nature,* vol. 469, no. 7330, pp. 389-392, 2010.

[100] X. Li, W. Cai, J. An, S. Kim, J. Nah, D. Yang, R. Piner, A. Velamakanni, I. Jung, E. Tutuc, S. K. Banerjee, L. Colombo, and R. S. Ruoff, "Large-area synthesis of high-

quality and uniform graphene films on copper foils," *Science,* vol. 324, no. 5932, pp. 1312-1314, 2009.

[101] X. Li, C. W. Magnuson, A. Venugopal, R. M. Tromp, J. B. Hannon, E. M. Vogel, L. Colombo, and R. S. Ruoff, "Large-area graphene single crystals grown by low-pressure chemical vapor deposition of methane on copper," *Journal of the American Chemical Society,* vol. 133, no. 9, pp. 2816-2819, 2011.

[102] I. Vlassiouk, M. Regmi, P. Fulvio, S. Dai, P. Datskos, G. Eres, and S. Smirnov, "Role of hydrogen in chemical vapor deposition growth of large single-crystal graphene," *ACS Nano,* vol. 5, no. 7, pp. 6069-6076, 2011.

[103] J. D. Wood, S. W. Schmucker, A. S. Lyons, E. Pop, and J. W. Lyding, "Effects of polycrystalline Cu substrate on graphene growth by chemical vapor deposition," *Nano Letters,* vol. 11, no. 11, pp. 4547-4554, 2011.

[104] Q. Yu, L. A. Jauregui, W. Wu, R. Colby, J. Tian, Z. Su, H. Cao, Z. Liu, D. Pandey, D. Wei, T. F. Chung, P. Peng, N. P. Guisinger, E. A. Stach, J. Bao, S.-S. Pei, and Y. P. Chen, "Control and characterization of individual grains and grain boundaries in graphene grown by chemical vapour deposition," *Nature Materials,* vol. 10, no. 6, pp. 443-449, 2010.

[105] J. Rohrl, M. Hundhausen, K. V. Emtsev, T. Seyller, R. Graupner, and L. Ley, "Raman spectra of epitaxial graphene on SiC(0001)," *Applied Physics Letters,* vol. 92, no. 20, pp. 201918-201918-3, 2008.

[106] U. Starke and C. Riedl, "Epitaxial graphene on SiC(0001) and SiC(000[bar]1): From surface reconstructions to carbon electronics," *Journal of Physics: Condensed Matter,* vol. 21, no. 13, pp. 134016-134016-12, 2009.

[107] L. O. Nyakiti, R. L. Myers-Ward, V. D. Wheeler, E. A. Imhoff, F. J. Bezares, H. Chun, J. D. Caldwell, A. L. Friedman, B. R. Matis, J. W. Baldwin, P. M. Campbell, J. C. Culbertson, C. R. Eddy, G. G. Jernigan, and D. K. Gaskill, "Bilayer graphene grown on 4H-SiC (0001) step-free mesas," *Nano Letters,* vol. 12, no. 4, pp. 1749-1756, 2012.

[108] V. Wheeler, N. Garces, L. Nyakiti, R. Myers-Ward, G. Jernigan, J. Culbertson, C. Eddy, and D. K. Gaskill, "Fluorine functionalization of epitaxial graphene for uniform deposition of thin high-kappa dielectrics," *Carbon,* vol. 50, no. 6, pp. 2307-2314, 2012.

[109] L. O. Nyakiti, V. D. Wheeler, N. Y. Garces, R. L. Myers-Ward, C. R. Eddy, Jr., and D. K. Gaskill, "Enabling graphene-based technologies: Toward wafer-scale production of epitaxial graphene," *MRS Bulletin,* vol. 37, no. 12, pp. 1149-1157, 2012.

[110] K. V. Emtsev, A. Bostwick, K. Horn, J. Jobst, G. L. Kellogg, L. Ley, J. L. McChesney, T. Ohta, S. A. Reshanov, J. Rohrl, E. Rotenberg, A. K. Schmid, D. Waldmann, H. B.

Weber, and T. Seyller, "Towards wafer-size graphene layers by atmospheric pressure graphitization of silicon carbide," *Nature Materials,* vol. 8, no. 3, pp. 203-207, 2009.

[111] R. M. Tromp and J. B. Hannon, "Thermodynamics and kinetics of graphene growth on SiC(0001)," *Physical Review Letters,* vol. 102, no. 10, pp. 106104-106104-4, 2009.

[112] J. Hass, F. Varchon, J. E. Millán-Otoya, M. Sprinkle, N. Sharma, W. A. de Heer, C. Berger, P. N. First, L. Magaud, and E. H. Conrad, "Why multilayer graphene on 4H-SiC(0001[bar]) behaves like a single sheet of graphene," *Physical Review Letters,* vol. 100, no. 12, pp. 125504-125504-4, 2008.

[113] J. Hass, J. E. Millán-Otoya, P. N. First, and E. H. Conrad, "Interface structure of epitaxial graphene grown on 4H-SiC(0001)," *Physical Review B,* vol. 78, no. 20, pp. 205424-205424-10, 2008.

[114] C. Virojanadara, M. Syväjarvi, R. Yakimova, L. I. Johansson, A. A. Zakharov, and T. Balasubramanian, "Homogeneous large-area graphene layer growth on 6H-SiC(0001)," *Physical Review B,* vol. 78, no. 24, pp. 245403-245403-6, 2008.

[115] Quote (July 31, 2013). University Wafer. [Online]. Available: http://www.universitywafer.com/Wafers_Services/Silicon_Carbide/silicon_carbide.html

[116] J. D. Caldwell, T. J. Anderson, J. C. Culbertson, G. G. Jernigan, K. D. Hobart, F. J. Kub, M. J. Tadjer, J. L. Tedesco, J. K. Hite, M. A. Mastro, R. L. Myers-Ward, C. R. Eddy, P. M. Campbell, and D. K. Gaskill, "Technique for the dry transfer of epitaxial graphene onto arbitrary substrates," *ACS Nano,* vol. 4, no. 2, pp. 1108-1114, 2010.

[117] S. Unarunotai, J. C. Koepke, C.-L. Tsai, F. Du, C. E. Chialvo, Y. Murata, R. Haasch, I. Petrov, N. Mason, M. Shim, J. Lyding, and J. A. Rogers, "Layer-by-layer transfer of multiple, large area sheets of graphene grown in multilayer stacks on a single SiC wafer," *ACS Nano,* vol. 4, no. 10, pp. 5591-5598, 2010.

[118] Y. M. Lin, C. Dimitrakopoulos, K. A. Jenkins, D. B. Farmer, H. Y. Chiu, A. Grill, and P. Avouris, "100-GHz transistors from wafer-scale epitaxial graphene," *Science,* vol. 327, no. 5966, p. 662, 2010.

[119] A. Reina, X. T. Jia, J. Ho, D. Nezich, H. B. Son, V. Bulovic, M. S. Dresselhaus, and J. Kong, "Large area, few-layer graphene films on arbitrary substrates by chemical vapor deposition," *Nano Letters,* vol. 9, no. 8, pp. 30-35, 2009.

[120] Q. Yu, J. Lian, S. Siriponglert, H. Li, Y. P. Chen, and S.-S. Pei, "Graphene segregated on Ni surfaces and transferred to insulators," *Applied Physics Letters,* vol. 93, no. 11, pp. 113103-113103-3, 2008.

[121] J. C. Shelton, H. R. Patil, and J. M. Blakely, "Equilibrium segregation of carbon to a nickel (111) surface: A surface phase transition," *Surface Science*, vol. 43, no. 2, pp. 493-520, 1974.

[122] M. Singleton and P. Nash, "The C-Ni (carbon-nickel) system," *Bulletin of Alloy Phase Diagrams*, vol. 10, no. 2, pp. 121-126, 1989.

[123] L. C. Isett and J. M. Blakely, "Segregation isosteres for carbon at the (100) surface of nickel," *Surface Science*, vol. 58, no. 2, pp. 397-414, 1976.

[124] J. Gao, J. Yip, J. Zhao, B. I. Yakobson, and F. Ding, "Graphene nucleation on transition metal surface: Structure transformation and role of the metal step edge," *Journal of the American Chemical Society*, vol. 133, no. 13, pp. 5009-5015, 2011.

[125] I. Alstrup, I. Chorkendorff, and S. Ullmann, "The interaction of CH4 at high temperatures with clean and oxygen precovered Cu(100)," *Surface Science*, vol. 264, no. 1-2, pp. 95-102, 1992.

[126] S. T. Lee, S. Chen, G. Braunstein, X. Feng, I. Bello, and W. M. Lau, "Heteroepitaxy of carbon on copper by high-temperature ion implantation," *Applied Physics Letters*, vol. 59, no. 7, pp. 785-787, 1991.

[127] X. S. Li, W. W. Cai, J. H. An, S. Kim, J. Nah, D. X. Yang, R. Piner, A. Velamakanni, I. Jung, E. Tutuc, S. K. Banerjee, L. Colombo, and R. S. Ruoff, "Large-area synthesis of high-quality and uniform graphene films on copper foils," *Science*, vol. 324, no. 5932, pp. 1312-1314, 2009.

[128] X. S. Li, W. W. Cai, L. Colombo, and R. S. Ruoff, "Evolution of graphene growth on Ni and Cu by carbon isotope labeling," *Nano Letters*, vol. 9, no. 12, pp. 4268-4272, 2009.

[129] L. Gao, J. R. Guest, and N. P. Guisinger, "Epitaxial graphene on Cu(111)," *Nano Letters*, vol. 10, no. 9, pp. 3512-3516, 2010.

[130] Z. Sun, Z. Yan, J. Yao, E. Beitler, Y. Zhu, and J. M. Tour, "Growth of graphene from solid carbon sources," *Nature*, vol. 468, no. 7323, pp. 549-552, 2010.

[131] Z. Li, P. Wu, C. Wang, X. Fan, W. Zhang, X. Zhai, C. Zeng, Z. Li, J. Yang, and J. Hou, "Low-temperature growth of graphene by chemical vapor deposition using solid and liquid carbon sources," *ACS Nano*, vol. 5, no. 4, pp. 3385-3390, 2011.

[132] G. Ruan, Z. Sun, Z. Peng, and J. M. Tour, "Growth of graphene from food, insects, and waste," *ACS Nano*, vol. 5, no. 9, pp. 7601-7607, 2011.

[133] S. Bae, H. Kim, Y. Lee, X. Xu, J.-S. Park, Y. Zheng, J. Balakrishnan, T. Lei, H. Ri Kim, Y. I. Song, Y.-J. Kim, K. S. Kim, B. Ozyilmaz, J.-H. Ahn, B. H. Hong, and S. Iijima,

"Roll-to-roll production of 30-inch graphene films for transparent electrodes," *Nature Nanotechnology,* vol. 5, no. 8, pp. 574-578, 2010.

[134] T. Kobayashi, M. Bando, N. Kimura, K. Shimizu, K. Kadono, N. Umezu, K. Miyahara, S. Hayazaki, S. Nagai, Y. Mizuguchi, Y. Murakami, and D. Hobara, "Production of a 100-m-long high-quality graphene transparent conductive film by roll-to-roll chemical vapor deposition and transfer process," *Applied Physics Letters,* vol. 102, no. 2, pp. 023112-023112-4, 2013.

[135] A. Cupolillo, N. Ligato, and L. S. Caputi, "Two-dimensional character of the interface-π plasmon in epitaxial graphene on Ni(111)," *Carbon,* vol. 50, no. 7, pp. 2588-2591, 2012.

[136] G.-H. Lee, R. C. Cooper, S. J. An, S. Lee, A. van der Zande, N. Petrone, A. G. Hammerberg, C. Lee, B. Crawford, W. Oliver, J. W. Kysar, and J. Hone, "High-strength chemical-vapor-deposited graphene and grain boundaries," *Science,* vol. 340, no. 6136, pp. 1073-1076, 2013.

[137] A. Salehi-Khojin, D. Estrada, K. Y. Lin, M. H. Bae, F. Xiong, E. Pop, and R. I. Masel, "Polycrystalline graphene ribbons as chemiresistors," *Advanced Materials,* vol. 24, no. 1, pp. 53-57, 2012.

[138] J. C. Koepke, J. D. Wood, D. Estrada, Z.-Y. Ong, K. T. He, E. Pop, and J. W. Lyding, "Atomic-scale evidence for potential barriers and strong carrier scattering at graphene grain boundaries: A scanning tunneling microscopy study," *ACS Nano,* vol. 7, no. 1, pp. 75-86, 2013.

[139] O. V. Yazyev and S. G. Louie, "Electronic transport in polycrystalline graphene," *Nature Materials,* vol. 9, no. 10, pp. 806-809, 2010.

[140] A. W. Tsen, L. Brown, M. P. Levendorf, F. Ghahari, P. Y. Huang, R. W. Havener, C. S. Ruiz-Vargas, D. A. Muller, P. Kim, and J. Park, "Tailoring electrical transport across grain boundaries in polycrystalline graphene," *Science,* vol. 336, no. 6085, pp. 1143-1146, 2012.

[141] P. K. Mohseni, A. Behnam, J. D. Wood, C. D. English, J. W. Lyding, E. Pop, and X. Li, "$In_xGa_{1-x}As$ nanowire growth on graphene: van der Waals epitaxy induced phase segregation," *Nano Letters,* vol. 13, no. 3, pp. 1153-1161, 2013.

[142] K. Yan, H. Peng, Y. Zhou, H. Li, and Z. Liu, "Formation of bilayer Bernal graphene: Layer-by-layer epitaxy via chemical vapor deposition," *Nano Letters,* vol. 11, no. 3, pp. 1106-1110, 2011.

[143] K. T. He, J. D. Wood, G. P. Doidge, E. Pop, and J. W. Lyding, "Scanning tunneling microscopy study and nanomanipulation of graphene-coated water on mica," *Nano Letters,* vol. 12, no. 6, pp. 2665-2672, 2012.

[144] L. Brown, R. Hovden, P. Huang, M. Wojcik, D. A. Muller, and J. Park, "Twinning and twisting of tri- and bilayer graphene," *Nano Letters,* vol. 12, no. 3, pp. 1609-1615, 2012.

[145] R. W. Havener, H. Zhuang, L. Brown, R. G. Hennig, and J. Park, "Angle-resolved Raman imaging of interlayer rotations and interactions in twisted bilayer graphene," *Nano Letters,* vol. 12, no. 6, pp. 3162-3167, 2012.

[146] A. Righi, S. D. Costa, H. Chacham, C. Fantini, P. Venezuela, C. Magnuson, L. Colombo, W. S. Bacsa, R. S. Ruoff, and M. A. Pimenta, "Graphene Moiré patterns observed by umklapp double-resonance Raman scattering," *Physical Review B,* vol. 84, no. 24, pp. 241409-241409-4, 2011.

[147] X. Li, C. W. Magnuson, A. Venugopal, J. An, J. W. Suk, B. Han, M. Borysiak, W. Cai, A. Velamakanni, Y. Zhu, L. Fu, E. M. Vogel, E. Voelkl, L. Colombo, and R. S. Ruoff, "Graphene films with large domain size by a two-step chemical vapor deposition process," *Nano Letters,* vol. 10, no. 11, pp. 4328-4334, 2010.

[148] W. Zhang, P. Wu, Z. Li, and J. Yang, "First-principles thermodynamics of graphene growth on Cu surfaces," *The Journal of Physical Chemistry C,* vol. 115, no. 36, pp. 17782-17787, 2011.

[149] L. Tao, J. Lee, H. Chou, M. Holt, R. S. Ruoff, and D. Akinwande, "Synthesis of high quality monolayer graphene at reduced temperature on hydrogen-enriched evaporated copper (111) films," *ACS Nano,* vol. 6, no. 3, pp. 2319-2325, 2012.

[150] I. Vlassiouk, P. Fulvio, H. Meyer, N. Lavrik, S. Dai, P. Datskos, and S. Smirnov, "Large scale atmospheric pressure chemical vapor deposition of graphene," *Carbon,* vol. 54, no. pp. 58-67, 2013.

[151] A. Ismach, C. Druzgalski, S. Penwell, A. Schwartzberg, M. Zheng, A. Javey, J. Bokor, and Y. Zhang, "Direct chemical vapor deposition of graphene on dielectric surfaces," *Nano Letters,* vol. 10, no. 5, pp. 1542-1548, 2010.

[152] Y. A. Wu, Y. Fan, S. Speller, G. L. Creeth, J. T. Sadowski, K. He, A. W. Robertson, C. S. Allen, and J. H. Warner, "Large single crystals of graphene on melted copper using chemical vapor deposition," *ACS Nano,* vol. 6, no. 6, pp. 5010-5017, 2012.

[153] M. I. Katsnelson, K. S. Novoselov, and A. K. Geim, "Chiral tunnelling and the Klein paradox in graphene," *Nature Physics,* vol. 2, no. 9, pp. 620-625, 2006.

[154] V. V. Cheianov, V. Fal'ko, and B. L. Altshuler, "The focusing of electron flow and a Veselago lens in graphene p-n junctions," *Science,* vol. 315, no. 5816, pp. 1252-1255, 2007.

[155] J. P. Eisenstein and A. H. MacDonald, "Bose-Einstein condensation of excitons in bilayer electron systems," *Nature,* vol. 432, no. 7018, pp. 691-694, 2004.

[156] R. V. Gorbachev, A. K. Geim, M. I. Katsnelson, K. S. Novoselov, T. Tudorovskiy, I. V. Grigorieva, A. H. MacDonald, S. V. Morozov, K. Watanabe, T. Taniguchi, and L. A. Ponomarenko, "Strong Coulomb drag and broken symmetry in double-layer graphene," *Nature Physics,* vol. 8, no. 12, pp. 896-901, 2012.

[157] K. A. Ritter and J. W. Lyding, "The influence of edge structure on the electronic properties of graphene quantum dots and nanoribbons," *Nature Materials,* vol. 8, no. 3, pp. 235-242, 2009.

[158] Y. B. Zhang, T. T. Tang, C. Girit, Z. Hao, M. C. Martin, A. Zettl, M. F. Crommie, Y. R. Shen, and F. Wang, "Direct observation of a widely tunable bandgap in bilayer graphene," *Nature,* vol. 459, no. 7248, p. 820, 2009.

[159] G. Eda, G. Fanchini, and M. Chhowalla, "Large-area ultrathin films of reduced graphene oxide as a transparent and flexible electronic material," *Nature Nanotechnology,* vol. 3, no. 5, pp. 270-274, 2008.

[160] D. C. Elias, R. R. Nair, T. M. G. Mohiuddin, S. V. Morozov, P. Blake, M. P. Halsall, A. C. Ferrari, D. W. Boukhvalov, M. I. Katsnelson, A. K. Geim, and K. S. Novoselov, "Control of graphene's properties by reversible hydrogenation: Evidence for graphane," *Science,* vol. 323, no. 5914, pp. 610-613, 2009.

[161] J. T. Robinson, J. S. Burgess, C. E. Junkermeier, S. C. Badescu, T. L. Reinecke, F. K. Perkins, M. K. Zalalutdniov, J. W. Baldwin, J. C. Culbertson, P. E. Sheehan, and E. S. Snow, "Properties of fluorinated graphene films," *Nano Letters,* vol. 10, no. 8, pp. 3001-3005, 2010.

[162] A. Behnam, A. S. Lyons, M.-H. Bae, E. K. Chow, S. Islam, C. M. Neumann, and E. Pop, "Transport in nanoribbon interconnects obtained from graphene grown by chemical vapor deposition," *Nano Letters,* vol. 12, no. 9, pp. 4424-4430, 2012.

[163] Z. Chen, Y.-M. Lin, M. J. Rooks, and P. Avouris, "Graphene nano-ribbon electronics," *Physica E: Low-Dimensional Systems and Nanostructures,* vol. 40, no. 2, pp. 228-232, 2007.

[164] X. Li, X. Wang, L. Zhang, S. Lee, and H. Dai, "Chemically derived, ultrasmooth graphene nanoribbon semiconductors," *Science,* vol. 319, no. 5867, pp. 1229-1232, 2008.

[165] M. Fujita, K. Wakabayashi, K. Nakada, and K. Kusakabe, "Peculiar localized state at zigzag graphite edge," *Journal of the Physical Society of Japan,* vol. 65, no. 7, pp. 1920-1923, 1996.

[166] T. Fang, A. Konar, H. Xing, and D. Jena, "Mobility in semiconducting graphene nanoribbons: Phonon, impurity, and edge roughness scattering," *Physical Review B,* vol. 78, no. 20, p. 205403, 2008.

[167] X. Zhang, O. V. Yazyev, J. Feng, L. Xie, C. Tao, Y.-C. Chen, L. Jiao, Z. Pedramrazi, A. Zettl, S. G. Louie, H. Dai, and M. F. Crommie, "Experimentally engineering the edge termination of graphene nanoribbons," *ACS Nano,* vol. 7, no. 1, pp. 198-202, 2012.

[168] J. Cai, P. Ruffieux, R. Jaafar, M. Bieri, T. Braun, S. Blankenburg, M. Muoth, A. P. Seitsonen, M. Saleh, X. Feng, K. Mullen, and R. Fasel, "Atomically precise bottom-up fabrication of graphene nanoribbons," *Nature,* vol. 466, no. 7305, pp. 470-473, 2010.

[169] S. Linden, D. Zhong, A. Timmer, N. Aghdassi, J. H. Franke, H. Zhang, X. Feng, K. Müllen, H. Fuchs, L. Chi, and H. Zacharias, "Electronic structure of spatially aligned graphene nanoribbons on Au(788)," *Physical Review Letters,* vol. 108, no. 21, pp. 216801-216801-4, 2012.

[170] E. McCann and V. I. Fal'ko, "Landau-level degeneracy and quantum Hall effect in a graphite bilayer," *Physical Review Letters,* vol. 96, no. 8, pp. 086805-086805-4, 2006.

[171] H. Kim, I. Song, C. Park, M. Son, M. Hong, Y. Kim, J. S. Kim, H.-J. Shin, J. Baik, and H. C. Choi, "Copper-vapor-assisted chemical vapor deposition for high-quality and metal-free single-layer graphene on amorphous SiO_2 substrate," *ACS Nano,* vol. 7, no. 8, pp. 6575–6582, 2013.

[172] M. Z. Hossain, J. E. Johns, K. H. Bevan, H. J. Karmel, Y. T. Liang, S. Yoshimoto, K. Mukai, T. Koitaya, J. Yoshinobu, M. Kawai, A. M. Lear, L. L. Kesmodel, S. L. Tait, and M. C. Hersam, "Chemically homogeneous and thermally reversible oxidation of epitaxial graphene," *Nature Chemistry,* vol. 4, no. 4, pp. 305-309, 2012.

[173] X. Zhang, A. Hsu, H. Wang, Y. Song, J. Kong, M. S. Dresselhaus, and T. Palacios, "Impact of chlorine functionalization on high-mobility chemical vapor deposition grown graphene," *ACS Nano,* vol. 7, no. 8, pp. 7262–7270, 2013.

[174] Y. Li, H. Chen, L. Y. Voo, J. Ji, G. Zhang, G. Zhang, F. Zhang, and X. Fan, "Synthesis of partially hydrogenated graphene and brominated graphene," *Journal of Materials Chemistry,* vol. 22, no. 30, pp. 15021-15024, 2012.

[175] R. R. Nair, W. C. Ren, R. Jalil, I. Riaz, V. G. Kravets, L. Britnell, P. Blake, F. Schedin, A. S. Mayorov, S. J. Yuan, M. I. Katsnelson, H. M. Cheng, W. Strupinski, L. G. Bulusheva, A. V. Okotrub, I. V. Grigorieva, A. N. Grigorenko, K. S. Novoselov, and A. K. Geim, "Fluorographene: A two-dimensional counterpart of Teflon," *Small,* vol. 6, no. 24, pp. 2877-2884, 2010.

[176] J. Tauc and A. Menth, "States in the gap," *Journal of Non-Crystalline Solids,* vol. 8-10, no. 0, pp. 569-585, 1972.

[177] W. S. Hummers and R. E. Offeman, "Preparation of graphitic oxide," *Journal of the American Chemical Society,* vol. 80, no. 6, pp. 1339-1339, 1958.

[178] D. A. Dikin, S. Stankovich, E. J. Zimney, R. D. Piner, G. H. B. Dommett, G. Evmenenko, S. T. Nguyen, and R. S. Ruoff, "Preparation and characterization of graphene oxide paper," *Nature,* vol. 448, no. 7152, pp. 457-460, 2007.

[179] J. O. Sofo, A. S. Chaudhari, and G. D. Barber, "Graphane: A two-dimensional hydrocarbon," *Physical Review B,* vol. 75, no. 15, pp. 153401-153401-4, 2007.

[180] F. Withers, S. Russo, M. Dubois, and M. F. Craciun, "Tuning the electronic transport properties of graphene through functionalisation with fluorine," *Nanoscale Research Letters C7 - 526,* vol. 6, no. 1, pp. 1-11, 2011.

[181] J. O. Sofo, A. M. Suarez, G. Usaj, P. S. Cornaglia, A. D. Hernández-Nieves, and C. A. Balseiro, "Electrical control of the chemical bonding of fluorine on graphene," *Physical Review B,* vol. 83, no. 8, pp. 081411-081411-4, 2011.

[182] J. Chan, A. Venugopal, A. Pirkle, S. McDonnell, D. Hinojos, C. W. Magnuson, R. S. Ruoff, L. Colombo, R. M. Wallace, and E. M. Vogel, "Reducing extrinsic performance-limiting factors in graphene grown by chemical vapor deposition," *ACS Nano,* vol. 6, no. 4, pp. 3224-3229, 2012.

[183] Y. C. Lin, C. H. Jin, J. C. Lee, S. F. Jen, K. Suenaga, and P. W. Chiu, "Clean transfer of graphene for isolation and suspension," *ACS Nano,* vol. 5, no. 3, pp. 2362-2368, 2011.

[184] Y. C. Lin, C. C. Lu, C. H. Yeh, C. H. Jin, K. Suenaga, and P. W. Chiu, "Graphene annealing: How clean can it be?," *Nano Letters,* vol. 12, no. 1, pp. 414-419, 2012.

[185] A. Pirkle, J. Chan, A. Venugopal, D. Hinojos, C. W. Magnuson, S. McDonnell, L. Colombo, E. M. Vogel, R. S. Ruoff, and R. M. Wallace, "The effect of chemical residues on the physical and electrical properties of chemical vapor deposited graphene transferred to SiO_2," *Applied Physics Letters,* vol. 99, no. 12, pp. 122108-122108-3, 2011.

[186] A. Reina, H. Son, L. Jiao, B. Fan, M. S. Dresselhaus, Z. Liu, and J. Kong, "Transferring and identification of single- and few-layer graphene on arbitrary substrates," *The Journal of Physical Chemistry C,* vol. 112, no. 46, pp. 17741-17744, 2008.

[187] J. W. Suk, A. Kitt, C. W. Magnuson, Y. Hao, S. Ahmed, J. An, A. K. Swan, B. B. Goldberg, and R. S. Ruoff, "Transfer of CVD-grown monolayer graphene onto arbitrary substrates," *ACS Nano,* vol. 5, no. 9, pp. 6916-6924, 2011.

[188] M. Ishigami, J. H. Chen, W. G. Cullen, M. S. Fuhrer, and E. D. Williams, "Atomic structure of graphene on SiO_2," *Nano Letters,* vol. 7, no. 6, pp. 1643-1648, 2007.

[189] X. L. Liang, B. A. Sperling, I. Calizo, G. J. Cheng, C. A. Hacker, Q. Zhang, Y. Obeng, K. Yan, H. L. Peng, Q. L. Li, X. X. Zhu, H. Yuan, A. R. H. Walker, Z. F. Liu, L. M. Peng, and C. A. Richter, "Toward clean and crackless transfer of graphene," *ACS Nano,* vol. 5, no. 11, pp. 9144-9153, 2011.

[190] H. J. Park, J. Meyer, S. Roth, and V. Skakalova, "Growth and properties of few-layer graphene prepared by chemical vapor deposition," *Carbon,* vol. 48, no. 4, pp. 1088-1094, 2010.

[191] J. W. Suk, A. Kitt, C. W. Magnuson, Y. F. Hao, S. Ahmed, J. H. An, A. K. Swan, B. B. Goldberg, and R. S. Ruoff, "Transfer of CVD-grown monolayer graphene onto arbitrary substrates," *ACS Nano,* vol. 5, no. 9, pp. 6916-6924, 2011.

[192] G. G. Jernigan, T. J. Anderson, J. T. Robinson, J. D. Caldwell, J. C. Culbertson, R. Myers-Ward, A. L. Davidson, M. G. Ancona, V. D. Wheeler, L. O. Nyakiti, A. L. Friedman, P. M. Campbell, and D. K. Gaskill, "Bilayer graphene by bonding CVD graphene to epitaxial graphene," *Journal of Vacuum Science & Technology B: Microelectronics and Nanometer Structures,* vol. 30, no. 3, pp. 03D110-03D110-5, 2012.

[193] J. Kang, S. Hwang, J. H. Kim, M. H. Kim, J. Ryu, S. J. Seo, B. H. Hong, M. K. Kim, and J.-B. Choi, "Efficient transfer of large-area graphene films onto rigid substrates by hot pressing," *ACS Nano,* vol. 6, no. 6, pp. 5360-5365, 2012.

[194] C. J. L. de la Rosa, J. Sun, N. Lindvall, M. T. Cole, Y. Nam, M. Loffler, E. Olsson, K. B. K. Teo, and A. Yurgens, "Frame assisted H_2O electrolysis induced H_2 bubbling transfer of large area graphene grown by chemical vapor deposition on Cu," *Applied Physics Letters,* vol. 102, no. 2, pp. 022101-4, 2013.

[195] Y. Wang, Y. Zheng, X. Xu, E. Dubuisson, Q. Bao, J. Lu, and K. P. Loh, "Electrochemical delamination of CVD-grown graphene film: Toward the recyclable use of copper catalyst," *ACS Nano,* vol. 5, no. 12, pp. 9927-9933, 2011.

[196] X. Liang, B. A. Sperling, I. Calizo, G. Cheng, C. A. Hacker, Q. Zhang, Y. Obeng, K. Yan, H. Peng, Q. Li, X. Zhu, H. Yuan, A. R. Hight Walker, Z. Liu, L. Peng, and C. A. Richter, "Toward clean and crackless transfer of graphene," *ACS Nano,* vol. 5, no. 11, pp. 9144-9153, 2012.

[197] Y. Zhang, Y.-W. Tan, H. L. Stormer, and P. Kim, "Experimental observation of the quantum Hall effect and Berry's phase in graphene," *Nature,* vol. 438, no. 7065, pp. 201-204, 2005.

[198] I. Meric, M. Y. Han, A. F. Young, B. Ozyilmaz, P. Kim, and K. L. Shepard, "Current saturation in zero-bandgap, top-gated graphene field-effect transistors," *Nature Nanotechnology,* vol. 3, no. 11, pp. 654-659, 2008.

[199] V. E. Dorgan, A. Behnam, H. J. Conley, K. I. Bolotin, and E. Pop, "High-field electrical and thermal transport in suspended graphene," *Nano Letters,* vol. 13, no. pp. 4581-4586, 2013.

[200] J. Rafiee, X. Mi, H. Gullapalli, A. V. Thomas, F. Yavari, Y. Shi, P. M. Ajayan, and N. A. Koratkar, "Wetting transparency of graphene," *Nature Materials,* vol. 11, no. pp. 217-222, 2012.

[201] N. Y. Garces, V. D. Wheeler, and D. K. Gaskill, "Graphene functionalization and seeding for dielectric deposition and device integration," *Journal of Vacuum Science & Technology B: Microelectronics and Nanometer Structures,* vol. 30, no. 3, pp. 030801-030801-21, 2012.

[202] X. Wang, S. M. Tabakman, and H. Dai, "Atomic layer deposition of metal oxides on pristine and functionalized graphene," *Journal of the American Chemical Society,* vol. 130, no. 26, pp. 8152-8153, 2008.

[203] S. Kim, J. Nah, I. Jo, D. Shahrjerdi, L. Colombo, Z. Yao, E. Tutuc, and S. K. Banerjee, "Realization of a high mobility dual-gated graphene field-effect transistor with Al2O3 dielectric," *Applied Physics Letters,* vol. 94, no. 6, pp. 062107-062107-3, 2009.

[204] J. M. P. Alaboson, Q. H. Wang, J. D. Emery, A. L. Lipson, M. J. Bedzyk, J. W. Elam, M. J. Pellin, and M. C. Hersam, "Seeding atomic layer deposition of high-k dielectrics on epitaxial graphene with organic self-assembled monolayers," *ACS Nano,* vol. 5, no. 6, pp. 5223-5232, 2011.

[205] B. Lee, G. Mordi, M. J. Kim, Y. J. Chabal, E. M. Vogel, R. M. Wallace, K. J. Cho, L. Colombo, and J. Kim, "Characteristics of high-k Al_2O_3 dielectric using ozone-based atomic layer deposition for dual-gated graphene devices," *Applied Physics Letters,* vol. 97, no. 4, pp. 043107-043107-3, 2010.

[206] B. Lee, S.-Y. Park, H.-C. Kim, K. Cho, E. M. Vogel, M. J. Kim, R. M. Wallace, and J. Kim, "Conformal Al_2O_3 dielectric layer deposited by atomic layer deposition for graphene-based nanoelectronics," *Applied Physics Letters,* vol. 92, no. 20, pp. 203102-203102-3, 2008.

[207] D. B. Farmer, H.-Y. Chiu, Y.-M. Lin, K. A. Jenkins, F. Xia, and P. Avouris, "Utilization of a buffered dielectric to achieve high field-effect carrier mobility in graphene transistors," *Nano Letters,* vol. 9, no. 12, pp. 4474-4478, 2009.

[208] R. Pease, "An X-ray study of boron nitride," *Acta Crystallographica,* vol. 5, no. 3, pp. 356-361, 1952.

[209] J. R. H. Wentorf, "Cubic form of boron nitride," *The Journal of Chemical Physics,* vol. 26, no. 4, p. 956, 1957.

[210] G. W. Rowe, "Some observations on the frictional behaviour of boron nitride and of graphite," *Wear,* vol. 3, no. 4, pp. 274-285, 1960.

[211] A. W. Laubengayer, P. C. Moews, and R. F. Porter, "The condensation of borazine to polycyclic boron-nitrogen frameworks by pyrolytic dehydrogenation," *Journal of the American Chemical Society,* vol. 83, no. 6, pp. 1337-1342, 1961.

[212] F. P. Bundy and J. R. H. Wentorf, "Direct transformation of hexagonal boron nitride to denser forms," *The Journal of Chemical Physics,* vol. 38, no. 5, pp. 1144-1149, 1963.

[213] M. J. Rand and J. F. Roberts, "Preparation and properties of thin film boron nitride," *Journal of The Electrochemical Society,* vol. 115, no. 4, pp. 423-429, 1968.

[214] N. G. Coles, D. R. Glasson, and S. A. A. Jayaweera, "Formation and reactivity of nitrides. III. Boron, aluminium and silicon nitrides," *Journal of Applied Chemistry,* vol. 19, no. 6, pp. 178-181, 1969.

[215] T. Kuzuba, K. Era, T. Ishii, and T. Sato, "A low frequency Raman-active vibration of hexagonal boron nitride," *Solid State Communications,* vol. 25, no. 11, pp. 863-865, 1978.

[216] R. J. Nemanich, S. A. Solin, and R. M. Martin, "Light scattering study of boron nitride microcrystals," *Physical Review B,* vol. 23, no. 12, pp. 6348-6356, 1981.

[217] K. Inagawa, K. Watanabe, H. Ohsone, K. Saitoh, and A. Itoh, "Preparation of cubic boron nitride film by activated reactive evaporation with a gas activation nozzle," *Journal of Vacuum Science & Technology A: Vacuum, Surfaces, and Films,* vol. 5, no. 4, pp. 2696-2700, 1987.

[218] S.-I. Hirano, T. Yogo, S. Asada, and S. Naka, "Synthesis of amorphous boron nitride by pressure pyrolysis of borazine," *Journal of the American Ceramic Society,* vol. 72, no. 1, pp. 66-70, 1989.

[219] A. Lipp, K. A. Schwetz, and K. Hunold, "Hexagonal boron nitride: Fabrication, properties and applications," *Journal of the European Ceramic Society,* vol. 5, no. 1, pp. 3-9, 1989.

[220] N. G. Chopra, R. J. Luyken, K. Cherrey, V. H. Crespi, M. L. Cohen, S. G. Louie, and A. Zettl, "Boron nitride nanotubes," *Science,* vol. 269, no. 5226, pp. 966-967, 1995.

[221] F. Baitalow, J. Baumann, G. Wolf, K. Jaenicke-Rößler, and G. Leitner, "Thermal decomposition of B-N-H compounds investigated by using combined thermoanalytical methods," *Thermochimica Acta,* vol. 391, no. 1-2, pp. 159-168, 2002.

[222] K. Watanabe, T. Taniguchi, and H. Kanda, "Direct-bandgap properties and evidence for ultraviolet lasing of hexagonal boron nitride single crystal," *Nature Materials,* vol. 3, no. 6, pp. 404-409, 2004.

[223] Y. Kubota, K. Watanabe, O. Tsuda, and T. Taniguchi, "Deep ultraviolet light-emitting hexagonal boron nitride synthesized at atmospheric pressure," *Science,* vol. 317, no. 5840, pp. 932-934, 2007.

[224] L. Ci, L. Song, C. Jin, D. Jariwala, D. Wu, Y. Li, A. Srivastava, Z. F. Wang, K. Storr, L. Balicas, F. Liu, and P. M. Ajayan, "Atomic layers of hybridized boron nitride and graphene domains," *Nature Materials,* vol. 9, no. 5, pp. 430-435, 2010.

[225] C. R. Dean, A. F. Young, I. Meric, C. Lee, L. Wang, S. Sorgenfrei, K. Watanabe, T. Taniguchi, P. Kim, K. L. Shepard, and J. Hone, "Boron nitride substrates for high-quality graphene electronics," *Nature Nanotechnology,* vol. 5, no. 10, pp. 722-726, 2010.

[226] Y. Shi, C. Hamsen, X. Jia, K. K. Kim, A. Reina, M. Hofmann, A. L. Hsu, K. Zhang, H. Li, Z.-Y. Juang, M. S. Dresselhaus, L.-J. Li, and J. Kong, "Synthesis of few-layer hexagonal boron nitride thin film by chemical vapor deposition," *Nano Letters,* vol. 10, no. 10, pp. 4134-4139, 2010.

[227] C. R. Dean, A. F. Young, P. Cadden-Zimansky, L. Wang, H. Ren, K. Watanabe, T. Taniguchi, P. Kim, J. Hone, and K. L. Shepard, "Multicomponent fractional quantum Hall effect in graphene," *Nature Physics,* vol. 7, no. 9, pp. 693-696, 2011.

[228] A. S. Mayorov, R. V. Gorbachev, S. V. Morozov, L. Britnell, R. Jalil, L. A. Ponomarenko, P. Blake, K. S. Novoselov, K. Watanabe, T. Taniguchi, and A. K. Geim, "Micrometer-scale ballistic transport in encapsulated graphene at room temperature," *Nano Letters,* vol. 11, no. 6, pp. 2396-2399, 2011.

[229] K. S. Novoselov, D. Jiang, F. Schedin, T. J. Booth, V. V. Khotkevich, S. V. Morozov, and A. K. Geim, "Two-dimensional atomic crystals," *Proceedings of the National Academy of Sciences of the United States of America,* vol. 102, no. 30, pp. 10451-10453, 2005.

[230] J. Xue, J. Sanchez-Yamagishi, D. Bulmash, P. Jacquod, A. Deshpande, K. Watanabe, T. Taniguchi, P. Jarillo-Herrero, and B. J. LeRoy, "Scanning tunnelling microscopy and spectroscopy of ultra-flat graphene on hexagonal boron nitride," *Nature Materials,* vol. 10, no. 4, pp. 282-285, 2011.

[231] A. K. Geim and I. V. Grigorieva, "Van der Waals heterostructures," *Nature,* vol. 499, no. 7459, pp. 419-425, 2013.

[232] L. Britnell, R. M. Ribeiro, A. Eckmann, R. Jalil, B. D. Belle, A. Mishchenko, Y. J. Kim, R. V. Gorbachev, T. Georgiou, S. V. Morozov, A. N. Grigorenko, A. K. Geim, C. Casiraghi, A. H. C. Neto, and K. S. Novoselov, "Strong light-matter interactions in heterostructures of atomically thin films," *Science,* vol. 340, no. 6138, pp. 1311-1314, 2013.

[233] T. Georgiou, R. Jalil, B. D. Belle, L. Britnell, R. V. Gorbachev, S. V. Morozov, Y.-J. Kim, A. Gholinia, S. J. Haigh, O. Makarovsky, L. Eaves, L. A. Ponomarenko, A. K. Geim, K. S. Novoselov, and A. Mishchenko, "Vertical field-effect transistor based on graphene-WS2 heterostructures for flexible and transparent electronics," *Nature Nanotechnology,* vol. 8, no. 2, pp. 100-103, 2013.

[234] S. J. Haigh, A. Gholinia, R. Jalil, S. Romani, L. Britnell, D. C. Elias, K. S. Novoselov, L. A. Ponomarenko, A. K. Geim, and R. Gorbachev, "Cross-sectional imaging of individual layers and buried interfaces of graphene-based heterostructures and superlattices," *Nature Materials,* vol. 11, no. 9, pp. 764-767, 2012.

[235] M. T. Paffett, R. J. Simonson, P. Papin, and R. T. Paine, "Borazine adsorption and decomposition at Pt(111) and Ru(001) surfaces," *Surface Science,* vol. 232, no. 3, pp. 286-296, 1990.

[236] A. Nagashima, N. Tejima, Y. Gamou, T. Kawai, and C. Oshima, "Electronic dispersion relations of monolayer hexagonal boron nitride formed on the Ni(111) surface," *Physical Review B,* vol. 51, no. 7, pp. 4606-4613, 1995.

[237] W. Auwärter, H. U. Suter, H. Sachdev, and T. Greber, "Synthesis of one monolayer of hexagonal boron nitride on Ni(111) from B-Trichloroborazine (ClBNH)3," *Chemistry of Materials,* vol. 16, no. 2, pp. 343-345, 2003.

[238] M. Corso, W. Auwärter, M. Muntwiler, A. Tamai, T. Greber, and J. Osterwalder, "Boron nitride nanomesh," *Science,* vol. 303, no. 5655, pp. 217-220, 2004.

[239] A. Goriachko, He, M. Knapp, H. Over, M. Corso, T. Brugger, S. Berner, J. Osterwalder, and T. Greber, "Self-assembly of a hexagonal boron nitride nanomesh on Ru(0001)," *Langmuir,* vol. 23, no. 6, pp. 2928-2931, 2007.

[240] K. K. Kim, A. Hsu, X. Jia, S. M. Kim, Y. Shi, M. Hofmann, D. Nezich, J. F. Rodriguez-Nieva, M. Dresselhaus, T. Palacios, and J. Kong, "Synthesis of monolayer hexagonal boron nitride on Cu foil using chemical vapor deposition," *Nano Letters,* vol. 12, no. 1, pp. 161-166, 2012.

[241] L. Song, L. Ci, H. Lu, P. B. Sorokin, C. Jin, J. Ni, A. G. Kvashnin, D. G. Kvashnin, J. Lou, B. I. Yakobson, and P. M. Ajayan, "Large scale growth and characterization of atomic hexagonal boron nitride layers," *Nano Letters,* vol. 10, no. 8, pp. 3209-3215, 2010.

[242] A. L. Gibb, N. Alem, J.-H. Chen, K. J. Erickson, J. Ciston, A. Gautam, M. Linck, and A. Zettl, "Atomic resolution imaging of grain boundary defects in monolayer chemical vapor deposition-grown hexagonal boron nitride," *Journal of the American Chemical Society,* vol. 135, no. 18, pp. 6758-6761, 2013.

[243] A. Ismach, H. Chou, D. A. Ferrer, Y. Wu, S. McDonnell, H. C. Floresca, A. Covacevich, C. Pope, R. Piner, M. J. Kim, R. M. Wallace, L. Colombo, and R. S. Ruoff, "Toward the controlled synthesis of hexagonal boron nitride films," *ACS Nano,* vol. 6, no. 7, pp. 6378-6385, 2012.

[244] S. Frueh, R. Kellett, C. Mallery, T. Molter, W. S. Willis, C. King'ondu, and S. L. Suib, "Pyrolytic decomposition of ammonia borane to boron nitride," *Inorganic Chemistry,* vol. 50, no. 3, pp. 783-792, 2011.

[245] K. H. Lee, H.-J. Shin, J. Lee, I.-y. Lee, G.-H. Kim, J.-Y. Choi, and S.-W. Kim, "Large-scale synthesis of high-quality hexagonal boron nitride nanosheets for large-area graphene electronics," *Nano Letters,* vol. 12, no. 2, pp. 714-718, 2012.

[246] N. Petrone, C. R. Dean, I. Meric, A. M. van der Zande, P. Y. Huang, L. Wang, D. Muller, K. L. Shepard, and J. Hone, "Chemical vapor deposition-derived graphene with electrical performance of exfoliated graphene," *Nano Letters,* vol. 12, no. 6, pp. 2751-2756, 2012.

[247] S. Banerjee, J. Shim, J. Rivera, X. Jin, D. Estrada, V. Solovyeva, X. You, J. Pak, E. Pop, N. Aluru, and R. Bashir, "Electrochemistry at the edge of a single graphene layer in a nanopore," *ACS Nano,* vol. 7, no. 1, pp. 834-843, 2013.

[248] B. M. Venkatesan, D. Estrada, S. Banerjee, X. Z. Jin, V. E. Dorgan, M. H. Bae, N. R. Aluru, E. Pop, and R. Bashir, "Stacked graphene-Al_2O_3 nanopore sensors for sensitive detection of DNA and DNA-protein complexes," *ACS Nano,* vol. 6, no. 1, pp. 441-450, 2012.

[249] A. E. Eriksson, W. A. Baase, X. J. Zhang, D. W. Heinz, M. Blaber, E. P. Baldwin, and B. W. Matthews, "Response of a protein structure to cavity-creating mutations and its relation to the hydrophobic effect," *Science,* vol. 255, no. 5041, pp. 178-183, 1992.

[250] D. Cohen-Tanugi and J. C. Grossman, "Water desalination across nanoporous graphene," *Nano Letters,* vol. 12, no. 7, pp. 3602-3608, 2012.

[251] J. M. Yuk, K. Kim, B. Alemán, W. Regan, J. H. Ryu, J. Park, P. Ercius, H. M. Lee, A. P. Alivisatos, M. F. Crommie, J. Y. Lee, and A. Zettl, "Graphene veils and sandwiches," *Nano Letters,* vol. 11, no. 8, pp. 3290-3294, 2011.

[252] J. M. Yuk, J. Park, P. Ercius, K. Kim, D. J. Hellebusch, M. F. Crommie, J. Y. Lee, A. Zettl, and A. P. Alivisatos, "High-resolution EM of colloidal nanocrystal growth using graphene liquid cells," *Science,* vol. 336, no. 6077, pp. 61-64, 2012.

[253] P. Ball, "Chemical physics: How to keep dry in water," *Nature,* vol. 423, no. 6935, pp. 25-26, 2003.

[254] Z. Li, Y. Wang, A. Kozbial, G. Shenoy, F. Zhou, R. McGinley, P. Ireland, B. Morganstein, A. Kunkel, S. P. Surwade, L. Li, and H. Liu, "Effect of airborne

contaminants on the wettability of supported graphene and graphite," *Nature Materials*, vol. 12, no. pp. 925-931, 2013.

[255] C.-J. Shih, Q. H. Wang, S. Lin, K.-C. Park, Z. Jin, M. S. Strano, and D. Blankschtein, "Breakdown in the wetting transparency of graphene," *Physical Review Letters*, vol. 109, no. 17, pp. 176101-176101-4, 2012.

CHAPTER 2. SUBSTRATE EFFECTS ON GRAPHENE GROWTH ON POLYCRYSTALLINE CU FOIL

2.1. Introduction to Graphene Chemical Vapor Deposition

Mechanical exfoliation of graphene has enabled many fundamental studies of this novel material [1]. While most exfoliated samples are of high quality, the lateral dimensions are at most tens of micrometers, limiting the fabrication of consistent, wafer-scale graphene structures. To that end, techniques have been developed for the fabrication of large-area graphene samples by epitaxy on SiC [2] and by chemical vapor deposition (CVD) on catalytic metals like Ni [3-5] or Cu [6]. Graphene grown by CVD on Cu foils has generated interest due to low cost and the prospect of large-area monolayer coverage [6]. While these are promising characteristics, dendritic growth [7], multilayer formation [8], and lower carrier mobilities [6] than those of exfoliated samples [9] suggest non-optimal quality of graphene grown on Cu. Lower quality likely results from heightened graphene nucleation and the formation of graphene grain boundaries (GBs) [10] on the polycrystalline Cu substrates typically used, both of which are deleterious to transport [11, 12]. The initial nucleation and growth dynamics of graphene play a critical role in determining the final film quality. However, such characteristics are dependent on Cu surface structure, suggesting that the underlying Cu substrate has a detailed influence on the nucleating carbon species during growth [13, 14].

In this study, we grow graphene by CVD on polycrystalline Cu foils with two carbon source gases, CH_4 and C_2H_4. We perform partial growths at 700 °C and 900 °C with C_2H_4 and full growths with CH_4 at 1000 °C. After high temperature processing the Cu surface contains many structures, namely polycrystalline facets, grain boundaries, and annealing twins. We

[*]Material presented in this chapter is reproduced with permission from J. D. Wood, S. W. Schmucker, A. S. Lyons, E. Pop, and J. W. Lyding, "Effects of polycrystalline Cu substrate on graphene growth by chemical vapor deposition," *Nano Letters* 11, no. 11, pp. 4547-4554, 2011. Copyright American Chemical Society, 2011.

determine that the Cu(100) surface causes slow, multilayer graphene growth. High index Cu facets cause compact graphene island formation, but their growth rates are still faster than on Cu(100). In contrast, the Cu(111) surface promotes fast, monolayer graphene growth with few defects. It is therefore apparent that the Cu substrate influences graphene nucleation and growth significantly.

2.2. Correlating Graphene Growth to Cu-Based Crystallography

Previous work has suggested that the Cu-graphene interaction is relatively weak after growth [6, 15] based on negligible copper carbide formation [16] and minimal graphene epitaxial alignment with the Cu substrate [13]. Nevertheless, in early stages of graphene growth, the interaction between the carbon source and the Cu substrate becomes quite important. Low-energy electron microscopy (LEEM) studies have shown a preferred growth front for carbon species on the Cu(100) surface [17]. These results were corroborated indirectly by scanning tunneling microscopy (STM) studies through an *in-situ* C_2H_4 decomposition process on both single crystal Cu(111) [13] and Cu(100) [3]. However, most graphene growth by CVD on Cu is done with polycrystalline Cu foils, which have different growth transients and dynamics than single-crystal substrates.

To determine the crystal structure of our underlying Cu foil substrates, we perform electron-backscatter diffraction (EBSD) measurements. These measurements give us crystallographic orientation in the x-, y-, and z-directions, but here we will only consider the z-plane of the copper surface [13, 18]. Figure 2.1 shows the partial growth of graphene at 700 °C with 20 sccm C_2H_4, 50 sccm H_2, and a 5 min growth time (30 s ramp up and fall times) on 5 mil thick (~125 μm) Cu foil (Basic Copper, Carbondale, IL). Our growths employ lower flow rates of carbon-containing gas with respect to the H_2 flow to decrease the chemical potential

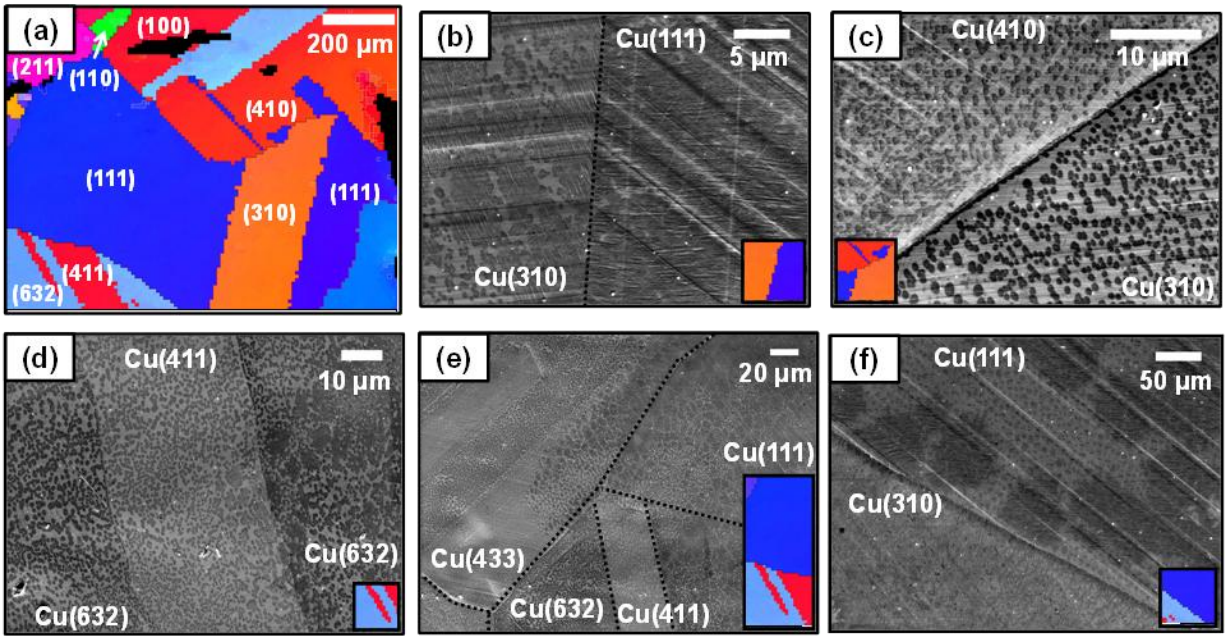

Figure 2.1. Scanning electron microscopy (SEM) imaging of graphene on different Cu facets. **(a)** Electron-backscatter diffraction (EBSD) image of a region of 5 mil Cu foil with graphene partially grown on it at 700 °C with C_2H_4. EBSD data shows the underlying Cu crystal structure. **(b)** Graphene on two Cu grains, Cu(310) and Cu(111). The low-index facet Cu(111) has faster, dendritic graphene growth which spills into the neighboring Cu(310) facet. Cu(310) has compact graphene islands away from the boundary, and the black line indicates the Cu grain boundary (GB). **(c)** Cu(410)-Cu(310) GB, with graphene islands of differing size on either side. **(d)** Cu(632)-Cu(411)-Cu(632) twinning boundary, showing both islands and graphene overgrowth from the presence of neighboring Cu(111) facets. **(e)** Large-area scan, indicating Cu(111) coverage. High-index planes show island formation. **(f)** Cu(111)-Cu(310) GB, showing large graphene islands near the boundary. Insets for (b-f) show EBSD data from (a) for the SEM regions.

difference [18], promoting crystallographic graphene edges [19] and monolayer growth [8]. An EBSD map of this foil in Fig. 2.1a shows a crystallographically diverse Cu surface, composed of Cu(111), Cu(310), Cu(410), Cu(411), Cu(632), Cu(211), Cu(110), and Cu(100) facets. The Cu(111) facet dominates the crystallographic map, which is expected as Cu(111) is the lowest energy Cu surface [20]. Next, we correlate the EBSD map with scanning electron microscope (SEM) imaging to assess graphene coverage visually. In Fig. 2.1b, we see nearly complete graphene coverage on the Cu(111) facet [21], whereas its neighboring Cu(310) facet is not completely covered. Moreover, graphene growth on the Cu(111) facet appears to spill over into the Cu(310) facet (crystallographic cross section given in the supplemental information),

suggesting that the presence of the Cu(111) facet influences nearby growth dynamics. In the supplemental information, we show how graphene preferentially nucleates on the Cu grain boundaries (GBs), consistent with predictions for Ni [3, 5] and surface roughness based diamond nucleation [22]. As graphene starts to nucleate at the Cu GBs (e.g. the Cu(111)-Cu(310) GB) and grows faster on the Cu(111) surface, additional carbon molecules from the gas adsorb on the existing graphene-Cu(111), diffuse on the film, and make their way quickly to the film edges, where the Cu catalyst dehydrogenates them [18, 23]. In these diffusion limited processes, graphene films on or near the Cu(111) surface appear dendritic, akin to STM studies of adsorbed atoms on Pt(111) [24]. Similar dendrites were recently reported by LEEM of graphene on single-crystal Cu(111) [25].

Far from the Cu GB in Fig. 2.1b, graphene forms compact islands on the Cu(310) surface, which is expected for surfaces not containing (111) terraces [24]. A higher island density will lead to a higher density of graphene GBs, and adverse transport effects [12, 26]. However, it has been suggested that at high temperature (~1000 °C) the thermal energy is high enough to restructure compact islands and prevent formation of GBs where the islands meet [27, 28]. Nevertheless, typical CVD growths have heightened Cu sublimation at high growth temperature, Cu GB migration causing elongated graphene film formation [29], and graphene wrinkles and ripples induced by thermal expansion [30]. These phenomena suggest that the dynamics of merging graphene islands is complex and is likely to form a chain of defects [31].

Additional compact island formation is shown in Fig. 2.1c for two high-index surfaces, Cu(410) and Cu(310). On these surfaces, hydrocarbons adsorb at certain preferential locations, such as point defects, surface kinks, adatom vacancies, or terrace steps [32]. At these sites, carbon species readily adsorb and dehydrogenate until the active Cu site is covered, terminating

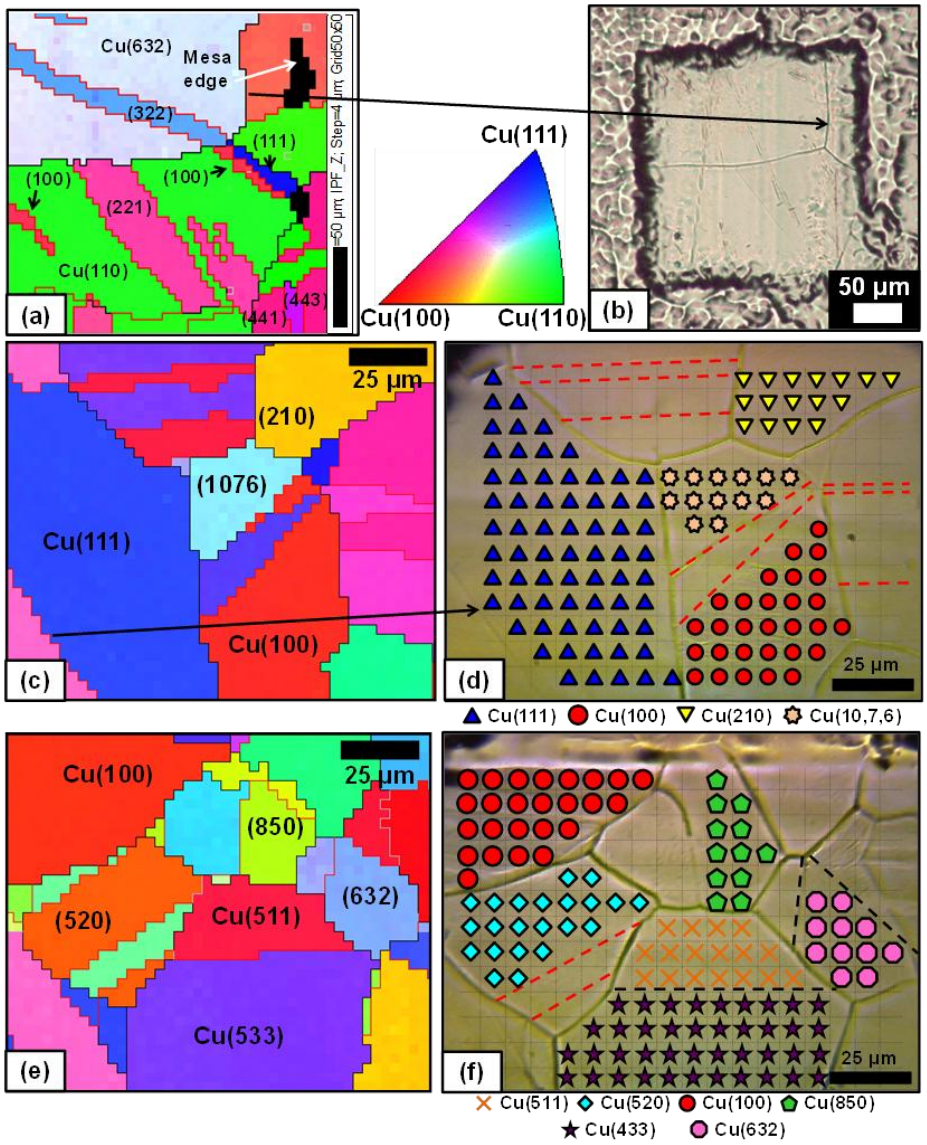

Figure 2.2. Defining Cu crystal structure and registry mesas for CVD graphene. **(a)** Electron-backscatter diffraction (EBSD) of a Cu registry mesa shown optically in **(b)**. EBSD black lines are copper grain boundaries, and EBSD red lines are annealing twins. Cu mesa is composed of many crystal facets. **(c)** EBSD and optical **(d)** information for another Cu mesa. The optical image of (d) shows the Raman spectra locations for different Cu facets, indicated by symbols (within the dotted lines). **(e)** Upper section of the Cu mesa in (c), showing high-index Cu facets. **(f)** Optical image of (e), with Raman spectra locations given by the symbols.

the reaction [7, 27]. However, carbonaceous species have lowered carbon diffusion and dimerization on these surfaces [21], making them less likely to propagate from the nucleation site. Hence, these sites have been called undersaturated or saturated, but not supersaturated [33], which is necessary to propagate growth. While raising the growth temperature improves

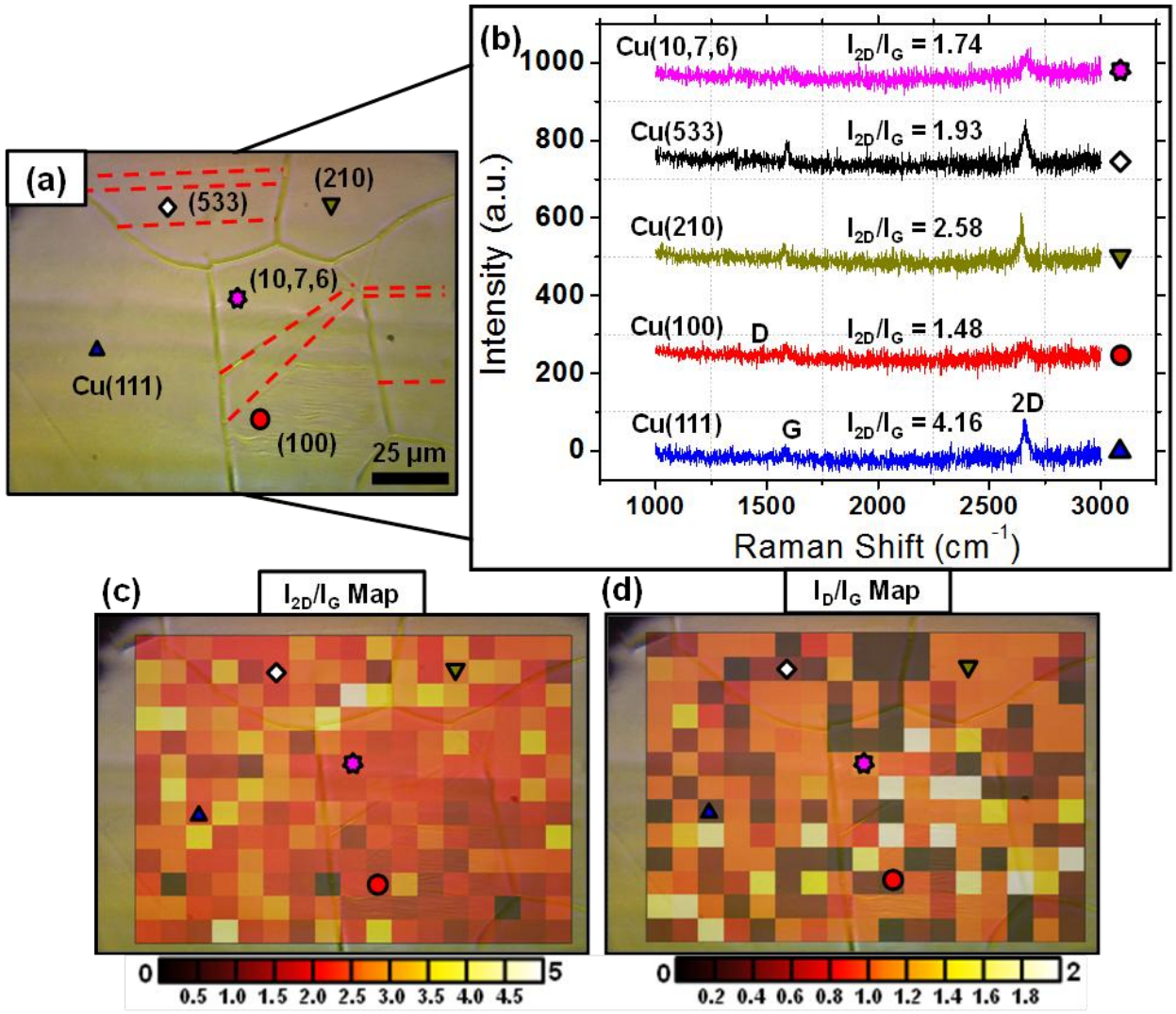

Figure 2.3. Reconciling graphene coverage with Cu facets by Raman spectroscopy. **(a)** Optical image of Cu mesa, with Cu crystal facets identified and annealing twins (dotted) present. Raman spectra taken at the colored shapes. **(b)** Raman point spectra of selected spots, with D, G, and 2D bands indicated. The graphene overall has few defects, but graphene on the Cu(100) has the lowest I_{2D}/I_G intensity ratio, indicative of few-layer growth. Cu(111) has pristine, monolayer graphene. **(c)** Raman spatial map of graphene monolayer intensity ratio I_{2D}/I_G for the region in (a). The Cu(100) surface as well as highly faceted regions like Cu(10,7,6) have lower monolayer intensity ratios, limited by carbon surface diffusion. **(d)** Graphene defect intensity ratio I_D/I_G for the same region. Defect distribution looks uniform, with differences due to Raman sampling of graphene nucleation sites. Raman pixel size is 7.5 μm at 633 nm excitation.

diffusion and can cause supersaturation, these sites' structure makes them temperature-invariant. The lack of supersaturation results in slower growth and defective [19], multilayer graphene. Within Figs. 2.1c-e, the presence of Cu(111) terraces influences growth within the other high-

index facets, such as Cu(411) or Cu(433). Graphene from Cu(111) can overgrow onto the high-index surfaces before compact islands can form.

Nonetheless, SEM imaging is insufficient for characterization of graphene coverage, as higher contrast regions are not necessarily graphene. Furthermore, when discussing the matter of graphene supersaturation on Cu, it is important to see if higher growth temperature influences complete film coverage. To further examine the graphene film properties by Raman spectroscopy [34-36] and atomic force microscopy (AFM), we pattern raised mesas (~20 μm high) on 1.4 mil Cu foil (Basic Copper) using standard photolithography. Two example mesas are shown optically by bright field imaging in Figs. 2.2b,d,e. We grow graphene at 1000 °C with 850 sccm of CH_4 for the mesa of Figs. 2.2a-b. Additionally, we grow graphene at 1000 °C with 100 sccm of CH_4 for the mesa of Figs. 2.2c-f. Both growths use 50 sccm of H_2, and a 30 min growth time. As before, we identify the Cu substrate facets by EBSD, indicated in Figs. 2.2a,c,f. The two mesas are highly polycrystalline, as seen in the EBSD mosaic. We give schematics of the mesas' relevant facets in the supplemental information, elucidating this high vicinality. The different shapes within the optical images of Figs. 2.2d,f show Raman point spectra positions for the varying Cu facets.

To see whether nucleation and initial growth transients manifest themselves in the steady-state film, we perform spatially resolved Raman spectroscopy of fully grown graphene on Cu for the mesa in Fig. 2.2d. Spatially resolved Raman spectra for the regions of Figs. 2.2b,f are given in Fig. 2.4. Within the optical image of Fig. 2.3.a, we identify the underlying Cu facets and annealing twins (red lines) using information from Fig. 2.2c. Point Raman spectra of Fig. 2.3b—taken at the points indicated by the shapes in Fig. 2.3.a—indicate more multilayer coverage [34-36] (intensity ratio I_{2D}/I_G ~ 1.48) on the Cu(100) surface and the high-index Cu(533) and

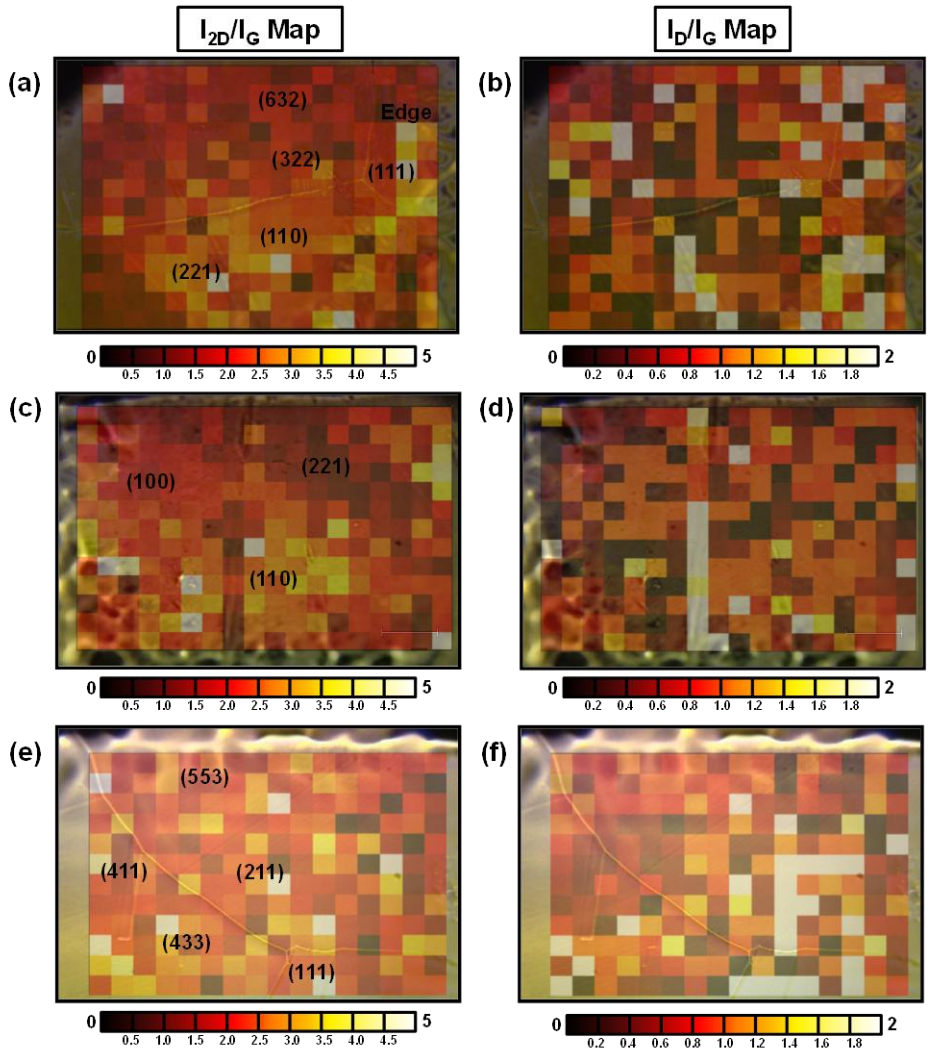

Figure 2.4. Additional Raman mapping of CVD graphene on polycrystalline copper. All growths performed with H_2 flow rate at 50 sccm. **(a)** I_{2D}/I_G map for fully grown graphene at 1000 °C with 850 sccm CH_4 (25 min growth). High-index facets show more multilayer coverage. **(b)** I_D/I_G map for growth in (a). No discernible pattern present. **(c)** I_{2D}/I_G map for fully grown graphene, same parameters as (a). Cu(110) produces more monolayer graphene than Cu(100) and Cu(221). Large intensity on the Cu wrinkle in this map (and in the I_D/I_G map) is due to a surface plasmonic effect [37]. **(d)** I_D/I_G map for growth in (c). Nucleation is uniform on low-index facets. **(e)** I_{2D}/I_G map for partially grown graphene at 900 °C with 20 sccm C_2H_4 (5 min growth, no gas flow after growth). **(f)** I_D/I_G map for growth in (e). Cu grain boundaries give large graphene defect ratios. Spectra taken with a 633 nm laser at 18 mW power, 50x objective, and 30 s acquisition time.

Cu(10,7,6) surfaces (I_{2D}/I_G ~ 1.93 and I_{2D}/I_G ~ 1.74, respectively). On the Cu(111) surface, the graphene coverage is high-quality monolayer (I_{2D}/I_G ~ 4.16). The D band, which normally assesses the graphene quality, is weak or inexistent in these point spectra.

Analyzing the Raman intensity ratio I_{2D}/I_G (monolayer ratio) spatial map of Fig. 2.3c, we see a lower monolayer ratio for the Cu(100) surface and larger ratios for the high-index surfaces and Cu(111). This suggests that the diffusion of carbon-containing species is slower on Cu(100) compared to the higher-index surfaces and Cu(111). Adatom diffusion on Cu(100) compared to Cu(111) has been studied previously [38], with Cu(100) requiring surface atom exchange. Surface atom exchange is markedly slower than simple adatom hopping, which occurs on Cu(111). Thus, on Cu(100) surfaces, C atoms could stack in a multilayer configuration to lower surface [38] and adsorption energy [18]. Conversely, carbon's higher diffusion rate on Cu(111) will promote monolayer formation. The higher-index surfaces are composed of Cu(100), Cu(110), and Cu(111) monatomic terraces and steps, as discussed in the supplemental information. We find that carbon diffusion and graphene growth on those surfaces is dependent on the percentage of Cu(111) surface present in the decomposed high-index facet. A high-index surface close to Cu(111) on the stereographic triangle, namely, with a high (111) percentage, will likely have a higher diffusion rate and predominantly monolayer graphene.

For the I_D/I_G (defect ratio) map of Fig. 2.3d, the distribution looks more uniform across the mesa, with some sparse points differing from the norm. On the coarse scale of our Raman map (~100 μm by ~130 μm), it is likely that these sparse points correspond to graphene nucleation centers [39]. These nucleation centers appear consistently across the different Cu crystals, regardless of whether they are low- or high-index surfaces. For the C_2H_4 partially grown graphene in Figs. 2.1b-f, it is evident that that high-index Cu surfaces cause compact island formation for initial graphene nucleation and ultimately slow down growth. However, higher graphene diffusion on Cu(111) confounds our ability to discern individual nucleation sites by SEM. It is therefore possible that both the low- and high-index facets would have similar

nucleation densities but different growth rates, hiding the nucleation sites. It is more likely, however, that this nucleation difference is from both higher nucleation site adsorption energy on high-index surfaces and lower hydrocarbon cracking efficacy at the growth temperatures in Fig. 2.1 (700 °C). At low temperature, the high probability of vicinal, high-index facets forming compact islands follows from this adsorption energy argument, resulting in denser nucleation. Moreover, for fully grown graphene at 750 °C, this was shown to lead to higher disorder and smaller graphene domains [40]. Hydrocarbons at 1000 °C for the full graphene film of Fig. 2.3d have high cracking efficacy and diffusion, leading to fewer nucleation sites and Cu facet invariance in I_D/I_G from carbon supersaturation [33].

2.3. Graphene Quantitative Analysis

In Fig. 2.5 we present a quantitative assessment of graphene coverage from the SEM images shown in Fig. 2.1 and from the Raman analysis within Figs. 2.3 and 2.4. Figure 2.5a shows the I_{2D}/I_G monolayer ratio for all the Cu facets explored in Figs. 2.3 and Fig. 2.4. Overall, the distribution is monolayer-like and normal, peaked at $I_{2D}/I_G = 1.95 \pm 0.63$. However, the high standard deviation suggests some non-uniformity in the distribution due to the different Cu facets. Within Figs. 2.5b-c we explore the defect ratio I_D/I_G shown in Fig. 2.3d more carefully. In Fig. 2.5b, we show I_D/I_G for partially grown graphene with 20 sccm C_2H_4 (5 min growth time) at 900 °C, whose value is $I_D/I_G = 0.67 \pm 0.48$ ($n = 174$). Conversely, the fully grown graphene sample from Fig. 2.3 and Fig. 2.4 has a value of $I_D/I_G = 0.69 \pm 0.47$ ($n = 436$), as Fig. 2.5c indicates. We are unable to reject the null hypothesis at the 99% level suggesting that these samples may share a population. Similar hypothesis tests only supported the conclusion of differing populations at a statistically unreasonable 50% level. Compared to a full growth, partial graphene growths like Fig. 2.5b should have more Raman active armchair edges [39] which

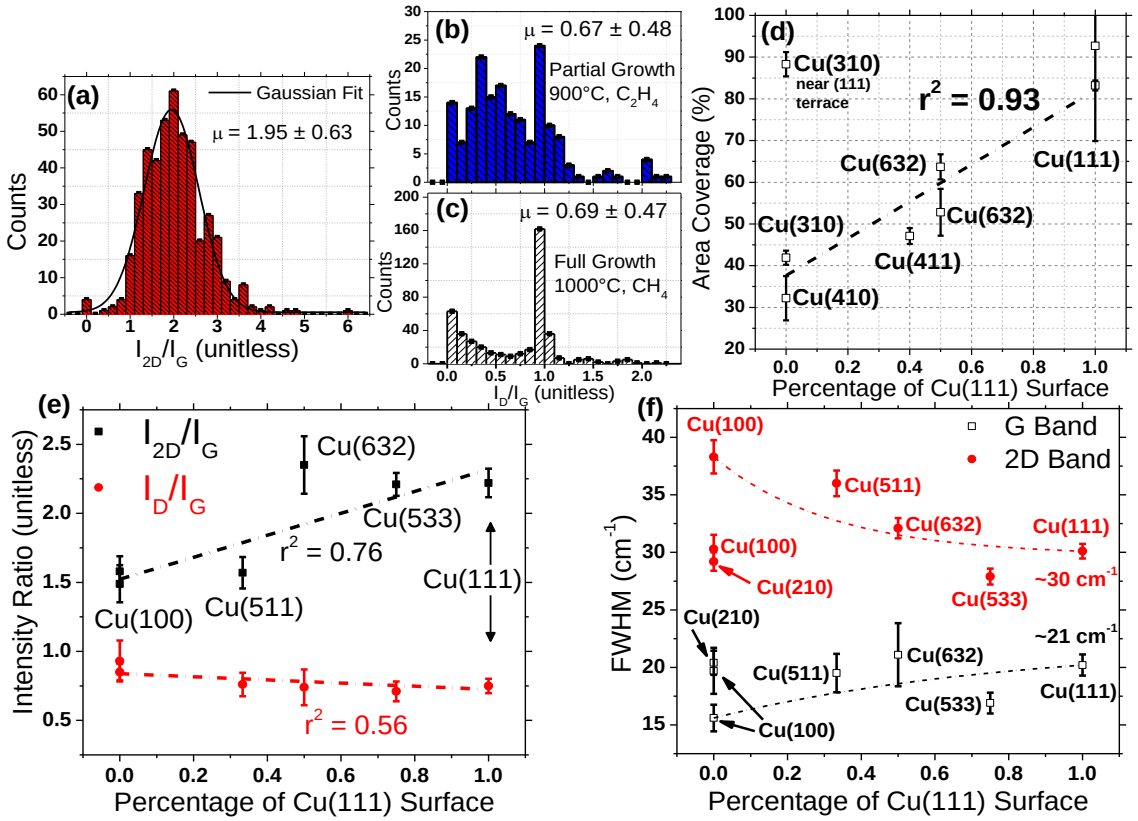

Figure 2.5. Quantitative assessment of graphene coverage. **(a)** Monolayer ratio (I_{2D}/I_G) histogram from Raman mapping for all Cu facets. Distribution is normal with a mean of I_{2D}/I_G ~ 2, expected for monolayer graphene. **(b)** Partially grown graphene defect ratio (I_D/I_G) histogram. Growth occurred at 900 ºC with ethylene. **(c)** Fully grown graphene defect ratio (I_D/I_G) histogram, from the data in (a). The means and standard deviations of (b) and (c) are markedly similar, despite the partial growth. **(d)** Area coverage of facets containing the Cu(111) surface. More (111) surfaces have higher graphene coverage. These data values are extracted from the SEM images in Figure 2.1. **(e)** Intensity ratios I_{2D}/I_G and I_D/I_G for different Cu facets. The independent variable gives the percentage of (111) terraces or steps in the facet. Cu(111) gives monolayer graphene, whereas the other facets give more multilayer coverage. Defect distribution appears invariant across the facets, indicating uniform nucleation and GB density. **(f)** 2D and G band FWHM for different Cu facets from (e), with lines to guide the eye. Cu(100) and the higher index facets deviate from monolayer graphene value at ~30 cm^{-1} for the 2D band. Further, they have a lower G band FWHM, highlighting substrate doping and strain in the graphene. Raman spectra collected at 633 nm excitation, 50X objective, and ~9 mW power.

contribute to a higher I_D/I_G value. While this changes the shape of the distribution relative to Fig. 2.5c, the large sample size averages out these edge effects and points to a common source for the I_D/I_G value. Our results suggest that this source is substrate invariant nucleation sites, as argued by a recent work [28].

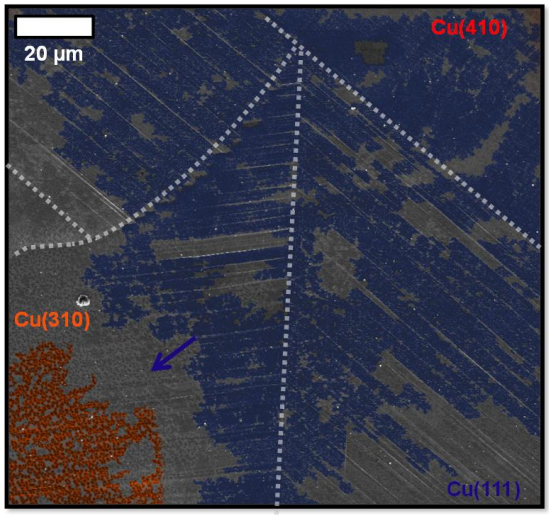

Figure 2.6. SEM of graphene overgrowth from Cu(111). The graphene shown in this SEM image is a partial graphene growth on 5 mil thick Cu with 20 sccm C_2H_4 and 50 sccm of H_2 at 700 °C. The graphene from the Cu(111) region (blue) overgrows into the neighboring Cu(310) (orange) and Cu(410) (red, none shown) facets. The Cu GBs are indicated by dotted lines. The Cu(310) forms compact graphene islands far from the Cu GB which are not overgrown by the graphene that originated on Cu(111). Graphene overgrowth is due to heightened carbon diffusion on Cu(111) compared to higher index facets.

From contrast differences in the SEM images of Figs. 2.1b-f, we extract the amount of graphene area coverage following a procedure detailed in the supplemental information. Figure 2.5d gives this area coverage as a percentage of the Cu(111) surface, which we determine by decomposing high-index facets into a superposition of (111), (110), and (100) facets. Surfaces containing (111) terraces—like Cu(411), Cu(632), and Cu(111)—show a linear increase in graphene coverage for the same growth time (5 min) when compared to surfaces with only (100) terraces (e.g. Cu(410), Cu(310)). In the case where surfaces were spatially near (111) terraces, like the Cu(310) surface near Cu(111) in Fig. 2.1b, the heightened carbon diffusion on Cu(111) allowed graphene overgrowth into the Cu(310) facet, raising the area coverage on that facet (see Fig. 2.6). The Cu(632) surface contains both (111) and (100) facets, giving a larger overall area coverage than (100) containing surfaces alone, but less than surfaces with a larger percentage of (111). Figures 2.5e-f give Raman spectroscopic measurements (I_{2D}/I_G, I_D/I_G, 2D FWHM, and G FWHM of the regions assessed in Figs. 2.5a-c) obtained using 633 nm laser excitation and ~9

mW power. Tables 2.1–2.3 present a full tabulation of these measurements with sample numbers. Figure 2.5e details the monolayer (I_{2D}/I_G) and defect (I_D/I_G) ratios for different Cu facets as a percentage of the Cu(111) surface, as in Fig. 2.5d. Figure 2.7 shows similar information as a percentage of the Cu(100) surface. The intensity ratios for a particular facet are comprised of an entire population of point Raman spectra at the positions indicated in Fig. 2.2d,f. We note that graphene grown on Cu(111) is primarily monolayer with low defect density. The other facets appear more multilayer, especially Cu(100) (I_{2D}/I_G ~ 1.5). Error bars represent standard error of the mean. Surfaces which contain (111) terraces therefore have more monolayer graphene than those with (100) terraces. We ascribe this to a better lattice match of hexagonal graphene with the hexagonal Cu(111), promoting higher adsorption of carbon-containing species [18] and giving a quasi-epitaxial relationship, as was observed by STM [13]. Conversely, we attribute multilayer regions on Cu(100) to slow, adatom-

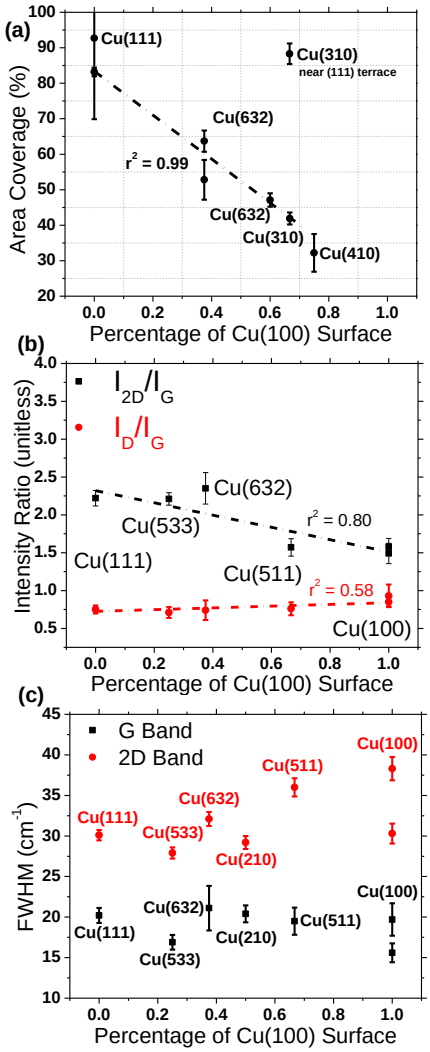

Figure 2.7. Graphene coverage as a function of a facet's Cu(100) percentage. **(a)** Area coverage of facets containing the Cu(100) surface. More (100) surfaces have linearly lower graphene coverage. These data are extracted from the SEM images in Figure 2.1. **(b)** Intensity ratios I_{2D}/I_G and I_D/I_G for different Cu facets. As the surface becomes Cu(100), the graphene coverage becomes more multilayer. **(c)** 2D and G band FWHM for different Cu facets from (b). The (100)-containing facets have a lower G band FWHM, highlighting substrate doping and strain in the graphene. Raman spectra collected at 633 nm excitation, 50x objective, and ~9 mW power.

exchange mediated carbon diffusion [38] and heighted atomic carbon adsorption energy [18], as evident from the area coverage of Fig. 2.5d. Interestingly, the I_D/I_G ratio is invariant across the facets listed. As is the case with Figs. 2.5b-c, we attribute this to common nucleation densities across the different facets. While Cu(100) gives relatively more defective graphene than Cu(111), in agreement with recent STM results [14], there is insufficient statistical evidence to claim a crystalline influence on the number of graphene defects. Based on the results shown in Fig. 2.5, at growth temperatures above 900 °C carbonaceous species do not preferentially nucleate on kinks, vacancies, and Cu GBs, unlike low temperature growth at 700 °C.

In Fig. 2.5f, we show the 2D and G full width at half maximum (FWHM) as a function of the facet Cu(111) percentage. Figure 2.7 shows similar data for the Cu(100) facet. The 2D band FWHM for exfoliated graphene is an indicator of the graphene layer number [34, 35], whereas the G band FWHM indicates doping [41], strain [42], and layer number. For surfaces with a higher percentage of Cu(111), the 2D FWHM approaches ~30 cm^{-1}, consistent with monolayer graphene [35]. Graphene on Cu(100) has a 2D FWHM of ~38 cm^{-1}, close to 40 cm^{-1} for turbostratically stacked multilayer graphene [43]. It is likely that graphene grown on Cu has been doped or strained due to its Cu underlayer [13], and it is possible that these effects change with respect to the underlying facet. Using the Cu workfunction Φ_{Cu} ~ 4.7 eV and graphene workfunction Φ_G ~ 4.5 eV [44], we estimate that the doping-induced shift in the FWHM of the G peak is ~6 cm^{-1} with E_F ~ 0.2 eV in the graphene [45]. Adding this to the known G FWHM [41] of 15 cm^{-1} gives an expected FWHM of ~21 cm^{-1} for p-doped graphene on Cu. The G FWHM approaches this value on the Cu(111) surface and is lower on high-index surfaces and Cu(100) due to doping and G peak phonon stiffening [41]. Since the presence of the graphene overlayer strains the Cu, forming stepped surfaces [13, 28] and hillocks [17], it is possible that the Cu

strains the conformal graphene as well, thereby contributing to G FWHM shift by strain [42]. However, the strain required to produce this shift would break the graphene, and we conclude that these facets also mainly dope the graphene.

Nevertheless, we must consider the possibility that the reduced surface roughness of Cu(111) and (111) containing surfaces could be the origin of this high-quality graphene growth. In Fig. 2.8, we investigate the effects of Cu facet root mean square (RMS) surface roughness on graphene nucleation and quality. Figures 2.8a-f show 5×5 μm AFM images of different Cu facets. Figure 2.8a is an AFM image of the partially grown graphene on Cu(111) analyzed in Fig. 2.1. Figures 2.8b-f are AFM images of the fully grown graphene in Figs. 2.2 and 2.3,

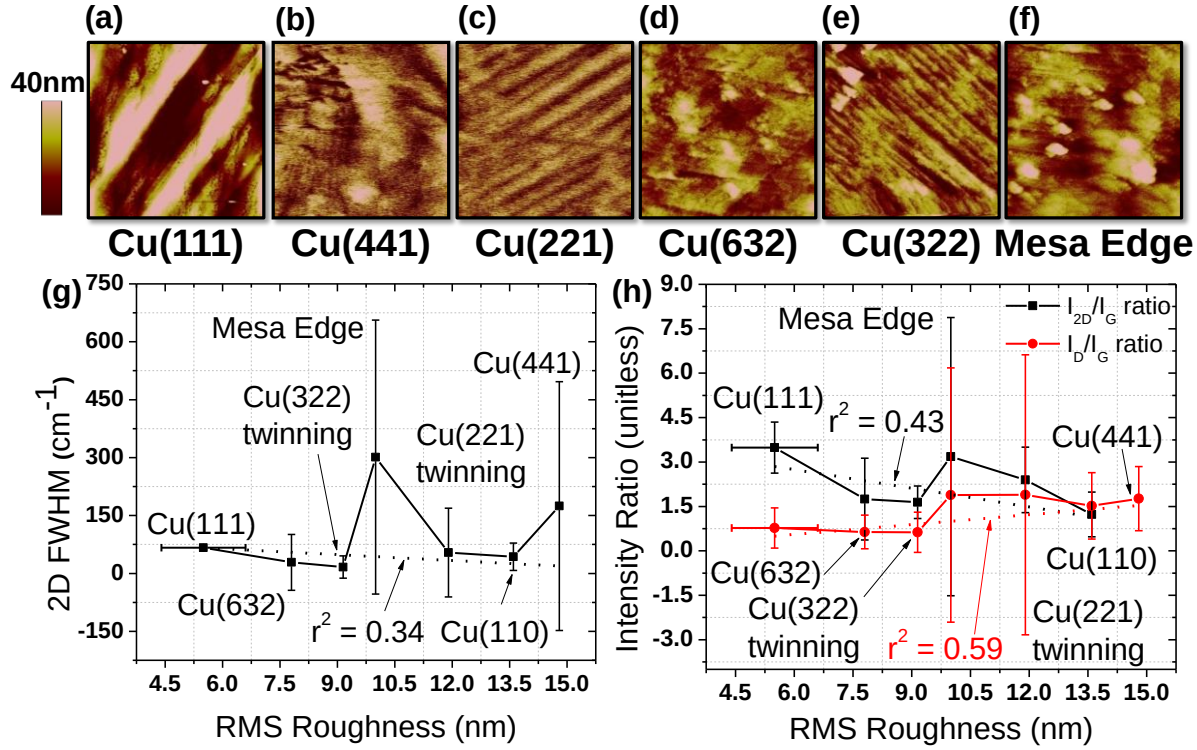

Figure 2.8. RMS roughness effects on graphene nucleation and quality. **(a-f)** 5 μm by 5 μm atomic force microscopy (AFM) images of the Cu(111), Cu(441), Cu(221), Cu(322), and Cu(632) facets, as well as the edge of the lithographically defined mesa. **(g)** AFM determined RMS roughnesses and 2D peak full width at half-maximum (FWHM) values for different facets. Within the error, there is no apparent FWHM dependence on RMS roughness. Average 2D FWHM is ~56 cm^{-1}, higher than ~30 cm^{-1} for graphene on SiO_2 due to Cu substrate doping and strain. **(h)** I_{2D}/I_G (graphene coverage) and I_D/I_G (graphene quality) ratios with respect to the RMS roughnesses from (a-f), showing no dependence on roughness.

respectively. The Cu foil of Fig. 2.8a is wrinkled, giving the bright undulations apparent in the AFM image. We take RMS roughness measurements within those regions and report the error for ensemble RMS roughness. Conversely, RMS roughness measurements for Figs. 2.8b-f are taken for the entire AFM image, without a statistical sampling that would allow an error bar in the RMS measurement. We then plot the Raman 2D band FWHM and intensity ratios I_{2D}/I_G and I_D/I_G with respect to the facet RMS roughness in Figs. 2.8g-h. It is apparent that the trend between the graphene quality metrics and the roughness is weak. A linear fit of the 2D FWHM against the RMS roughness gives a Pearson correlation coefficient $|r| = 0.58$, suggesting that there is no correlation between the 2D FWHM and RMS roughness at 99% statistical significance. Furthermore, linear fitting the intensity ratios I_{2D}/I_G and I_D/I_G give $|r| = 0.81$ and $|r| = 0.74$, respectively, which are not correlated with RMS roughness at 99% significance. This supports the notion that the RMS roughness does not play a critical role in monolayer graphene growth quality. Hence, it is likely that that Cu crystallinity is playing a stronger role in the initial growth dynamics and eventual steady-state graphene film.

We have also examined the oxidation of our graphene-coated Cu foils. For instance, previous work [46] had reported oxidation resistance in ambient environments up to 200 ºC, however here we found that the degraded graphene quality on Cu facets causes Cu oxidation at lower temperatures. The Cu begins to oxidize at 135 ºC, with thicker CuO forming at higher temperatures as shown in the successively oxidized images of Figs. 2.9a-d (full oxidation at 275 ºC, Fig. 2.9d). The graphene film was only partially grown on the Cu foil; thus, it is possible that oxygen atoms are diffusing under the graphene to oxidize the Cu, and oxidizing the Cu between the small graphene islands. However, subsurface oxidation is unexpected considering the low permeability of atoms under graphene [47]. Oxidation might be explained by oxygen etching of

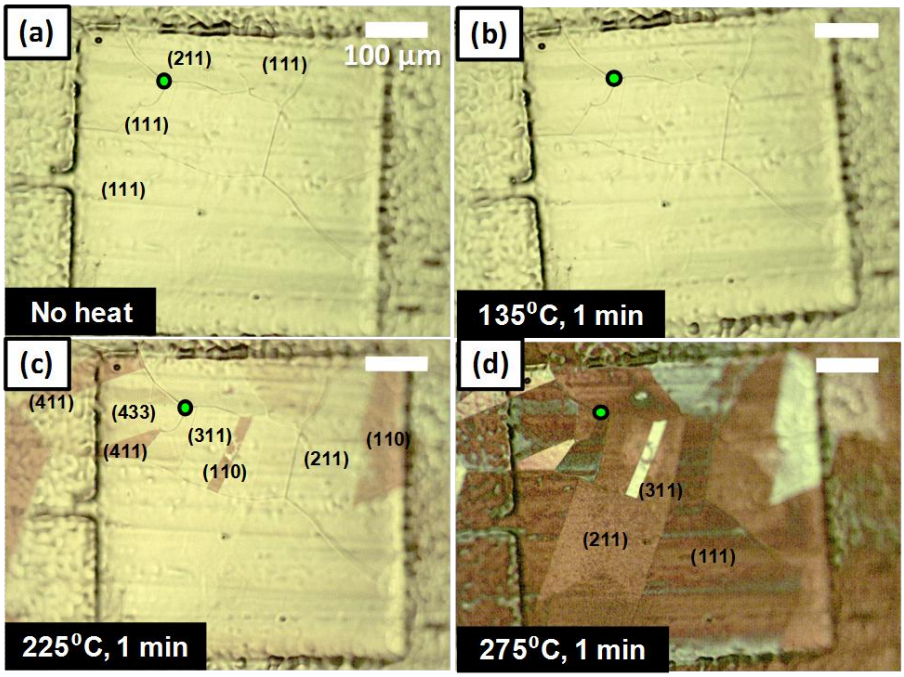

Figure 2.9. Reduced oxidation resistance for graphene on polycrystalline Cu facets. **(a)** Optical image showing a Cu mesa with partially grown graphene at 900 °C. EBSD-identified facets shown and green circle is used to guide the eye through successive images. **(b)** Mesa raised to 135 °C for 1 min on a hot plate in ambient. No noticeable oxide formation is observed by optical contrast. **(c)** Mesa raised to 225 °C after treatment in (b). Cu(110), Cu(411), and Cu(433) show CuO oxide formation. **(d)** Mesa raised to 275 °C after treatment in (c), where all copper has been oxidized despite the original presence of graphene. Differences in color are due to CuO oxide thickness [49]. In these images, sparser graphene coverage on particular Cu facets allowed those facets to oxidize first.

graphene edges [48] and GBs. In the latter case, a higher level of compact island formation—occurring on high-index surfaces—will lead to more GBs. Consequently, those films will likely oxidize first. It is still possible that the exposed Cu is oxidizing and the graphene-coated regions are not oxidized. However, when we reduce the oxide by immersing the CuO foil into concentrated acetic acid for ~5 min and then reoxidize it, we find that this reoxidized film has a lower oxidation temperature, with full oxidation at 225 ºC. Further, Raman spectra show high amorphous carbon coverage, suggesting graphene film damage during oxidation.

2.4. Conclusions

In summary, we find that the growth of high-quality, large-domain graphene depends on the underlying Cu crystal structure. By EBSD, we determine that the Cu foils used in typical

CVD growth are highly polycrystalline, containing Cu GBs, annealing twins, and high-index crystal facets. Low-index Cu facets produce more monolayer graphene with fewer defects compared to the high-index surfaces. Raman spectroscopy shows that the Cu(111) surface grows the highest quality monolayer graphene, with high area coverage and short growth time. We attribute this to high diffusion [13, 14] and improved adsorption [18] of carbon-containing species on Cu(111). The dendritic arms that we observe in our SEM images are consistent with molecular adsorption on fcc(111) surfaces [24]. Conversely, high-index facets form compact graphene islands based on lowered diffusion, nucleation, and pinning at rough surface sites, like step edges, adatom vacancies, and terrace kinks. Since Cu(111) is the lowest-energy Cu surface [20], longer pre-growth anneals under Ar/H_2 flow at ~900 ºC can help in the production of Cu(111) facets on the polycrystalline Cu substrate while mitigating Cu sublimation and GB migration [29]. Moreover, careful, high vacuum evaporation of single-crystal Cu(111) on basal-plane sapphire [50] might be another means by which to take advantage of the improved graphene growth qualities of Cu(111).

2.5. Materials and Methods

2.5.1. Graphene Growth

Unless otherwise noted, we used 1.4 mil copper foil (~35 μm thick, 99.9% pure, from Basic Copper, Carbondale, IL USA) in an Atomate hot-wall commercial CVD system for graphene growth. These Cu foils were annealed at ~1000 °C under Ar/H_2 flow for ~1 hr, and we grew graphene with the growth gases, flow rates, growth times, and growth temperatures listed in the main manuscript or in this document. The resulting substrates were cooled to room temperature at ~20 °C/min under the same gas flow, except in the case of the partially grown films, which had only Ar/H_2 flow during cool down.

2.5.2. Mesa Definition

Cu mesas were patterned by photolithography using a Shipley 1813 positive tone photoresist (PR). After ultraviolet exposure (20 s), MF-319 development (20 s), and a PR hard bake, the PR exposed regions were etched in oxone (potassium peroxymonosulfate, Alfa Aesar), a Cu etchant. Mesas in Fig. 2.2c-f were etched for ~5 min, raising the mesas approximately ~5 μm from the surface. Mesas in Fig. 2.2a-b and Fig. 2.3e-f were etched for ~1 hr, raising the mesas approximately ~60 μm. The xy mesa size used depended on the Raman map.

2.5.3. Electron Backscatter Diffraction (EBSD) Analysis

EBSD was collected using a JEOL 7000F Analytical SEM with HDL Technology EBSD System. During EBSD collection, the probe current is 5 nA, the accelerating voltage is 25 kV, and the angle of incidence is 70 degrees. Data is collected as an array of points with 10 μm lateral spacing. For the sparse Raman mapping in our experiments (~7.5 μm data pixels), we hold that this 10 μm resolution is sufficient to get the average facet value and correlate effects between the graphene and facet value. In the case where the color of our electron-backscatter diffraction (EBSD) readout was not obviously a low-index facet, e.g. (100), (110), or (111), we extrapolated the average EBSD value using the stereographic triangle. For example, a yellow pixel would fall between Cu(100) and Cu(110), which extrapolates to Cu(210). High-index surfaces were decomposed into a number of microfacets for further analysis, according to the procedure of Section 2.5.7 of this document.

2.5.4. Scanning Electron Microscopy (SEM) Imaging

Scanning electron microscopy (SEM) images with low graphene contrast relative to the supporting Cu substrate were contrast enhanced. This contrast enhancement consisted of increasing the pixel contrast by at least 70% and the pixel brightness by 0–20%.

2.5.5. Raman Data Collection

Unless otherwise noted, Raman data was collected using a Renishaw Raman microscope with inVia WiRE 3.2 software. Experimental parameters include the following: laser excitation was 633 nm; a 50x objective was used; laser was at 50% power (18 mW output power); and the acquisition time was 30 s. The output Raman spatial maps were swept from 1000 cm^{-1} to 3000 cm^{-1} for each data point and imported into MATLAB for analysis. Each Raman spectra was fit to Lorentzians about the D, G, and 2D bands. The bands were centered at [1325, 1375] cm^{-1}, [1560, 1600] cm^{-1}, and [2640, 2740] cm^{-1}, respectively, for the D, G, and 2D. The program attempted 20 Lorentzian fits before declaring that the Lorentzian fit had failed (see Tables 2.1-2.3). To avoid effects from Cu grain boundaries (GBs), we selected point Raman spectra for individual Cu facets, according to the positions outlined in Fig. 2.2d,f. These spectra are ~5 μm from the GBs, which we consider sufficient to avoid GB migration [29] and heightened carbonaceous deposit (see [5] and Fig. 2.10). Some histograms (Fig. 2.4a, Fig. 2.7) were produced with all Raman data collected, including data which landed on Cu GBs or on mesa edges.

2.5.6. Atomic Force Microscopy (AFM) Data Collection

AFM images were gathered using a Veeco (Bruker) Dimension IV controller with a Dimension 3100 head in tapping mode. Si cantilevers with a resonant frequency of 300 kHz were employed. We calculated RMS roughness values using the Nanoscope 6.14R1 software provided by Veeco. Cu foils were flattened prior to AFM imaging to ensure good vacuum contact between the sample and the stage.

2.5.7. Assigning Percentages to Cu Crystals

Within the text and this supplemental document, we assign percentages of (111) and (100) Cu surface to the different high-index crystals. To accurately determine these percentages,

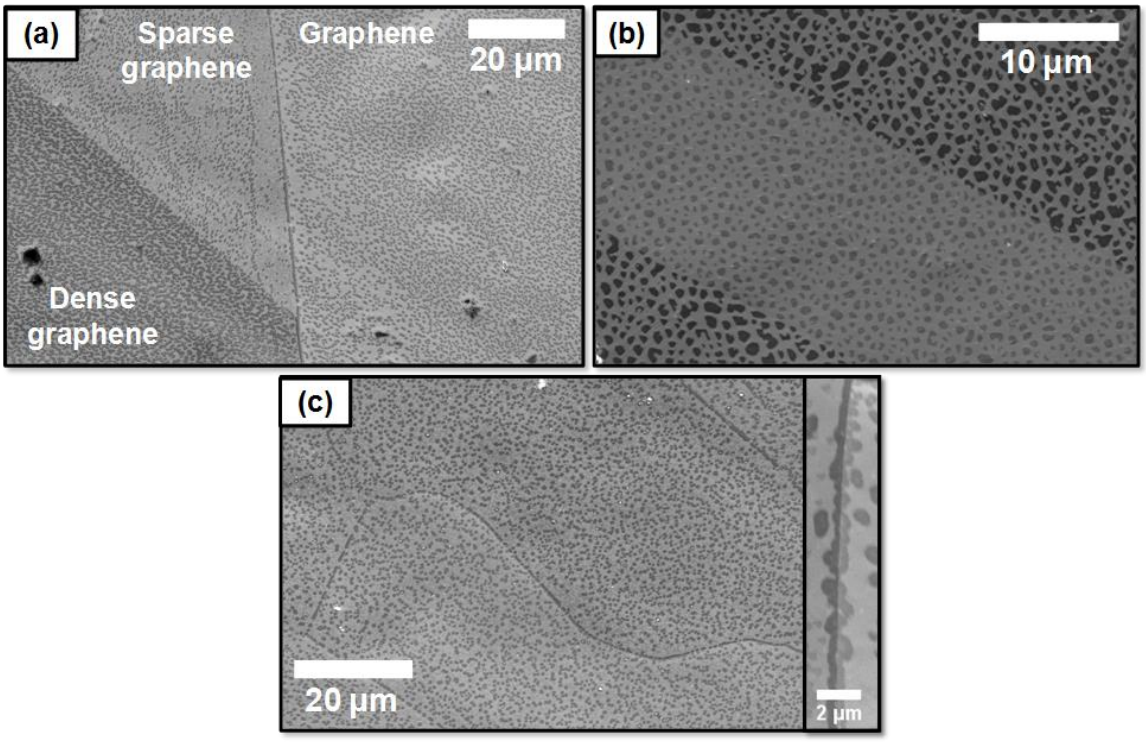

Figure 2.10. SEM identification of graphene nucleation on polycrystalline Cu. **(a)** Partial graphene growth on 5 mil thick Cu with 20 sccm C_2H_4 and 50 sccm of H_2 at 700 °C. Growth time is 5 min. Graphene platelet density varies based on the Cu grain, each of which is different crystallographically. **(b)** Graphene on 5 mil Cu grown at 900 °C with 20 sccm of C_2H_4 and 50 sccm of H_2. Growth is cycled two times, with 30 s of growth time followed by 5 min of annealing in the growth stage. Graphene grain size is larger on the surrounding region than on the center annealing twin. **(c)** Preferential graphene growth on winding Cu grain boundaries. Growth parameters same as (a). **Inset:** close-up of graphene nucleating on a Cu GB.

we must decompose the high-index Cu crystals into a surface basis of (100), (110), and (111) microfacets (see Fig. 2.11 for representative images). To that end, we follow the method discussed by van Hove and Somorjai [51], which splits these high-index surfaces into a microfacet notation [32, 52] and a unit cell notation [51]. We derive the percentages from the number of unit cells present on the crystal surface. The interaction of carbonaceous species and high-index surfaces is complex. When considering the adsorption energy of carbonaceous species, one cannot simply use a superposition of the adsorption energies of basis low-index facets. However, one can use the adsorption energy of carbon on Cu(111) [18] as a first estimate for how the adsorption energy might change on a more vicinal surface.

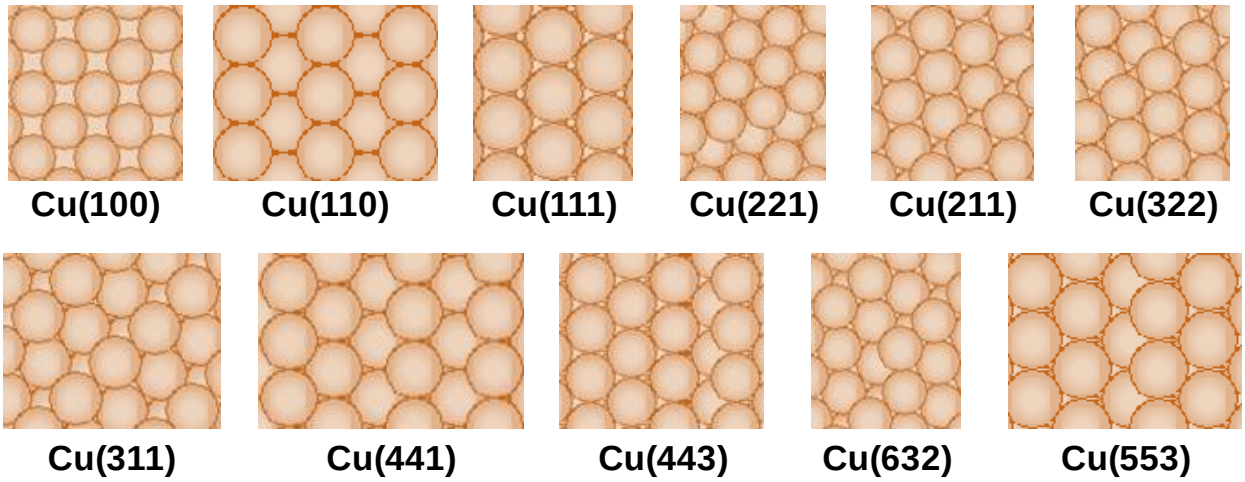

Figure 2.11. Schematic examples of low-index and high-index Cu facets.

2.6. Tables

Table 2.1. Raman statistics for graphene on different Cu crystals. F stands for failed Lorentzian fits, and these values correspond to the metric to the left. A Lorentzian fit was attempted for all peaks for a maximum of 20 trials; failure to converge upon a Lorentzian peak within this number of trials resulted in a failed fit. All normality tests done with Lilliefors normality (two-tailed) test at 95% confidence, with p statistics listed. The normality results are given in Table 2.2. Peaks' FWHM are cutoff at 100 cm^{-1}, where fits with FWHM greater than 100 cm^{-1} are considered failed fits. Three samples worth of data are included. Crystals with no designation were grown at 100 sccm of CH_4 and 50 sccm of H_2 at 1000 ºC for 25 min, with CH_4 present during cool down to room temperature. The samples with 850 sccm CH_4 designation were grown similarly, except with 850 sccm of CH_4 instead of 100 sccm of CH_4. The samples with partial designation were partially grown at 900 ºC with 20 sccm of C_2H_4 and 50 sccm of H_2. There was no C_2H_4 present during cool down.

Cu Facet	n	I_{2D}/I_G	F	I_D/I_G	F	2D FWHM	F	G FWHM	F	D FWHM	F	G Peak Position
Cu(111)	68	2.22±0.85, p=0.46	0	0.75±0.43, p=0.001	1	30.1±5.2 cm^{-1}, p=0.5	0	20.2±7.6 cm^{-1}, p=0.019	0	17.0±11.2 cm^{-1}, p=0.028	14	N/A
Cu(100)	29	1.58±0.59, p=0.0057	0	0.93±0.80, p=0.001	4	30.3±6.6 cm^{-1}, p=0.5	0	19.7±10.8 cm^{-1}, p=0.0285	1	15.2±12.1 cm^{-1}, p=0.382	8	N/A
Cu(210)	16	2.53±0.59, p=0.289	0	0.92±0.18, p=0.001	2	29.2±3.2 cm^{-1}, p=0.2	0	20.4±4.2 cm^{-1}, p=0.5	0	15.1±5.6 cm^{-1}, p=0.386	2	N/A
Cu(511)	17	1.57±0.47, p=0.5	0	0.76±0.35, p=0.001	3	36.0±4.6 cm^{-1}, p=0.280	0	19.5±6.9 cm^{-1}, p=0.311	0	15.4±9.5 cm^{-1}, 0.053	3	N/A
Cu(520)	22	2.07±0.59, p=0.5	0	0.76±0.35, p=0.001	4	33.6±5.8 cm^{-1}, p=0.025	0	18.7±7.9 cm^{-1}, p=0.125	0	15.0±11.3 cm^{-1}, p=0.061	6	N/A

Table 2.1. Raman statistics for graphene on different Cu crystals (cont.).

Cu Facet	n	I_{2D}/I_G	F	I_D/I_G	F	2D FWHM	F	G FWHM	F	D FWHM	F	G Peak Position
Upper mesa, Cu(100)	25	1.49±0.67, p=0.106	0	0.85±0.30, p=0.001	3	38.3±7.2 cm^{-1}, p=0.341	0	15.6±5.8 cm^{-1}, p=0.489	0	11.9±5.3 cm^{-1}, p=0.228	3	N/A
Cu(533)	41	2.21±0.53, p=0.5	0	0.71±0.46, p=0.039	7	27.9±4.4 cm^{-1}, p=0.5	0	16.9±5.8 cm^{-1}, p=0.009	0	18.9±20.7 cm^{-1}, p=0.009	9	N/A
Cu(850)	12	2.59±1.30, p=0.094	0	0.96±0.76, p=0.030	2	30.3±3.9 cm^{-1}, p=0.072	0	20.0±6.0 cm^{-1}, p=0.092	1	29.5±29.4 cm^{-1}, p=0.053	2	N/A
Cu(632)	11	2.35±0.69, p=0.5	0	0.74±0.43, p=0.5	3	32.1±2.9 cm^{-1}, p=0.5	0	21.1±9.1 cm^{-1}, p=0.5	0	15.8±10.7 cm^{-1}, p=0.5	3	N/A
Cu (10,7,6)	13	1.96±0.45, p=0.060	0	1.42±2.10, p=0.001	3	32.0±4.3 cm^{-1}, p=0.022	0	23.0±10.0 cm^{-1}, p=0.075	0	18.2±19.6 cm^{-1}, p=0.006	4	1586.1±2.5 cm^{-1}, p=0.5
Cu(110), 850 sccm CH_4	47	1.74±0.82, p=0.002	0	0.65±0.48, p=0.010	10	33.9±7.8 cm^{-1}, p=0.101	2	19.8±5.8 cm^{-1}, p=0.331	0	22.2±15.5 cm^{-1}, p=0.011	12	1591.9±4.1 cm^{-1}, p=0.5
Cu(221), 850 sccm CH_4	13	2.73±0.84, p=0.004	0	0.77±0.51, p=0.024	1	36.2±5.8 cm^{-1}, p=0.005	0	19.5±4.0 cm^{-1}, p=0.5	0	26.4±18.8 cm^{-1}, p=0.009	1	1592.0±3.1 cm^{-1}, p=0.252
Cu(632), 850 sccm CH_4	78	1.41±0.49, p=0.046	0	0.89±0.70, p=0.001	9	37.1±9.2 cm^{-1}, p=0.465	0	26.3±11.4 cm^{-1}, p=0.001	0	23.1±12.2 cm^{-1}, p=0.5	20	1591.0±3.7 cm^{-1}, p=0.283
Cu(221), lower, 850 sccm CH_4	57	1.31±0.70, p=0.010	1	0.89±0.82, p=0.001	5	32.0±10.2 cm^{-1}, p=0.5	0	30.0±14.4 cm^{-1}, p=0.001	3	22.7±17.2 cm^{-1}, p=0.001	16	1590.8±6.5 cm^{-1}, p=0.001
Cu(110), lower, 850 sccm CH_4	91	2.13±1.02, p=0.109	1	0.86±0.66, p=0.001	9	37.1±8.9 cm^{-1}, p=0.5	1	20.2±5.7 cm^{-1}, p=0.028	2	26.0±17.1 cm^{-1}, p=0.001	17	1590.6±4.5 cm^{-1}, p=0.001
Cu(221), partial, 20 sccm C_2H_4	56	1.78±0.99, p=0.034	1	1.06±1.19, p=0.001	2	37.8±9.8 cm^{-1}, p=0.001	0	24.0±17.3 cm^{-1}, p=0.020	2	28.9±23.4 cm^{-1}, p=0.095	6	1596.2±12.9 cm^{-1}, p=0.001

Table 2.2. Lilliefors two-tailed normality tests for different graphene distributions on Cu.

Cu Facet	I_{2D}/I_G	I_D/I_G	2D FWHM	G FWHM	D FWHM	G Peak Position
Cu(111)	X		X	X		N/A
Cu(100)			X		X	N/A
Cu(210)	X		X	X	X	N/A
Cu(511)	X		X	X	X	N/A
Cu(520)	X			X	X	N/A
Upper mesa, Cu(100)	X		X	X	X	N/A
Cu(533)	X		X			N/A
Cu(850)	X		X	X	X	N/A
Cu(632)	X	X	X	X	X	N/A
Cu(10,7,6)	X			X		X
Cu(110), 850 sccm CH_4			X	X		X
Cu(221), 850 sccm CH_4				X		X
Cu(632), 850 sccm CH_4			X		X	X
Cu(221), lower, 850 sccm CH_4			X			
Cu(110), lower, 850 sccm CH_4	X		X			
Cu(221), partial, 20 sccm C_2H_4					X	

Table 2.3. Raman analysis of graphene partially grown on different Cu crystal facets. Growth parameters are 20 sccm ethylene, 50 sccm H_2, and 5 min at 700 °C. Pre-anneal and Crystal surfaces containing (111) terraces have more consistent values for the G FWHM and G position, indicative more uniform, high-quality graphene. Moreover, the monolayer coverage (I_{2D}/I_G) and disorder coverage (I_D/I_G) ratios are higher and lower, respectively, for (111)–containing surfaces [53]. Surfaces with known compact islands exhibit higher I_D/I_G values due to edge effects. Note that all Raman spectra within this table and in the supplement have their Cu backgrounds subtracted and are Lorentzian-fitted around the peak centers.

Cu Facet	D FWHM (cm^{-1})	G FWHM (cm^{-1})	2D FWHM (cm^{-1})	G Position (cm^{-1})	2D Position (cm^{-1})	I_{2D}/I_G	I_D/I_G
Cu(111)	34.1 ± 5.8	21.1 ± 2	50.1 ± 1.2	1596.3 ± 0.7	2650.4 ± 0.4	3.12	0.49
Cu(111) islands	328.9 ± 23.1	114.3 ± 19.5	123.9 ± 5.8	1547.8 ± 4.9	2645.1 ± 1.7	2.47	1.79
Cu(111) near Cu(310)	49 ± 12.4	31.6 ± 4	46 ± 1.4	1595.1 ± 1.2	2649.3 ± 0.4	3.97	0.45
Cu(111) near Cu(310)	59.1 ± 18.5	25 ± 3.6	46.3 ± 1.4	1593.6 ± 1.1	2647 ± 0.4	4.39	0.36
Cu(211) near Cu(111)	60 ± 9.3	125.2 ± 23	69.9 ± 17.7	1589.34.5	2678.3 ± 5	0.73	1.51
Cu(411)	12.5 ± 6.5	47.5 ± 10	59.7 ± 3.7	1597 ± 3	2659.1 ± 1.1	3.5	0.68
Cu(411) near Cu(111)	19.5 ± 5.9	166.9 ± 35.1	49.7 ± 2.8	1568.9 ± 6.1	2646 ± 0.8	4.46	1.01
Cu(411) near Cu(310)	44 ± 5	51.6 ± 11.5	591.8 ± 51.6	1603 ± 3.2	2555.2 ± 6.5	3.6	2.21
Cu(411) near Cu(632)	21.5 ± 14.5	43.3 ± 12.7	53.9 ± 2.9	1577.5 ± 3.7	2646.1 ± 0.9	5.4	0.61
Cu(411) between Cu(632) terraces	52.3 ± 3.1	131.7 ± 15.1	62.6 ± 10.7	1589.5 ± 2.8	2653.5 ± 3.1	0.67	2.39
Cu(632) near Cu(411)	70.1 ± 18.4	162.4 ± 36.6	47.6 ± 11.7	1572.9 ± 6.4	2660 ± 2.9	1.33	1.06
Cu(310) islands	36.4 ± 21.5	377.2 ± 95.4	61.1 ± 6.9	1519.7 ± 13.4	2650.2 ± 2	1.13	0.25
Cu(310) near Cu(111)	54.7 ± 38	80 ± 18.3	55.9 ± 4.9	1570.9 ± 4.6	2652 ± 1.5	3.23	0.43
Cu(310) right Cu(111)	305.8 ± 517.1	40.4 ± 8	63.6 ± 4.7	1593 ± 2.4	2662.1 ± 1.4	2.79	0.93
Cu(310) right Cu(111), bulk	37.6 ± 11.6	100.2 ± 26.2	64.9 ± 3.2	1580.5 ± 5.9	2656 ± 1.1	4.8	1.03
Cu(310) near Cu(411)	59.5 ± 6.8	170.1 ± 25	69.6 ± 24.1	1580.3 ± 4.1	2665.6 ± 6.9	0.39	1.68
Cu(310) near Cu(111), right	103.9 ± 109.6	296.4 ± 83.3	53.5 ± 5.1	1559.1 ± 9.5	2646.7 ± 1.6	2.36	0.26
Cu(410) near Cu(111)	53.2 ± 7.8	69.9 ± 16.3	102.9 ± 38.3	1604.9 ± 4.1	2665.7 ± 6.5	0.98	2.04

2.7. References

[1] A. H. Castro Neto, F. Guinea, N. M. R. Peres, K. S. Novoselov, and A. K. Geim, "The electronic properties of graphene," *Reviews of Modern Physics*, vol. 81, no. 1, pp. 109-162, 2009.

[2] K. V. Emtsev, A. Bostwick, K. Horn, J. Jobst, G. L. Kellogg, L. Ley, J. L. McChesney, T. Ohta, S. A. Reshanov, J. Rohrl, E. Rotenberg, A. K. Schmid, D. Waldmann, H. B. Weber, and T. Seyller, "Towards wafer-size graphene layers by atmospheric pressure graphitization of silicon carbide," *Nature Materials*, vol. 8, no. 3, pp. 203-207, 2009.

[3] J. Gao, J. Yip, J. Zhao, B. I. Yakobson, and F. Ding, "Graphene nucleation on transition metal surface: Structure transformation and role of the metal step edge," *Journal of the American Chemical Society,* vol. 133, no. 13, pp. 5009-5015, 2011.

[4] K. S. Kim, Y. Zhao, H. Jang, S. Y. Lee, J. M. Kim, K. S. Kim, J.-H. Ahn, P. Kim, J.-Y. Choi, and B. H. Hong, "Large-scale pattern growth of graphene films for stretchable transparent electrodes," *Nature,* vol. 457, no. 7230, pp. 706-710, 2009.

[5] Y. Zhang, L. Gomez, F. N. Ishikawa, A. Madaria, K. Ryu, C. Wang, A. Badmaev, and C. Zhou, "Comparison of graphene growth on single-crystalline and polycrystalline Ni by chemical vapor deposition," *The Journal of Physical Chemistry Letters,* vol. 1, no. 20, pp. 3101-3107, 2010.

[6] X. Li, W. Cai, J. An, S. Kim, J. Nah, D. Yang, R. Piner, A. Velamakanni, I. Jung, E. Tutuc, S. K. Banerjee, L. Colombo, and R. S. Ruoff, "Large-area synthesis of high-quality and uniform graphene films on copper foils," *Science,* vol. 324, no. 5932, pp. 1312-1314, 2009.

[7] X. Li, C. W. Magnuson, A. Venugopal, R. M. Tromp, J. B. Hannon, E. M. Vogel, L. Colombo, and R. S. Ruoff, "Large-area graphene single crystals grown by low-pressure chemical vapor deposition of methane on copper," *Journal of the American Chemical Society,* vol. 133, no. 9, pp. 2816-2819, 2011.

[8] S. Bhaviripudi, X. Jia, M. S. Dresselhaus, and J. Kong, "Role of kinetic factors in chemical vapor deposition synthesis of uniform large area graphene using copper catalyst," *Nano Letters,* vol. 10, no. 10, pp. 4128-4133, 2010.

[9] V. E. Dorgan, M. H. Bae, and E. Pop, "Mobility and saturation velocity in graphene on SiO_2," *Applied Physics Letters,* vol. 97, no. 8, pp. 082112-082112-3, 2010.

[10] J. C. Koepke, J. D. Wood, D. Estrada, Z.-Y. Ong, K. T. He, E. Pop, and J. W. Lyding, "Atomic-scale evidence for potential barriers and strong carrier scattering at graphene grain boundaries: A scanning tunneling microscopy study," *ACS Nano,* vol. 7, no. 1, pp. 75-86, 2013.

[11] K. Kim, Z. Lee, W. Regan, C. Kisielowski, M. F. Crommie, and A. Zettl, "Grain boundary mapping in polycrystalline graphene," *ACS Nano,* vol. 5, no. 3, pp. 2142-2146, 2011.

[12] P. Y. Huang, C. S. Ruiz-Vargas, A. M. van der Zande, W. S. Whitney, M. P. Levendorf, J. W. Kevek, S. Garg, J. S. Alden, C. J. Hustedt, Y. Zhu, J. Park, P. L. McEuen, and D. A. Muller, "Grains and grain boundaries in single-layer graphene atomic patchwork quilts," *Nature,* vol. 469, no. 7330, pp. 389-392, 2010.

[13] L. Gao, J. R. Guest, and N. P. Guisinger, "Epitaxial graphene on Cu(111)," *Nano Letters,* vol. 10, no. 9, pp. 3512-3516, 2010.

[14] L. Zhao, K. T. Rim, H. Zhou, R. He, T. F. Heinz, A. Pinczuk, G. W. Flynn, and A. N. Pasupathy, "Influence of copper crystal surface on the CVD growth of large area monolayer graphene," *Solid State Communications,* vol. 151, no. 7, pp. 509-513, 2011.

[15] G. Giovannetti, P. A. Khomyakov, G. Brocks, V. M. Karpan, J. van den Brink, and P. J. Kelly, "Doping graphene with metal contacts," *Physical Review Letters,* vol. 101, no. 2, pp. 026803-026803-4, 2008.

[16] S. Esconjauregui, C. M. Whelan, and K. Maex, "The reasons why metals catalyze the nucleation and growth of carbon nanotubes and other carbon nanomorphologies," *Carbon,* vol. 47, no. 3, pp. 659-669, 2009.

[17] J. M. Wofford, S. Nie, K. F. McCarty, N. C. Bartelt, and O. D. Dubon, "Graphene islands on Cu foils: The interplay between shape, orientation, and defects," *Nano Letters,* vol. 10, no. 12, pp. 4890-4896, 2010.

[18] W. Zhang, P. Wu, Z. Li, and J. Yang, "First-principles thermodynamics of graphene growth on Cu surfaces," *The Journal of Physical Chemistry C,* vol. 115, no. 36, pp. 17782-17787, 2011.

[19] I. Vlassiouk, M. Regmi, P. Fulvio, S. Dai, P. Datskos, G. Eres, and S. Smirnov, "Role of hydrogen in chemical vapor deposition growth of large single-crystal graphene," *ACS Nano,* vol. 5, no. 7, pp. 6069-6076, 2011.

[20] D. Chatain, V. Ghetta, and P. Wynblatt, "Equilibrium shape of copper crystals grown on sapphire," *Interface Science,* vol. 12, no. 1, pp. 7-18, 2004.

[21] H. Chen, W. Zhu, and Z. Zhang, "Contrasting behavior of carbon nucleation in the initial stages of graphene epitaxial growth on stepped metal surfaces," *Physical Review Letters,* vol. 104, no. 18, pp. 186101-186101-4, 2010.

[22] P. E. Pehrsson, J. Glesener, and A. Morrish, "Chemical vapor deposition diamond nucleation induced by sp^2 carbon on unscratched silicon," *Thin Solid Films,* vol. 212, no. 1-2, pp. 81-90, 1992.

[23] Z. Li, P. Wu, C. Wang, X. Fan, W. Zhang, X. Zhai, C. Zeng, Z. Li, J. Yang, and J. Hou, "Low-temperature growth of graphene by chemical vapor deposition using solid and liquid carbon sources," *ACS Nano,* vol. 5, no. 4, pp. 3385-3390, 2011.

[24] Z. Zhang and M. G. Lagally, "Atomistic processes in the early stages of thin-film growth," *Science,* vol. 276, no. 5311, pp. 377-383, 1997.

[25] S. Nie, J. M. Wofford, N. C. Bartelt, O. D. Dubon, and K. F. McCarty, "Origin of the mosaicity in graphene grown on Cu(111)," *Physical Review B,* vol. 84, no. 15, pp. 155425-155425-7, 2011.

[26] O. V. Yazyev and S. G. Louie, "Electronic transport in polycrystalline graphene," *Nature Materials,* vol. 9, no. 10, pp. 806-809, 2010.

[27] X. Li, W. Cai, L. Colombo, and R. S. Ruoff, "Evolution of graphene growth on Ni and Cu by carbon isotope labeling," *Nano Letters,* vol. 9, no. 12, pp. 4268-4272, 2009.

[28] H. I. Rasool, E. B. Song, M. J. Allen, J. K. Wassei, R. B. Kaner, K. L. Wang, B. H. Weiller, and J. K. Gimzewski, "Continuity of graphene on polycrystalline copper," *Nano Letters,* vol. 11, no. 1, pp. 251-256, 2011.

[29] W. W. Mullins, "The effect of thermal grooving on grain boundary motion," *Acta Metallurgica,* vol. 6, no. 6, pp. 414-427, 1958.

[30] Y. Zhang, T. Gao, Y. Gao, S. Xie, Q. Ji, K. Yan, H. Peng, and Z. Liu, "Defect-like structures of graphene on copper foils for strain relief investigated by high-resolution scanning tunneling microscopy," *ACS Nano,* vol. 5, no. 5, pp. 4014-4022, 2011.

[31] J. Lahiri, Y. Lin, P. Bozkurt, I. I. Oleynik, and M. Batzill, "An extended defect in graphene as a metallic wire," *Nature Nanotechnology,* vol. 5, no. 5, pp. 326-329, 2010.

[32] R. I. Masel, *Principles of Adsorption and Reaction on Solid Surfaces,* 1st ed., New York, NY: Wiley Interscience, 1996.

[33] X. Li, C. W. Magnuson, A. Venugopal, J. An, J. W. Suk, B. Han, M. Borysiak, W. Cai, A. Velamakanni, Y. Zhu, L. Fu, E. M. Vogel, E. Voelkl, L. Colombo, and R. S. Ruoff, "Graphene films with large domain size by a two-step chemical vapor deposition process," *Nano Letters,* vol. 10, no. 11, pp. 4328-4334, 2010.

[34] M. S. Dresselhaus, A. Jorio, A. G. Souza, and R. Saito, "Defect characterization in graphene and carbon nanotubes using Raman spectroscopy," *Philosophical Transactions of the Royal Society A-Mathematical Physical and Engineering Sciences,* vol. 368, no. 1932, pp. 5355-5377, 2010.

[35] A. C. Ferrari, J. C. Meyer, V. Scardaci, C. Casiraghi, M. Lazzeri, F. Mauri, S. Piscanec, D. Jiang, K. S. Novoselov, S. Roth, and A. K. Geim, "Raman spectrum of graphene and graphene layers," *Physical Review Letters,* vol. 97, no. 18, pp. 187401-187401-4, 2006.

[36] Y. K. Koh, M. H. Bae, D. G. Cahill, and E. Pop, "Reliably counting atomic planes of few-layer graphene (n > 4)," *ACS Nano,* vol. 5, no. 1, pp. 269-274, 2011.

[37] M. S. Anderson, "Locally enhanced Raman spectroscopy with an atomic force microscope," *Applied Physics Letters,* vol. 76, no. pp. 3130-3132, 2000.

[38] L. Hansen, P. Stoltze, K. W. Jacobsen, and J. K. Nørskov, "Self-diffusion on copper surfaces," *Physical Review B,* vol. 44, no. 12, pp. 6523-6526, 1991.

[39] Q. Yu, L. A. Jauregui, W. Wu, R. Colby, J. Tian, Z. Su, H. Cao, Z. Liu, D. Pandey, D. Wei, T. F. Chung, P. Peng, N. P. Guisinger, E. A. Stach, J. Bao, S.-S. Pei, and Y. P. Chen, "Control and characterization of individual grains and grain boundaries in graphene grown by chemical vapour deposition," *Nature Materials,* vol. 10, no. 6, pp. 443-449, 2010.

[40] I. Vlassiouk, S. Smirnov, I. Ivanov, P. F. Fulvio, S. Dai, H. Meyer, M. Chi, D. Hensley, P. Datskos, and N. V. Lavrik, "Electrical and thermal conductivity of low temperature CVD graphene: The effect of disorder," *Nanotechnology,* vol. 22, no. 27, pp. 275716-275716-9, 2011.

[41] J. Yan, Y. B. Zhang, P. Kim, and A. Pinczuk, "Electric field effect tuning of electron-phonon coupling in graphene," *Physical Review Letters,* vol. 98, no. 16, pp. 116802-116802-4, 2007.

[42] M. Huang, H. Yan, C. Chen, D. Song, T. F. Heinz, and J. Hone, "Phonon softening and crystallographic orientation of strained graphene studied by Raman spectroscopy," *Proceedings of the National Academy of Sciences,* vol. 106, no. 18, pp. 7304-7308, 2009.

[43] M. A. Pimenta, G. Dresselhaus, M. S. Dresselhaus, L. G. Cancado, A. Jorio, and R. Saito, "Studying disorder in graphite-based systems by Raman spectroscopy," *Physical Chemistry Chemical Physics,* vol. 9, no. 11, pp. 1276-1291, 2007.

[44] Y.-J. Yu, Y. Zhao, S. Ryu, L. E. Brus, K. S. Kim, and P. Kim, "Tuning the graphene work function by electric field effect," *Nano Letters,* vol. 9, no. 10, pp. 3430-3434, 2009.

[45] L. M. Malard, M. A. Pimenta, G. Dresselhaus, and M. S. Dresselhaus, "Raman spectroscopy in graphene," *Physics Reports,* vol. 473, no. 5-6, pp. 51-87, 2009.

[46] S. Chen, W. Cai, R. D. Piner, J. W. Suk, Y. Wu, Y. Ren, J. Kang, and R. S. Ruoff, "Synthesis and characterization of large-area graphene and graphite films on commercial Cu-Ni alloy foils," *Nano Letters,* vol. 11, no. 9, pp. 3519-3525, 2011.

[47] J. S. Bunch, S. S. Verbridge, J. S. Alden, A. M. van der Zande, J. M. Parpia, H. G. Craighead, and P. L. McEuen, "Impermeable atomic membranes from graphene sheets," *Nano Letters,* vol. 8, no. 8, pp. 2458-2462, 2008.

[48] E. Starodub, N. C. Bartelt, and K. F. McCarty, "Oxidation of graphene on metals," *The Journal of Physical Chemistry C,* vol. 114, no. 11, pp. 5134-5140, 2010.

[49] H. A. Miley, "Copper oxide films," *Journal of the American Chemical Society,* vol. 59, no. 12, pp. 2626–2629, 1937.

[50] K. M. Reddy, A. D. Gledhill, C.-H. Chen, J. M. Drexler, and N. P. Padture, "High quality, transferrable graphene grown on single crystal Cu(111) thin films on basal-plane sapphire," *Applied Physics Letters,* vol. 98, no. 11, pp. 113117-113117-3, 2011.

[51] M. A. van Hove and G. A. Somorjai, "A new microfacet notation for high-Miller index surfaces of cubic materials with terrace, step and kink structures," *Surface Science,* vol. 92, no. pp. 489-518, 1980.

[52] K. Oura, V. G. Liftshits, A. A. Saranin, A. V. Zotov, and M. Katayama, *Surface Science: An Introduction,* New York, NY: Springer, 2003.

[53] A. C. Ferrari and D. M. Basko, "Raman spectroscopy as a versatile tool for studying the properties of graphene," *Nature Nanotechnology,* vol. 8, no. 4, pp. 235-246, 2013.

CHAPTER 3. HIGH-K DIELECTRIC SEEDING ON FLUORINATED GRAPHENE

3.1. Introduction to Graphene Dielectric Deposition

The excellent electronic [1], mechanical [2], and thermal [3] properties of graphene have made it a subject of intense study. While global back gates (e.g. 100 nm SiO_2 on n^{++}–Si) allow researchers to probe the electronic properties of graphene [4], most electronic applications require top-gate dielectrics which promote scaling and individual device control. However, the sp^2 honeycomb network of graphene is hydrophobic [5] and chemically inert [6], making conventional atomic layer deposition (ALD) difficult [7, 8]. Adding interfacial layers [8-11] and surface fluorine [12] to graphene improves the ALD of dielectrics. Nevertheless, many issues persist in scaling and placing uniform dielectrics on graphene, such as a reduction in graphene mobility [13] and leakage [14] through ultra-thin (e.g. <2 nm) dielectric films. By uniform dielectrics, we mean films possessing high breakdown fields and lacking cracks and pinholes.

Recent work showed that hexagonal boron nitride (h-BN) could be transferred on top of graphene, acting as an interfacial layer [15] before depositing high-κ [16] (relative to $\kappa = 4$ for SiO_2) dielectrics. While insulating h-BN can improve graphene performance [17], its controlled, layer-by-layer chemical vapor deposition (CVD) growth remains challenging, and typically 10 to 50 nm films have been previously used [15, 18]. This limits thickness scaling when seeding a top-gate dielectric. Alternatively, fluorinated graphene [19, 20] (FG), another insulating interfacial layer, offers monolayer thickness control by direct chemical conversion of monolayer CVD graphene films on Cu or SiO_2/Si. Moreover, the top layer in bilayer graphene stacks can be chemically converted to FG [21], allowing a uniform top-gate dielectric to be placed on the FG/G ensemble.

Single-sided graphene fluorination on the Cu growth substrate produces C_4F [20], and dual-sided fluorination of transferred graphene on SiO_2/Si produces perfluorographane or fluorographene (CF) [19, 20]. We find that these C_4F and perfluorographane layers promote ALD dielectric seeding, allowing conventional transfer [15] of the dielectrics to additional graphene layers. The improved ALD seeding occurs by enhanced surface chemistries from reactive F anions and puckered [22], sp^3 hybridization [19] that occur in FG. For graphene on Cu substrates, adding that reactivity with the "polar trapping" Cu [10] CVD growth substrate should further improve the deposition. Regardless of the substrate for graphene, we note that non-fluorinated graphene does not produce a uniform dielectric. Graphene fluorination produces a more uniform high-κ dielectric.

Herein, we use scanning electron microscopy (SEM), optical microscopy, atomic force microscopy (AFM), and X-ray photoelectron spectroscopy (XPS) to show that the ALD of HfO_2 is more uniform on CVD FG on Cu, compared against CVD graphene from the same growth. Furthermore, we demonstrate that ALD of HfO_2 on highly FG ($x < 4$ in C_xF, hereafter also termed ~CF) on SiO_2/Si has even better uniformity and morphology than ~C_4F on CVD Cu. These highly fluorinated films allow for ultra-thin HfO_2 scaling down to 2 nm physical thickness. We then transfer these dielectrics to various substrates (SiO_2/Si and epitaxial graphene on SiC) to further assess the coverage and investigate the feasibility of placing the dielectrics on graphene.

3.2. HfO_2 Deposition on Fluorinated Graphene Derivatives

We grow graphene on Cu by CVD using low pressure CVD following our previous reports [21, 23]. Some samples are poly(methyl methacrylate) (PMMA) transferred to SiO_2 (100 nm)/Si substrates, and other samples are transferred by thermal release tape (TRT) to SiO_2 (300

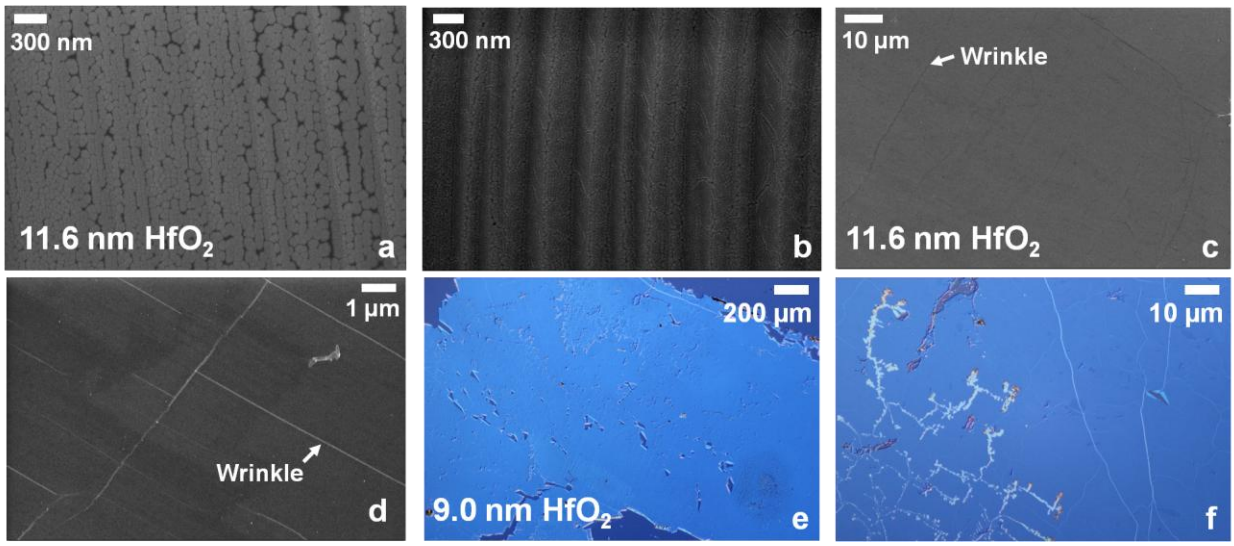

Figure 3.1. Differing atomic layer deposition (ALD) coverages for HfO_2 based on the graphene substrate and the transfer method. **(a)** Scanning electron microscopy (SEM) image of 11.6 nm of HfO_2 deposited on chemical vapor deposition (CVD) grown graphene on Cu. The dielectric has cracks and pinholes near the Cu striations and graphene hillocks. **(b)** SEM image of HfO_2 on fluorinated graphene (FG) on Cu from the same growth and using the same dielectric thickness as (a), giving improved HfO_2 coverage. **(c)** SEM image of 11.6 nm HfO_2 on fluorographene (~CF) on SiO_2(100 nm)/Si, with no dielectric cracks or depressions evident, unlike (a) or (b). **(d)** Small area SEM image of the sample from (c), showing uniform HfO_2 coverage over FG-based features like wrinkles. Large area **(e)** and small area **(f)** optical images of PMMA transferred 9.0 nm of HfO_2 deposited on FG/Cu on SiO_2(100 nm)/Si. HfO_2 dendrites likely form on film defects in (e).

nm)/Si substrates. To make FG, we expose all of our samples for 300 s (30 s per cycle, 10 cycles) to XeF_2 gas at 1 Torr vapor pressure with 35 Torr N_2 in a Xactix X3 Si etcher [12, 20, 21]. This process ultimately yields ~C_4F on Cu and perfluorographane (~CF) on SiO_2/Si [20, 21], respectively. We perform all HfO_2 ALD at T = 200 °C, and we determine the HfO_2 thickness by spectroscopic ellipsometry (SE) on Si witness samples (see Section 3.6.4).

Figure 3.1 shows the improvement of HfO_2 deposition when utilizing FG on Cu rather than graphene on Cu alone. Our results clarify a recent report [10] that claimed better ALD with 3 nm of Al_2O_3 and 10 nm of HfO_2 on just CVD graphene on Cu. This report argued that the polar, wetting-transparent [5] Cu (G/Cu) enhanced deposition [10]. Despite that paper, Fig. 3.1a presents a SEM image of 11.6 nm HfO_2 on G/Cu, with islands and cracks in the dielectric. Figure 3.1b shows improved HfO_2 coverage in a SEM image for FG/Cu at the same dielectric thickness,

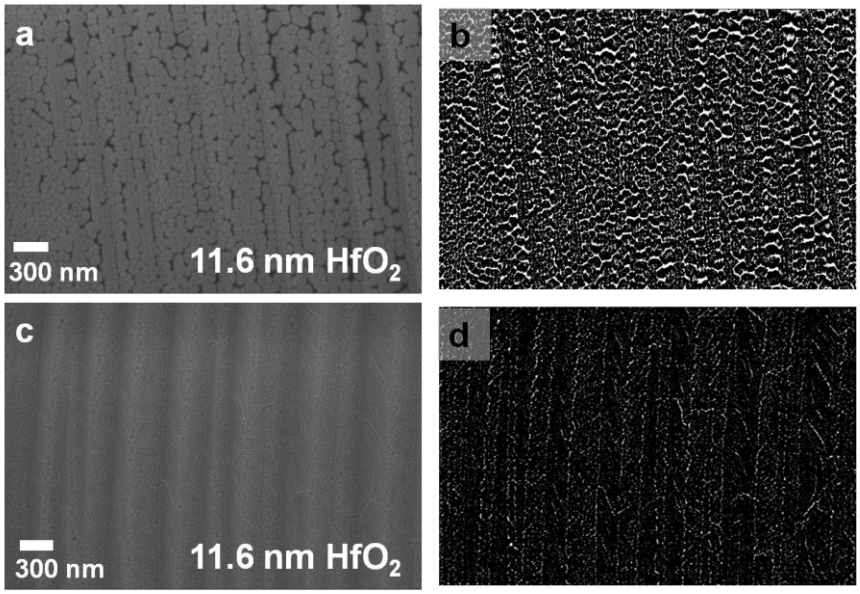

Figure 3.2. Thresholding analysis for HfO_2 on graphene and fluorinated graphene on the Cu growth surface. **(a)** Scanning electron microscopy (SEM) image of HfO2 on graphene on Cu (G/Cu), taken from Fig. 3.1. **(b)** Thresholded image of (a) after bandpass filtering, showing holes and cracks (white) in the HfO_2 film on Cu. Crack coverage is 19.4%. **(c)** SEM image of HfO_2 deposited on fluorinated graphene (FG) on Cu from Fig. 3.1. **(d)** Thresholded image of (c) after bandpass filtering, showing small HfO_2 cracks near the Cu striations. Crack coverage is 4.6%, four fold better for HfO_2 on FG/Cu versus G/Cu. Thus, a more continuous dielectric film is formed on FG/Cu over and against G/Cu.

deposited at the same time as Fig. 3.1a. From the image processing in Figs. 3.2 and 3.3, we estimate the crack density to decrease from 19.4% on G/Cu to 4.6% on FG/Cu, a fourfold improvement. Thus, the overall area coverage for HfO_2 deposited on FG/Cu (Fig. 3.1b) is higher than G/Cu (Fig. 3.1a).

In addition to FG on Cu, we investigate the HfO_2 coverage for transferred graphene films on SiO_2(100 nm)/Si that have been fluorinated. For highly FG films (i.e., perfluorographane), the graphene layer is mostly sp^3 hybridized [19, 20], with some oxygen-related sp^3 moieties (Fig. 3.4). Capacitance–voltage (*C*–*V*) of these highly FG films (Fig. 3.5) give a dielectric constant of κ_{FG} = 2.3, close to fluorinated amorphous carbon (κ_{FAC} = 2.1) [24], confirming the high fluorination degree. Figures 3.1c and 3.1d show large-area and small-area SEM images, respectively, of FG/SiO_2/Si after the deposition of 11.6 nm HfO_2. In these images, we observe transfer-induced wrinkles [25] in the FG. Nevertheless, there is no morphological evidence [12]

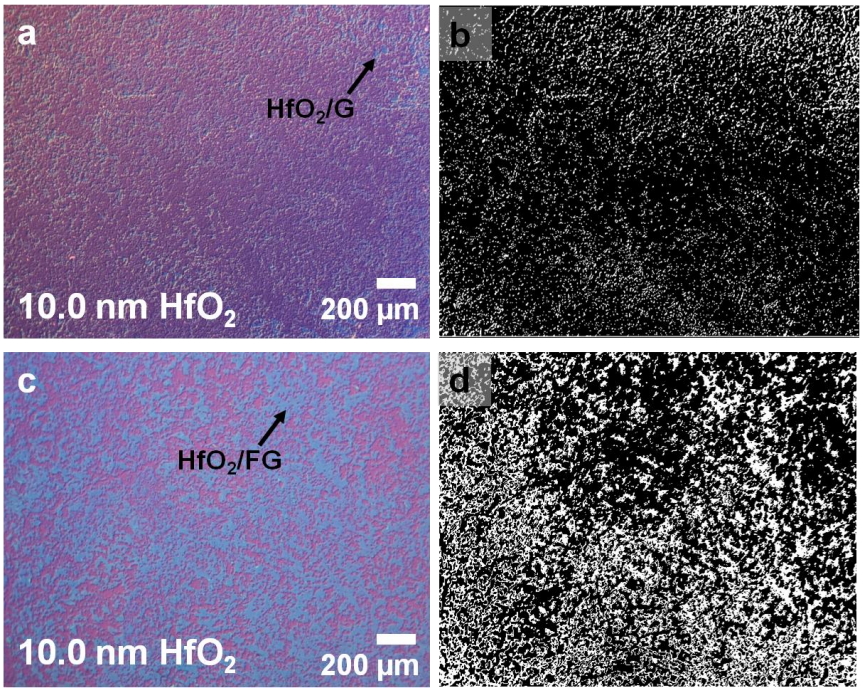

Figure 3.3. Thresholding analysis for HfO_2 on graphene and fluorinated graphene and transferred by thermal release tape (TRT). **(a)** Nomarksi filtered optical image of HfO_2 deposited on graphene on Cu and transferred by TRT to 300 nm SiO_2/Si, a different oxide thickness than that used in the main text. Dark purple is the substrate, and the blue regions are HfO_2/G. Poor coverage is from poor TRT adhesion [27] to the HfO_2/G film on Cu. **(b)** Thresholded image of (a), where the white regions represent the HfO_2/G film. Area coverage is 13.1%. **(c)** Nomarksi filtered optical image of HfO_2 deposited on fluorinated graphene (FG) on Cu and transferred by TRT to 300 nm SiO_2/Si. Light blue regions are HfO_2/FG. **(d)** Thresholded image of (c), where the white regions represent the HfO_2/FG film. Area coverage for FG/Cu is 33.9%, better than G/Cu in (b). This is from a more continuous dielectric film being produced on FG/Cu versus G/Cu.

of a cracked, pinholed, or otherwise inhomogeneous HfO_2 layer on the highly FG/SiO_2/Si surface. While PMMA-transferred films can have residues [26] that promote ALD deposition, our transfers prove clean enough to get electronic interactions between two PMMA-transferred graphene layers [21]. Thus, the improved ALD is related to the fluorine content and not the surface contamination.

Once the HfO_2 films are deposited on G/Cu, FG/Cu, or FG/SiO_2/Si, we can transfer them using established procedures [10, 15, 20]. We employ a PMMA support for the HfO_2/G/Cu and HfO_2/FG/Cu structures and transfer them to SiO_2 (100 nm)/Si. Figures 3.1e and 3.1f show Nomarski-filtered images of 9.0 nm HfO_2/FG on SiO_2/Si. Compared to TRT transfers, the area

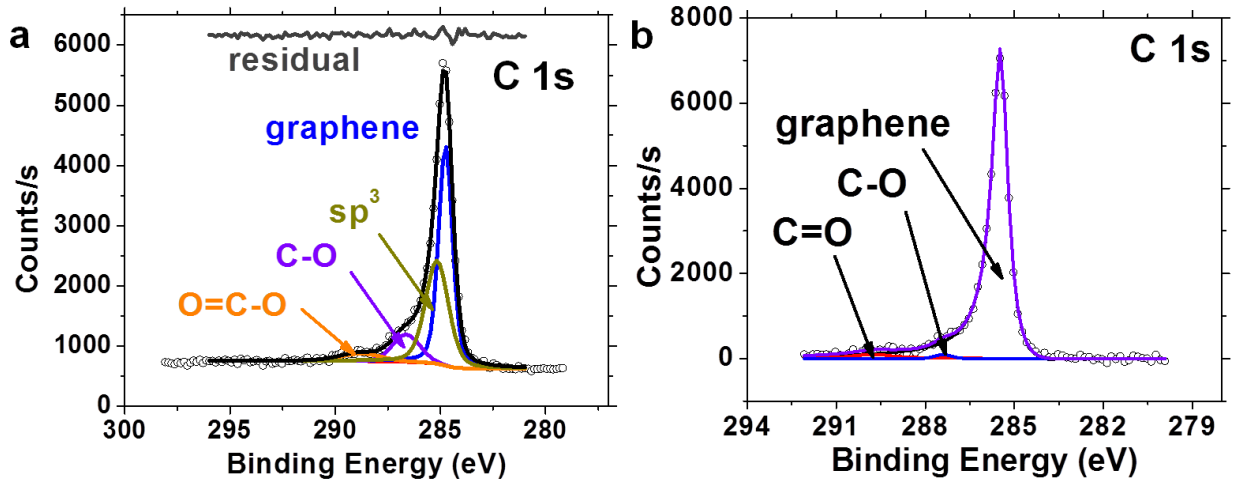

Figure 3.4. O 1s sp^3 domains in graphene. **(a)** XPS C 1s photoelectron spectrum for PMMA-transferred graphene on SiO_2/Si, fitted against a Shirley background. Residual value offset above the spectrum. All sub-peaks are Gaussian-Lorentzian lineshapes, and with ether (–C–O–) and ester (–O=C–O–) functionals present. Energetically, these functionals are likely sp^3 in character, but it is possible that they could be graphitic. The sp^3 peak thus has contributions from oxygen and from hydrocarbon contaminants. This spectrum is representative of oxygen functionals on transferred graphene or **(b)** on graphene on Cu. These oxygen contributions are removed from our fluorination stoichiometry analyses.

coverage of Figs. 3.1e and 3.1f is high, suggesting that PMMA transfer could be used for large-area transfer of FG-based dielectrics to arbitrary surfaces. Further, any PMMA-induced residues can be removed by O_2 plasma treatment of the HfO_2. Figure 3.1f also reveals thicker HfO_2 regions [7], corresponding to heightened ALD incubation on defective like graphene edges [8], dangling bonds, grain boundaries [28], and wrinkles.

3.3. X-Ray Photoelectron Spectroscopy (XPS) Analysis

We further corroborate the HfO_2 film quality on FG/Cu against G/Cu by using XPS. Before deposition, we analyze the C 1s and F 1s photoelectron spectra for CVD graphene on Cu, shown in Fig. 3.6a. We report our XPS sub-peak fitting procedure and the extracted sub-peak positions and linewidths in Section 3.6.6. We observe the strong sp^2 C signal typical of graphene [12, 29, 30] with shoulders from sp^3 hybridization and C–O and C=O bonding. After exposing the sample of Fig. 3.6a to XeF_2, we obtain the F 1s and C 1s spectra given in Fig. 3.6b. For this particular region, the sp^2 surface stoichiometry (see Section 3.6.6) without oxygen is $C_{4.77}F$,

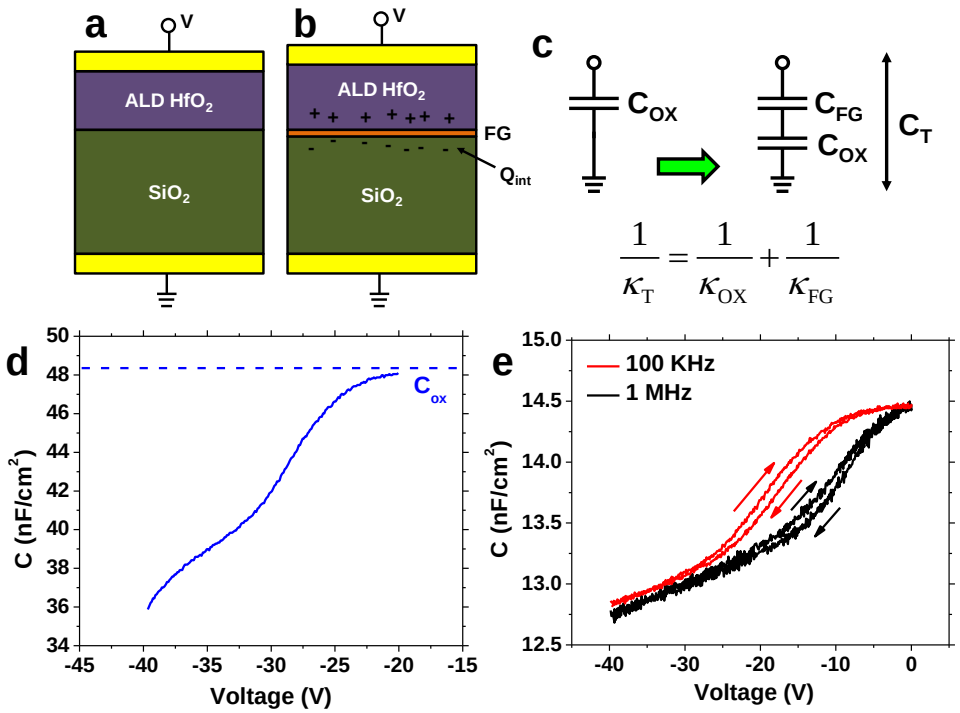

Figure 3.5. Capacitance measurements on ultra-thin HfO_2 on FG. Capacitor schematics for ALD HfO_2 (2.0 nm) on SiO_2 (100 nm) **(a)** and ALD HfO_2 (~2.0 nm) on FG (~CF) on SiO_2 **(b)**. Note the interfacial charge Q_{int} induced by the presence of the polar FG layer. **(c)** Equivalent circuit diagram for the two sets of capacitors, with the dielectric constant relationship given. **(d)** Capacitance–voltage (*C*–*V*) data for the ALD HfO_2/SiO_2 stack shown in (a). In the oxide-limited regime, the capacitance is ~48 nF/cm^2, giving a dielectric constant κ_{OX} = 4.2 (*d* ~ 102.0 nm). The increased dielectric constant is from the thin high-κ HfO_2. **(e)** *C*–*V* data for the ALD $HfO_2/FG/SiO_2$ stack shown in (b). The frequency dependence indicates the presence of static charge (Q_{int}), and the decreased capacitance relative to (d) corresponds to contributions from the FG layer. Simple parallel-plate models for the FG layer give unreasonable dielectric constants, due to the trapped charge Q_{int} (Q_{int} >> Q, where Q is the charge on the capacitor plates) in the HfO_2 and SiO_2 dielectrics. Thus, we extract the FG film's dielectric constant using the relationship shown in (c), giving κ_{FG} = 2.3, on the same order as Teflon.

differing from the theoretical prediction of C_4F for single-sided fluorinated graphene [20]. The discrepancy occurs from difficult to deconvolve oxygen-fluorine compounds and the presence of ca. ~19% bilayer graphene islands [23]. F 1s shows only covalent fluorine [12, 20, 30] at ~688 eV binding energy (BE), and the C 1s spectrum gives covalent C–F and $C–F_2$ bonding, with the pre-existing C–O and C=O bonding [31]. The F 1s area and $C–F_x$ sub-peak areas are in good agreement for covalent fluorine. It is challenging to assign a peak for semi-ionic (SI) C–F [30] due to possible carbonyls (C=O) there [31].

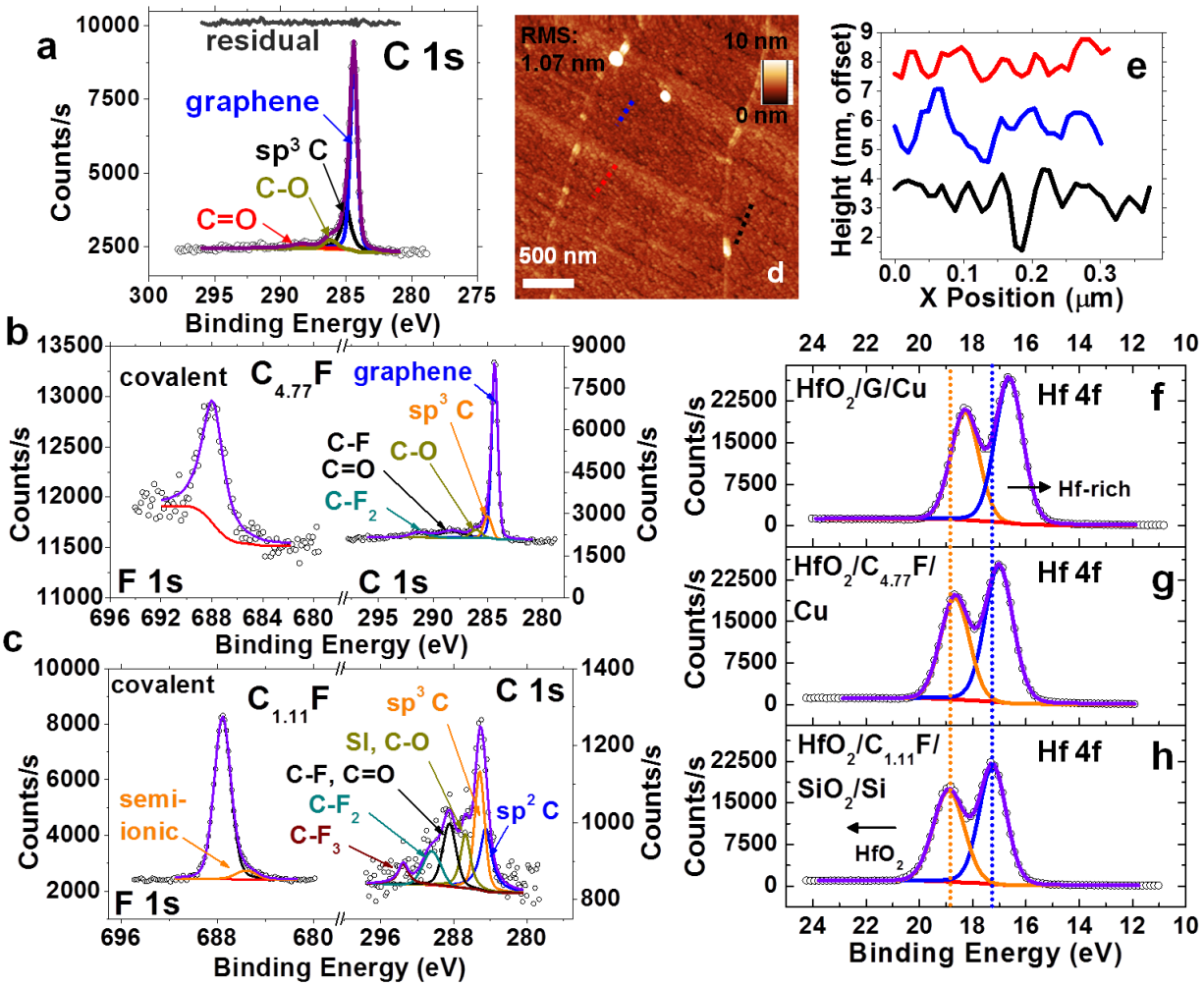

Figure 3.6. More uniform HfO_2 deposition via higher fluorine content in fluorinated graphene. **(a)** XPS C 1s photoelectron spectrum for graphene as grown on Cu. **(b)** F 1s and C 1s spectra for FG on Cu, with a surface stoichiometry (Section 3.6.6) of $C_{4.77}F$. **(c)** F 1s and C 1s spectra for highly FG on SiO_2/Si, with a stoichiometry of $C_{1.17}F$. C–F, C–F_2, and C–F_3 bonding is apparent. **(d)** AFM image of HfO_2 deposited on FG/Cu after PMMA-based transfer. **(e)** HfO_2/FG height profiles (vertically offset for clarity) for (d), showing shallow (1-2 nm) depressions within the dielectric. XPS Hf 4f spectra for **(f)** G/Cu, **(g)** FG ($C_{4.77}F$) on Cu, and **(h)** highly FG ($C_{1.11}F$) on SiO_2/Si. The doublet's downshift for HfO_2/G/Cu indicates a metallic, Hf-rich overlayer on G/Cu.

With XPS, we also analyze transferred and fluorinated films on SiO_2(100 nm)/Si, similar to those given in Figs. 3.1c-d. When fluorinating transferred graphene on SiO_2/Si, fluorine from the XeF_2 source can interact with both graphene sides from transfer-induced holes, edges, and wrinkles. Additionally, XeF_2 etches SiO_2, albeit 1000 times slower than Si [32], providing fluorine the ability to reach the graphene underside. This dual-side exposure can fully fluorinate the graphene [19]. In Fig. 3.6c, we show F 1s and C 1s photoelectron spectra for highly FG on

SiO_2/Si. From these spectra, the sample has a surface stoichiometry of $C_{1.11}F$—a nearly complete fluorination. The F 1s spectrum shows the signatures of covalent (~688 eV) and semi-ionic (~686 eV) [22, 30] fluorine bonding. By comparison, the C 1s spectrum has a high level of sp^3 hybridization, with covalent C–F and more defective $C–F_2$ and $C–F_3$ bonding.

Using the fluorinated graphene derivatives of Figs. 3.6b-c, we can deposit HfO_2 and study the dielectric coverage as a function of sp^3 hybridization. Figure 3.6d gives an AFM image of 11.6 nm HfO_2 deposited on FG/Cu after PMMA transfer to SiO_2/Si. Figure 3.6d shows depressions in the transferred HfO_2/FG film, and line profiles (offset for clarity) in Fig. 3.6e reveal that these features are only ~1-2 nm deep. Thus, it appears that they do not pass all the way through the dielectric and are rather areas of lowered deposition. Nevertheless, we cannot fully rule out dielectric pinholes or cracks, as those features could be smaller than our AFM tip's radius of curvature. Experiments utilizing conductive AFM [9] and electrical transport [33, 34] can reveal this, and they will be the subject of future work.

To ascertain the chemical state for our deposited HfO_2, we analyze Hf 4f photoelectron (PE) spectra, given in Figs. 3.6f-h. We compare the spectra for HfO_2 on G/Cu and on FG/Cu ($C_{4.77}F$) in Figs. 3.6f and 3.6g, respectively. Both spectra show the oxidized $Hf_{4f,5/2}$ and $Hf_{4f,7/2}$ doublet [35] (1.7 eV spin-orbit induced separation) characteristic of a high-quality HfO_2 deposition, with no obvious suboxides and or Hf carbides (C 1s spectrum confirmed, not shown) [36]. The lower BE position of the HfO_2/G/Cu spectrum versus the HfO_2/FG/Cu spectrum indicates that the HfO_2/G/Cu sample is less oxidized and more Hf-rich [35], which decreases the dielectric constant. HfO_2 on G/Cu is hence a worse dielectric by comparison to FG/Cu. Figure 3.6h gives the Hf 4f spectrum for the highly FG sample ($C_{1.11}F$) analyzed in Fig. 3.6c. The HfO_2 is more oxygen-rich than G/Cu or FG/Cu, making it a better dielectric with fewer interstitials and

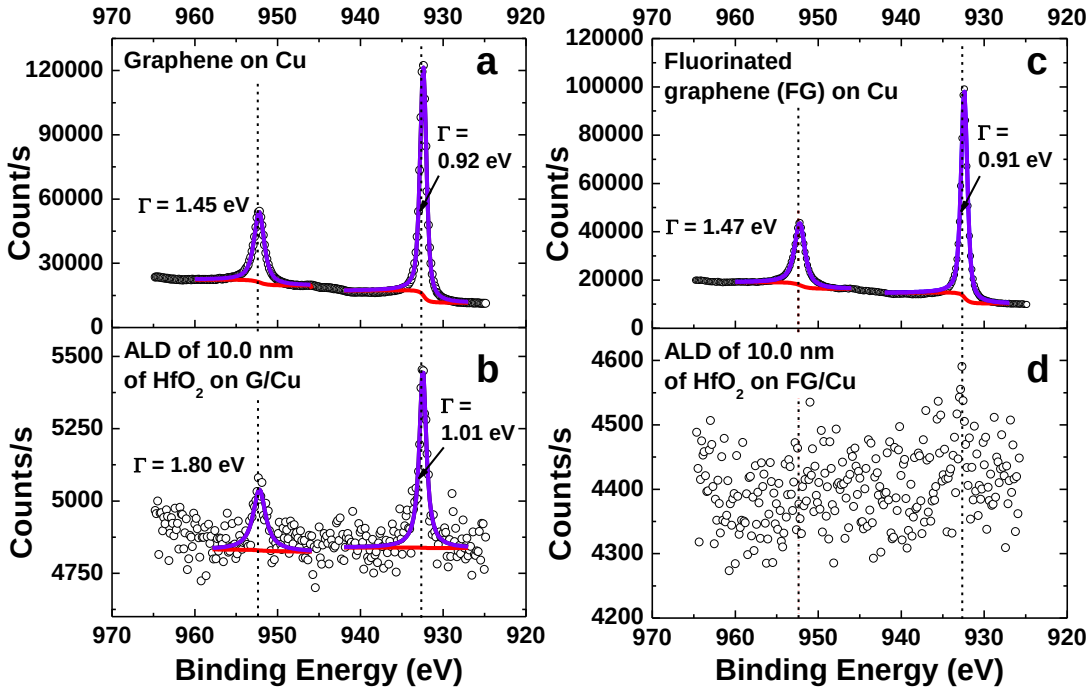

Figure 3.7. XPS evidence for more uniform HfO_2 coverage on FG/Cu versus G/Cu. Cu 2p photoelectron spectra for G/Cu before **(a)** and after **(b)** deposition of 10 nm of HfO_2. The Cu doublet remains after deposition, indicative of pinholes within the dielectric. Cu 2p spectra for FG/Cu before **(c)** and after **(d)** deposition of 10 nm of HfO_2. The noisy Cu data cannot be fit, suggesting effective attenuation of the Cu substrate by a uniform HfO_2 dielectric.

traps [36]. As shown in Fig. 3.1, the Cu surface is rougher than the SiO_2/Si surface, but ALD is generally conformal to even rough surfaces. Thus, the more oxygen-rich, uniform HfO_2 dielectric results from increased sp^3 hybridization on highly FG/SiO_2/Si and is not roughness related. Fluorine has been shown to passivate oxygen vacancies in defective HfO_2 [37]. Assuming our HfO_2 films have XPS-detectable fluorine incorporated in them, we arrive at HfO_x stoichiometries of $HfO_{1.68}$, $HfO_{1.79}$, and $HfO_{1.83}$ for G/Cu, FG/Cu, and highly FG/SiO_2/Si, respectively. This supports BE shift seen in Figs. 3.6f-h, corroborating the improved character of HfO_2 on FG.

XPS can reveal information about an overlayer's pinhole density and uniformity if that overlayer is thicker than the attenuation length of PEs from the substrate. An examination of the Cu 2p spectra for G/Cu and FG/Cu before and after HfO_2 deposition can reveal any pinholes in

the HfO_2 dielectric overlayer. Figures 3.7a and 3.7b show the Cu 2p spectra for G/Cu before and after 10.0 nm HfO_2 deposition, respectively. In Fig. 3.7b, the Cu doublet intensity decreases and widens relative to the before case (Fig. 3.7a), but it and an oxidized Cu sub-peak [38] are still present. Hence, the Cu substrate is still visible through the HfO_2 overlayer. Figures 3.7c-d also show Cu 2p spectra, but in this case for FG/Cu before and after 10.0 nm HfO_2 deposition. The before case in Fig. 3.7c appears similar to Fig. 3.7a, highlighting the substrate's invariance to fluorination. After deposition, in Fig. 3.7d, the PE data become noisy, preventing sub-peak fitting. On FG/Cu, the 10.0 nm of HfO_2 suppresses photoelectrons from the Cu substrate, possible only if the number of pinholes and cracks in the 400 μm spot is low. We reject the notion that the attenuation is derived by a thicker HfO_2 layer on FG/Cu versus G/Cu. While uniform HfO_2 overlayers of thickness $d \geq 9.7$ nm (see Section 3.6.6) will give the attenuated Cu spectra in Fig. 3.7d, the lowered Hf 4f area in Fig. 3.6g relative to Fig. 3.6f suggests less HfO_2 material for FG/Cu. Therefore, the HfO_2 layer on FG/Cu is either the same thickness or thinner—and more continuous—than HfO_2 on G/Cu. We thereby conclude that the HfO_2 is less pinholed and more uniform on FG/Cu compared against G/Cu.

3.4. Ultra-Thin HfO_2 Scaling

For Figs. 3.8a-d, we utilize highly FG on SiO_2/Si sample with XPS spectra given in Figs. 3.8c and 3.8h ($C_{1.11}F$). Figures 3.8a and 3.8b give large-area and small-area AFM images, respectively, of the sample of Fig. 3.1c. Besides the transfer-induced wrinkles and folds (Fig. 3.8a), these AFM images are featureless, as shown on the overlaid height profiles. Once again, the dielectric pinholes could be smaller than the AFM tip radius of curvature (~20–40 nm), but the lack of obvious large island and crack formation suggests a homogeneous HfO_2 layer. Figure 3.8c shows an AFM image of a bilayer graphene region on top of the entire graphene film. At

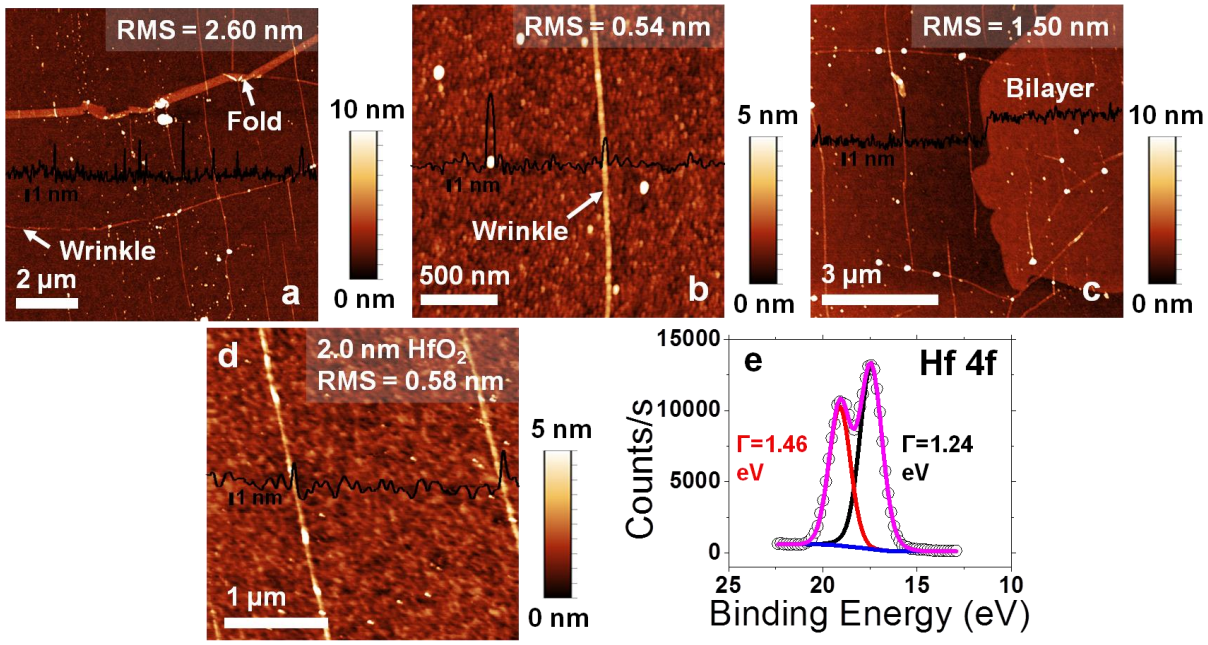

Figure 3.8. Ultra-thin HfO_2 scaling on highly fluorinated graphene on SiO_2/Si. **(a)** Large area AFM image of 11.6 nm HfO_2 deposition on FG on SiO_2(100 nm)/Si, where the dielectric coats wrinkles, folds, and tears conformally. Profile shown in black. **(b)** Small area AFM image of 11.6 nm HfO_2 coated FG on SiO_2/Si, showing a crackless and pinhole free dielectric layer. **(c)** AFM image of a graphene bilayer with similar dielectric coverage as monolayer graphene. **(d)** Morphology of ultra-thin 2 nm HfO_2 deposited on highly fluorinated CF near a wrinkle. **(e)** XPS Hf 4f photoelectron spectrum for the sample in (d), confirming successful deposition of 2.0 nm HfO_2.

these length scales, the graphene-based morphological features in Figs. 3.8c-e do not change the HfO_2 layer's continuity. To test the scalability of HfO_2 dielectrics on FG, we deposit 2 nm of HfO_2 on highly FG on SiO_2(100 nm)/Si. Figure 3.8d provides an AFM image of this dielectric layer near a wrinkle; again, there are no obvious morphological changes from the dielectric. Finally, in Fig. 3.8f we confirm the high-quality chemical identity of the ultra-thin 2.0 nm HfO_2 in Fig. 3.8d with the Hf 4f PE doublet for HfO_2. From the areas under the F 1s, Si 2p, O 1s, and Hf 4f PE spectra, we derive a HfO_x stoichiometry of $HfO_{1.69}$, in good agreement with expected results for uniform, ultra-thin HfO_2 films with sub-oxides [35].

3.5. Conclusions

Spatial inhomogeneities in G/Cu versus FG/Cu and highly FG on SiO_2/Si lead to the marked difference in HfO_2 quality. For Cu, the local polar site density [10] and wetting

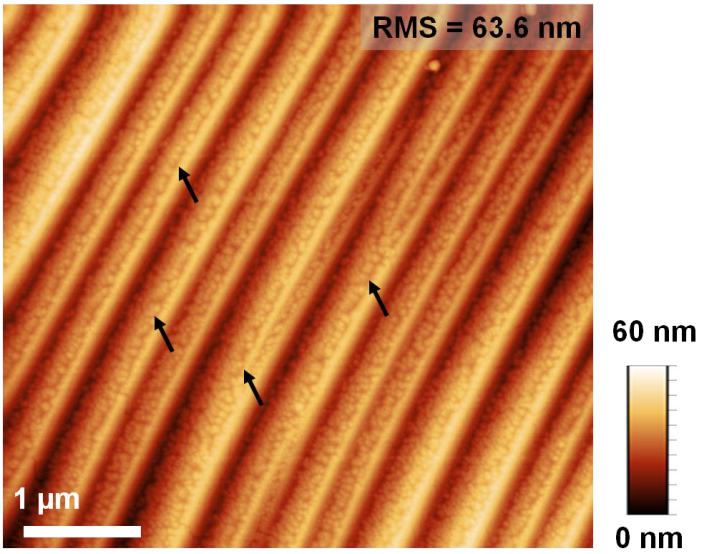

Figure 3.9. AFM image of non-transferred HfO_2 deposited on FG/Cu. Striations from the dead-annealing process and hillocks from thermal mismatch are visible in the Cu. This results in the image having a high RMS roughness. These features locally strain [39] the graphene, thereby changing the workfunction [41] and affecting the fluorination [20]. Consequently, the local fluorination changes affect how the HfO_2 is deposited, giving dielectric depressions in regions of high topography and strain. Note that the depressions do not go all the way through this 11.6 nm dielectric.

transparency [5] will change based on the roughness of the different polycrystalline Cu surfaces [23], affecting the ALD. Conversely, fluorination makes the surface chemistry on Cu more homogeneous, promoting ALD on all sites, regardless of polar site density or wetting. Additionally, fluorination locally puckers the graphene and breaks bonds [12, 19, 20], giving the necessary strained sites and dangling bonds for ALD. Nevertheless, sp^3 graphene fluorination strongly depends on the local doping [40], and thus Cu-based workfunction changes [41] will lower the sp^3 sites available for ALD. This explains the small spatial inhomogeneities seen in Fig. 3.6 and in Fig. 3.9. For highly FG on SiO_2/Si, the featureless, uniform HfO_2 films occur as a result of elimination of the spatial inhomogeneity inherent to Cu. Graphene films on SiO_2/Si are uniformly doped, smooth, and can be fluorinated on both sides [20] through etched SiO_2 (Section 3.6.3). These factors all promote increased sp^3 hybridization and a homogeneous FG film. In turn, that homogeneity, combined with additional reactive fluorine, will allow for better HfO_2 dielectric deposition.

In conclusion, we showed continuous, uniform deposition of HfO_2 on FG/Cu and on highly FG on SiO_2/Si, as compared with G/Cu. With our HfO_2/FG stacks, we scaled our films to ~2.0 nm physical thickness, thinner than what was achieved with transferred h-BN on epitaxial graphene [15]. The HfO_2 films were transferable to SiO_2/Si and other arbitrary surfaces using the standard PMMA transfer method. The improved deposition resulted from the heightened sp^3 character of the FG films, either on Cu or on SiO_2/Si. Our process is a scalable method to place dielectrics on top of inert graphene. Also, our technique allows chemical conversion of the top layer of bilayer graphene into a buffer layer for seeding high-κ dielectric stacks.

3.6. Materials and Methods

3.6.1. Graphene Growth

Graphene is grown using chemical vapor deposition (CVD) in a hot-wall CVD furnace employing a Cu foil enclosure method at ~1030 °C for 1.5 to 2 hr [21, 42]. The flow rates for CH_4 and H_2 are in excess of 10 sccm each, and the flow rate ratio for CH_4/H_2 is greater than 30. The growth produces large, monolayer graphene grains (~5 to 100 μm) within the enclosure. Samples for the fluorinated graphene (FG) studies on SiO_2/Si are transferred using the conventional PMMA-based transfer [21].

3.6.2. Thermal Release Tape

We also transfer graphene using thermal release tape (TRT). In air, the tape (Nitto Denko, no. 3159, adhesion strength of ~7 N / 20 mm) is flattened onto the HfO_2/x/Cu samples, where x is fluorinated graphene (FG) or graphene (G). For both PMMA and TRT transfers, the Cu is etched away with ammonium persulfate (Transene Company, APS-100) overnight, and the films are rinsed in DI water and N_2 dried. We press the tape onto hot 300 nm SiO_2/Si, and then we release it at 121 °C in air. The tape's residues are removed a 1:1:1 toluene:acetone:methanol

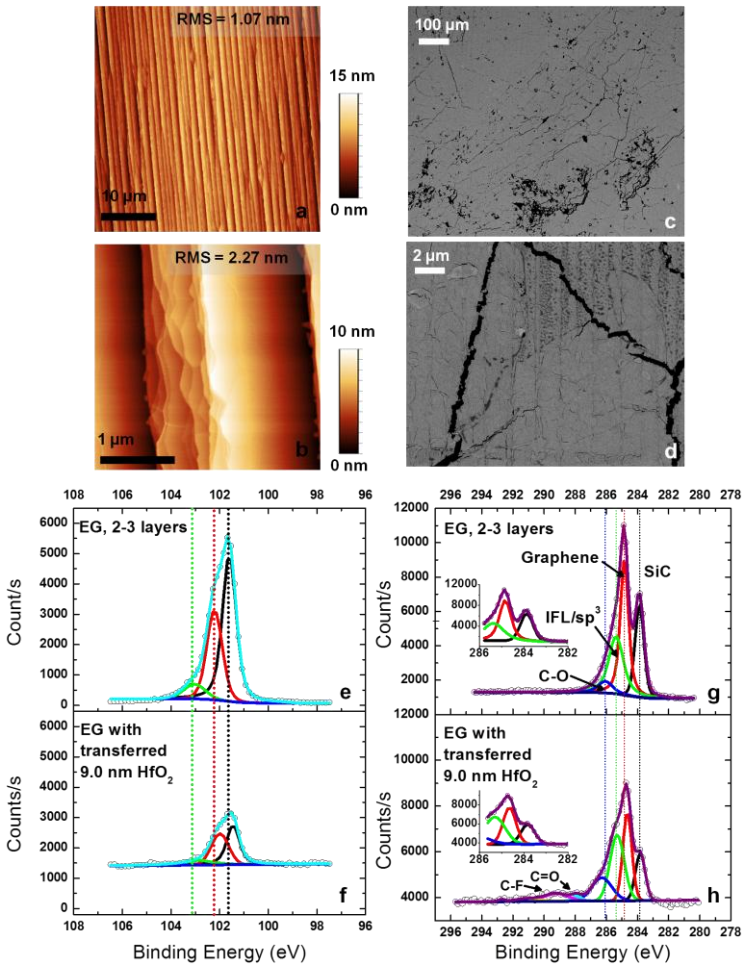

Figure 3.10. Transferred HfO_2/FG films on epitaxial graphene (EG) on SiC. Large-area **(a)** and small-area **(b)** AFM images of EG on Si-face SiC. Step bunching is present, and graphene multilayers form near the step edges. Terrace width is ~1 µm, and the sample is 3.5 ± 0.1 layers thick [29]. Large-area **(c)** and small-area **(d)** SEM images of TRT transferred (by wafer bonding [27]) 9.0 nm HfO_2/FG on the EG sample in (a) and (b). Cracks within the film result from poor TRT adhesion. XPS Si 2p photoelectron data before **(e)** and after **(f)** HfO_2/FG transfer. The SiC peaks [12] (black and red) are suppressed by the dielectric, but not completely so from transfer-induced cracks. XPS C 1s photoelectron data before **(g)** and after **(h)** HfO_2/FG transfer. The HfO_2 overlayer strains the SiC sub-peak (black), pushing it closer to the graphene sub-peak (red). The spectra also somewhat suppressed and shows C–F bonding from the FG in the HfO_2/FG film. **Insets:** Zoom-in on the SiC, graphene, and sp^3/interfacial layer (i.e., layer 0) sub-peaks in the XPS.

clean for at least 5 min. We note that the patchiness of the transfers in Fig. 3.3a and Fig. 3.3c is from lowered TRT adhesion strength. The TRT loses its "stickiness" with respect to time.

3.6.3. Graphene Fluorination and ALD

After graphene growth and PMMA-based transfer, there is some remaining PMMA which is not fully removed [26]. However, when we fluorinate our samples prior to ALD, the

resist is consumed by XeF_2. All of our fluorinated samples are sealed in N_2 bags before XPS examination. We take survey and core level photoelectron data with a Thermo Fisher Avantage XPS monochromatic Al-K_α (1486.6 eV) source and a ~400 μm spot size. Immediately after XPS, we perform ALD on the samples. HfO_2 ALD occurs at 200 °C with TEMAH (Tetrakis(ethylmethylamino)hafnium) kept at 84 °C and H_2O. Each ALD cycle consists of a TEMAH dose of 1.5 s, a TEMAH purge of 5 s, a H_2O dose of 0.015 s, and a H_2O purge of 10 s.

3.6.4. Spectroscopic Ellipsometry

The film thickness is characterized using an ex-situ CompleteEASE spectroscopic ellipsometer from J. A. Woollam. Data values are obtained at three different angles, 65, 70, and 75 degrees and fit to a Cauchy model. From the fitting procedure (Cauchy-HfO_2 model on Si with a transparent film), we extract the thickness and index of refraction of the films on silicon witnesses. ALD is performed on these samples at the same time as the Cu and SiO_2/Si samples.

3.6.5. AFM, SEM, and XPS

We carry out further characterization using a Bruker Dimension III AFM and Si tips (~40 nm radius of curvature), a Leo SEM with in-lens detection mode, a Nomarski filtered optical microscope, and the aforementioned XPS system. In the XPS data, we correct for charging effects on the insulating substrates that we examine. Furthermore, we use Shirley backgrounds for all photoelectron spectra. Sub-peaks within the XPS spectra are fit so that their full-width at half maximum (FWHM) values are less than 3 eV, with the sub-peaks' Gaussian-Lorentzian lineshapes determined dynamically by the fit. We add peaks until the overall residual value is ~0.

3.6.6. XPS Analysis

From our XPS C 1s spectra, we define the surface stoichiometry as the reciprocal of the total weighted contributions of surface fluorine. We sum the areas of each of the fluorine

bonding configurations under C 1s, namely, C–F, C–F_2, and C–F_3, and employ a multiplier based on the number of F atoms present (1, 2, 3). The inverse of this sum relative to sp^2 carbon (e.g. graphene) gives x in the surface stoichiometry C_xF. Single-sided fluorinated graphene usually gives surface stoichiometries near ~C_4F [19-21]. Highly fluorinated or fully fluorinated graphene films usually give surface stoiochiometries near ~CF (termed perflurographane or fluorographene) [19-21]. In the main text, any film that is highly fluorinated has a surface stoichiometry greater than ~C_4F, typically resulting in ~CF ($x < 4$, C_xF).

We discuss attenuation of substrate photoelectrons when analyzing XPS data in the main manuscript. Based on the attenuation expression $I = I_0 \cdot \exp(-d/(\lambda \cdot \cos\ \theta))$, where I is the attenuated intensity (counts/s), I_0 is the original intensity, d is the overlayer thickness, λ is the attenuation length (Å), and θ is the detector angle (~54°), we deduce that the substrate's photoelectrons are attenuated if the overlayer is uniform and possessing a thickness $d \geq 9.7$ nm. This extracted thickness is determined by the Cu 2p spectra in Figs. 3.7a-b, using an attenuation length of λ = 72 Å. We start with a known thickness of 10.0 nm for the above attenuation expression to find the attenuation length λ. Then, we use that attenuation length and detector angle to extrapolate for the Cu 2p spectra for the FG film in Figs. 3.7c-d.

3.7. References

[1] A. H. Castro Neto, F. Guinea, N. M. R. Peres, K. S. Novoselov, and A. K. Geim, "The electronic properties of graphene," *Reviews of Modern Physics*, vol. 81, no. 1, pp. 109-162, 2009.

[2] J. S. Bunch, S. S. Verbridge, J. S. Alden, A. M. van der Zande, J. M. Parpia, H. G. Craighead, and P. L. McEuen, "Impermeable atomic membranes from graphene sheets," *Nano Letters*, vol. 8, no. 8, pp. 2458-2462, 2008.

[3] E. Pop, V. Varshney, and A. K. Roy, "Thermal properties of graphene: Fundamentals and applications," *MRS Bulletin*, vol. 37, no. 12, pp. 1273-1281, 2012.

[4] M.-H. Bae, S. Islam, V. E. Dorgan, and E. Pop, "Scaling of high-field transport and localized heating in graphene transistors," *ACS Nano,* vol. 5, no. 10, pp. 7936-7944, 2011.

[5] J. Rafiee, X. Mi, H. Gullapalli, A. V. Thomas, F. Yavari, Y. Shi, P. M. Ajayan, and N. A. Koratkar, "Wetting transparency of graphene," *Nature Materials,* vol. 11, no. pp. 217-222, 2012.

[6] Q. H. Wang, Z. Jin, K. K. Kim, A. J. Hilmer, G. L. C. Paulus, C.-J. Shih, M.-H. Ham, J. D. Sanchez-Yamagishi, K. Watanabe, T. Taniguchi, J. Kong, P. Jarillo-Herrero, and M. S. Strano, "Understanding and controlling the substrate effect on graphene electron-transfer chemistry via reactivity imprint lithography," *Nature Chemistry,* vol. 4, no. 9, pp. 724-732, 2012.

[7] N. Y. Garces, V. D. Wheeler, and D. K. Gaskill, "Graphene functionalization and seeding for dielectric deposition and device integration," *Journal of Vacuum Science & Technology B: Microelectronics and Nanometer Structures,* vol. 30, no. 3, pp. 030801-030801-21, 2012.

[8] X. Wang, S. M. Tabakman, and H. Dai, "Atomic layer deposition of metal oxides on pristine and functionalized graphene," *Journal of the American Chemical Society,* vol. 130, no. 26, pp. 8152-8153, 2008.

[9] J. M. P. Alaboson, Q. H. Wang, J. D. Emery, A. L. Lipson, M. J. Bedzyk, J. W. Elam, M. J. Pellin, and M. C. Hersam, "Seeding atomic layer deposition of high-k dielectrics on epitaxial graphene with organic self-assembled monolayers," *ACS Nano,* vol. 5, no. 6, pp. 5223-5232, 2011.

[10] B. Dlubak, P. R. Kidambi, R. S. Weatherup, S. Hofmann, and J. Robertson, "Substrate-assisted nucleation of ultra-thin dielectric layers on graphene by atomic layer deposition," *Applied Physics Letters,* vol. 100, no. 17, pp. 173113-173113-4, 2012.

[11] D. B. Farmer, H.-Y. Chiu, Y.-M. Lin, K. A. Jenkins, F. Xia, and P. Avouris, "Utilization of a buffered dielectric to achieve high field-effect carrier mobility in graphene transistors," *Nano Letters,* vol. 9, no. 12, pp. 4474-4478, 2009.

[12] V. Wheeler, N. Garces, L. Nyakiti, R. Myers-Ward, G. Jernigan, J. Culbertson, C. Eddy, and D. K. Gaskill, "Fluorine functionalization of epitaxial graphene for uniform deposition of thin high-kappa dielectrics," *Carbon,* vol. 50, no. 6, pp. 2307-2314, 2012.

[13] B. Fallahazad, S. Kim, L. Colombo, and E. Tutuc, "Dielectric thickness dependence of carrier mobility in graphene with HfO_2 top dielectric," *Applied Physics Letters,* vol. 97, no. 12, pp. 123105-123105-3, 2010.

[14] B. Fallahazad, K. Lee, G. Lian, S. Kim, C. M. Corbet, D. A. Ferrer, L. Colombo, and E. Tutuc, "Scaling of Al_2O_3 dielectric for graphene field-effect transistors," *Applied Physics Letters,* vol. 100, no. 9, pp. 093112-093112-4, 2012.

[15] M. S. Bresnehan, M. J. Hollander, M. Wetherington, M. LaBella, K. A. Trumbull, R. Cavalero, D. W. Snyder, and J. A. Robinson, "Integration of hexagonal boron nitride with quasi-freestanding epitaxial graphene: Toward wafer-scale, high-performance devices," *ACS Nano,* vol. 6, no. 6, pp. 5234-5241, 2012.

[16] G. D. Wilk, R. M. Wallace, and J. M. Anthony, "High-kappa gate dielectrics: Current status and materials properties considerations," *Journal of Applied Physics,* vol. 89, no. 10, pp. 5243-5275, 2001.

[17] C. R. Dean, A. F. Young, I. Meric, C. Lee, L. Wang, S. Sorgenfrei, K. Watanabe, T. Taniguchi, P. Kim, K. L. Shepard, and J. Hone, "Boron nitride substrates for high-quality graphene electronics," *Nature Nanotechnology,* vol. 5, no. 10, pp. 722-726, 2010.

[18] K. K. Kim, A. Hsu, X. Jia, S. M. Kim, Y. Shi, M. Hofmann, D. Nezich, J. F. Rodriguez-Nieva, M. Dresselhaus, T. Palacios, and J. Kong, "Synthesis of monolayer hexagonal boron nitride on Cu foil using chemical vapor deposition," *Nano Letters,* vol. 12, no. 1, pp. 161-166, 2012.

[19] R. R. Nair, W. C. Ren, R. Jalil, I. Riaz, V. G. Kravets, L. Britnell, P. Blake, F. Schedin, A. S. Mayorov, S. J. Yuan, M. I. Katsnelson, H. M. Cheng, W. Strupinski, L. G. Bulusheva, A. V. Okotrub, I. V. Grigorieva, A. N. Grigorenko, K. S. Novoselov, and A. K. Geim, "Fluorographene: A two-dimensional counterpart of Teflon," *Small,* vol. 6, no. 24, pp. 2877-2884, 2010.

[20] J. T. Robinson, J. S. Burgess, C. E. Junkermeier, S. C. Badescu, T. L. Reinecke, F. K. Perkins, M. K. Zalalutdniov, J. W. Baldwin, J. C. Culbertson, P. E. Sheehan, and E. S. Snow, "Properties of fluorinated graphene films," *Nano Letters,* vol. 10, no. 8, pp. 3001-3005, 2010.

[21] J. T. Robinson, S. W. Schmucker, C. B. Diaconescu, J. P. Long, J. C. Culbertson, T. Ohta, A. L. Friedman, and T. E. Beechem, "Electronic hybridization of large-area stacked graphene films," *ACS Nano,* vol. 7, no. 1, pp. 637-644, 2013.

[22] Y. Sato, K. Itoh, R. Hagiwara, T. Fukunaga, and Y. Ito, "On the so-called 'semi-ionic' C-F bond character in fluorine-GIC," *Carbon,* vol. 42, no. 15, pp. 3243-3249, 2004.

[23] J. D. Wood, S. W. Schmucker, A. S. Lyons, E. Pop, and J. W. Lyding, "Effects of polycrystalline Cu substrate on graphene growth by chemical vapor deposition," *Nano Letters,* vol. 11, no. 11, pp. 4547-4554, 2011.

[24] K. Endo and T. Tatsumi, "Fluorinated amorphous carbon thin films grown by plasma enhanced chemical vapor deposition for low dielectric constant interlayer dielectrics," *Journal of Applied Physics,* vol. 78, no. 2, pp. 1370-1372, 1995.

[25] X. Li, W. Cai, J. An, S. Kim, J. Nah, D. Yang, R. Piner, A. Velamakanni, I. Jung, E. Tutuc, S. K. Banerjee, L. Colombo, and R. S. Ruoff, "Large-area synthesis of high-quality and uniform graphene films on copper foils," *Science,* vol. 324, no. 5932, pp. 1312-1314, 2009.

[26] Y. C. Lin, C. C. Lu, C. H. Yeh, C. H. Jin, K. Suenaga, and P. W. Chiu, "Graphene annealing: How clean can it be?," *Nano Letters,* vol. 12, no. 1, pp. 414-419, 2012.

[27] J. D. Caldwell, T. J. Anderson, J. C. Culbertson, G. G. Jernigan, K. D. Hobart, F. J. Kub, M. J. Tadjer, J. L. Tedesco, J. K. Hite, M. A. Mastro, R. L. Myers-Ward, C. R. Eddy, P. M. Campbell, and D. K. Gaskill, "Technique for the dry transfer of epitaxial graphene onto arbitrary substrates," *ACS Nano,* vol. 4, no. 2, pp. 1108-1114, 2010.

[28] J. C. Koepke, J. D. Wood, D. Estrada, Z.-Y. Ong, K. T. He, E. Pop, and J. W. Lyding, "Atomic-scale evidence for potential barriers and strong carrier scattering at graphene grain boundaries: A scanning tunneling microscopy study," *ACS Nano,* vol. 7, no. 1, pp. 75-86, 2013.

[29] G. G. Jernigan, B. L. VanMil, J. L. Tedesco, J. G. Tischler, E. R. Glaser, A. Davidson, P. M. Campbell, and D. K. Gaskill, "Comparison of epitaxial graphene on Si-face and C-face 4H SiC formed by ultrahigh vacuum and RF furnace production," *Nano Letters,* vol. 9, no. 7, pp. 2605-2609, 2009.

[30] J.-M. Lee, S. J. Kim, J. W. Kim, P. H. Kang, Y. C. Nho, and Y.-S. Lee, "A high resolution XPS study of sidewall functionalized MWCNTs by fluorination," *Journal of Industrial and Engineering Chemistry,* vol. 15, no. 1, pp. 66-71, 2009.

[31] C. D. Wagner, W. M. Riggs, L. E. Davis, J. F. Moulder, and G. E. Muilenberg, *Handbook of X-ray Photoelectron Spectroscopy*. Waltham, MA: Perkin-Elmer, 1979.

[32] Information from Xactix Inc. (Aug. 29, 2012). [Online]. Available: http://www.xactix.com/Xenon_difluoride.html

[33] L. Liao, J. Bai, R. Cheng, Y.-C. Lin, S. Jiang, Y. Huang, and X. Duan, "Top-gated graphene nanoribbon transistors with ultrathin high-K dielectrics," *Nano Letters,* vol. 10, no. 5, pp. 1917-1921, 2010.

[34] L. G. Rizzi, M. Bianchi, A. Behnam, E. Carrion, E. Guerriero, L. Polloni, E. Pop, and R. Sordan, "Cascading wafer-scale integrated graphene complementary inverters under ambient conditions," *Nano Letters,* vol. 12, no. 8, pp. 3948-3953, 2012.

[35] C. Morant, L. Galán, and J. M. Sanz, "An XPS study of the initial stages of oxidation of hafnium," *Surface and Interface Analysis,* vol. 16, no. 1-12, pp. 304-308, 1990.

[36] A. Pirkle, Y. J. Chabal, L. Colombo, and R. M. Wallace, "In-situ studies of high-K dielectrics for graphene-based device," *ECS Transactions,* vol. 19, no. 5, pp. 215-224, 2009.

[37] W. S. Chen, Q.-Q., S.-J. Ding, D. W. Zhang, and L.-K. Wang, "First principles calculations of oxygen vacancy passivation by fluorine in hafnium oxide," *Applied Physics Letters,* vol. 89, no. 15, pp. 152904-152904-3, 2006.

[38] M. C. Biesinger, L. W. M. Lau, A. R. Gerson, and R. S. C. Smart, "Resolving surface chemical states in XPS analysis of first row transition metals, oxides and hydroxides: Sc, Ti, V, Cu and Zn," *Applied Surface Science,* vol. 257, no. 3, pp. 887-898, 2010.

[39] R. He, L. Zhao, N. Petrone, K. S. Kim, M. Roth, J. Hone, P. Kim, A. Pasupathy, and A. Pinczuk, "Large physisorption strain in chemical vapor deposition of graphene on copper substrates," *Nano Letters,* vol. 12, no. 5, pp. 2408-2413, 2012.

[40] J. O. Sofo, A. M. Suarez, G. Usaj, P. S. Cornaglia, A. D. Hernández-Nieves, and C. A. Balseiro, "Electrical control of the chemical bonding of fluorine on graphene," *Physical Review B,* vol. 83, no. 8, pp. 081411-081411-4, 2011.

[41] S.-M. Choi, S.-H. Jhi, and Y.-W. Son, "Effects of strain on electronic properties of graphene," *Physical Review B,* vol. 81, no. 8, pp. 081407-081407-4, 2010.

[42] X. Li, C. W. Magnuson, A. Venugopal, R. M. Tromp, J. B. Hannon, E. M. Vogel, L. Colombo, and R. S. Ruoff, "Large-area graphene single crystals grown by low-pressure chemical vapor deposition of methane on copper," *Journal of the American Chemical Society,* vol. 133, no. 9, pp. 2816-2819, 2011.

CHAPTER 4. CLEAN NANOMATERIAL TRANSFER WITH POLY(BISPHENOL A CARBONATE)

4.1. Introduction to Transfer of Graphene and Related Nanomaterials

Graphene, an atomically thin, two-dimensional sheet, has garnered considerable interest from its noteworthy thermal [1, 2] and electronic [3] characteristics. Initial studies used graphite exfoliation [4-6] to isolate graphene, producing high quality but relatively small samples (e.g. <40 μm). Scalability concerns were addressed partially by the chemical vapor deposition (CVD) of graphene on transition metals like Ni [7], Ni–Cu alloy [8], and Cu [9-12]. CVD of graphene on Cu has proven the most fruitful platform for large-area graphene growth, as the low atomic C solubility promotes monolayer growth [9]. Nevertheless, most applications using CVD-grown graphene require that the films be transferred to insulating substrates. The de facto graphene transfer approach is by using a poly(methyl methacrylate) (PMMA) scaffold [13-18]. In this method, the PMMA polymer coats the graphene, supporting it during Cu removal, underside contaminant cleaning, and placement on its destination substrate [19, 20].

However, PMMA removal from graphene after film transfer has proven challenging [16]. Approaches to remove it by high-temperature Ar/H_2 forming gas annealing [15, 21, 22], O_2 based annealing [16, 23, 24], and in situ annealing [17, 25, 26] have been marginally successful in removing PMMA without affecting the graphene. Furthermore, these processes are all at high-temperature, excluding graphene applications with low thermal budgets, such as those involving flexible electronics and biomolecule encapsulation. Another process separated the graphene from the PMMA support by an Au interfacial layer [27], but that process is subject to effective interfacial Au-graphene wetting. Recent transfer results using thermal release tape (TRT) [28-30], poly(bisphenol A carbonate) (PC) [31, 32], and sacrificial polymer release layers [33]

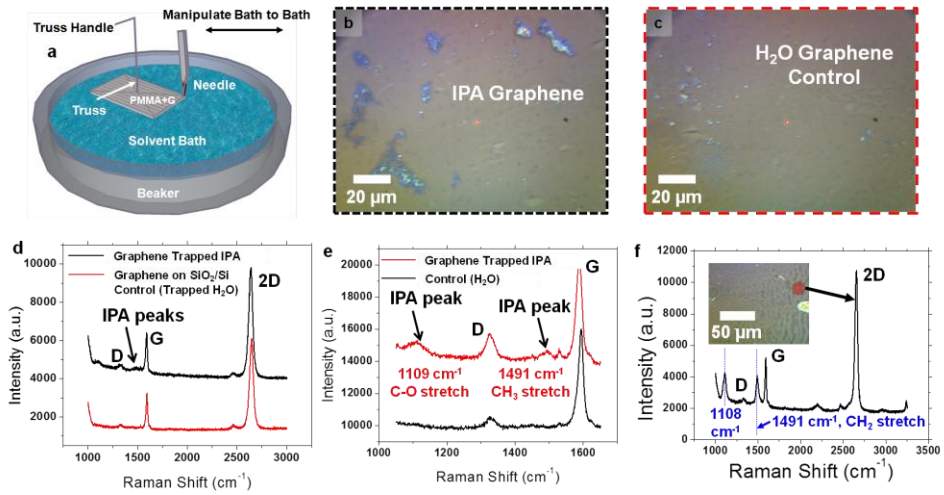

Figure 4.1. PMMA-transferred graphene with different final solvent baths. **(a)** Schematic of the PMMA scaffold transfer process used for transferring graphene into other final solvent solutions. Note that the high surface tension of water supports the graphene film during conventional wet transfer; the graphene does not float on the water. When the solvent is changed to something besides water, the lower surface tension causes the PMMA-graphene film to sink in the solvent. To counteract this, a metal truss is employed to prevent the PMMA-graphene from tumbling into solution. Optical images of graphene truss-transferred in 2-propanol **(b)** and in a H_2O **(c)** control. **(d)** Point Raman spectra (λ_{exc} = 633 nm, ~2 mW power, 50X, 30 s acquisition) for the optical images in (b) and (c), showing additional peaks from the IPA. **(e)** Zoom-in Raman spectra for the samples in (d). Peaks at 1109 cm^{-1} and 1491 cm^{-1} correspond to entrapped IPA solvent. The 1109 cm^{-1} peak corresponds to the C–O stretching mode in IPA, and the 1491 cm^{-1} peak corresponds to the CH_3 stretching mode [34-36]. **(f)** Point Raman spectrum for graphene truss-transferred in ethylene glycol. Optical image is shown inset. Graphene Raman peaks (D, G, and 2D) are present, and peaks at 1108 cm^{-1} and 1491 cm^{-1}, respectively, correspond to C–O and CH_2 stretching modes [37].

required elevated temperature (over 100 °C) during transfer and differed considerably in terms of surface contamination and graphene area coverage. To exploit the intrinsic properties of large-area graphene, a room temperature transfer process that comes off more cleanly than the established methods is needed.

In this study, we compare the transfer of graphene with the conventional PMMA polymer scaffold with alternative poly(lactic acid) (PLA), poly(phthalaldehyde) (PPA), PC, and bilayer PMMA/PC scaffolds. We choose both PLA and PPA as scaffolds as they can supposedly be removed by modest heating or acid exposure. Further, we choose PC from its heightened reactivity as a condensation polymer and its former use [31, 32] in small-area graphene transfer. We find that PC scaffolds can be fully removed off the graphene by room temperature

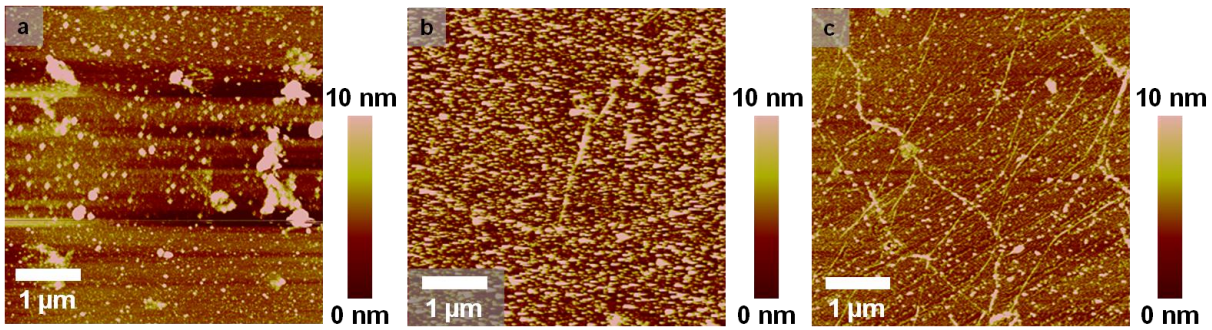

Figure 4.2. Room temperature removal of PMMA with different solvents and substrates. Graphene grown at 1000 °C for 25 min with 75 sccm CH_4 and 50 sccm H_2 on Cu using a pocketed approach [10, 11]. **(a)** AFM image of PMMA-transferred graphene on mica, with the PMMA partially removed by a 20 min acetone soak. **(b)** AFM image of PMMA-transferred graphene on SiO_2/Si, with the PMMA removed by a 20 min acetone soak. Compared to (a), the PMMA removal on SiO_2/Si is considerably lower. **(c)** AFM image of PMMA-transferred graphene on mica, with the PMMA removed by a 20 min dichloromethane : methanol (1:1 ratio) soak. Dichloromethane appears effective in PMMA disentanglement.

dissolution in chloroform. Contrasted against previous work, our process produces large-area graphene transfers, highlights the amount of polymer contamination clearly, and examines the fundamental chemistries involved in transfer polymer dissolution. Additionally, we ascertain that the PC-transferred graphene samples are atomically clean, as compared to the room temperature removal of PMMA, PLA, and PPA. The PC transfer process is general, allowing us to cleanly layer two-dimensional materials like graphene, CVD fluorinated graphene (FG), and CVD hexagonal boron nitride (h-BN).

4.2. Graphene Transfer Characterization

We grow graphene by CVD on Cu using previously established recipes [9, 12, 25]. We then spin coat the PMMA [22, 25, 26], PLA [38], PPA [39], PC [32, 40], and PMMA/PC scaffolds. The growth and transfer processes are outlined in more detail in Section 4.7. After fabricating these scaffolds, we etch the Cu away and mainly transfer to thermally grown 90 nm SiO_2 on Si (SiO_2) substrates. Water is trapped in this process, but other solvents can be used (Fig. 4.1). Further, we transfer to other nanomaterial layers (e.g. graphene and h-BN) on SiO_2 and to mica substrates [25]. Room temperature removal of the scaffolds takes place in a chloroform

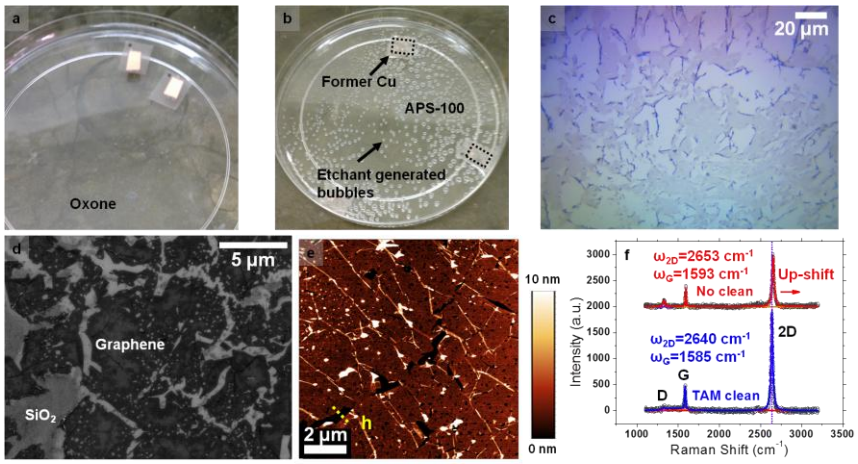

Figure 4.3. Graphene transfer using thermal release tape (TRT). (**a)** Photograph of Cu on thermal tape floating on potassium peroxymonosulfate (Oxone), a similar etchant to the commonly used ammonium persulfate. **(b)** Photograph of etched Cu in ammonium persulfate from Transene (APS-100). Etchant produces considerable amounts of bubbles due to the Cu reduction reaction. **(c)** Optical image of TRT-transferred graphene on SiO_2/Si. Many tears and scrolled edges are present. TRT-transferred film was released at 185 °C and cleaned with a 10 min toluene : acetone : methanol bath. **(d)** SEM image of TRT-transferred graphene on SiO_2/Si. TRT with graphene is dried with N_2 before transferring to the SiO_2/Si. Poor tape release [29, 30] and bad adhesion between the SiO_2/Si produces holes and tears within the transferred film. **(e)** AFM topographic image of TRT-transferred graphene on SiO_2/Si. Height from a tear edge to the substrate is h = 3.0 ± 0.6 nm. Large height likely results from the backside graphene on Cu not being removed. Note that the circular, graphene-free depressions occur from bubbles produced by the etchant during transfer. **(f)** Point Raman spectra (λ_{exc} = 633 nm, ~2 mW power, 50X, 30 s acquisition) for TRT-transferred graphene to SiO_2/Si for a sample with its TRT residues cleaned by a toluene : acetone : methanol clean (TAM clean) [29, 30] and for an unclean sample. The cleaned sample has considerably lower doping, as determined by the concurrent down shifts of the 2D and G bands.

bath for at least 1 hr; we have considered other solvents for PMMA removal and found them ineffective (Fig. 4.2). We also use thermal release tape (TRT) (Fig. 4.3), photoresist (AZ5214 PR) (Fig. 4.4), and aromatic poly(aniline) (PANI) based transfers (Fig. 4.5). The former transfer method results in many holes in our samples, and the latter methods give brittle films with substantial residue. Therefore, we avoid these strategies, as discussed in Section 4.8.

Figure 4.6a shows our transfer process for polymer-based graphene scaffolds. The schematic demonstrates that, even with the typical Ar/H_2 anneal, polymer contaminants remain on the graphene after transfer. Without this anneal, the polymer contamination level on the graphene is considerably worse. Still, we are interested in a polymer removal process that takes place at room temperature, and thus we will focus on non-annealed samples for the majority of

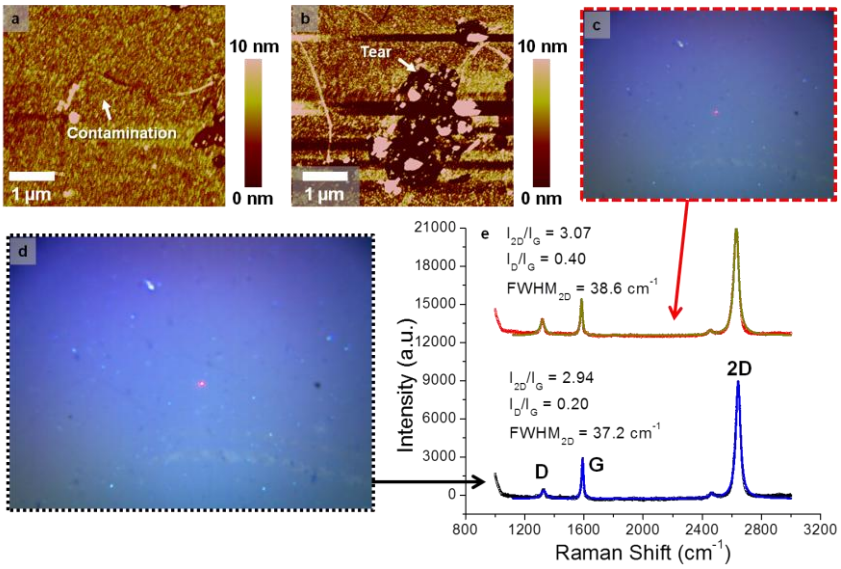

Figure 4.4. Graphene transfer using AZ5214 photoresist. AFM images of a continuous (a) and torn (b) graphene region on SiO_2/Si transferred by flood-exposed AZ5214 photoresist. 1 min UV flood exposure time used after the AZ5214 film was transferred to a SiO_2/Si chip, and then the film was developed in MF-319 developer. Both (a) and (b) show considerable contamination introduced by the photoresist, despite the flood exposure and development. Optical images **(c, d)** of the AZ5214 transferred film on SiO_2/Si. Tears apparent in both (c) and (d). **(e)** Point Raman spectra (λ_{exc} = 633 nm, ~2 mW power, 50X, 30 s acquisition) corresponding to the optical images in (c) and (d). Both spectra are of monolayer graphene, but the large 2D FWHM (greater than 30 cm^{-1}) indicates strain in the film. The G FWHM values (not listed) are less than 15 cm^{-1}, revealing AZ5214 induced doping in the graphene film.

the following work. In Fig. 4.6b, we give the chemical formulas for aliphatic PMMA, aliphatic PLA, aromatic PPA, and aromatic PC. Figures 4.6c-g show optical images of graphene transferred with different polymer scaffolds on SiO_2, with the scaffolds dissolved in chloroform at room temperature. We give the polymer scaffolds' thicknesses in the supporting information, as determined by profilometry. The polymer repeating unit is shown inset for each of the different scaffolds. In Fig. 4.6c, the PMMA-transferred film is continuous, with no contamination optically evident. Conversely, in Fig. 4.6d, the PLA-transferred film is discontinuous, with folded and contaminated edges. This suggests that the PLA transfer scaffold is less elastic, less robust, and interacts with the graphene more strongly than PMMA. Figure 4.6e shows the PPA-transferred graphene film; it too is discontinuous and contaminated like the PLA-transferred graphene. In contrast, the PC and PMMA/PC bilayer transferred graphene films

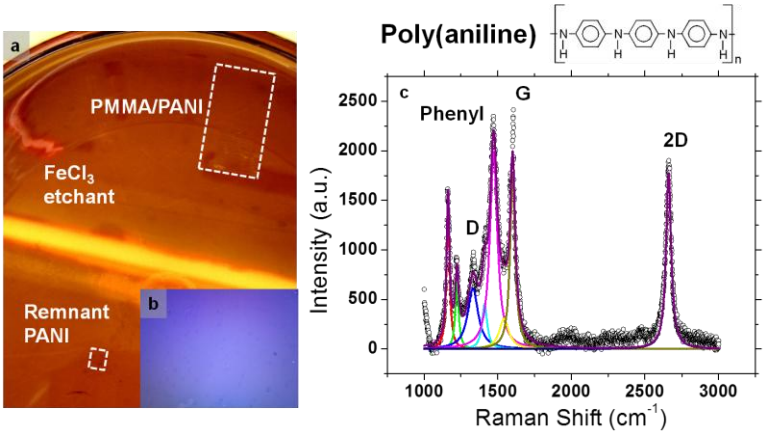

Figure 4.5. Graphene transfer with aromatic poly(aniline). **(a)** Photograph of poly(aniline) (PANI) transferred graphene and PMMA/PANI-transferred graphene on $FeCl_3$ Cu etchant. The PANI-supported graphene, without a PMMA overlayer, breaks apart within the etchant. The PMMA/PANI supported film survives the transfer. **(b)** Optical image of PMMA/PANI transferred graphene after polymer removal (in chloroform) on 90 nm SiO_2/Si. **(c)** Raman spectrum of the sample in **(b)**, showing considerable surface PANI residue. The spectrum shows vibrational modes related to the phenyl group [42] in PANI and as well as other hydrocarbon stretch modes. We hold that the residue level originates from strong π–π interactions between the aromatic phenyl group and the graphene.

in Figs. 4.6f and 4.6g, respectively, appear continuous and uncontaminated, like the PMMA-transferred graphene films. Selected area electron diffraction (SAED) measurements on the PMMA/PC sample—shown inset in Fig. 4.6g—reveal monolayer graphene domains within the CVD-controlled, ~5 μm grain size. The single set of diffraction spots suggests that turbostratic ordering from transfer-induced folds [26, 41] is non-existent.

We can assess the chemistries present on the graphene surface after polymer dissolution by means of X-ray photoelectron spectroscopy (XPS). Within Fig. 4.6h, we show offset C 1s photoelectron spectra for PMMA and PC transferred graphene films, both of which were from the same graphene growth (curves offset by 1000 counts/s, for clarity). Several reports analyzing the thermal decomposition of PMMA on graphene via XPS [13, 17, 43] fit sub-peaks for the C–C backbone, the $–CH_3$ sub-group, oxygenated (ester and ether) functionals, and others in the PMMA repeating unit. It is challenging to discriminate conclusively amongst these sub-groups and the innate functionals introduced by graphene CVD growth and ambient exposure. We

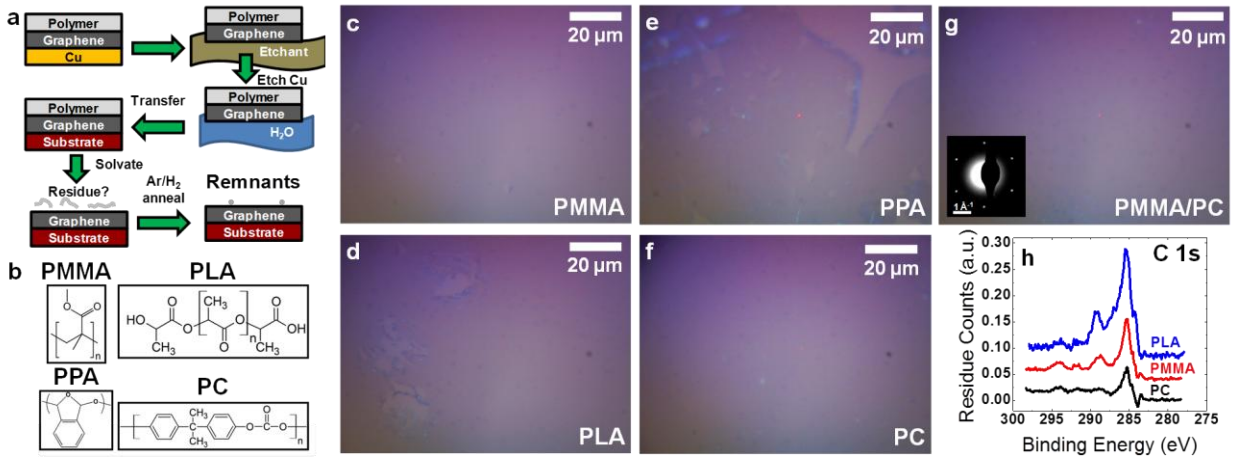

Figure 4.6. Polymer residues introduced by the chemical vapor deposition (CVD) graphene transfer process. **(a)** CVD graphene transfer process flow. Polymer residues often remain after a forming Ar/H_2 gas anneal. **(b)** Chemical formulas for the different polymers used. Optical images of large-area graphene transferred by **(c)** poly(methyl methacrylate) (PMMA), **(d)** poly(lactic acid) (PLA), **(e)** poly(phthaldehyde) (PPA), **(f)** poly(bisphenol A carbonate) (PC), and **(g)** PMMA/PC bilayer polymer scaffolds. Inset in (g) gives a representative, monolayer graphene diffraction pattern transferred by bilayer PMMA/PC. **(h)** C 1s photoelectron spectra after main graphene peak subtraction (sp^2 and sp^3) for PLA-, PMMA-, and PC-transferred graphene on SiO_2/Si. The residue counts are lowest for PC transfers.

consider the sp^2 C, sp^3 C (introduced by $–CH_3$ and others), carboxyl C–O, carbonyl C=O, oxygenated aryl [44], and carbonate CO_3 sub-peaks in our PLA-, PMMA-, and PC-transferred graphene films (see Fig. 4.7). We find that the amount of residual functionals relative to graphene (sp^2 sub-peak with sp^3 contributions removed) is 28.4%, 11.2%, and 2.1% for PLA-, PMMA-, and PC- transferred graphene, respectively. At a typical PMMA doping concentration of $p \sim 1\times10^{12}$ cm^{-2} [17], these amounts correspond to concentrations of 3×10^{12} cm^{-2} and 2×10^{11} cm^{-2} for PLA- and PC-transferred graphene. Doping levels of $\sim2\times10^{11}$ cm^{-2} have been reported in samples that were undoped [45], suggesting atomic cleanliness at our estimated doping level for PC.

We additionally examine the effects of the different polymer scaffolds on graphene on SiO_2/Si with scanning electron microscopy (SEM) in Fig. 4.8. Figure 4.8a gives a SEM image for PMMA-transferred graphene, revealing strand-like features and larger debris (green arrows). The strand-like features follow closely the Cu step flow direction [12, 46, 47], despite the

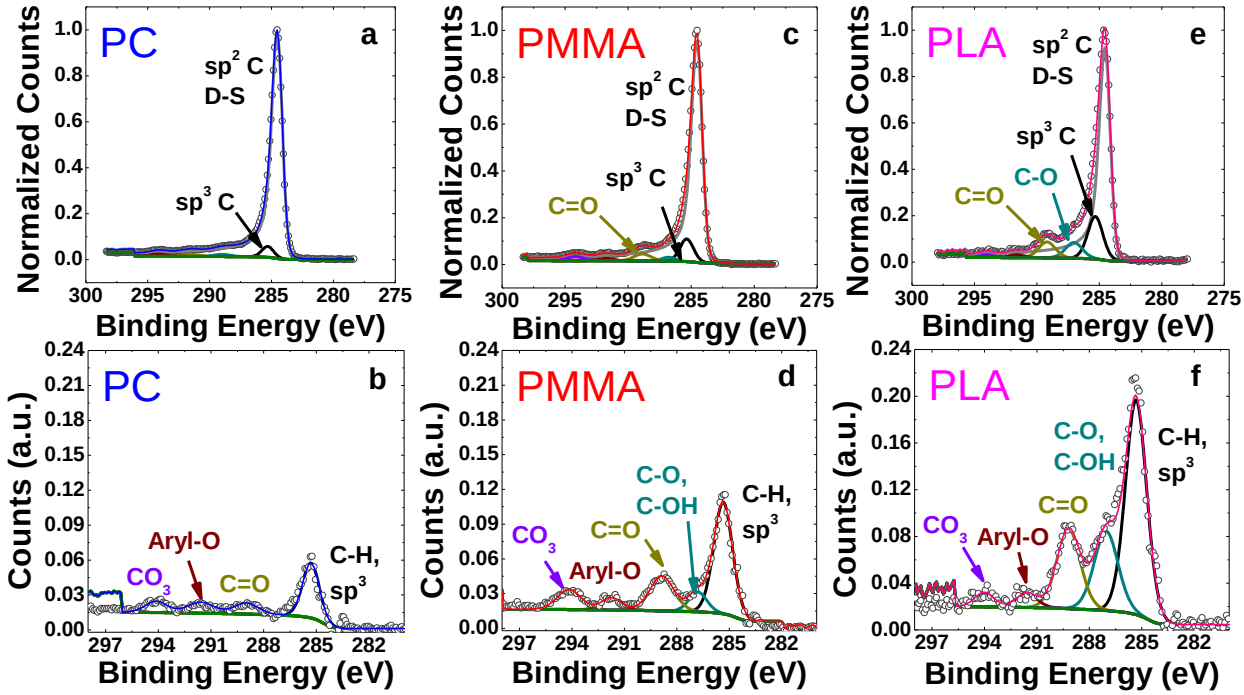

Figure 4.7. X-ray photoelectron spectra (XPS) for graphene transferred with different polymers. C 1s core level spectra (normalized to graphene) for PC-transferred **(a)**, PMMA-transferred **(c)**, and PLA-transferred **(e)** graphene films on 90 nm SiO_2/Si. A Doniach-Sunjic (D-S) lineshape was used to fit the asymmetric sp^2 carbons characteristic of metallic graphene. Other functionals, such as sp^3 carbon, carboxyls C–O, and carbonyls C=O, are also shown. PC-transferred graphene shows no obvious sub-peaks, indicative of low amounts of residue. Zoomed-in C 1s core level spectra for PC-transferred **(b)**, PMMA-transferred **(d)**, and PLA-transferred **(f)** graphene, with the sp^2 carbon contribution removed. PC-transferred graphene shows a small sp^3 peak, likely resulting from the graphene CVD growth process itself. Additionally, some weak carbonyl, oxygenated aryl, and carbonate (CO_3) groups are present. PMMA-transferred graphene has more significant contributions for the different functional groups, as compared to PC-transferred graphene. The higher sp^3 peak also corresponds to more aliphatic groups, like the end methoxy group and the C–C backbone in PMMA. PLA-transferred graphene is more substantially contaminated than PMMA-transferred graphene, despite attempted PLA gasification at temperatures above 180 °C [38]. Large contributions from sp^3 carbon, carboxyls, and carbonyls originate from the aliphatic ester and ether linkages within the PLA repeat unit. To quantitatively analyze the residue differences between PMMA- and PLA-transferred graphene with respect to PC-transferred graphene, we subtract the PC sp^3 contribution (in area) and oxygenated aryl from the other two samples' spectra. We then sum the resultant sub-peak areas of Figs. 4.7b,d,f. These sums are compared relative to the D-S sp^2 peak area, thereby giving the PMMA, PLA, and PC percentages reported in the main text.

removal of the Cu growth substrate. Graphene grain boundaries (GBs) [26] and twisted bilayers [48] are also evident. The PMMA will conform over the Cu steps and be thicker in their vicinity. Thicker PMMA regions are more likely to cross-link, to swell, and to impede disentanglement

via solvent permeation and dissolution [49]. Therefore, the duplicated Cu morphology in the partially removed PMMA is not entirely surprising.

Figure 4.8b shows a SEM image for PLA-transferred graphene. Similar to the PMMA-transferred graphene, there is PLA-based contamination (green arrows) roughly following the former Cu step flow morphology. Solid phase PLA polymers are known to rapidly depolymerize and transition into the gas phase at temperatures above 200 °C [38]. This depolymerization appears to be impeded by the graphene, as we notice PLA-based contamination even after this gasification process (see Fig. 4.9). Figure 4.8c demonstrates a SEM image for our PMMA/PPA transfer scaffold; here, we use the PMMA as an overlayer support, as the PPA-only transfers proved to be fragile and highly sensitive to moisture. The contamination and wrinkles (blue arrows) are significant in Fig. 4.8c. The PMMA/PPA scaffold was dissolved in chloroform and subsequently soaked in water, which should cleanly remove the PPA. Thus, the contamination in Fig. 4.8c is unexpected, since the PMMA only touches the PPA layer and the PPA should rapidly depolymerize from acid exposure, hydrolysis, and thermal treatment.

In Fig. 4.8d, a SEM image of PC-transferred graphene does not show the same polymer strands that are present in the PMMA-, PLA-, and PPA-transferred graphene films. The graphene film comes from the same growth as Fig. 4.8a. There are some wrinkles (blue arrows) introduced in the transfer, resulting from the considerably thinner (~70 nm, see Table 4.1) PC scaffold. We can estimate wrinkle densities in the resultant graphene film by using simple elasticity arguments. Besides the wrinkles, however, the film is relatively clean, again showing the effective PC dissolution [16, 32]. To eliminate the wrinkles introduced by the thin PC scaffold, we support the PC on graphene with a PMMA overlayer, similar to our procedure for PPA in Fig. 4.8c. Figure 4.8e shows a large-area SEM image for the PMMA/PC bilayer transferred

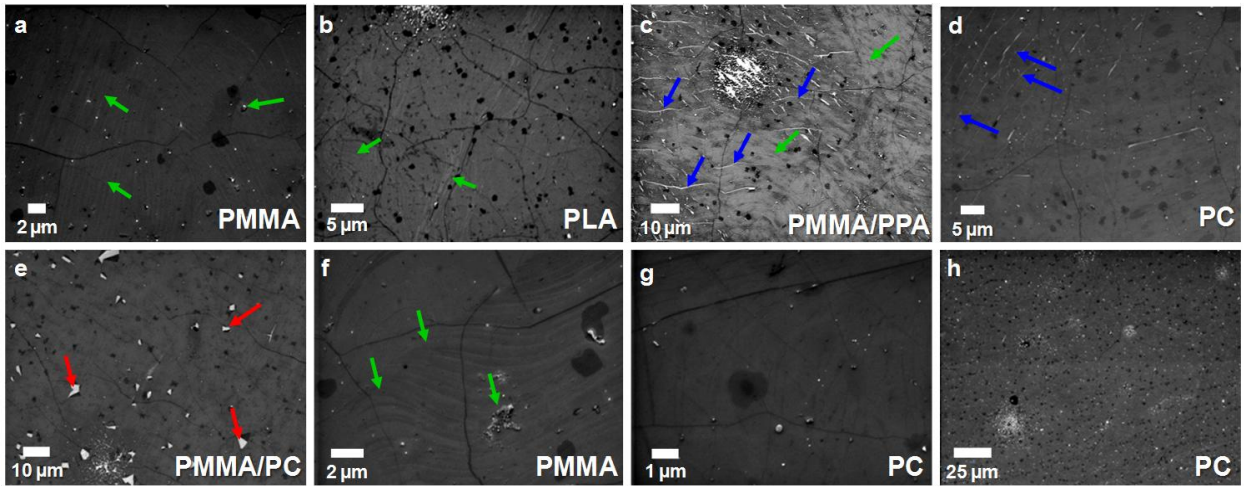

Figure 4.8. Scanning electron microscopy (SEM) imaging of coverage and contamination of different graphene transfer scaffolds on 90 nm SiO_2/Si. Green arrows show contamination, blue arrows show wrinkles, and red arrows show film breaks. Polymers removed in chloroform with no annealing. **(a)** PMMA transferred graphene with contamination. **(b)** PLA transferred graphene for a poorer quality graphene growth than (a) **(c)** PMMA/PPA bilayer transferred graphene, with low film integrity and high contamination. **(d)** PC transferred graphene for the same growth as (a). No obvious polymer contamination present. **(e)** PMMA/PC bilayer transferred graphene. PC layer contacts the graphene, with the PMMA layer providing structural support. Tears are evident, with no significant contamination. **(f)** Close-up image of the PMMA transferred sample in (a), showing larger-scale debris. **(g)** Close-up image of the PC transferred sample in (d). Only graphene bilayers, grain boundaries, and wrinkles evident. **(h)** Another PC transferred sample for a poorer quality graphene growth. Despite the growth, the polymer contamination is minimal.

graphene. Wrinkles and residue have been effectively mitigated, but the film possesses micron-sized cracks (red arrows). To better assess the contamination on PMMA- and PC-transferred graphene, we give smaller scale SEM images for PMMA and PC transfers in Figs. 4.8f and 4.8g, respectively. Figure 4.8f shows the same PMMA strands as Fig. 4.8a, as well as larger-scale PMMA debris. Conversely, the PC-transferred film in Fig. 4.8g manifests no obvious PC-based strands or debris. For a low-quality (small grain size and high bilayer density), PC-transferred graphene growth in Fig. 4.8h, we still observe a clean surface. We observe a higher density of white particles for this sample, suggesting that they originate from the poor growth.

4.3. Residual Doping Assessment

Raman spectroscopy has proven to be a powerful, non-destructive tool for determining the vibrational and electronic properties of carbon-based nanomaterials. For graphene layers,

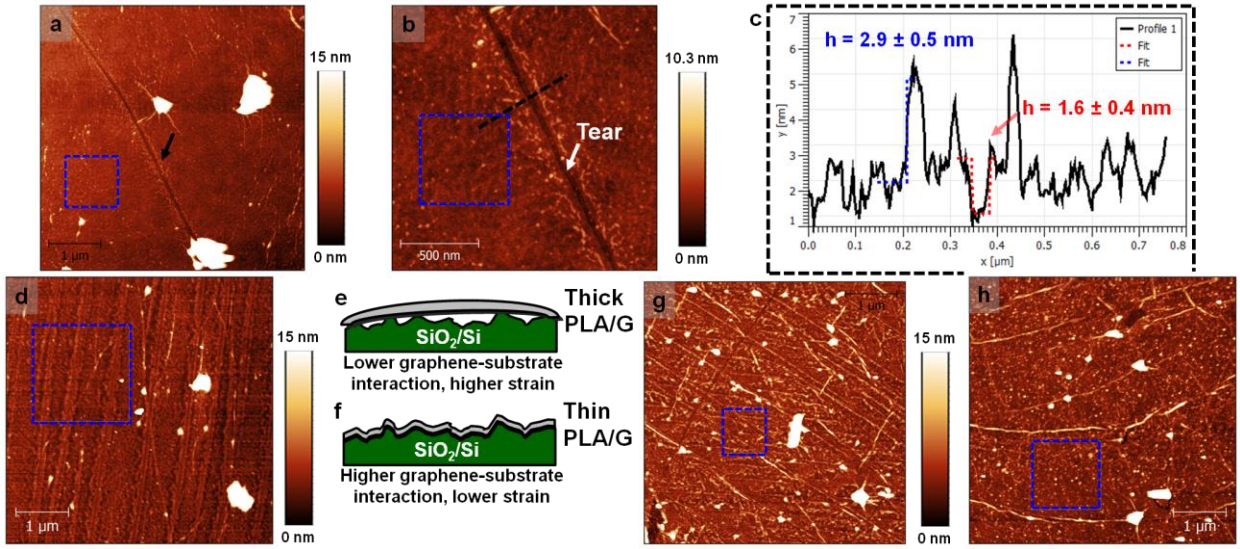

Figure 4.9. Poly(lactic acid) (PLA) and poly(phthalaldehyde) (PPA) transfer of graphene. **(a)** AFM image of PLA transferred graphene with a tear in the film. Sample annealed at 400 °C in a low pressure (~1 torr) environment to gasify [38] the PLA. RMS roughness within the blue box is 0.63 nm, and the image's RMS roughness is 6.83 nm. **(b)** AFM close-up of the region indicated by the arrow in (a). RMS roughness within the blue box is 0.49 nm, and the entire image's RMS roughness is 0.67 nm. **(c)** Topographic profiles of the region indicated by the black line in (b). The red cut over the graphene tear reveals monolayer graphene (with water and adsorbates), whereas the blue cut shows PLA decoration near the tear. **(d)** AFM of a different PLA transfer, wherein the PLA solution for (a) and (b) was diluted in chloroform (5:1, chloroform : original PLA). This sample underwent a 200 °C anneal in a low pressure (~1 torr) environment as well. RMS roughness within the blue box is 1.04 nm, and image's RMS roughness is 3.34 nm. **(e)** Cartoon schematic of a thick PLA/G film on a SiO_2/Si surface. Here, the thicker polymer prevents the graphene from coming into intimate contact with the SiO_2/Si substrate. This increases strain but lowers graphene's influence on polymer dissolution and gasification. Thus, the gasification of PLA at temperatures above 180 °C proceeds as expected for the bulk polymer. **(f)** Cartoon schematic of a thin PLA/G film on a SiO_2/Si surface. In this case, the thin polymer allows the graphene to be conformal to the SiO_2/Si substrate. Consequently, this lowers the amount of strain in the graphene but increases the graphene-substrate interaction. That increased interaction affects PLA gasification [38] above 180 °C. **(g)** AFM image of PPA transferred graphene employing a PMMA overlayer (PMMA/PPA bilayer, with PPA contacting the graphene). RMS roughness within the blue box is 1.45 nm, and the image's RMS roughness is 3.38 nm. Tears, wrinkles, and contamination are present. **(h)** Additional AFM image of PMMA/PPA transferred graphene. RMS roughness within the blue box is 1.24 nm, and the image's RMS roughness is 3.77 nm. Image possesses similar contamination as (g).

there are three major Raman bands called the D, G, and 2D (also known as G') bands, respectively. These bands' positions and full-width at half maximum (FWHM) values determine information about layer number, doping, and strain in the graphene films [50-54]. In Fig. 4.10, we give our Raman statistics for G and 2D band positions and FWHM for the PMMA, PMMA/PC, and PC transfer scaffolds. Table 4.2 also summarizes the statistics for several

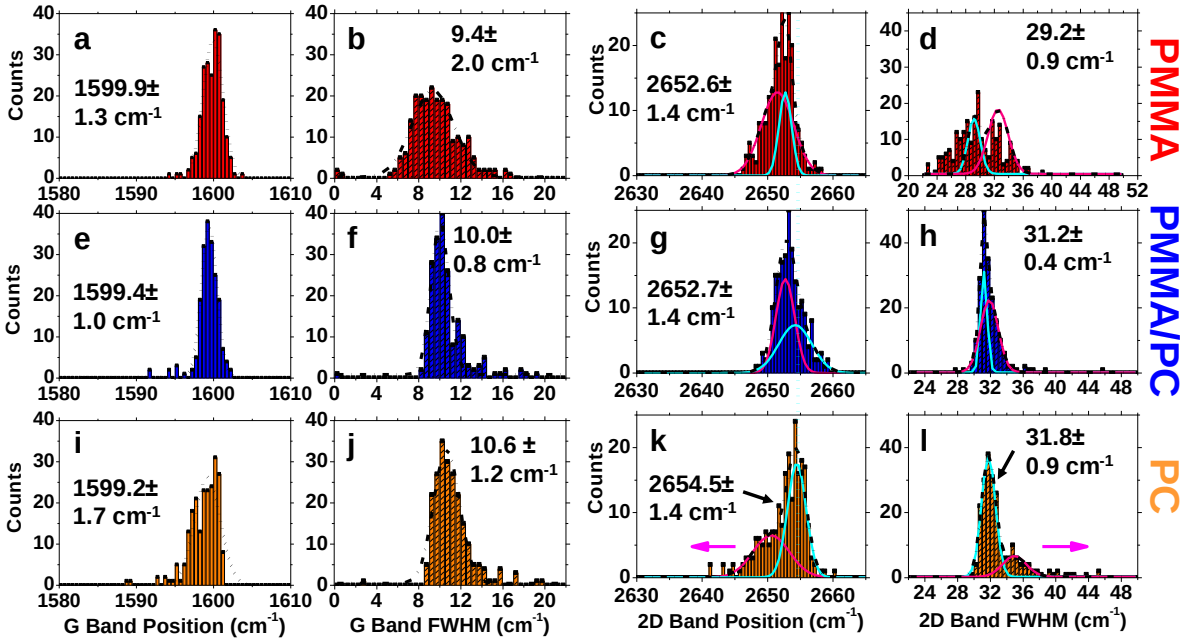

Figure 4.10. Raman spectra maps for graphene transferred by different polymer scaffolds. Distributions of G band position **(a)**, G band full-width at half maximum (FWHM) **(b)**, 2D band position **(c)**, and 2D band FWHM for graphene transferred with PMMA. The upshifted G band position, stiffened G band FWHM, downshifted 2D band position, and bipartite 2D band FWHM distribution highlight doping from PMMA contamination. Mean and standard deviations listed, and strain-based contributions to the distribution are fit with pink Gaussians. Distributions of G band position **(e)**, G band FWHM **(f)**, 2D band position **(g)**, and 2D band FWHM **(h)** for graphene transferred with PMMA/PC (PC contacting graphene). Compared to PMMA, doping has marginally improved. However, the difference is not statistically significant at a 99% confidence level. Distributions of the G band position **(i)**, G band FWHM **(j)**, 2D band position **(k)**, and 2D band FWHM **(l)** for graphene transferred with PC. Doping is lowest with PC, and the PC and PMMA populations are statistically different at 99% confidence level.

polymer scaffolds extracted by Gaussian fitting the Raman parameters. To date, no reports have concurrently assessed complex co-doping and strain effects present in the Raman spectra of CVD graphene films. In Section 4.9, we carefully account for all of these factors and develop a general empirical model that will work for most small-grain CVD samples.

The 2D band FWHM is quite sensitive to strain [50, 52, 53], and in Fig. 4.10d we can decouple the strain (magenta, softened FWHM) and doping (cyan, stiffened FWHM) contributions. Following the model detailed in Section 4.9, we find a strain in the PMMA films of $\varepsilon = -0.19 \pm 0.07\%$ and a doping increase of $\Delta n = (1.59 \pm 0.03) \times 10^{13}$ cm^{-2}. The n-type character results from graphene encapsulation of water decorated silanol groups [55, 56]. We

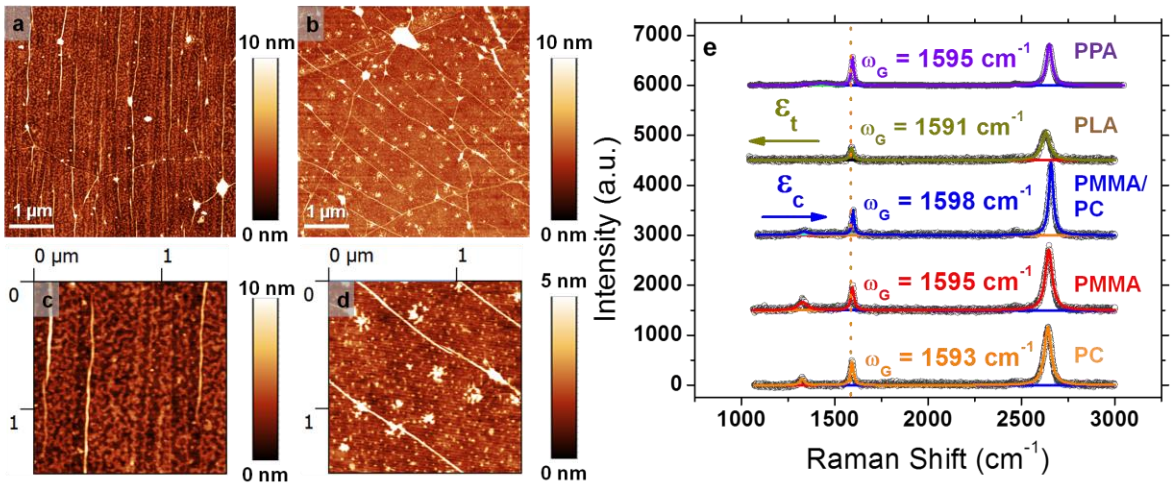

Figure 4.11. Graphene doping from trapped water under graphene on SiO_2/Si. **(a)** AFM image of PMMA-transferred graphene on SiO_2/Si with no anneal. Note that this region is reasonably free of PMMA contamination, but regions like this were rare. Tendril-like features (see Chapter 5) between the graphene wrinkles are evident, showing trapped water at the graphene-SiO_2/Si interface. **(b)** AFM image of PC-transferred graphene on SiO_2/Si with no anneal. Tendrils are also present, but the sample possess more point-like water features. Close-up AFM images of the PMMA **(c)** and the PC **(d)** samples in (a) and (b), respectively. Aforementioned water features are more obvious in (c) and (d). **(e)** Point Raman spectra for all of the transfer scaffolds: PPA (with a PMMA support), PLA, PMMA/PC, PMMA, and PC. The upshifted G band position (ω_G > 1590 cm^{-1}) and downshifted 2D band position (ω_{2D} < 2655 cm^{-1} at λ_{exc} = 633 nm) reveal common n-type doping for all the non-annealed, transferred films. Additional upshifts in the G band result from p-type doping caused by polymer contamination. PC transferred films possess the lowest amount of doping, supporting the conclusion that they dissolve off the graphene top-side cleanly. Compressive strain is present in the PMMA/PC film, and tensile strain is evident in the PLA film.

have morphological evidence of this trapped water on graphene on SiO_2, which is noteworthy as graphene trapped water was only seen on ultraflat substrates like mica [25] and diamond (see Section 4.8, Fig. 4.11, and Fig. 4.12) [57]. Figures 4.10e-h show the Raman metrics for graphene transferred with a PMMA/PC bilayer. Following the previous discussion, we find a strain of ε = –0.18 ± 0.06% and doping of Δn = (1.40 ± 0.03) × 10^{13} cm^{-2}, again n-type (see Section 4.8). The PMMA/PC-transferred and the PMMA-transferred graphene differ in doping by (1.90 ± 0.44) × 10^{12} cm^{-2}, a small difference in cleanliness. Nevertheless, by hypothesis testing, we cannot conclude at that this difference is statistically significant (99% confidence).

Finally, Figs. 4.10i-l give the PC-transferred graphene film's Raman metrics. The strain in the PC-transferred films (magenta, 2D) is ε = –0.27 ± 0.07% with doping of Δn = (2.00 ±

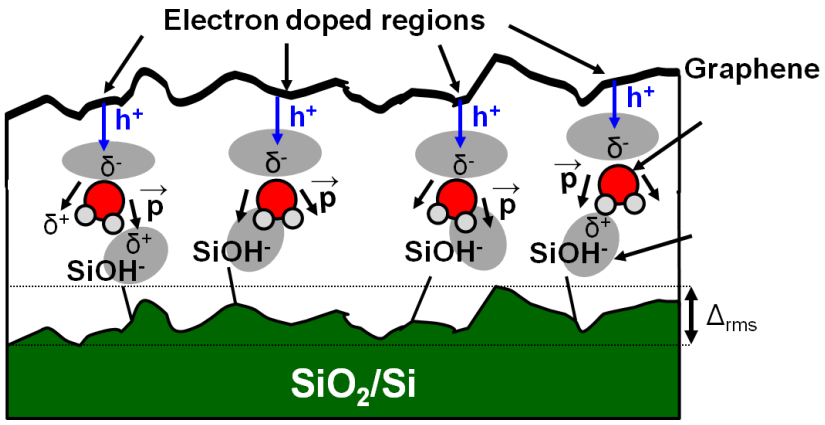

Figure 4.12. Mechanism of water-induced n-type doping in graphene. As shown in the schematic, the SiO_2/Si surface can expose silanol (Si–OH) functionals, which tend to be negatively charged. Water has an innate dipole moment **p** which will electrostatically align the hydrogens to the charged Si–OH^-. This places the electronegative (δ^-) oxygen into alignment with the graphene overlayer. Hole transfer to the electronegative oxygen leaves an accumulation of electrons within the graphene, thereby n-type doping the layer. The density of Si–OH groups in dry oxidized SiO_2/Si (90 nm) is $n_{imp} = 8\times10^{18}$ cm^{-3} [55]. Within a 1 nm RMS roughness (Δ_{rms}) exposed layer, the estimated surface density of Si–OH groups is $n_s = 8\times10^{11}$ cm^{-2}. Assuming that multiple water molecules could be electrostatically attracted to a single Si–OH moiety, an electron concentration of $n \sim 10^{12}$ cm^{-2} could be induced. This is in qualitative agreement ($n_{Raman} \approx 4\times10^{12}$ cm^{-2}) with the G band upshift and 2D band downshift observed in Fig. 4.11.

0.04) × 10^{13} cm^{-2}. Despite the heightened strain, the PC-transferred films have a higher n-type doping (i.e., lowered co-doping) than the PMMA- and PMMA/PC-transferred graphene films. This results in a doping difference of (4.10 ± 0.52) × 10^{12} cm^{-2} between the films. At a 99% confidence level, these two populations are statistically different, caused by the inherent p-type doping in the PMMA-transferred graphene films. Previous reports gave a p-type doping due to the PMMA of $p \sim 10^{12}$ cm^{-2} (electrical) [13, 17] and ~1.6×10^{12} cm^{-2} (for 495K molecular weight) [58], both consistent with the ~4×10^{12} cm^{-2} change we are seeing here between PC- and PMMA-transferred graphene. Hence, these Raman data show the PMMA-induced p-doping occurring in transferred films.

Directly observing the polymer residues at relevant length scales is important for assessing how severe the contamination is for electronic devices, encapsulation layers, and other graphene applications. First, in Fig. 4.13a we show an atomic force microscopy (AFM) image for PMMA-transferred graphene on SiO_2 after a 2 hr Ar/H_2 forming gas anneal at 400 °C. The

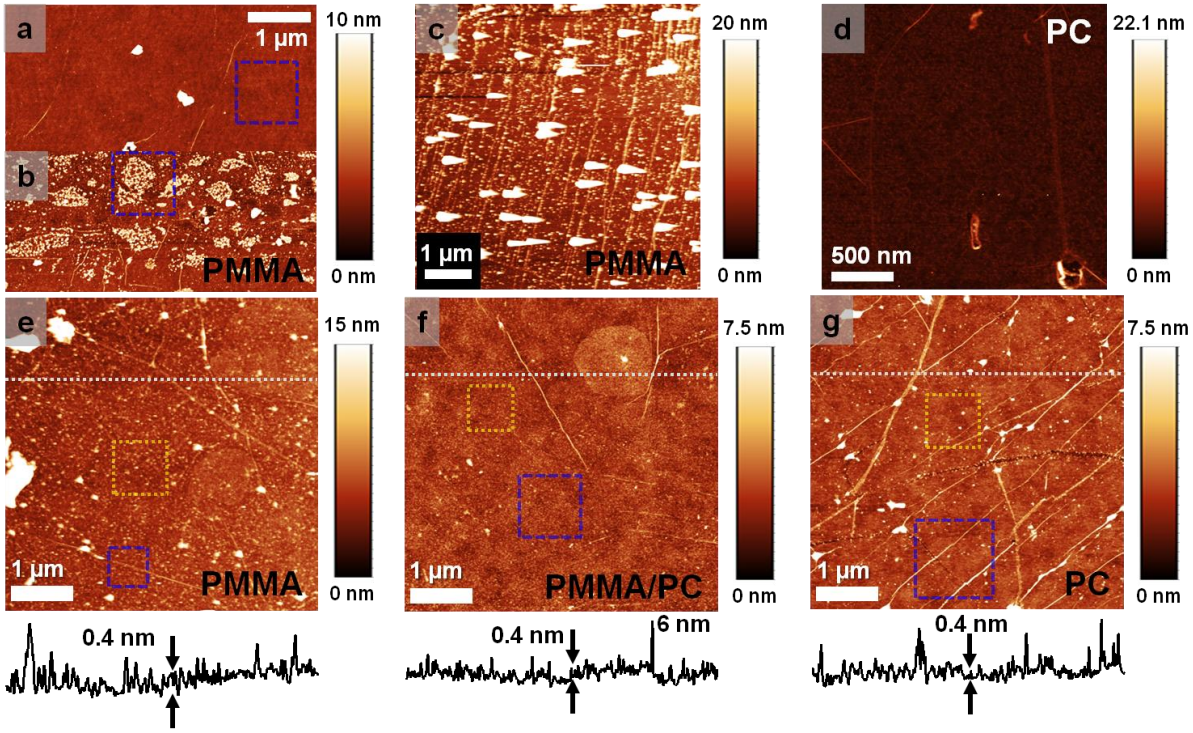

Figure 4.13. Changes in graphene surface morphology caused by the transfer polymers. AFM images **(a,b)** of PMMA-transferred graphene after a 90 min, 400 °C Ar/H_2 anneal. While the region in (a) is clean, considerable, partially depolymerized PMMA remains on the graphene in (b). RMS roughness values: 0.33 nm (box, *a*), 1.72 nm (image, *a*), 2.8 nm (box, *b*), and 3.58 nm (image, *b*). AFM images of PMMA-transferred **(c)** and PC-transferred **(d)** graphene (same growth) without a forming gas anneal. The PC graphene surface is markedly smoother. Morphologies of PMMA-transferred **(e)**, PMMA/PC-transferred **(f)**, and PC-transferred **(g)** graphene films, all transferred from the same growth material. Both PMMA/PC and PC films are cleaner than PMMA films, with PMMA/PC films having fewer transfer-induced wrinkles. The overlaid gray lines correspond to the line profiles below each respective image. RMS roughness values: 1.21 nm (yellow, *e*), 1.05 nm (blue, *e*), 3.58 nm (image, *e*), 0.57 nm (yellow, *f*), 0.62 nm (blue, *f*), 0.71 nm (image, *f*), 0.71 nm (yellow, *g*), 1.07 nm (blue, *g*), and 1.76 nm (image, *g*).

surface of Fig. 4.13a is smooth post anneal, with a 0.33 nm root-mean-square (RMS) roughness in the blue box. Note that we give RMS roughness values for the subsequent images in the relevant figure captions (Fig. 4.13, etc.). Despite the clean surface of Fig. 4.13a, the depolymerization of PMMA by thermal degradation and bond scission [60] is inherently inhomogeneous. To demonstrate this, we show an AFM image of a different area of the same annealed sample in Fig. 4.13b. The surface is quite rough from incompletely removed PMMA strands. This inhomogeneity, coupled with the deleterious chemical [16, 40] and electrical effects

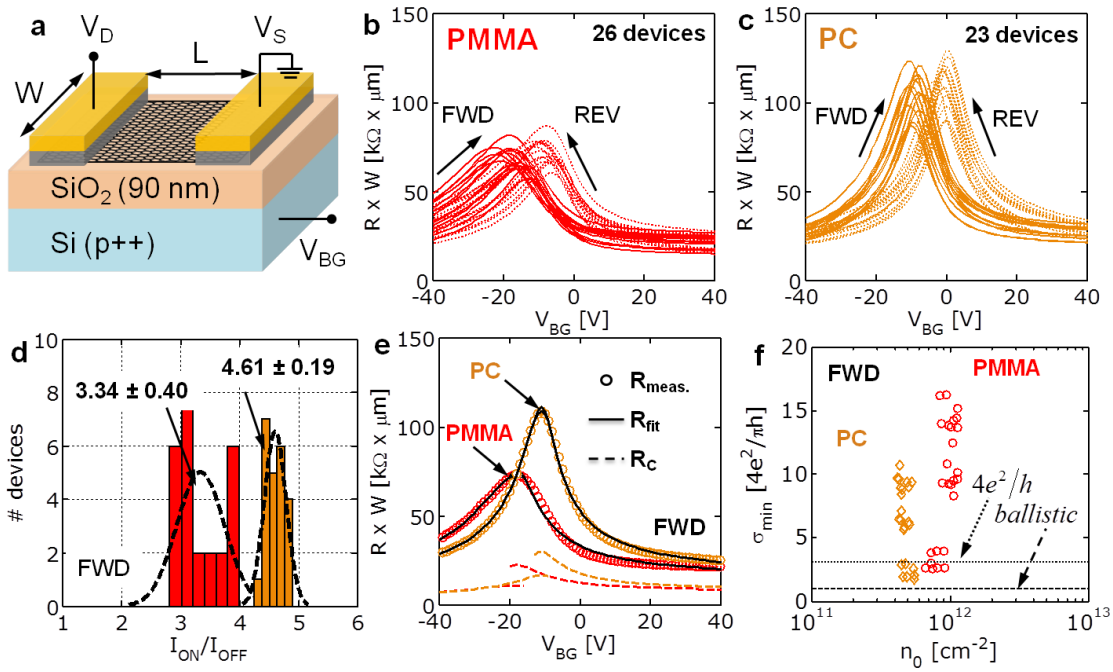

Figure 4.14. Electrical characteristics of graphene field-effect transistors (GFETs) in vacuum. Graphene films transferred using PMMA and PC based scaffolds without undergoing any thermal annealing. **(a)** Schematic of back-gated GFETs used in this work. Transfer characteristics for PMMA **(b)** and PC **(c)** based FETs respectively. Back gate voltage (V_{BG}) is swept consecutively in forward (FWD) and reverse (REV) directions. A shift in Dirac voltage (ΔV_0) as FWD and REV sweeps are completed is observed in both cases. This n-type hysteresis suggests the presence of charge trapping mechanisms at the graphene/SiO_2 interface, possibly from left over polymer (PMMA or PC) residues. **(d)** I_{ON}/I_{OFF} ratios for PMMA (red) and PC (orange) based FETs devices. Note that from histograms and distributions that GFETs from PC transferred films exhibit higher I_{ON}/I_{OFF} and reduced device variability. **(e)** R-V_{BG} measured (circles) and fitted (solid lines) data from Fig. 4.14b-c. Fitted electron and hole contact resistances (R_C) (dashed lines) also shown. Fitting model described in [64]. **(f)** Measured minimum conductivity (σ_{min}) as a function of minimum carrier density (n_0) extracted from transport model [64]. Ballistic and $4e/h^2$ limits also shown with dashed and dotted lines, respectively.

[61] that happen after Ar/H_2 annealing, illustrates the need for a room temperature polymer removal method.

Figure 4.13c demonstrates the level of surface contamination that occurs without annealing PMMA-transferred graphene in forming gas. PMMA strands thoroughly decorate the graphene/SiO_2/Si surface, and the tip's image convolves with larger PMMA debris. Comparatively, the PC-transferred graphene in Fig. 4.13d is remarkably cleaner without a thermal anneal. Both films in Figs. 4.13c and 4.13d come from the same graphene growth. Outside of growth-related morphological features [10-12], Fig. 4.13d is featureless, suggesting

that the room temperature dissolution of PC off graphene in chloroform is effective. Figures 4.13e-g show AFM images for PMMA-, PMMA/PC-, and PC-transferred graphene films on SiO_2, all from the same growth with the polymers dissolved in chloroform simultaneously. We give line profiles given below the images, all taken along the inset gray, dotted lines. The sample in Fig. 4.13e is less rough compared to Fig. 4.13c, as chloroform solvates polymers better than dichloromethane and acetone (see Fig. 4.2). Nevertheless, there is a still a sizable amount of PMMA residue on the sample, as demonstrated by a higher RMS roughness and the jagged line profile. Nevertheless, the PMMA/PC bilayer and PC scaffolds in Figs. 4.13f-g have lower RMS roughness values and smoother line profiles than the PMMA scaffold in Fig. 4.13e. This gives additional evidence that scaffolds with PC layers in contact to the graphene are sufficiently removed at room temperature. We note that the wrinkle density in the PC-transferred film of Fig. 4.13g is high, caused by the thin (~70 nm, Table 4.1) PC scaffold used. These wrinkles are mitigated with the stronger PMMA/PC bilayer in Fig. 4.13f.

4.4. Electrical Measurements and Nanomaterial Layering

We then turn to examine the improved cleanliness of non-annealed PMMA- and PC-transferred graphene on SiO_2 in field-effect transistor (FET) measurements. Figure 4.14a shows a schematic of back gated devices used (Section 4.7 for fabrication details). The measured (in vacuum) transfer characteristics (V_D = 0.1 V) for PMMA (red) and PC (orange) based FETs are shown in Figs. 4.14b and 4.14c. Both sets of device data are primarily n-type and exhibit a noticeable Dirac voltage shift (hysteresis) ΔV_0 as V_{BG} is swept in forward (FWD) and reverse (REV) directions. Trapped water (Figs. 4.11 and 4.12) [55] as well as leftover polymer residues are possible sources of this hysteretic behavior. Overall, PC-transferred devices exhibit higher I_{ON}/I_{OFF} ratios (Fig. 4.14d), higher maximum resistance values (or lower minimum conductivity)

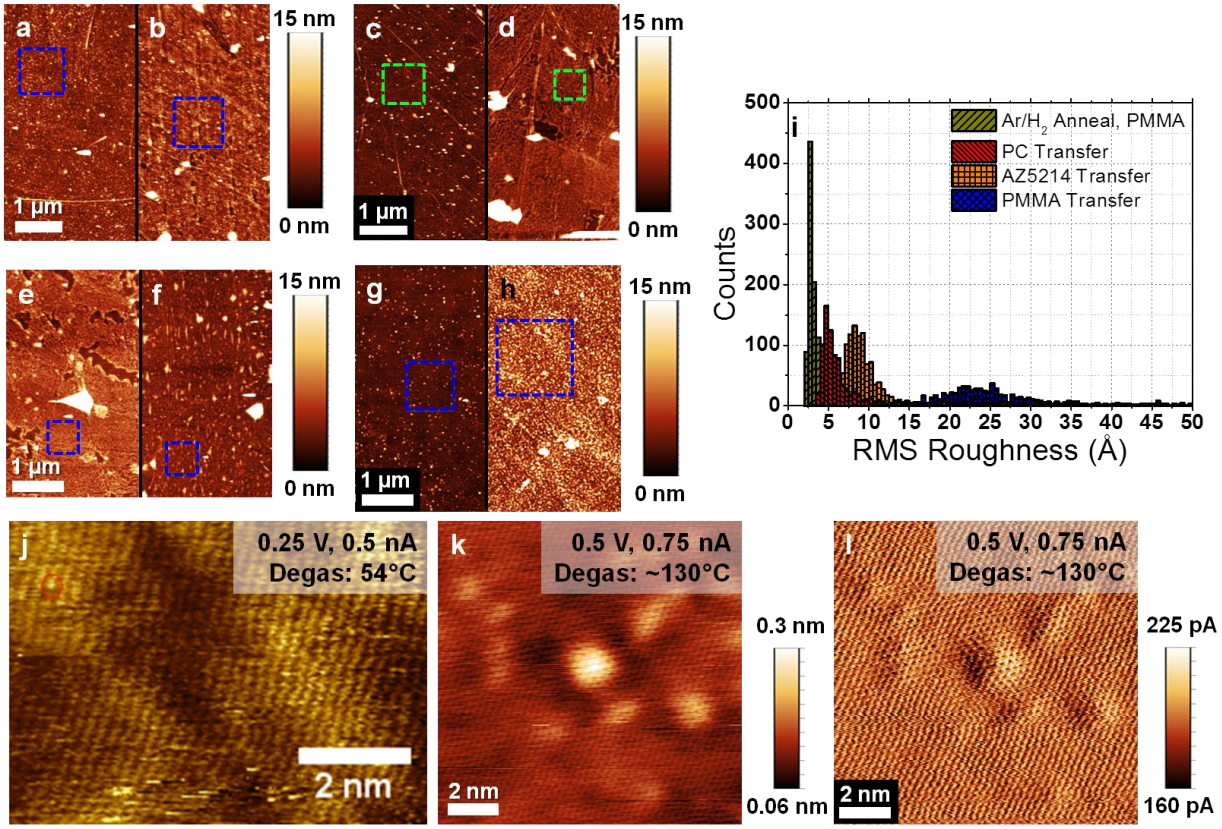

Figure 4.15. PC-enabled layering of low dimensional nanomaterials and atomic cleanliness of PC removal. One layer **(a)** and two layer **(b)** PMMA-transferred graphene on SiO_2/Si. The graphene layers are separated by trapped water, which does not layer from PMMA contamination. RMS roughness values: 1.4 nm (box, *a*), 1.87 nm (image, *a*), 1.65 nm (box, *b*), and 2.51 nm (image, *b*). One layer **(c)** and two layer **(d)** PC-transferred graphene on SiO_2/Si. In (d), water forms layers and tendrils between the graphene layers due to a PC-enabled, clean surface. RMS roughness values: 0.94 nm (box, *c*), 1.99 nm (image, *c*), 1.10 nm (box, *d*), and 11.5 nm (image, *d*). (**e)** Water trapped between two PC-transferred graphene (G) layers. **(f)** Water trapped between PC-transferred graphene on a fluorinated, PC-transferred graphene (FG) layer. There is water layering in the G/H_2O/G stack, compared to point-like, trapped water in G/H_2O/FG stack. RMS roughness values: 0.9 nm (box, *e*), 4.7 nm (image, *e*), 1.1 nm (box, *f*), and 5.4 nm (image, *f*). One layer **(g)** and two layers **(h)** of PC-transferred, CVD hexagonal boron nitride (h-BN). Like the G/H_2O/FG stack, point-like water accumulates between the layers in (h). RMS roughness values: 0.93 nm (box, *g*), 1.7 nm (image, *g*), 2.4 nm (box, *h*), and 3.2 nm (image, *h*). **(i)** RMS roughness histogram for different transfer scaffolds, revealing that PC-transferred graphene is as smooth as Ar/H_2 annealed graphene. **(j)** Scanning tunneling microscopy (STM) derivative image of a PC-transferred graphene film on SiO_2/Si. Sample was degassed in situ at 54 °C, and the image shows atomic resolution. STM topograph image **(k)** and current image **(l)** for PC-transferred graphene on mica. Sample was degassed in situ at ~130 °C, and both images reveal the atomic-level, honeycomb structure of the graphene. These low degas temperatures would not remove PMMA-based contamination on the graphene, thereby obscuring lattice resolution.

and smaller ΔV_0 compared with PMMA-transferred FETs. These three factors suggest a lower impurity density (n_0) that comes from improved cleanliness of graphene surface in PC-

transferred samples.

To help quantify residual doping in our devices [62, 63], we take PMMA R–V_{BG} data and Lorentzian fit about the Dirac point. In Fig. 4.14b, we determine a broadening of $\Gamma_{PMMA} \approx 17$ V, remarkably similar to published results for non-annealed graphene FETs transferred in water ($\Gamma_{PMMA,H2O} \approx 17$ V) [17] and in isopropanol ($\Gamma_{PMMA,IPA} \approx 16.8$ V) [13]. Since the H_2O and IPA are similarly broadened, we conclude that the topside residuals, namely, the PMMA contaminants, have a dominant effect in the R–V_{BG} measurement. Conversely, the PC devices have a broadening of $\Gamma_{PC} \approx 15$ V, thereby suggesting a cleaner topside.

Figure 4.14e shows representative measured (circles) and fitted (solid lines) data (FWD sweep) for PMMA and PC transferred FETs. We use the fitting model previously described in reference [64] to extract values for impurity carrier density (n_0) and contact resistance (R_{CON}) (dashed lines) for all data. Furthermore, in Fig. 4.14f we calculated minimum conductivity (σ_{min}) (from Figs. 4.14b and 4.14c) as a function of n_0 (obtained from model) for each device. We note that for PMMA based devices n_0 ($(5.7 \pm 0.8)\times10^{11}$ cm^{-2}) is higher compared to PC transferred FETs ($(4.8 \pm 0.4)\times10^{11}$ cm^{-2}), and the minimum conductivity is slightly higher. Both of these factors suggest that presence of lower PC residue [63], since we observe a lower contribution from impurity charges (n_0) [62].

We also make use of our PC transfer process in the heterogeneous layering of graphene, fluorinated graphene (FG), and CVD hexagonal boron nitride (h-BN). In Figs. 4.15a and 4.15b, respectively, we show AFM images for one layer (Fig. 4.15a) and two layers (Fig. 4.15b) of PMMA-transferred graphene. The surface of Fig. 6a is akin in morphology to Figs. 4.13e and 4.13h. In Fig. 4.15b, when we wet-transfer [25] a second PMMA-based graphene layer, water is trapped at the graphene-graphene interface. We do not see intercalated chloroform in our

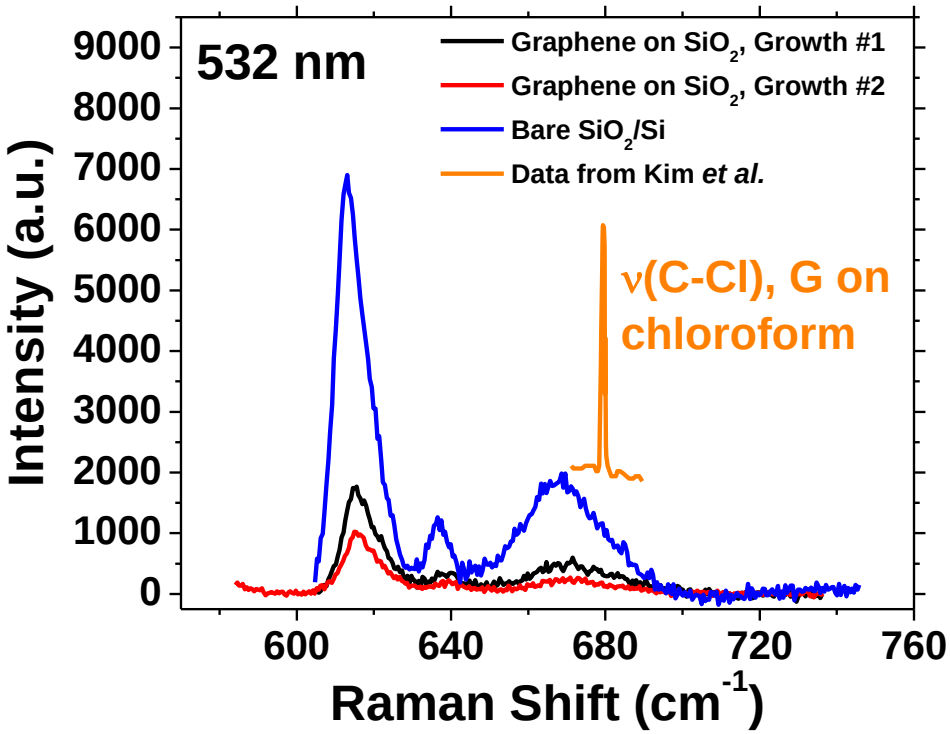

Figure 4.16. Lack of chloroform intercalation under graphene. Point Raman spectra (λ_{exc} = 532 nm, ~10 mW power, 100X, 60 s acquisition) of two different graphene growths on SiO_2/Si and a bare SiO_2/Si control. Chloroform has been shown to intercalate under graphene [65], giving the Raman signature seen in orange above. Since the polymer scaffold in our samples is often removed by chloroform, we consider the possibility that chloroform could intercalate under our graphene films. We only see signatures of the SiO_2/Si in the region where intercalated chloroform modes are expected. Therefore, we conclude the amount of intercalated chloroform under the graphene is minimal.

samples (Fig. 4.16), contrasting a recent study [65]. The water gives a rough morphology affected by the remnant hydrophobic PMMA strands, resulting in pinholes and no obvious water layering [25]. On the contrary, PC-transferred graphene results in a smoother morphology, as shown for one PC-transferred layer (Fig. 4.15c) and for two PC-transferred layers (Fig. 4.15d). Water is again trapped at the graphene-graphene interface of Fig. 4.15d, forming filaments and layers [25, 66] and not an amorphous film. Water layering is only possible if graphene's wetting properties are preserved, whereby the SiO_2/Si substrate templates the water through the graphene [67]. Hence, the PC-transferred graphene films leave insufficient residue to affect those wetting properties and disrupt water layering.

To examine these wetting phenomena in more detail, we layer different low-dimensional nanomaterials with PC. Figure 4.15e gives an AFM image a PC-transferred (no annealing) graphene/water/graphene stack. In Fig. 4.15f, we show an AFM section of a PC-transferred CVD graphene layer on top of a FG layer (for fluorination details, see Section 4.7) [11]. Here, the superhydrophobic FG layer disrupts the graphene wetting transparency [67] and brings about point-like water accumulation. Without PC, these hydration characteristics would be obscured. h-BN is also hydrophobic, and we PC-transfer one layer (Fig. 4.15g) and two layers (Fig. 4.15h) of CVD h-BN. Like the graphene/H_2O/FG stack, the entrapped water is point-like, from the hydrophobic h-BN. We also note that h-BN transfer must take place with PC, as a forming gas Ar/H_2 "clean" attacks h-BN (see Chapter 7 and reference [68]).

Both Table 4.3 and Fig. 4.15i summarize the RMS roughness values from several AFM measurements of PMMA-, PC-, annealed PMMA-, and photoresist-transferred graphene films. While the Ar/H_2 annealed PMMA-transferred films have the lowest RMS roughness ($\Delta = 2.9 \pm 0.4$ Å), PC-transferred films are also fairly smooth ($\Delta = 5.1 \pm 0.8$ Å). Nevertheless, the inhomogeneous PMMA removal, more pronounced graphene-substrate interaction [61], and covalent PMMA re-hybridization [16] introduced by annealing make it less desirable. Moreover, graphene's temperature sensitive applications, like those involving biomolecule encapsulation or flexible substrates, prohibit the anneal. Non-annealed PMMA transfers have a fourfold higher RMS roughness ($\Delta = 23.4 \pm 4.1$ Å) than non-annealed PC transfers, and AZ5214-transferred films are marginally smoother ($\Delta = 8.6 \pm 1.4$ Å) yet brittle (see Section 4.8, Fig. 4.4).

Finally, we give atomic-level evidence of the cleanliness of PC-transferred graphene. In Figs. 4.15j-l, we show atomic resolution ultrahigh vacuum scanning tunneling microscopy (UHV-STM) images of PC-transferred graphene at two different degas [25, 26] temperatures.

Figure 4.15j reveals a STM derivative image of non-annealed, PC-transferred graphene on 90 nm SiO_2/Si, degassed at ~54 °C. Atomic structure of the graphene is present, albeit noisy. We note that the PMMA bond scission is not possible at this temperature [60]. As determined from the previous AFM images, equivalently prepared, PMMA-transferred samples have autocorrelation lengths of ~10 nm (25 μm^2). Comparatively, PC-transferred samples have autocorrelation lengths greater than ~100 nm (25 μm^2). The PMMA autocorrelation length is well within the AFM tip's radius of curvature and does not necessarily imply clean graphene regions between PMMA strands. Thus, the probability of serendipitously encountering an atomically clean graphene region for PMMA-transferred samples via STM is low. Figures 4.15k and 4.15l show a STM topograph and derivative image, respectively, for PC-transferred graphene on mica, degassed at ~130 °C. The scan shows improved resolution and graphene's atomic lattice is evident. The higher temperature degas likely removes adsorbed water, thereby improving the surface resolution. Regardless, PMMA bond scission [60] or sublimation [17] do not occur at ~130 °C, further confirming the atomic-level cleanliness of the PC transfer. Table 4.3 summarizes all of our metrics describing the relative levels of contamination for the different polymers.

4.5. Discussion

We now comment on the mechanism of PC removal compared over and against PMMA, PLA, PPA, and other transfer scaffolds. An atomically clean graphene surface depends on the graphene-polymer interfacial adsorption and charge transfer, as well as the polymer's molecular weight and reactivity. For aromatic polymers like PC and PANI, the presence of electron withdrawing groups (EWGs) or electron donating groups (EDGs) [69] within the polymer's repeat unit will affect the interfacial graphene-polymer adsorption and charge transfer. Despite

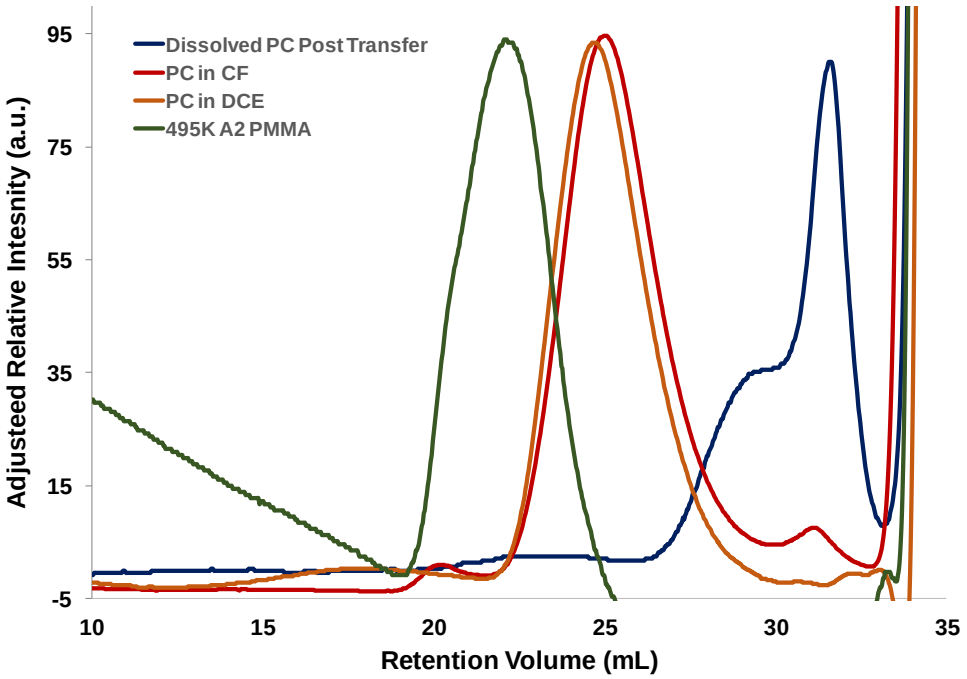

Figure 4.17. Gel permeation chromatography (GPC) of PC before and after dissolution. GPC of our commercial PMMA (495K in anisole solvent, 2% by wt.), PC in CF (1.5% by wt.), PC in DCE (3% by wt.), and the dissolved PC after graphene transfer (from a PC dispersed in DCE scaffold). From analysis of the calibrated intensity versus the retained volume, we determine that the PMMA has a molecular weight (MW) of 470 kDa (polydispersity PDI of 2.7), the PC-CF has a MW of 46 kDa (PDI = 2.1), the PC-DCE has a MW of 51 kDa (PDI = 1.8), and the PC post transfer has a possible MW of 1-2 kDa. In the dissolved PC case, the GPC shows a shoulder which likely corresponds to dissolved PC oligomers (MW of 1-2 kDa). We note that the signal-to-noise ratio here is low from the small (~μg) amount of PC mass dissolved during transfer. Thus, this shoulder could occur from instrument noise and/or impurities in the tetrahydrofuran (THF) solvent. Void volume peak is at a retention volume of 34.8 mL for all polymers.

its nature as a conductive polymer, PANI-based scaffolds show strong doping in graphene (Fig. 4.5). This occurs from the nitrogen moiety functioning as a strong EDG, donating its electron pair into the aromatic ring by resonance. Such charge transfer increases the polymer's adsorption energy on graphene at room temperature, like perylene-3,4,9,10-tetracarboxylic dianhydride (PTCDA) [70].

Conversely, the ester linkage within PC functions as a weak EDG in the repeat unit's aromatic rings via competing resonance and induction. Thus, this slight charge transfer in the aromatic rings of PC should drive adsorption by a "medium-range π–π*" electrostatic attraction with graphene, similar to benzoic acid on graphite [71]. The ordered interface allows for more

effective polymer dissolution mechanically. PPA, which has an aliphatic backbone with pendant aromatic rings, is weaker in its EDG compared to PC. Compared against PANI and PC, PPA exhibits a smaller π–π electrostatic interaction with graphene, but it can share charge by its secondary ether linkage. Lacking an aromatic core, non-conjugated, aliphatic PLA and PMMA do not interface with graphene via π–π interactions and theoretically more weakly adsorb. In turn, they should be easier to dissolve.

In addition to the graphene-polymer interfacial chemistry, the bulk polymer's molecular weight (MW) has a critical effect on its ultimate removal off graphene. To first order, high MW polymers have a larger area footprint on graphene, increasing the interaction probability with graphene features having high adsorption energy (i.e., grain boundaries) [26]. Dissolving high MW polymers off graphene requires permeation through a gelling layer and disentanglement

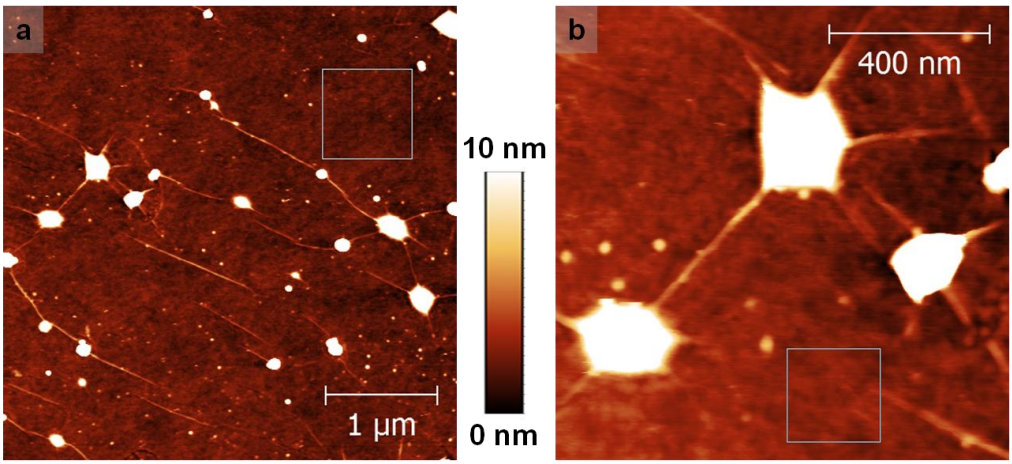

Figure 4.18. Clean graphene transfer with low molecular weight PMMA. **(a)** Large-area AFM image of graphene transferred with a 4 K molecular weight (MW) PMMA layer supported by a 495 K overlayer. RMS roughness is 0.35 nm in the box, 5.11 nm in the image. Both layers were spun at 3000 RPM for 30 s and baked out at 200 °C for 2 min. A PMMA overlayer was necessary, as unsupported 4 K PMMA scaffolds broke apart mechanically in the water rinses. Low MW polymers have a smaller footprint on the graphene. This smaller footprint circumvents possible interaction with graphene morphologies like wrinkles and grain boundaries. Consequently, this promotes effective polymer dissolution if the polymer does not electrostatically interact with the graphene, as is the case with aliphatic PMMA. **(b)** Small-area AFM image of graphene transferred with 4 K PMMA, showing again a smooth film with trapped water at the large protrusions. RMS roughness is 0.31 nm in the box, 3.77 nm in the image.

[49]. This process is inversely proportional to the MW [49], provided there are no strong adsorption sites. Our high MW PMMA (~495 K) has a large footprint (~2×10^{-8} cm^2) and, as aliphatic addition polymer, is invariant to possible depolymerization without thermal bond scission [16, 60]. Recent reports [33, 72] also discovered that PMMA exposure to $FeCl_3$, a common Cu etchant, made the PMMA harder to remove, as Fe^{+3} in acidic media potentially promotes PMMA cross-link [73]. Our PMMA's high MW and acid exposure explain its difficult removal off graphene (Table 4.3) [13, 17, 40].

Furthermore, our aliphatic PLA films, despite being lower in MW (55.4 K) and having a lower footprint (~6×10^{-10} cm^2), do not fully remove off graphene, even when heated past the gasification temperature [38]. PLA cannot readily depolymerize, likely as a result of increased graphene-polymer charge transfer from the proximity of its ester group. Both factors make PLA's removal off graphene challenging. Conversely, as a condensation polymer, PC can partially depolymerize via acid-induced hydrolysis, lowing the MW and promoting effective dissolution. This raises the question of how the acid would reach the PC films during transfer. Since PPA is an acid-sensitive polymer [69], its depolymerization during the $FeCl_3$ Cu etching step can serve as an indicator of present, permeable acid vapor. In a supporting movie (not shown), we show rapid dissolution of a PPA/graphene sample, with PC/graphene and PMMA/graphene controls left intact. Thus, there is substantial acid vapor, enough to appear to lower the MW of PC from its starting 45 K to 1-2 K (see Fig. 4.17). PC's lowered MW, combined with the quasi-ordered, "medium-range π–π*" interaction for PC-graphene, makes its removal more effective than the aliphatic polymers like PLA and PMMA.

We will note we transferred graphene with PMMA at 4 K, a low MW similar to partially depolymerized PC oligomers (see Figs. 4.17 and 4.18). Interestingly, low MW PMMA comes off

graphene cleanly, as observed by AFM (Fig. 4.18). Since PMMA does not interact with graphene via π–π interactions (i.e., no strong adsorption), the requisite condition for effective PMMA dissolution is a low enough MW to avoid entanglement and adsorption on graphene morphology. For medium to weakly interacting polymers, it appears that MW values less 10 K are required for clean transfer. However, graphene supported by lower MW scaffolds suffers mechanical failure during transfer; the scaffolds must have a high MW overlayer (e.g. 495 K PMMA). Conveniently, PC scaffolds partially depolymerize from the polymer's reactive character as a condensation polymer, obviating the need for an overlayer support, though one could be used.

4.6. Conclusions

In summary, we show atomically clean graphene transfer onto SiO_2 and mica using PC as a transfer scaffold. We remove the PC scaffold at room temperature with chloroform, and no aggressive forming gas annealing is necessary to eliminate PC-based residues. PC transfers are significantly cleaner than the typical PMMA support and alternative scaffolds using PLA, PPA, PANI, TRT, and AZ5214 photoresist. We confirm the cleanliness of our PC transfer method against the alternative polymers by a thorough number of multi-scale characterization methods. PC-transferred films enable the heterogeneous layering of CVD graphene, FG, and CVD h-BN. Compared next to PMMA-transferred films, PC-transferred films preserve atomic interfaces and allow for the homogeneous layering of trapped water. We find that effective, room temperature removal of the scaffold off graphene requires a low molecular weight polymer with "medium-range" graphene-polymer interfacial interactions. PC fulfills all of these criteria, whereas the other polymers do not. PC-transferred films will also enable nanomaterial applications that are inherently more sensitive, such as graphene on flexible substrates, graphene as a biomaterial encapsulatory membrane, or CVD h-BN on arbitrary surfaces.

4.7. Materials and Methods

4.7.1. Chemical Vapor Deposition (CVD) of Graphene on Cu

To remove an anti-oxidation surface layer and reduce spurious nucleation sites [74], we pre-cleaned our Alfa Aesar Cu foils in 10:1 H_2O:HCl for at least 3 min. We then rinsed excess HCl off the Cu and dried the foils in N_2. We mounted the foils onto a cleaned quartz boat and annealed them at 1000°C in an Atomate CVD furnace using a 1:1 Ar:H_2 flow for 30 min. We only used Cu growth tubes that underwent a minimal number of growth runs, as backflowing Cu vapor from previous growths affected the growth. We then grew graphene for 25 min at 1000 °C with 75 to 100 sccm of CH_4 and 50 sccm H_2. Samples were cooled under Ar, CH_4, and H_2, following established procedures [12, 25, 26]. These growths gave 90-95% monolayer coverage on the Cu surface with an approximate grain size of ~1 μm, as estimated by AFM, SEM, and Raman spectroscopy. Foils were stored under N_2 until used to mitigate Cu oxidation through graphene grain boundaries [75].

4.7.2. CVD of Hexagonal Boron Nitride (h-BN) on Cu

We also used 99.8% Alfa Aesar foils for the CVD of h-BN. The foils underwent the same pre-cleaning procedure. We grew h-BN by heated sublimation of ammonia borane (NH_3–BH_3, Sigma Aldrich) in a stainless steel ampoule. The Cu substrate was annealed for 2 hrs under Ar/H_2 at 1000 °C. After annealing, we grew h-BN in an Ar/H_2 background for 25 min, subliming the precursor at ~95 °C. See Chapter 7 for additional details surrounding our CVD h-BN growth conditions and setup.

4.7.3. Fluorination of Graphene

We fluorinated graphene with a Xactix silicon etcher at 1 T XeF_2 vapor pressure with a 35 torr N_2 overpressure in normal (no pulse) mode. We fluorinated for 10 cycles at 60 s / cycle,

consistent with previous work [11] and Chapter 3. These fluorination conditions are known to give highly fluorinated graphene (~C_xF, where $x < 4$).

4.7.4. Poly(Methyl Methacrylate) (PMMA) Transfer

As detailed above, we used a 495 K A2 and 950 K A4 PMMA bilayer (Anisole base solvent, 2% by wt. and 4% by wt., MicroChem) for PMMA-based transfer and overlayer support. Graphene on Cu (G/Cu) was cut to proper size and flattened by piranha cleaned glass slides. We coated each PMMA layer on G/Cu at 3000 RPM for 30 s, and then we cured each layer at 200 °C for 2 min. More subtle details regarding the etching, cleaning, and ultimate graphene substrate transfer are given in Section 4.7.5. After the PMMA/graphene film was on the substrate of choice, the PMMA was dissolved by chloroform solvation for at least 1 hr. Most polymer dissolution took place overnight, covered by a glass beaker. The samples were removed from the solvent and degreased with methanol, acetone, and IPA. Any optically obvious residues on the graphene chips were removed by further chloroform dissolution.

4.7.5. Poly(Bisphenol A Carbonate) (PC) Transfer

We purchased poly(bisphenol A carbonate) (PC) from Sigma Aldrich (#181625, molecular weight of ~45 K). We used the polymer as received. We dispersed PC in a chloroform (CF) solution at 1.5 wt. percent by volume, a more dilute weight percent than previous reports [16, 32]. We note that lower weight percents are imperative, because more concentrated PC solutions can gel during storage [76]. Amber-tinted bottles were used for solvent storage, as clear bottles lead to UV photodegradation of CF to phosgene. We also utilized dichloroethane as a solvent for PC, wherein we dissolved 3 wt. percent PC by volume in solution. DCE-based dispersions worked as well as CF-based ones, save the higher weight percent. For CF-based dispersions, very low weight percents (< 0.8 wt. percent) made the solutions less viscous, made

the transfer scaffolds thinner (< 50 nm), and caused poor graphene transfer; therefore, we avoided solutions at lower weight percents. We added PC to a piranha cleaned amber bottle with chloroform and agitated the solution until no visible PC solid remained. Occasionally, we employed an additional 30 min sonication to more fully disperse the PC. The PC with chloroform solution was sealed with paraffin wax to avoid chloroform evaporative loss and concentration modification.

The G/Cu was placed on a spin coater with no additional support, and the PC films were spun onto the G/Cu at 3000 RPM for 30 s. We also spun PC at higher rates (5000 RPM and 7000 RPM for 30 s, each), giving a thinner polymer support. However, PC dissolution in solvent was not improved for these thinner PC films, and the structural support of these films was compromised. We performed no bake out of the solvent for PC samples, which is normally 200 °C for 2 min for our PMMA-based transfers. For thicker PC scaffolds, we repeated the 3000 RPM for 30 s spin-coating process three times more (see Table 4.1).

We removed the backside graphene on the Cu by 90 W O_2 plasma operated at a throttle pressure of 100 mTorr for ~30 s. We optically assessed the topside of the film to ensure that the plasma did not degrade the polymer scaffold. We etched the Cu substrate overnight in a $FeCl_3$ etchant (Transene Co., CE-100), covered at room temperature. Occasionally, we etched the Cu with ammonium persulfate (Transene Co., APS-100), which etched more cleanly but produced bubbles on the PC/graphene film underside. These bubbles prevented further Cu etching and gave circular depressions within the transferred film (Fig. 4.3).

After overnight etching, we raised the $FeCl_3$ etchant fluid level by careful DI water dilution. The raised fluid level made PC/graphene removal from the solution easier. With piranha cleaned glass slides, we wicked the graphene out of the solution and onto the slides. We then

cleaned residual etchant off the PC/graphene films by placing them on DI water for ~15 min. After this bath, we transferred (with glass slides) the PC/graphene films into a series of modified RCA cleaning baths [19]. The modified RCA cleaning baths were made up of SC-2 and SC-1, respectively, with the SC-2 composed of 20:1:1 H_2O:H_2O_2:HCl and the SC-1 composed of 20:1:1 H_2O:H_2O_2:NH_4OH. We cleaned PC/graphene in SC-2 for ~15 min. In early experiments, we transferred the films into a SC-1 bath for ~15 min. In later experiments, we determined that the NH_4OH from the SC-1 gave adsorbed nitrogen on the underside of the graphene films. After identifying this, we eliminated the SC-1 cleaning step. We manipulated the PC/graphene films into a final DI water bath. From this bath, we transferred the films to the substrates of interest, usually piranha cleaned 90 nm SiO_2/Si. We also performed the RCA clean and an O_2 plasma descum (90 W for 15 min) on the SiO_2/Si substrates. Compared with the piranha clean, these procedures did not improve the residual doping in the graphene or assist in the transfer.

After the PC/graphene films were on the substrate, we spun off excess water from the graphene-substrate interface at 7000 RPM for 60 s. The competing capillary and centripetal forces prevented the PC/graphene films from delaminating from the substrate. We found that the spinning step was imperative for more hydrophobic substrates like H-passivated Si(100) or graphene already on SiO_2/Si. We then drove off additional water by placing the samples on a hot plate at 60 °C for ~5 min. After that heating step, we ramped the hot plate [19] to 150 °C and, when the 150 °C temperature was reached, we held the samples there for ~5 min. We dissolved the PC scaffold in chloroform overnight. We then degreased the chips with methanol, acetone, and IPA, and we dried the chips with house N_2.

We note that our samples were incidentally exposed to UV light by ambient exposure before polymer dissolution. Thus, it is possible that UV-catalyzed chloroform, in a phosgene

derivative, could proceed through transesterification with PC to produce additional phosgene and bisphenol A (BPA). While in the main text we argue for partial PC depolymerization by acid-based hydrolysis, the UV exposure during polymer liftoff could also partially depolymerize the PC. This would assist in the polymer removal, as it results in a lower molecular weight.

4.7.6. PMMA/PC Bilayer Transfer

PC layers were spun onto G/Cu first and not cured at elevated temperature. Approximately ~1 min after spinning, the PMMA bilayer was spun onto the PC/G/Cu structure. Curing and transfer then proceeded per the practice outlined above.

4.7.7. Poly(Lactic Acid) (PLA) Transfer

For the sample shown in Figs. 4.9a-c, we transferred the graphene using ~1 g of 55.4 K MW poly(lactic acid) [38] dissolved in ~25 mL of chloroform, giving a solution with a 2.7 wt. percent. For the sample in Fig. 4.9d, this solution was diluted 3:1 in chloroform. G/Cu samples were placed on a spin coater with no additional support, and the PLA films were spun onto the G/Cu at 3000 RPM for 30 s, regardless of the dilution. No sample bake out was performed, and the subsequent steps followed those detailed in Section 4.7.5.

4.7.8. Poly(Phthalaldehyde) (PPA) Transfer

We purified O-phthalaldehyde (OPA, purchased from Alfa-Aesar) according to a literature procedure [77], and we dried the sample under high vacuum for 24 hours. OPA (1.00 g, 7.5 mmol) is weighed into a Schlenck flask and dissolved in anhydrous dichloromethane (10 mL). The solution is cooled to –78 °C and boron trifluoride etherate is added (purchased from Sigma-Aldrich, 8 µL, 60 µmol). The reaction is left stirring at –78 °C for 2 hours, then acetic anhydride (purchased from Fisher, 0.25 mL, 2.6 mmol) and pyridine (purchased from Alfa-Aesar, 0.22 mL, 2.7 mmol) are added. The mixture is left stirring 2 hours at –78 °C, then the

polymer precipitated by pouring into methanol (100 mL). The product is collected by filtration, then re-precipitated from dichloromethane and washed in methanol and diethyl ether (0.84 g, 84%). ^{1}H NMR (500 MHz, DMSO-d_6) δ 7.85-7.00 ppm (br, 4H, aromatic), 7.00-6.20 ppm (br, 2H, acetal). $^{13}C\{^{1}H\}$ NMR (500 MHz, $CDCl_3$) δ 138.8 ppm, 130.2 ppm, 123.5 ppm, 105.0-101.8 ppm. We subsequently refer to this product as PPA [39, 69, 78, 79]. GPC on PPA revealed a molecular weight (MW) of 27.1 kDa (polydispersity PDI = 2.09).

We mixed 0.16 g and 0.24 g of 27.1 K PPA in ~15 mL and ~18 mL of chloroform, respectively. We refer to the 0.16 g solution as M1 and the 0.24 g solution as M2. The mixture was allowed to sit overnight, and it was sealed with wax. Three samples were made with PPA overlayers only (SA1, SB1, SC1). Samples SA1 and SB1 had M1 solution spun onto G/Cu substrates at 3000 RPM for 30 s. SA1 was etched using ammonical Cu (Transene Co., BTP) etchant, and SA1 contained undesirable intercalated contaminants from the etch. Sample SC1 had M2 solution spun onto G/Cu at 6000 RPM for 30 s. SB1 and SC1 were etched in ammonium persulfate (Transene Co., APS-100), and both samples structurally decomposed (not shown).

All other PPA samples had M1 solution spun onto G/Cu at 3000 RPM for 30 s. These samples were coated with PMMA (495 K and 950 K) following our aforementioned procedure.

4.7.9. Poly(Aniline) (PANI) Transfer

We purchased emeraldine salt poly(aniline) (PC) from Sigma Aldrich (#556386, molecular weight of ~50 K). We dissolved 0.193 g of poly(aniline) (PANI) in 10 mL of chloroform. This solution was agitated until the PANI was fully dissolved. All PANI samples were spun with this solution at 3000 RPM for 30 s with no solvent bakeout. PANI samples with a PMMA overlayer support had the PANI layer spun first, followed by a 495 K and 950 K PMMA layer. Solvent bakeout at 200 °C was performed on the PMMA layers.

4.7.10. Annealing

We performed anneals on PMMA-based CVD graphene chips in 400 sccm Ar with 400 sccm H_2 for 90 min at 400 °C. Both gases were of ultra-high purity (99.999% pure or better), minimizing graphene-based etching from gas contaminants [80]. If deemed necessary, we annealed PC-based CVD graphene chips in Ar/H_2 for 90 min at 450 °C. To examine how water leaves the CVD graphene-CVD graphene and the CVD graphene-SiO_2/Si interface (Figs. 4.11 and 4.12), we annealed PMMA- and PC-based chips in Ar only for 60 min at 200 °C. All anneals took place in an Atomate CVD furnace at atmospheric pressure with a throttled roughing pump configuration.

4.7.11. Scanning Electron Microscopy (SEM)

We used a FEI environmental SEM at 5 kV on graphene. All images were taken using a ultra high-definition mode, which increases the dwell time and the beam current. We maintained similar brightness and contrast values, so that the images in Fig. 4.8 can be adequately compared.

4.7.12. X-Ray Photoelectron Spectroscopy (XPS)

A Kratos ULTRA XPS with a monochromatic Kα-Al X-ray line was used to collect data. We fitted all sub-peaks with Shirley backgrounds and Gaussian-Lorentzian (GL) mixing. The amount of GL character was optimized (i.e., not fixed) in our fits, so as to lower the chi-squared value and be representative of the true chemical state of the sub-peak in question. All other procedures follow the details given in Chapter 3. For the C 1s photoelectron, we employed the asymmetric Doniach-Sunjic (D-S) lineshape for the sp^2 carbon sub-peak [81].

4.7.13. Raman Spectroscopy

We took most Raman spectra using a Renishaw Raman spectrometer at 633 nm excitation (~1-10 mW, ~2 μm spot) and inVia software. The acquisition time was 30 s, and the

grating was 1800 lines/mm. During mapping, a 50X objective (~0.7 NA) was used, and the pixel-to-pixel distance was much larger than the spot size (~5 μm). To correctly identify the position of the D, G, and 2D bands from the mapping data, a Lorentzian fitting procedure was used, as detailed elsewhere [12]. For the graphene point Raman spectra shown in this document, we subtracted a polynomial background from the data, thereby lowering fluorescence. We then fitted the resultant data with Lorentzians using a Levenburg-Marquardt fitting procedure in Fityk. Occasionally, a Horiba Raman spectrometer was used (specifically, the PPA data in this document). The laser line was again 633 nm, and the power was below 10 mW. The acquisition time was 30 s, using a 300 lines/mm grating and a 100X (~0.8 NA) backscattering objective.

4.7.14. Atomic Force Microscopy (AFM)

We performed atomic force microscopy (AFM) measurements in tapping mode with ~300 kHz Si cantilevers on a Bruker AFM with a Dimension IV controller. Scan rates were slower than 2 Hz, and sampling is at least 512 samples per line by 512 lines. Most images were sampled at 1024 samples per line by 1024 lines. Images without substantial noise and stable phase imaging were selected for analysis. Images were de-streaked, plane fit, and analyzed using Gwyddion. RMS roughness values were determined by Gwyddion and through an algorithm written in MATLAB. Autocorrelation values were also determined and fit in Gwyddion. The AFM images shown in this document for graphene transferred with 4 K molecular weight PMMA were taken on an Asylum Research MFP-3D AFM. On that system, tapping mode AFM was done using ~300 kHz resonant frequency Si cantilevers (NSG30 AFM tips from NT-MDT).

4.7.15. Device Transport

Graphene was transferred onto 90 nm SiO_2/Si as previously described, using PMMA and PC based scaffolds. No annealing was performed. Source/drain electrodes (Ti/Au) and graphene

channels were defined using a PMGI/PR stack and UV lithography. PMGI (MicroChem) was spun at 3500 RPM for 30 s and cured at 165 °C for 5 min. Shipley 1813 PR (MicroChem) was spun on top of the cured PMGI at 5000 RPM for 30 s. The PR was soft baked at 110 °C for 70 s, exposed to UV for 4 s on a Karl-Suss aligner (i-line) and developed for 50 s in MF-319 (MicroChem). In the case of electrodes, Ti (0.7 nm) and Au (40 nm) were e-beam evaporated followed by lift-off in hot n-methyl pyrrolidone (Remover PG, MicroChem). Channels were defined using an O_2 plasma RIE. Channel length (L) and width (W) ranged from 2 to 3 μm and 5 to 10 μm respectively. All measurements were performed in vacuum at room temperature with a Keithley 4200 Semiconductor Characterization System (SCS).

4.7.16. Scanning Tunneling Microscopy (STM)

Our experiments employed a homebuilt, room temperature ultrahigh vacuum scanning tunneling microscope (UHV-STM) with a base pressure of $\sim 3\times10^{-11}$ Torr [82] and electrochemically etched W and PtIr tips [83]. We scanned the samples in constant-current mode to get topographic data. In this procedure, the tip height was feedback-controlled, maintaining a current set point while rastering the tip across the surface. We grounded the STM tip through a current amplifier, and we applied the tunneling bias to the sample. For the mica substrate in Figs. 4.15k-l, we mounted a Si backing through which we could resistively heat the sample. Regardless, sample degasses occurred using a hot filament to heat the samples to ~54 °C (thermocouple readout) and ~130 °C.

4.7.17. Gel Permeation Chromatography (GPC)

Analytical gel permeation chromatography (GPC) analyses were performed on a system composed of a Waters 515 HPLC pump, a Thermoseparations Trace series AS100 autosampler, a series of three Waters HR Styragel columns (7.8’ 300 mm, HR3, HR4, and HR5), and a

Viscotek TDA Model 300 triple detector array, in HPLC grade THF (flow rate = 0.9 mL/min) at 25 °C. The GPC was calibrated using a series of monodisperse polystyrene standards.

4.8. Transfer with Thermal Release Tape (TRT) and AZ5214 Photoresist

TRT-based transfers were previously reported for epitaxial graphene on C-face SiC [29] and for graphene on Cu [28, 30]. In these reports, the TRT-transferred graphene films often had transfer-induced holes in them from adhesion issues with the TRT, the graphene, and the substrate. We also see holes in our TRT transfers (Fig. 4.3), corroborating the adhesion concern. Some of these holes can be mitigated by hot press transferring [30]. Regardless, we observe significant sample-to-sample variability in the TRT transfers, resulting from inhomogeneities in the Cu growth substrate and from the TRT losing adhesive strength. Moreover, the TRT introduces contamination on the topside of the graphene. Proper solvent treatment [29] can lower this doping but not eliminate it entirely. The adhesion and contamination issues make the TRT-based transfers less appealing.

AZ5214-based transfers are equally as holey as TRT transfers, and the scaffolds are more susceptible to mechanical breakage during transfer. In this transfer process, we coat and develop the AZ5214 PR onto the graphene on Cu following the procedures given in this document. Despite the PR development, we observe substantial contamination on the graphene caused by the PR (Fig. 4.4). This contamination, combined with the scaffold's poor structural integrity, make the AZ5214-based transfers intractable.

4.9. Strain and Doping Model for Raman Spectra Populations

In graphene-based Raman spectroscopy, the energy-dispersive D band originates from defects [54], grain boundaries [25, 26, 84], and edges [22, 54] within the graphene, and this band is centered about ~1335 cm^{-1} (E_L = 1.96 eV) [51, 52, 54, 85]. Doubly-degenerate, Γ point iTO

phonons give rise to the G band at 1588 cm^{-1} for intrinsic, monolayer graphene [45]. The energy-dispersive, two iTO phonon 2D band at 2645 cm^{-1} (CVD, E_L = 1.96 eV [25]) comes from a double resonance process between the *K* and *K*' valleys [51, 52, 54, 85]. Both the G and 2D bands are strongly affected by charge-transfer doping [45] and strain [53] in the graphene.

From previously published in-plane strain data on CVD graphene films [50], we determine an expression for the 2D FWHM for compressive strains ($\varepsilon < 0$): $\Gamma_{2D}(\varepsilon) = (26.1 \pm 0.3) + (-33.2 \pm 1.4)\cdot\varepsilon$. This expression accounts for the standard error in the fit. Using this expression with the data in Fig. 4.10d, we find a strain in the PMMA films of $\varepsilon = -0.19 \pm 0.07\%$. With this strain, we can estimate the graphene band shifts using proper Grüneisen parameters [50], where the G band and 2D band shifts are 41.1 cm^{-1}/% and –72.3 cm^{-1}/%, respectively. Starting from ~1588 cm^{-1} for the G band (typical of graphene on SiO_2/Si [45]) and ~2645 cm^{-1} for the 2D band (at excitation E_L = 1.96 eV), our strain-shifted band positions are ω_G = 1580.0 ± 2.8 cm^{-1} and ω_{2D} = 2659.0 ± 4.8 cm^{-1}, respectively. To arrive at the PMMA G band position at 1599.9 cm^{-1} (Fig. 4.10a), we must upshift the G band by $\Delta\omega_G = 19.9 \pm 3.0$ cm^{-1}.

We also can determine an empirical model that accounts for the strain-based increase [50] in the G band FWHM: $\Delta\Gamma_G(\varepsilon) = (-12.7 \pm 1.0)\cdot\varepsilon$. For the PMMA-based films, $\Delta\Gamma_G = 2.5 \pm 0.9$ cm^{-1}. The doping contribution appears high ($|n| > 5\times10^{12}$ cm^{-2}) in all of the samples in Fig. 4.10, prohibiting G band electron-hole pairs for $E_F > \hbar\omega_G/2$ and making the doping contribution negligible [86]. Therefore, the G band FWHM reduces to non-electronic and strain-based contributions. Ubiquitous in our Raman spectra is an inhomogeneous G band broadening of approximately ~8 cm^{-1}, as previously noted [45, 86]. Combining the broadening with the strain increase, we arrive at a G band FWHM for the PMMA-transferred graphene films of $\Gamma_G = 10.5 \pm$

0.9 cm^{-1}, close to our measured value of 9.4 ± 2.0 cm^{-1}. This bolsters our proposed descriptions thus far regarding strain and doping in the PMMA-transferred film.

To reconcile the G band's position, we assign the aforementioned 19.9 ± 3.0 cm^{-1} upshift required to doping in the PMMA-transferred graphene film. The upshift corresponds to a doping increase of $\Delta n = (1.59 \pm 0.03) \times 10^{13}$ cm^{-2} [54]. Herein, we have assigned the carrier type as n-type, for reasons that momentarily become evident. Analyzing the 2D band position allows us to assign the carrier type. Using the strain-shifted 2D band position of 2659.0 ± 4.8 cm^{-1}, we must downshift the band by 6.4 ± 5.0 cm^{-1}. The presence of a downshift implies n-type doping in the graphene [51]. Moreover, the approximate twofold doping shift increase for the G band relative to the 2D band agrees well with the discrepancy in electron-phonon coupling for iTO phonons at the Γ and K points [34]. Thus, it appears that our room temperature and 200 °C annealed graphene films on 90 nm SiO_2/Si have trapped water under them, despite being rough [25, 57]. Earlier in this chapter, we claimed that this trapped water n-type dopes the graphene from the electrostatic interaction between the Si–OH groups and the encapsulated water (Figs. 4.11 and 4.12).

We apply our model to the PMMA/PC bilayer of Figs. 4.10e-h. From the model, we ascertain a compressive strain of strain of $\varepsilon = -0.18 \pm 0.06\%$, along with doping shifts of $\Delta\omega_G$ = 18.6 ± 2.7 cm^{-1} and $\Delta\omega_{2D} = -5.0 \pm 4.6$ cm^{-1}, respectively. The G band upshift gives a doping in the graphene film of $\Delta n = (1.40 \pm 0.03) \times 10^{13}$ cm^{-2}, again n-type due to the entrapped water. Nonetheless, the lower doping concentration could result from p-type co-doping, resulting from co-mixed PMMA [87] in the PC interfacial layer. The PMMA/PC bilayer transferred graphene and the PMMA-transferred graphene of Figs. 4.10a-d differ in doping by $(1.90 \pm 0.44) \times 10^{12}$ cm^{-2}, as discussed in the main text. Indeed, when we test the difference between the two G band

datasets (i.e., Figs. 4.10a and 4.10e, respectively), we cannot conclude at that they come from different populations at 99% statistical significance. Even though the PC contacts the graphene, it is possible that the PMMA partially co-mixes [87] during the 200 °C bakeout (Section 4.7 and following).

Finally, we calculate the strain in doping present in our PC-based Raman data (Figs. 4.10i-l) using the aforementioned model. We find a strain of $\varepsilon = -0.27 \pm 0.07\%$ with doping of $\Delta n = (2.00 \pm 0.04) \times 10^{13}$ cm^{-2} occurring from G and 2D band shifts of $\Delta\omega_G = 22.3 \pm 3.4$ cm^{-1} and $\Delta\omega_{2D} = -10.0 \pm 5.3$ cm^{-1}, respectively. Water doping is again present, and the higher n-type behavior seen results from a lack of co-doping due to a cleaner graphene surface. Further comparisons between the PC, PMMA, and PMMA/PC films are made in the main text and in Tables 4.2 and 4.3.

4.10. Tables

Table 4.1. Thickness of different polymer scaffolds. All polymers are placed on 90 nm SiO_2/Si witnesses, and the thicknesses are determined by profilometry.

Polymer (on SiO_2/Si)	Thickness (nm)	Spin Conditions	Bakeout Conditions
495K PMMA, then 950K PMMA	290 ± 10 nm	3000 RPM, 30 s for 495K; 3000 RPM, 30 s for 950K	200°C for 2 min for each PMMA layer
495K PMMA, then 950K PMMA	235 ± 15 nm	3000 RPM, 30 s for 495K; 3000 RPM, 30 s for 950K	None
4K PMMA (2% wt. in anisole)	23 ± 2 nm	3000 RPM, 30 s	200°C for 2 min
4K PMMA	24 ± 2 nm	3000 RPM, 30 s	None
4K PMMA, then 495K PMMA	59 ± 4 nm	3000 RPM, 30 s	200°C for 2 min for each PMMA layer
PC dispersed in chloroform (CF)	70 ± 20 nm	3000 RPM, 30 s	None
PC dispersed in CF	80 ± 20 nm	3000 RPM, 60 s	None
PC dispersed in CF	60 ± 15 nm	5000 RPM, 30 s	None
PC dispersed in CF	60 ± 15 nm	7000 RPM, 30 s	None
PC dispersed in CF, then 495K PMMA, then 950K PMMA	240 ± 20 nm	3000 RPM, 30 s for PC; 3000 RPM, 30 s for 495K; 3000 RPM, 30 s for 950K	None for PC layer; 200°C for 2 min for each PMMA layer
PC dispersed in CF, then 495K PMMA, then 950K PMMA	295 ± 10 nm	3000 RPM, 30 s for PC; 3000 RPM, 30 s for 495K; 3000 RPM, 30 s for 950K	None
PC dispersed in dichloroethane (DCE)	40 ± 3 nm	3000 RPM, 30 s	None
4K PMMA, then PC dispersed in DCE	45 ± 5 nm	3000 RPM, 30 s	None
0.24 g PPA dispersed in 18 mL CF	60 ± 5 nm	3000 RPM, 30 s	None
0.24 g PPA solution	< 10 nm – not reliable	3000 RPM, 30 s	200°C for 2 min
0.16 g PPA dispersed in 15 mL CF, then 495K PMMA, then 950K PMMA	230 ± 10 nm	3000 RPM, 30 s for PPA; 3000 RPM, 30 s for 495K; 3000 RPM, 30 s for 950K	None
0.16 g PPA solution, then 495K PMMA, then 950K PMMA	280 ± 10 nm	3000 RPM, 30 s for PPA; 3000 RPM, 30 s for 495K; 3000 RPM, 30 s for 950K	None for PPA layer; 200°C for 2 min for each PMMA layer
60K phenyl methacrylate in CF	< 20 nm *ca.* 10 ± 5 nm	3000 RPM, 30 s	200°C for 2 min
60K phenyl methacrylate in CF	< 20 nm *ca.* 10 ± 5 nm	3000 RPM, 30 s	None
Poly(aniline) (PANI) in CF	< 10 nm – not reliable	3000 RPM, 30 s	200°C for 2 min
PANI in CF, then 495K PMMA	36 ± 6 nm	3000 RPM, 30 s	200°C for 2 min for each layer

Table 4.2. Graphene Raman mapping statistics for different transfer scaffolds.

Polymer	ω_D (cm^{-1})	Γ_D (cm^{-1})	ω_G (cm^{-1})	Γ_G (cm^{-1})	ω_{2D} (cm^{-1})	Γ_{2D} (cm^{-1})	I(2D)/ I(G)	I(D)/ I(G)
PMMA	1333.2±13.1	15.6±21.4	1599.9±2.5	9.1±3.3	2652.3±3.3	29.6±6.4	1.29±0.39	0.12±0.11
PMMA/PC	1333.2±5.3	23.4±17.0	1600.3±1.9	13.0±2.8	2657.9±3.3	32.5±2.5	1.96±0.32	0.07±0.03
PC	1329.1±4.9	16.6±14.6	1599.3±3.5	10.6±2.3	2653.9±4.2	31.9±1.8	1.60±0.18	0.11±0.04
PLA	1327.6±8.5	15.0±1.9	1592.5±3.2	18.1±2.1	2633.2±7.7	46.2±2.3	2.06±0.20	0.08±0.06
PMMA/PANI	1333.3±2.1	17.3±2.9	1603.6±1.7	18.6±4.7	2660.3±1.9	29.9±1.6	1.09±0.11	0.17±0.08

Table 4.3. Overall polymer cleanliness metrics.

Polymer	RMS Roughness (nm)	Defect Separation L_D (nm)	Autocorrelation at 1 μm^2 (nm)	XPS Residue Percentage (relative to sp^2 carbon)	Estimated Raman Doping Compared to PC (10^{12} cm^{-2})	Minimum Electrical Carrier Concentration n_0 (10^{12} cm^{-2})
PMMA	1.41±0.53	19.8±5.7	17.5±2.1	11.2%	4.10 ± 0.52	0.57 ± 0.08
PMMA/PC	0.66±0.15	26.2±5.6	18.0±8.2	–	6.00 ± 0.50	–
PC	0.57±0.15	20.8±3.1	19.3±7.4	2.1%	0	0.48 ± 0.04
PLA (200°C anneal)	0.96±0.09	24.4±6.1	29.5±4.8	28.4%	3.20 ± 0.70	–
PLA (no anneal)	1.05±0.17	–	14.6±0.7	–	–	–
PMMA/PPA	1.32±0.40	41.0 (point)	19.9±4.6	–	2.33 (point)	–
PMMA/PANI	–	16.6±3.1	–	–	3.33 ± 0.57	–

4.11. References

[1] A. A. Balandin, S. Ghosh, W. Bao, I. Calizo, D. Teweldebrhan, F. Miao, and C. N. Lau, "Superior thermal conductivity of single-layer graphene," *Nano Letters,* vol. 8, no. 3, pp. 902-907, 2008.

[2] E. Pop, V. Varshney, and A. K. Roy, "Thermal properties of graphene: Fundamentals and applications," *MRS Bulletin,* vol. 37, no. 12, pp. 1273-1281, 2012.

[3] K. I. Bolotin, K. J. Sikes, Z. Jiang, M. Klima, G. Fudenberg, J. Hone, P. Kim, and H. L. Stormer, "Ultrahigh electron mobility in suspended graphene," *Solid State Communications,* vol. 146, no. 9-10, pp. 351-355, 2008.

[4] A. H. Castro Neto, F. Guinea, N. M. R. Peres, K. S. Novoselov, and A. K. Geim, "The electronic properties of graphene," *Reviews of Modern Physics,* vol. 81, no. 1, pp. 109-162, 2009.

[5] V. E. Dorgan, M. H. Bae, and E. Pop, "Mobility and saturation velocity in graphene on SiO_2," *Applied Physics Letters,* vol. 97, no. 8, pp. 082112-082112-3, 2010.

[6] K. S. Novoselov, A. K. Geim, S. V. Morozov, D. Jiang, M. I. Katsnelson, I. V. Grigorieva, S. V. Dubonos, and A. A. Firsov, "Two-dimensional gas of massless Dirac fermions in graphene," *Nature,* vol. 438, no. 7065, pp. 197-200, 2005.

[7] K. S. Kim, Y. Zhao, H. Jang, S. Y. Lee, J. M. Kim, K. S. Kim, J.-H. Ahn, P. Kim, J.-Y. Choi, and B. H. Hong, "Large-scale pattern growth of graphene films for stretchable transparent electrodes," *Nature,* vol. 457, no. 7230, pp. 706-710, 2009.

[8] S. Chen, W. Cai, R. D. Piner, J. W. Suk, Y. Wu, Y. Ren, J. Kang, and R. S. Ruoff, "Synthesis and characterization of large-area graphene and graphite films on commercial Cu-Ni alloy foils," *Nano Letters,* vol. 11, no. 9, pp. 3519-3525, 2011.

[9] X. Li, W. Cai, J. An, S. Kim, J. Nah, D. Yang, R. Piner, A. Velamakanni, I. Jung, E. Tutuc, S. K. Banerjee, L. Colombo, and R. S. Ruoff, "Large-area synthesis of high-quality and uniform graphene films on copper foils," *Science,* vol. 324, no. 5932, pp. 1312-1314, 2009.

[10] X. Li, C. W. Magnuson, A. Venugopal, R. M. Tromp, J. B. Hannon, E. M. Vogel, L. Colombo, and R. S. Ruoff, "Large-area graphene single crystals grown by low-pressure chemical vapor deposition of methane on copper," *Journal of the American Chemical Society,* vol. 133, no. 9, pp. 2816-2819, 2011.

[11] J. T. Robinson, S. W. Schmucker, C. B. Diaconescu, J. P. Long, J. C. Culbertson, T. Ohta, A. L. Friedman, and T. E. Beechem, "Electronic hybridization of large-area stacked graphene films," *ACS Nano,* vol. 7, no. 1, pp. 637-644, 2013.

[12] J. D. Wood, S. W. Schmucker, A. S. Lyons, E. Pop, and J. W. Lyding, "Effects of polycrystalline Cu substrate on graphene growth by chemical vapor deposition," *Nano Letters,* vol. 11, no. 11, pp. 4547-4554, 2011.

[13] J. Chan, A. Venugopal, A. Pirkle, S. McDonnell, D. Hinojos, C. W. Magnuson, R. S. Ruoff, L. Colombo, R. M. Wallace, and E. M. Vogel, "Reducing extrinsic performance-limiting factors in graphene grown by chemical vapor deposition," *ACS Nano,* vol. 6, no. 4, pp. 3224-3229, 2012.

[14] L. Gao, W. Ren, H. Xu, L. Jin, Z. Wang, T. Ma, L.-P. Ma, Z. Zhang, Q. Fu, L.-M. Peng, X. Bao, and H.-M. Cheng, "Repeated growth and bubbling transfer of graphene with millimetre-size single-crystal grains using platinum," *Nature Communications,* vol. 3, no. 699, pp. 1-7, 2012.

[15] X. Li, Y. Zhu, W. Cai, M. Borysiak, B. Han, D. Chen, R. D. Piner, L. Colombo, and R. S. Ruoff, "Transfer of large-area graphene films for high-performance transparent conductive electrodes," *Nano Letters,* vol. 9, no. 12, pp. 4359-4363, 2009.

[16] Y. C. Lin, C. C. Lu, C. H. Yeh, C. H. Jin, K. Suenaga, and P. W. Chiu, "Graphene annealing: How clean can it be?," *Nano Letters,* vol. 12, no. 1, pp. 414-419, 2012.

[17] A. Pirkle, J. Chan, A. Venugopal, D. Hinojos, C. W. Magnuson, S. McDonnell, L. Colombo, E. M. Vogel, R. S. Ruoff, and R. M. Wallace, "The effect of chemical residues on the physical and electrical properties of chemical vapor deposited graphene transferred to SiO_2," *Applied Physics Letters*, vol. 99, no. 12, pp. 122108-122108-3, 2011.

[18] A. Reina, H. Son, L. Jiao, B. Fan, M. S. Dresselhaus, Z. Liu, and J. Kong, "Transferring and identification of single- and few-layer graphene on arbitrary substrates," *The Journal of Physical Chemistry C*, vol. 112, no. 46, pp. 17741-17744, 2008.

[19] X. Liang, B. A. Sperling, I. Calizo, G. Cheng, C. A. Hacker, Q. Zhang, Y. Obeng, K. Yan, H. Peng, Q. Li, X. Zhu, H. Yuan, A. R. Hight Walker, Z. Liu, L. Peng, and C. A. Richter, "Toward clean and crackless transfer of graphene," *ACS Nano*, vol. 5, no. 11, pp. 9144-9153, 2012.

[20] J. W. Suk, A. Kitt, C. W. Magnuson, Y. Hao, S. Ahmed, J. An, A. K. Swan, B. B. Goldberg, and R. S. Ruoff, "Transfer of CVD-grown monolayer graphene onto arbitrary substrates," *ACS Nano*, vol. 5, no. 9, pp. 6916-6924, 2011.

[21] M. Ishigami, J. H. Chen, W. G. Cullen, M. S. Fuhrer, and E. D. Williams, "Atomic structure of graphene on SiO_2," *Nano Letters*, vol. 7, no. 6, pp. 1643-1648, 2007.

[22] A. Salehi-Khojin, D. Estrada, K. Y. Lin, M. H. Bae, F. Xiong, E. Pop, and R. I. Masel, "Polycrystalline graphene ribbons as chemiresistors," *Advanced Materials*, vol. 24, no. 1, pp. 53-57, 2012.

[23] P. Y. Huang, C. S. Ruiz-Vargas, A. M. van der Zande, W. S. Whitney, M. P. Levendorf, J. W. Kevek, S. Garg, J. S. Alden, C. J. Hustedt, Y. Zhu, J. Park, P. L. McEuen, and D. A. Muller, "Grains and grain boundaries in single-layer graphene atomic patchwork quilts," *Nature*, vol. 469, no. 7330, pp. 389-392, 2010.

[24] W. Regan, N. Alem, B. Aleman, B. Geng, C. Girit, L. Maserati, F. Wang, M. Crommie, and A. Zettl, "A direct transfer of layer-area graphene," *Applied Physics Letters*, vol. 96, no. 11, pp. 113102-113102-3, 2010.

[25] K. T. He, J. D. Wood, G. P. Doidge, E. Pop, and J. W. Lyding, "Scanning tunneling microscopy study and nanomanipulation of graphene-coated water on mica," *Nano Letters*, vol. 12, no. 6, pp. 2665-2672, 2012.

[26] J. C. Koepke, J. D. Wood, D. Estrada, Z.-Y. Ong, K. T. He, E. Pop, and J. W. Lyding, "Atomic-scale evidence for potential barriers and strong carrier scattering at graphene grain boundaries: A scanning tunneling microscopy study," *ACS Nano*, vol. 7, no. 1, pp. 75-86, 2013.

[27] M. G. Lemaitre, E. P. Donoghue, M. A. McCarthy, B. Liu, S. Tongay, B. Gila, P. Kumar, R. K. Singh, B. R. Appleton, and A. G. Rinzler, "Improved transfer of graphene for gated

Schottky-junction, vertical, organic, field-effect transistors," *ACS Nano,* vol. 6, no. 10, pp. 9095-9102, 2012.

[28] S. Bae, H. Kim, Y. Lee, X. Xu, J.-S. Park, Y. Zheng, J. Balakrishnan, T. Lei, H. Ri Kim, Y. I. Song, Y.-J. Kim, K. S. Kim, B. Ozyilmaz, J.-H. Ahn, B. H. Hong, and S. Iijima, "Roll-to-roll production of 30-inch graphene films for transparent electrodes," *Nature Nanotechnology,* vol. 5, no. 8, pp. 574-578, 2010.

[29] J. D. Caldwell, T. J. Anderson, J. C. Culbertson, G. G. Jernigan, K. D. Hobart, F. J. Kub, M. J. Tadjer, J. L. Tedesco, J. K. Hite, M. A. Mastro, R. L. Myers-Ward, C. R. Eddy, P. M. Campbell, and D. K. Gaskill, "Technique for the dry transfer of epitaxial graphene onto arbitrary substrates," *ACS Nano,* vol. 4, no. 2, pp. 1108-1114, 2010.

[30] J. Kang, S. Hwang, J. H. Kim, M. H. Kim, J. Ryu, S. J. Seo, B. H. Hong, M. K. Kim, and J.-B. Choi, "Efficient transfer of large-area graphene films onto rigid substrates by hot pressing," *ACS Nano,* vol. 6, no. 6, pp. 5360-5365, 2012.

[31] Y.-C. Lin, C. Jin, J.-C. Lee, S.-F. Jen, K. Suenaga, and P.-W. Chiu, "Clean transfer of graphene for isolation and suspension," *ACS Nano,* vol. 5, no. 3, pp. 2362-2368, 2011.

[32] H. J. Park, J. Meyer, S. Roth, and V. Skákalová, "Growth and properties of few-layer graphene prepared by chemical vapor deposition," *Carbon,* vol. 48, no. 4, pp. 1088-1094, 2010.

[33] J. Song, F.-Y. Kam, R.-Q. Png, W.-L. Seah, J.-M. Zhuo, G.-K. Lim, P. K. H. Ho, and L.-L. Chua, "A general method for transferring graphene onto soft surfaces," *Nature Nanotechnology,* vol. 8, no. 5, pp. 356-362, 2013.

[34] M. Kalbac, H. Farhat, J. Kong, P. Janda, L. Kavan, and M. S. Dresselhaus, "Raman spectroscopy and in situ Raman spectroelectrochemistry of bilayer $^{12}C/^{13}C$ graphene," *Nano Letters,* vol. 11, no. 5, pp. 1957-1963, 2011.

[35] D. W. McCamant, P. Kukura, and R. A. Mathies, "Femtosecond broadband stimulated Raman: A new approach for high-performance vibrational spectroscopy," *Applied Spectroscopy,* vol. 57, no. 11, pp. 1317-1323, 2003.

[36] P. K. Narayanaswamy, "The Raman spectra of cyclohexane, glycol and glycerine," *Proceedings of the Indian Academy of Sciences - Section A,* vol. 27, no. 4, pp. 336-341, 1948.

[37] H. Torii and M. Tasumi, "Local order and transition dipole coupling in liquid methanol and acetone as the origin of the Raman noncoincidence effect," *The Journal of Chemical Physics,* vol. 99, no. 11, pp. 8459-8465, 1993.

[38] A. P. Esser-Kahn, P. R. Thakre, H. Dong, J. F. Patrick, V. K. Vlasko-Vlasov, N. R. Sottos, J. S. Moore, and S. R. White, "Three-dimensional microvascular fiber-reinforced composites," *Advanced Materials,* vol. 23, no. 32, pp. 3654-3658, 2011.

[39] C. G. Willson, R. R. Dammel, and A. Reiser, "Photoresist materials: A historical perspective," *Proceedings of the SPIE,* vol. 3048, no. pp. 28-41, 1997.

[40] Y. C. Lin, C. H. Jin, J. C. Lee, S. F. Jen, K. Suenaga, and P. W. Chiu, "Clean transfer of graphene for isolation and suspension," *ACS Nano,* vol. 5, no. 3, pp. 2362-2368, 2011.

[41] V. Carozo, C. M. Almeida, E. H. M. Ferreira, L. G. Cançado, C. A. Achete, and A. Jorio, "Raman signature of graphene superlattices," *Nano Letters,* vol. 11, no. 11, pp. 4527-4534, 2011.

[42] M. Ohira, T. Sakai, M. Takeuchi, Y. Kobayashi, and M. Tsuji, "Raman and infrared spectra of polyaniline," *Synthetic Metals,* vol. 18, no. 1-3, pp. 347-352, 1987.

[43] Y. Ahn, H. Kim, Y.-H. Kim, Y. Yi, and S.-I. Kim, "Procedure of removing polymer residues and its influences on electronic and structural characteristics of graphene," *Applied Physics Letters,* vol. 102, no. 9, pp. 091602-091602-5, 2013.

[44] D. J. Pawson, A. P. Ameen, R. D. Short, P. Denison, and F. R. Jones, "An investigation of the surface chemistry of poly(ether etherketone). I. The effect of oxygen plasma treatment on surface structure," *Surface and Interface Analysis,* vol. 18, no. 1, pp. 13-22, 1992.

[45] S. Berciaud, S. Ryu, L. E. Brus, and T. F. Heinz, "Probing the intrinsic properties of exfoliated graphene: Raman spectroscopy of free-standing monolayers," *Nano Letters,* vol. 9, no. 1, pp. 346-352, 2008.

[46] H. I. Rasool, E. B. Song, M. J. Allen, J. K. Wassei, R. B. Kaner, K. L. Wang, B. H. Weiller, and J. K. Gimzewski, "Continuity of graphene on polycrystalline copper," *Nano Letters,* vol. 11, no. 1, pp. 251-256, 2011.

[47] J. M. Wofford, S. Nie, K. F. McCarty, N. C. Bartelt, and O. D. Dubon, "Graphene islands on Cu foils: The interplay between shape, orientation, and defects," *Nano Letters,* vol. 10, no. 12, pp. 4890-4896, 2010.

[48] M. S. Bresnehan, M. J. Hollander, M. Wetherington, M. LaBella, K. A. Trumbull, R. Cavalero, D. W. Snyder, and J. A. Robinson, "Integration of hexagonal boron nitride with quasi-freestanding epitaxial graphene: Toward wafer-scale, high-performance devices," *ACS Nano,* vol. 6, no. 6, pp. 5234-5241, 2012.

[49] J. Manjkow, J. S. Papanu, D. W. Hess, D. S. Soane, and A. T. Bell, "Influence of processing and molecular parameters on the dissolution rate of poly(methyl methacrylate) thin films," *Journal of The Electrochemical Society,* vol. 134, no. 8, pp. 2003-2007, 1987.

[50] M. A. Bissett, W. Izumida, R. Saito, and H. Ago, "Effect of domain boundaries on the Raman spectra of mechanically strained graphene," *ACS Nano,* vol. 6, no. 11, pp. 10229-10238, 2012.

[51] A. Das, S. Pisana, B. Chakraborty, S. Piscanec, S. K. Saha, U. V. Waghmare, K. S. Novoselov, H. R. Krishnamurthy, A. K. Geim, A. C. Ferrari, and A. K. Sood, "Monitoring dopants by Raman scattering in an electrochemically top-gated graphene transistor," *Nature Nanotechnology,* vol. 3, no. 4, pp. 210-215, 2008.

[52] A. C. Ferrari and D. M. Basko, "Raman spectroscopy as a versatile tool for studying the properties of graphene," *Nature Nanotechnology,* vol. 8, no. 4, pp. 235-246, 2013.

[53] M. Huang, H. Yan, C. Chen, D. Song, T. F. Heinz, and J. Hone, "Phonon softening and crystallographic orientation of strained graphene studied by Raman spectroscopy," *Proceedings of the National Academy of Sciences,* vol. 106, no. 18, pp. 7304-7308, 2009.

[54] L. M. Malard, M. A. Pimenta, G. Dresselhaus, and M. S. Dresselhaus, "Raman spectroscopy in graphene," *Physics Reports,* vol. 473, no. 5-6, pp. 51-87, 2009.

[55] W. Kim, A. Javey, O. Vermesh, Q. Wang, Y. Li, and H. Dai, "Hysteresis caused by water molecules in carbon nanotube field-effect transistors," *Nano Letters,* vol. 3, no. 2, pp. 193-198, 2003.

[56] R. H. Miwa, T. M. Schmidt, W. L. Scopel, and A. Fazzio, "Doping of graphene adsorbed on the a-SiO_2 surface," *Applied Physics Letters,* vol. 99, no. 16, pp. 163108-163108-3, 2011.

[57] C. H. Y. Xuan Lim, A. Sorkin, Q. Bao, A. Li, K. Zhang, M. Nesladek, and K. P. Loh, "A hydrothermal anvil made of graphene nanobubbles on diamond," *Nature Communications,* vol. 4, no. 1, pp. 1556-1573, 2013.

[58] M. K. Awad, "Effect of alkyl substituents on the thermal degradation of poly(alkyl methacrylate): A molecular orbital study using the ASED-MO method," *Polymer Degradation and Stability,* vol. 49, no. 3, pp. 339-346, 1995.

[59] A. Hartstein and D. R. Young, "Identification of electron traps in thermal silicon dioxide films," *Applied Physics Letters,* vol. 38, no. 8, pp. 631-633, 1981.

[60] G. Madras, J. M. Smith, and B. J. McCoy, "Degradation of poly(methyl methacrylate) in solution," *Industrial & Engineering Chemistry Research,* vol. 35, no. 6, pp. 1795-1800, 1996.

[61] Z. Cheng, Q. Zhou, C. Wang, Q. Li, C. Wang, and Y. Fang, "Toward intrinsic graphene surfaces: A systematic study on thermal annealing and wet-chemical treatment of SiO_2-supported graphene devices," *Nano Letters,* vol. 11, no. 2, pp. 767-771, 2011.

[62] J. H. Chen, C. Jang, S. Adam, M. S. Fuhrer, E. D. Williams, and M. Ishigami, "Charged-impurity scattering in graphene," *Nature Physics,* vol. 4, no. 5, pp. 377-381, 2008.

[63] C. R. Dean, A. F. Young, I. Meric, C. Lee, L. Wang, S. Sorgenfrei, K. Watanabe, T. Taniguchi, P. Kim, K. L. Shepard, and J. Hone, "Boron nitride substrates for high-quality graphene electronics," *Nature Nanotechnology,* vol. 5, no. 10, pp. 722-726, 2010.

[64] M.-H. Bae, S. Islam, V. E. Dorgan, and E. Pop, "Scaling of high-field transport and localized heating in graphene transistors," *ACS Nano,* vol. 5, no. 10, pp. 7936-7944, 2011.

[65] H. H. Kim, J. W. Yang, S. B. Jo, B. Kang, S. K. Lee, H. Bong, G. Lee, K. S. Kim, and K. Cho, "Substrate-induced solvent intercalation for stable graphene doping," *ACS Nano,* vol. 7, no. 2, pp. 1155-1162, 2013.

[66] N. Severin, P. Lange, I. M. Sokolov, and J. P. Rabe, "Reversible dewetting of a molecularly thin fluid water film in a soft graphene mica slit pore," *Nano Letters,* vol. 12, no. 2, pp. 774-779, 2012.

[67] J. Rafiee, X. Mi, H. Gullapalli, A. V. Thomas, F. Yavari, Y. Shi, P. M. Ajayan, and N. A. Koratkar, "Wetting transparency of graphene," *Nature Materials,* vol. 11, no. pp. 217-222, 2012.

[68] P. Sutter, J. Lahiri, P. Albrecht, and E. Sutter, "Chemical vapor deposition and etching of high-quality monolayer hexagonal boron nitride films," *ACS Nano,* vol. 5, no. 9, pp. 7303-7309, 2011.

[69] J. A. Kaitz and J. S. Moore, "Functional phthalaldehyde polymers by copolymerization with substituted benzaldehydes," *Macromolecules,* vol. 46, no. 3, pp. 608-612, 2013.

[70] Q. H. Wang and M. C. Hersam, "Room-temperature molecular-resolution characterization of self-assembled organic monolayers on epitaxial graphene," *Nature Chemistry,* vol. 1, no. 3, pp. 206-211, 2009.

[71] A. Rochefort and J. D. Wuest, "Interaction of substituted aromatic compounds with graphene," *Langmuir,* vol. 25, no. 1, pp. 210-215, 2008.

[72] G.-H. Lee, R. C. Cooper, S. J. An, S. Lee, A. van der Zande, N. Petrone, A. G. Hammerberg, C. Lee, B. Crawford, W. Oliver, J. W. Kysar, and J. Hone, "High-strength chemical-vapor-deposited graphene and grain boundaries," *Science,* vol. 340, no. 6136, pp. 1073-1076, 2013.

[73] N. Holten-Andersen, M. J. Harrington, H. Birkedal, B. P. Lee, P. B. Messersmith, K. Y. C. Lee, and J. H. Waite, "pH-induced metal-ligand cross-links inspired by mussel yield self-healing polymer networks with near-covalent elastic moduli," *Proceedings of the National Academy of Sciences,* vol. 108, no. 7, pp. 2651-2655, 2011.

[74] G. H. Han, F. Güneş, J. J. Bae, E. S. Kim, S. J. Chae, H.-J. Shin, J.-Y. Choi, D. Pribat, and Y. H. Lee, "Influence of copper morphology in forming nucleation seeds for graphene growth," *Nano Letters,* vol. 11, no. 10, pp. 4144-4148, 2011.

[75] D. L. Duong, G. H. Han, S. M. Lee, F. Gunes, E. S. Kim, S. T. Kim, H. Kim, Q. H. Ta, K. P. So, S. J. Yoon, S. J. Chae, Y. W. Jo, M. H. Park, S. H. Chae, S. C. Lim, J. Y. Choi, and Y. H. Lee, "Probing graphene grain boundaries with optical microscopy," *Nature,* vol. 490, no. 7419, pp. 235-239, 2012.

[76] H. Schnell, *Chemistry and Physics of Polycarbonates,* New York, NY: Interscience Publishers, 1964, p. 190.

[77] A. M. DiLauro, J. S. Robbins, and S. T. Phillips, "Reproducible and scalable synthesis of end-cap-functionalized depolymerizable poly(phthalaldehydes)," *Macromolecules,* vol. 46, no. 8, pp. 2963-2968, 2013.

[78] C. Aso, S. Tagami, and T. Kunitake, "Polymerization of aromatic aldehydes. II. Cationic cyclopolymerization of phthalaldehyde," *Journal of Polymer Science Part A-1: Polymer Chemistry,* vol. 7, no. 2, pp. 497-511, 1969.

[79] C. Aso and S. Tagami, "Polymerization of aromatic aldehydes. III. The cyclopolymerization of phthaldehyde and the structure of the polymer," *Macromolecules,* vol. 2, no. 4, pp. 414-419, 1969.

[80] S. Choubak, M. Biron, P. L. Levesque, R. Martel, and P. Desjardins, "No graphene etching in purified hydrogen," *The Journal of Physical Chemistry Letters,* vol. 4, no. 7, pp. 1100-1103, 2013.

[81] S. Unarunotai, Y. Murata, C. E. Chialvo, H.-S. Kim, S. MacLaren, N. Mason, I. Petrov, and J. A. Rogers, "Transfer of graphene layers grown on SiC wafers to other substrates and their integration into field effect transistors," *Applied Physics Letters,* vol. 95, no. 20, pp. 202101-202101-3, 2009.

[82] J. W. Lyding, S. Skala, J. S. Hubacek, R. Brockenbrough, and G. Gammie, "Variable-temperature scanning tunneling microscope," *Review of Scientific Instruments,* vol. 59, no. 9, pp. 1897-1902, 1988.

[83] S. W. Schmucker, N. Kumar, J. R. Abelson, S. R. Daly, G. S. Girolami, M. R. Bischof, D. L. Jaeger, R. F. Reidy, B. P. Gorman, J. Alexander, J. B. Ballard, J. N. Randall, and J. W. Lyding, "Field-directed sputter sharpening for tailored probe materials and atomic-scale lithography," *Nature Communications,* vol. 3, no. 935, pp. 1-8, 2012.

[84] W. Zhang, P. Wu, Z. Li, and J. Yang, "First-principles thermodynamics of graphene growth on Cu surfaces," *The Journal of Physical Chemistry C,* vol. 115, no. 36, pp. 17782-17787, 2011.

[85] A. C. Ferrari, J. C. Meyer, V. Scardaci, C. Casiraghi, M. Lazzeri, F. Mauri, S. Piscanec, D. Jiang, K. S. Novoselov, S. Roth, and A. K. Geim, "Raman spectrum of graphene and graphene layers," *Physical Review Letters,* vol. 97, no. 18, pp. 187401-187401-4, 2006.

[86] S. Pisana, M. Lazzeri, C. Casiraghi, K. S. Novoselov, A. K. Geim, A. C. Ferrari, and F. Mauri, "Breakdown of the adiabatic Born-Oppenheimer approximation in graphene," *Nature Materials,* vol. 6, no. 3, pp. 198-201, 2007.

[87] M. Nishimoto, H. Keskkula, and D. R. Paul, "Role of slow phase separation in assessing the equilibrium phase behaviour of PC-PMMA blends," *Polymer,* vol. 32, no. 2, pp. 272-278, 1991.

CHAPTER 5. GRAPHENE-BASED WATER ENTRAPMENT ON MICA AND OTHER SUBSTRATES

5.1. Introduction to Water Entrapment

The interface between water and different surfaces [1-3] at room temperature has been of great interest to scientists due to its relevance in geology [4], biology [5], and most recently, electronics [6, 7]. It has been demonstrated that water behaves very differently at an interface than it does in the bulk state, forming semi-ordered "hydration layers" close to the solid surface [8-11]. However, the properties of these hydration layers are not well understood and remain controversial [12]. Recent studies using AFM and other methods have made progress toward putting some of these controversies to rest [7, 12-15], but atomic-resolution imaging of the interface had not yet been achieved.

Graphene [7, 16-20] has already been extensively characterized by surface imaging techniques on a variety of substrates [21-26], but only recently has it started to see use as a template for studying other molecules [15, 27, 28]. Graphene is ideal for coating and trapping volatile molecules for both scanning probe microscopy [15, 27, 29] and electron microscopy [28] studies in that it is conductive, chemically inert, impermeable [30], and atomically conforms to most substrates [31]. In this letter, we build upon the work performed by Xu et al. [15] and use the atomic resolution and cleanliness of the ultrahigh vacuum scanning tunneling microscope (UHV-STM) to characterize water confined between monolayer graphene and the mica surface at room temperature. Unlike previous studies of graphene on mica [7, 14, 15, 27, 31, 32], we use graphene grown on copper via chemical vapor deposition (CVD) [33-35] rather than graphene mechanically exfoliated from graphite [20]. While CVD graphene is inferior to exfoliated

[*]Material presented in this chapter is modified and reproduced with permission from K. T. He, J. D. Wood, G. P. Doidge, E. Pop, and J. W. Lyding, "Scanning tunneling microscopy study and nanomanipulation of graphene-coated water on mica," *Nano Letters* 12, no. 6, pp. 2665-2672, 2012. Copyright American Chemical Society, 2012.

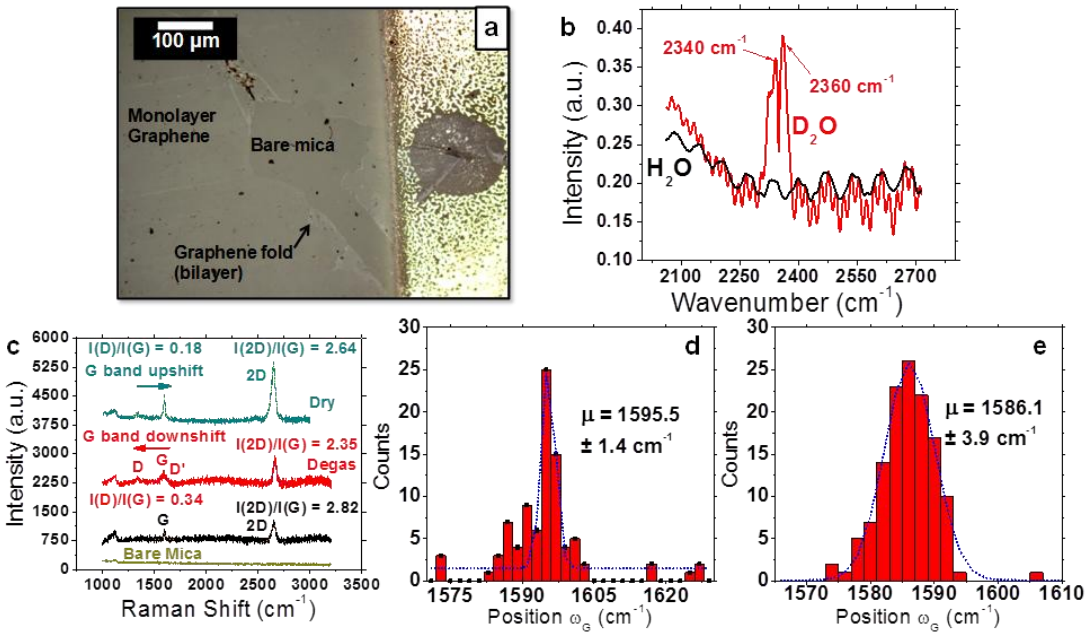

Figure 5.1. Optical characterization and spectroscopy of graphene-coated water on mica. **(a)** Optical image of the contacted sample used in STM experiments, showing monolayer graphene, folds in the CVD film, and the bare mica through a tear in the graphene. **(b)** Fourier transform infrared (FTIR) spectra of graphene transferred to mica in final baths composed of H_2O and D_2O showing a doubly-peaked signal for trapped D_2O under graphene. This is contrasts with the trapped H_2O signal, which is simply noise. Both peaks correspond to stretch modes for the O-D bond, confirming the heavy water trapped by graphene. **(c)** Point Raman spectra (λ_{exc} = 633 nm) of dry transferred monolayer graphene (intensity ratio $I_{2D}/I_G > 2$ from peak fitting) on mica and H_2O-transferred graphene before (black) and after (red) a high temperature degas. The dry transferred graphene's G band position is upshifted to ~1595 cm^{-1}, whereas the degas introduces some defects and downshifts the G band to ~1586 cm^{-1} for trapped few-layer water. Histogram of G band position from Raman mapping before **(d)** and after **(e)** the ~ 650 °C degas. After the degas, the G band's mean position is close to what is expected for graphene-coated, few-layer water on mica.

graphene in terms of carrier mobility, this drawback is offset by the ability to manufacture large, monolayer sheets and transfer them onto arbitrary substrates [33, 34].

5.2. Trapped Water Evidence

Our CVD process uses a methane-to-hydrogen partial pressure ratio of 2:1, as lower ratios give higher monolayer coverage [36, 37]. Previous work [35], Chapter 2, Chapter 4, and Section 5.7.1 give more details on our growth procedure. We transfer graphene to mica with poly(methyl methacrylate) (PMMA) and use successive deionized (DI) water baths to clean the graphene films from etchant contamination. The final transfer occurs on a freshly cleaved mica surface within a DI bath in contrast to previous graphene-water-mica studies [15, 27, 29]. In this

total water immersion, we expect there to be a high amount of water initially trapped under the graphene film. We subject the samples to 60 °C heating for 5 min in air to bring the PMMA-graphene system into intimate contact with the mica, driving out most of the excess water and achieving strong graphene adhesion [38]. Wet transfers had larger area coverage than dry transfers, thereby allowing STM experiments to be conducted. Thus, the water plays a critical role in bringing the graphene and mica into contact, similar to CNT film transfer [39]. After we transfer graphene onto water-coated mica, we confirm its presence by optical imaging and spectroscopy. After loading into UHV, we degas the samples at ~650-700 °C for several hours to remove surface adsorbates and contaminants.

Figure 5.1a gives an optical image of the STM sample with a tear in the monolayer film. Monolayer graphene on transparent mica gives ~2.3% white light absorbance per layer [40], assisting in identifying graphene coverage. To determine whether we have trapped water under the graphene, we show high wavenumber Fourier transform infrared (FTIR) spectra on samples transferred in a final bath of H_2O and D_2O (99.9% purity) in Fig. 5.1b. We subtract a reference mica signal from both the D_2O and H_2O transmission spectra, and then we renormalize the spectra to get absorbance information. The H_2O signal is noisy, as there is no H_2O IR active peak in this range. However, the D_2O signal peaks around 2340 and 2360 cm^{-1}, corresponding to the symmetric and asymmetric stretch modes of the O–D bond [41]. There is a negligible amount of D_2O adsorbed on the graphene from ambient exposure, and thus we conclude that the graphene must be trapping the D_2O, as seen in CNTs [41].

It is possible that the –OD group within D_2O could exchange with the interlayer –OH groups in mica. Still, we believe that this exchange is minimal in our graphene transfer, as previous work showed that this exchange within muscovite required many hours of 600 °C

exposure to pressurized D_2O vapor [42]. These conditions are quite different than our transfer conditions. The sensitivity of IR measurements to D_2O monolayers under graphene is also worth noting. Sum-frequency generation (SFG) IR spectroscopy measurements of sub-monolayer, adsorbed D_2O on mica gave a O–D stretch mode at ~2375 cm^{-1}, demonstrating the sensitivity of IR measurements to small amounts of D_2O (i.e., sub-monolayer to few-layer) [43]. Thus, the spectrum given in Fig. 5.1b most likely originates from graphene coated, adsorbed few-layer D_2O on mica. Additional experimental [44] and theoretical [45] work of D_2O adsorbed on graphene show similar qualitative trends (e.g. a doubly-peaked IR spectrum around 2500 cm^{-1}) to our observed FTIR spectra, albeit at higher wavenumbers. We attribute this shift due to graphene induced D_2O confinement [46].

Within Fig. 5.1c, we show point Raman spectra (λ_{exc} = 633 nm) of graphene on mica. We transferred graphene in water and using a modified dry transfer [47] process (see Section 5.7.1). For the graphene-coated water on mica, we show Raman spectra before and after a UHV high temperature degas at ~650 °C. We also give Raman spectra of the bare mica for reference. All graphene spectra are monolayer, as determined by the peak height I(2D)/I(G) ratio [48], the 2D band position, and the 2D full width at half maximum (FWHM) [49]. The dry transferred graphene possesses a G band at $\omega_{G,d}$ ~ 1595 cm^{-1}. Comparing the 2D band of the dry and wet (before degas) Raman spectra, one notes a redshift of the 2D band to $\omega_{2D,d}$ ~ 2647 cm^{-1} (wet transferred graphene at $\omega_{2D,b}$ ~ 2652 cm^{-1}). Strain, either uniaxial, biaxial, or inhomogeneous, can cause a peak position shift in the G and 2D bands and increase the G band FWHM [50, 51]. Thus, our Raman measurements on the wet, degassed, and dry transferred graphene films could reveal a combination of doping and strain. From the dry transferred graphene 2D band position and its FWHM (~44.8 cm^{-1}), we determine a tensile strain $\varepsilon \sim 0.25\%$, downshifting both the 2D

and G bands. Applying this shift to the G band (averaging the contributions from the G^- and G^+ bands) gives a $\omega_{Gd,no\text{-}strain} \sim 1597\ cm^{-1}$, consistent with graphene on bare mica [7]. Still, graphene on bare mica has a G band FWHM of ~8 cm^{-1}, a factor of two lower than this band's FWHM of 16.3 cm^{-1}. The anomalously high FWHM originates from the tensile strain as well as some inhomogeneous broadening caused by wrinkles in the dry transfer process. Hence, the dry transferred graphene shows the effects of missing interfacial water on graphene on mica.

In the case of wet transfer, the PMMA/graphene stacks underwent a modified RCA clean [52] (SC-2 followed by SC-1) to eliminate adsorbed metal and organic contaminants that might dope the graphene from underneath. Both spectra are of monolayer graphene [7, 48], though the onset of the D and D' bands indicates that the degassing process induced some defects (see Section 5.7.3). Notably, the G band downshifts after the degas (from $\omega_{G,b} = 1597\ cm^{-1}$ to $\omega_{G,a} = 1586\ cm^{-1}$), showing a change in doping [53, 54]. Furthermore, its full width at half maximum (FWHM) increases, implying that electron-phonon coupling is lessened by decreased doping [53]. The 2D band, however, shifts from $\omega_{2D,b} = 2651\ cm^{-1}$ to $\omega_{2D,a} = 2666\ cm^{-1}$ after the degas, the opposite direction of what is expected for the elimination of a p-type dopant [53]. Our analysis shows that the compressive strain required to satisfy the 2D band upshift post degas would subsequently upshift the G band, the opposite of what we observe. We give further discussion in Section 5.7.3.

We hold that our 2D band upshift is due to local graphene band structure modification by strongly adsorbed PMMA at defects, similar to a previous report of annealed PMMA on graphene [55]. These effects are not seen in our STM measurements but are observed in the Raman measurements, as each method has different fundamental length scales. As discussed in Section 5.7.3, the quasi-parabolic band structure of the PMMA/graphene decreases the Fermi

velocity, thereby blue-shifting the 2D band strongly and barely modifying the G band [56]. Furthermore, the invariance of the peak height I(2D)/I(G) ratio before and after the degas suggests that we have not introduced additional dopants in our processing [53]. Thus, the post-degas Raman point spectrum is characteristic of CVD graphene on water on mica. Still, we provide spatial mapping to strengthen this conclusion further.

Figure 5.1d gives a histogram of the G band position before the degas, a Gaussian distribution centered at 1596 cm^{-1} (population mean of $\omega_{G,b}$ = 1595.0 ± 8.9 cm^{-1}, n = 89). A previous report [7] showed that the G band for graphene on bare mica is around $\omega_G \sim 1595$ cm^{-1}. Despite the similarity in G band position, we hold that many layers of water are encapsulated by the graphene during water-based transfer, as shown in Fig. 5.1b. The introduction of this water, combined with its stability on mica [57], makes it unlikely that we have graphene on bare mica during our Raman measurement. Before the degas in UHV, we find that STM imaging of the surface is unstable, which we attribute to adsorbed contaminants. Therefore, the high value of the G band position likely originates from remaining p-type PMMA residue [58] from the graphene transfer. It is also possible that the many layers of water possess more residual dopants, shifting the G band. Doping effects are also present in other Raman metrics (Section 5.7.3).

After the ~650 °C degas, the G band's position shifts to $\omega_G \sim 1586$ cm^{-1} (population mean of $\omega_{G,a}$ = 1585.9 ± 4.4 cm^{-1}, n = 129), as shown in the histogram of Fig. 5.1e. The band's position is close to previous Raman measurements [7] for graphene on single-layer water on mica ($\omega_G \sim 1583$ cm^{-1}). Based on earlier reports for annealed CVD graphene (in UHV [58] and in air [55]), it appears that the high temperature degas removed most of the adsorbed PMMA residue from the graphene, downshifting the G band. The $\Delta\omega_G \sim 3$ cm^{-1} upshift between our mean G band position and the previously published work could be a sampling effect or could be attributed to p-type

atmospheric adsorbates [53] and some remaining PMMA [52] within the Raman spot. Only a few points within the Raman map composing Fig. 5.1e (see Section 5.7.3 for the map) are near what is expected for graphene on bare mica, $\omega_{G,m} \sim 1595\ cm^{-1}$, supporting the conclusion that the graphene is covering a full, multi-layered water film. The G band's lower position is due to the water screening interfacial charge transfer [7] between the graphene and heavily p-type mica. If graphene were p-type doped by the bare mica, we would expect a strong shift in the graphene Fermi level in scanning tunneling spectroscopy (STS) measurements. We do not see this (Section 5.7.7)

Scrutinizing the G band FWHM carefully raises the concern of inhomogeneous broadening [50] in the Raman spot. The large spatial sampling over which the data in Figs. 5.1c and 5.1d is collected makes it unlikely that the downshift in the G band and its broadened FWHM result from inhomogeneous broadening. However, if the thermal degas introduces wrinkles into the graphene, on a scale larger than the STM images but smaller than the Raman spot, inhomogeneous broadening could occur, thereby increasing the G band FWHM. Thermally induced wrinkles in graphene and their effects on Raman were previously studied [59], making this outcome feasible. However, we believe that doping is the dominant effect for the trends observed, but we cannot rule out inhomogeneous broadening entirely.

In Fig. 5.2, we show a 30 nm by 30 nm STM topographic image of a typical sample surface (Fig. 5.2a), and a spatial derivative (Fig. 5.2b) illustrating the honeycomb lattice of the monolayer graphene covering. We present a larger 100 nm by 100 nm false-colored STM topograph in Fig. 5.2c, which shows the relative heights of the different graphene and water related features. There are three distinct water layers visible, as well as a graphene grain boundary (GB) and some taller protrusions extending from the top water layer. The presence of

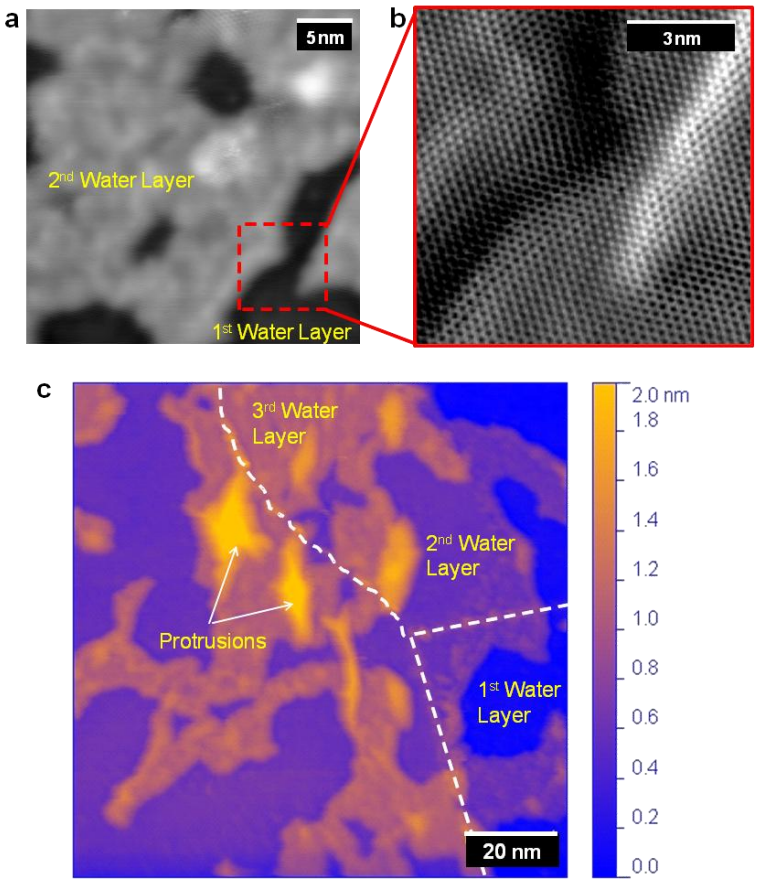

Figure 5.2. STM topographs of few-layered water confined between graphene and mica. **(a)** 30 nm by 30 nm image showing the first two water layers on the mica surface. **(b)** Zoomed-in spatial derivative of the boxed region in (a) showing the honeycomb lattice of the monolayer graphene coating. **(c)** 100 nm by 100 nm false-colored topographic image of graphene-water-mica system. Three layers of water are visible, as well as a graphene grain boundary, which is labeled by the dotted white line. The protrusions coming out of the third water layer could be due to either contaminants trapped under the graphene, or to the water displaying increasing bulk-like properties as it gets further from the mica surface. Scanning conditions are –0.35 V sample bias and 1 nA tunneling current.

the GB is not surprising, as CVD graphene is known to be polycrystalline [60, 61], but it is interesting to note that the water does not appear to preferentially congregate along the boundary. In light of recent AFM data suggesting that adsorbed water prefers to form droplets instead of layers centered on defects on hydrophobic surfaces [29], we can conclude that the hydrophobicity of the CVD graphene covering has little effect on the underlying water structure.

It is possible that our high temperature degas in UHV induces strain in the graphene as the water escapes, which could deform the graphene [62, 63] and influence the water structure

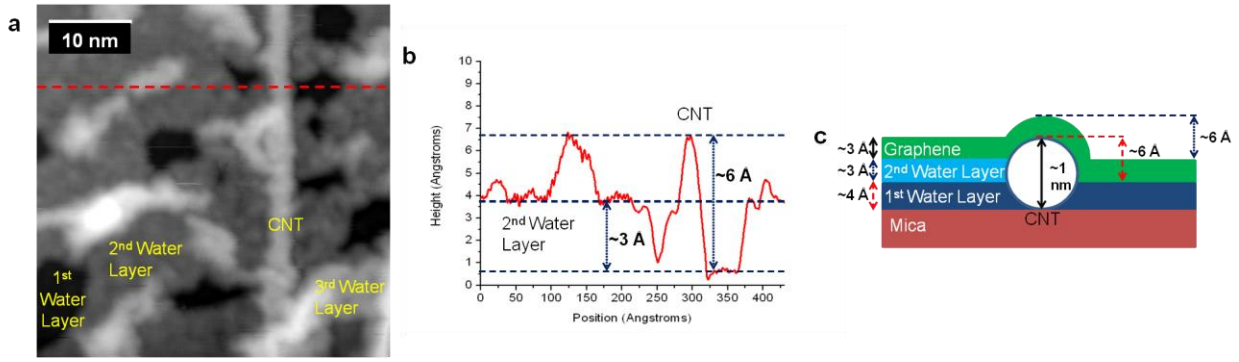

Figure 5.3. (a) 43 nm by 43 nm topographic STM image of a single-walled carbon nanotube embedded in the confined water layers between the graphene and mica. The first and second water layers are clearly defined, while the sporadic clusters appear to be the beginnings of a third water layer. **(b)** Height profile taken at the dotted red line in (a). Here, the second water layer appears to be approximately 3 Å tall, while the SWNT juts 6 Å above the first water layer. **(c)** Cartoon showing how we determine the heights of each of the water layers in this image. The dotted blue arrows are the values that we measured in (b): 3 Å for the second water layer and 6 Å for the part of the SWNT above the first water layer. The black arrows are the heights that we know from external references: ~3 Å in height for monolayer graphene and ~1 nm for our HiPco SWNTs. The red arrows represent the heights that we derived from our known quantities. Knowing the total height (~1 nm) of our SWNT and how much it juts out of the first water layer (~0.6 Å), we can subtract and determine that there is indeed only one layer of water between the graphene and mica, and that the height of this layer is ~4 Å. Scanning conditions were -0.35 V sample bias and 1 nA tunneling current.

that we observe. However, a recent AFM study demonstrated that water easily escapes from the edges of the graphene-mica interface. Therefore, some of the excess water can escape during the low-vacuum (0% relative humidity) process before degassing. Also, the presence of intact low-angle grain boundaries [61, 64] suggests that the remaining water does not exert enough pressure (see Chapter 6) when heated to seriously damage the graphene. We do not notice any major changes in the surface structure for degas times ranging from 5 hours to 30 hours. Temperature-induced stress deformities are generally large-scale wrinkles and should not affect the small surface features that we observe, such as the protrusions out of the top water layer. The protrusions range from several angstroms to over ~1 nm tall, only appearing on the second or third water layer. This implies that their formation is dependent on the underlying water structure rather than on the graphene coating. A more likely explanation for these protrusions would be that they are water-surrounded contaminants or perhaps nanodroplets that have nucleated out of

defects in the mica. They could also be additional layers of water which have started to exhibit bulk-like behavior due to their increasing distance from the mica surface. Molecular dynamics simulations and X-ray reflectivity data have indicated that water layers on mica cease to be easily distinguishable starting at around 1 nm away from the mica surface [57, 65]. The water structures are also extremely stable over the course of our experimental observation (several days for some areas), regardless of the water layer or protrusion size.

5.3. Water Layering

We measure the exact number of trapped water layers by using single-walled carbon nanotubes (SWNTs) as a "depth gauge" between the graphene and mica. The SWNTs are deposited onto the mica via ex-situ dry contact transfer [66] (DCT) before the graphene covering is applied. The mica is heated (> 100 °C) during DCT to prevent water adsorption and promote direct contact between the SWNTs and the reactive mica surface. We use HiPco SWNTs with narrow diameter distribution centered on 1 nm [67], which means that we can use the measured height of these nanotubes to extract the number of water layers. A STM topograph of a water-immersed SWNT sandwiched between graphene and mica is shown in Fig. 5.3a. Only part of the SWNT is shown in the 43 nm by 43 nm scan; the total length of the nanotube is approximately 100 nm. There is a monolayer of water trapped between the SWNT and the graphene coating, and this layer is removed using the STM tip before the height measurements are taken. More detail on this process can be found elsewhere [3]. Figure 5.3b shows a height profile taken at the dashed red line marked in Fig. 5.3a. The height of the second water layer is measured to be ~3 Å and the difference in height between the SWNT and the first water layer is ~6 Å. Due to convolution with the tip geometry, the measured width of the SWNT appears much broader than it actually is, but the height is unaffected by tip convolution and is a good gauge of the actual

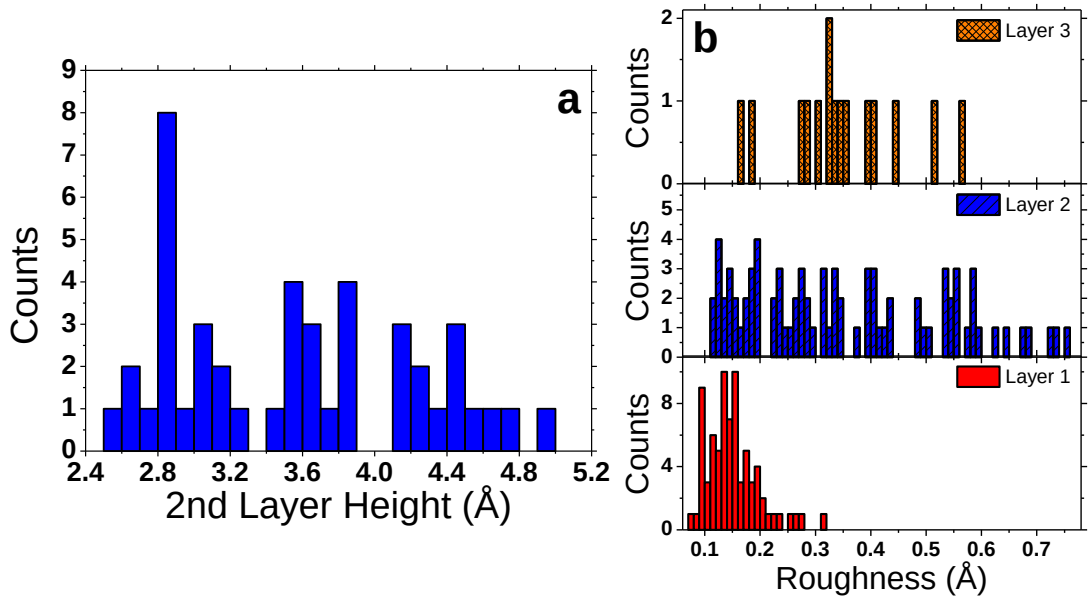

Figure 5.4. (a) Histogram of the height distribution of the second water layer. The data for this histogram was collected from four different samples, though each sample was prepared in a similar fashion. The average height is 3.5 Å, though the spread is quite large, and there is no clear trend. **(b)** Histogram of the roughness distribution for the three water layers that we have observed. This data was collected from the same four samples as the height measurements. We see that the roughness distribution of the first water layer is fairly narrow and centered at approximately 15 pm, similar to AFM measurements reported previously. The roughness distribution for the second and third water layers, however, similar to the height distribution of the second water layer, is very spread out without a clear trend. This suggests that while the first layer may have a more well-defined structure, the second and third layers are amorphous.

nanotube dimensions. Figure 5.3c shows a cartoon illustrating the different layer dimensions. The dotted blue arrows represent measured dimensions (second water layer height, difference in CNT height), the solid black arrows represent known dimensions (graphene height, total CNT height), and the dashed red arrows represent the calculated dimensions (first water layer height). Taking the difference between the measured height of the SWNT (~6 Å) and the known height of the SWNT (~10 Å), we can calculate the height of the water layer, which turns out to be ~4 Å. This means that there is only 4 Å of water between the bottom layer of the image that we show in Fig. 5.4a and the mica surface. This corresponds to approximately one layer of water and matches well with previous AFM data [7, 15].

In Fig. 5.4, we present some statistics on the height and roughness of the water layers that we have sampled. These histograms include data from different regions on the same sample as well as data from several different samples. Figure 5.4a shows the height distribution of the second water layer. The heights are spread over a wide range (average of 3.5 Å), suggesting that this layer does not have a definite crystal structure. This observation is further corroborated in Fig. 5.4b, which shows the roughness distribution of the water layers. The roughness of the second water layer again has a very wide range, suggestive of an amorphous structure. In contrast, the roughness of the first water layer is narrowly distributed and centered around 15 pm, similar to previous AFM measurements [15]. Further, if the water were crystallized, there would be moiré superstructures caused by it and the graphene. We do not observe this in the first or second water layers, further supporting the conclusion that the water is amorphous. We also perform nanomanipulation of the second water layers, which is discussed in more detail elsewhere [3].

5.4. Water in Graphene Layers on SiO_2

We can also perform STM on transferred graphene on SiO_2/Si [61]. We transfer the films using techniques described in Section 5.7.1 and in Chapter 4. Our STM topographs reveal an amorphous SiO_2 surface with a conformal graphene overlayer, like previous results [61, 68, 69]. However, we do not observe trapped water under the first graphene layer, despite SiO_2 being relatively hydrophilic (contact angle $\theta \sim 20°$ [52]) and moderate STM degas temperatures (Chapter 4). This potentially occurs because of the porous nature of amorphous SiO_2 [70], as opposed to well-packed mica lamellae. To the end of observing water on graphene/SiO_2 systems, we transfer a second graphene layer on top of the first graphene layer on SiO_2. Via graphene's wetting transparency [71], we end up with a graphene/H_2O/graphene (G/H_2O/G)

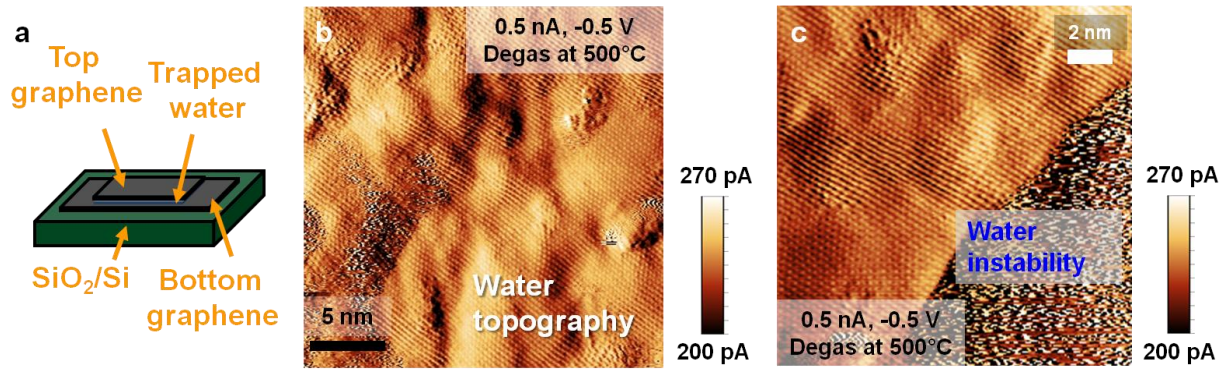

Figure 5.5. (a) Schematic of graphene/H_2O/graphene nanosandwich on SiO_2/Si. **(b)** STM current image of the structure in (a). Graphene's atomic structure is apparent. The "bumpiness" of the image does not correspond to the SiO2 [59, 68] but rather the water stuck between the two layers. **(c)** A second STM current image showing instability in the lower half, which likely originates from trapped liquid water.

"nanosandwich" on SiO_2/Si. We show a schematic of these samples in Fig. 5.5a, with corresponding STM current images in Figs. 5.5b and 5.5c. Compared to STM of typical G/SiO_2 samples, the G/H_2O/G sample appears rougher (Fig. 5.5b), and there are regions that are unstable (Fig. 5.5c). Figures 5.5b and 5.5c lack moiré electronic superstructures which normally occur if the two graphene layers electronically interact [72]. Furthermore, we do not notice the twisted bilayer optical absorbance enhancement or the Raman G band enhancement expected for typical bilayer samples [73]. All of these factors imply that there are trapped species within the G/H_2O/G nanosandwich (Chapter 4).

We calculate the height distribution and root-mean-square (RMS) roughness values for the G/H_2O/G on SiO_2 and G on SiO_2 systems in Fig. 5.6. Figure 5.6a shows a STM topograph for G/H_2O/G on SiO_2/Si, and Fig. 5.6b reveals the corresponding G on SiO_2/Si STM topograph. The RMS roughness for Fig. 5.6a (0.268 nm) is about threefold higher than Fig. 5.6b (0.096 nm). This higher roughness suggests that there are unidentified, trapped species between the graphene layers. Further, in Fig. 5.6c, the broadened height distribution for G/H_2O/G on SiO_2 versus G on SiO_2 bolsters the notion of graphene-encapsulated species. Still, our discussion up to this point

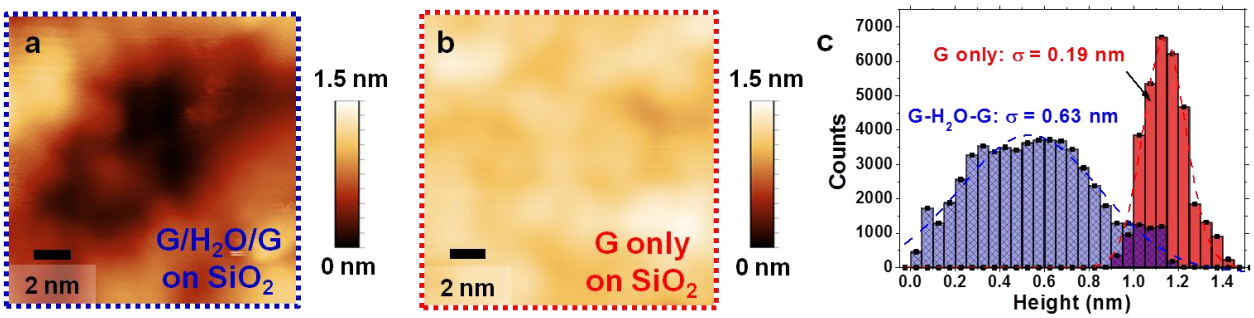

Figure 5.6. (a) STM topograph of a graphene/H_2O/graphene (G/H_2O/G) nanosandwich on SiO_2/Si, showing a high degree of height variation. **(b)** STM topograph of G/SiO_2 from [59] showing lower height variation. **(c)** Height histograms for (a) and (b). The larger variation and increased RMS roughness for G/H_2O/G versus G/SiO_2 comes from inhomogeneous trapped water and not oxide roughness.

has arbitrarily assigned the trapped species as H_2O. The transfer process (Section 5.7.1) introduces varied solvents and contaminants, any of which could be entrapped by conformal [14] graphene. Still, the graphene films have the highest exposure to H_2O during the transfer process, making its entrapment most probable. Further, the stability of the first water layer under graphene on mica suggests that water will readily template on graphene. Additionally, graphene's partial wetting transparency—for the bottom graphene layer on SiO_2—will present a 20-60° contact angle [52, 74] surface to water introduced from the second graphene transfer. All of these variables imply that the trapped species is H_2O. Regardless, we will provide chemical evidence to back this more rigorously in Chapter 6.

5.5. Discussion

A possible explanation for the structure of the first water layer on mica is that while it does not have a well-defined, periodic crystal structure, it is strongly bound to the mica surface. The hydration layer on mica has been the subject of many theoretical [65, 75] and experimental studies [9, 11, 57], though its exact thickness and behavior are still contested [10, 12]. From our data, as well as previous research [7, 13, 15, 57, 65], we argue that the thickness of the hydration layer on mica is ~1 nm, and is split into three distinct water layers. The first water layer is strongly bound to the mica surface, with a thickness of ~4 Å. This layer cannot be manipulated,

and exhibits properties similar to a crystalline solid. The second and third water layers, on the other hand, while still more viscous than bulk water, are much more amenable to manipulation than the first layer. They are stable in equilibrium at room temperature, but high tunneling conditions can break bonds and cause them to rearrange. Beyond layer three, the water begins to exhibit bulk-like behavior as the layers start to blend together.

5.6. Conclusions

In summary, we performed UHV-STM at room temperature on few-layered water trapped between monolayer graphene and mica. The graphene coating keeps the water stable on the surface and protects it from high temperature processing in vacuum, but does not otherwise perturb or alter the water bonding structure, even at the higher defect-density grain boundaries. We observe up to three layers of water trapped between the graphene and mica, with the first layer being strongly bound while the second and third layers are amorphous. We also demonstrate the ability to manipulate the amorphous water layers using the STM tip. This work demonstrates the feasibility of using CVD graphene coatings for nano-templating in high-resolution STM studies, as well as furthering our understanding of water behavior near the mica surface. Graphene-coated water will allow further STM-based research of other aqueous suspended structures, like the biomolecules in water discussed in Chapter 6.

5.7. Materials and Methods

5.7.1. Graphene Growth and Transfer

For samples not employing carbon nanotubes (CNT) as a height reference, we used 1.4 mil copper foil (Basic Copper, Carbondale, IL USA) in a hot-wall Atomate CVD system. These Cu foils were pre-annealed at ~1000 °C under Ar/H_2 flow for 45 min, and we grew graphene at ~1000 °C with 100 sccm of CH_4, 50 sccm of H_2, and 1000 sccm of Ar for 30 min following a

previously published procedure [35]. The operating pressure during growth was ~0.5 torr. The resulting substrates were cooled to room temperature at ~20 °C/min under the same gas flow. We cleaned mica (SPI Inc., V-1 grade muscovite) and a razor blade with acetone, isopropanol, and DI water rinses. Using the razor blade, we cleaved the freshly cleaned mica. We coated the graphene/Cu surface with a 495 K A2 and 950 K A4 PMMA bilayer (MicroChem). Each PMMA layer was spin coated at 3000 RPM for 30 s and cured at 200 °C for 2 min. The graphene on Cu backside was removed by an O_2 plasma in a reactive ion etcher (RIE). An additional protective layer of 950 K A4 PMMA was spun on and cured using the same parameters to protect the graphene film. The Cu foil was then etched by 1M $FeCl_3$ etchant overnight. Using a cleaned glass slide, the remaining graphene film was transferred to a DI water bath for ~5 min followed by a second DI bath to further clean the graphene from etchant residues. We transferred the film to the cleaned mica surface in the second DI bath. The PMMA was stripped with a 1:1 methylene chloride to methanol bath for 20 min, followed by annealing at 400 °C in Ar/H_2 for 1 hr.

For samples employing CNTs as a height reference, we deposited HiPco CNTs (Unidym, Inc. lot #R0223) by ex-situ dry contact transfer (DCT) [24, 57, 76] at elevated temperature (> 100 °C) to prevent water adsorption on the mica. The mica (SPI Inc.) was cleaved three times with scotch tape rather than a razor blade, giving a flatter overall mica surface with larger crystal planes. We confirmed the presence of CNTs by atomic force microscopy (AFM). For graphene growth, we used 1 mil copper foil (Alfa Aesar, 99.8% purity) in the same hot-wall Atomate CVD system. The pre-anneal and growth flow rates were the same as the previous samples, except for a decrease in CH_4 flow rate to 75 sccm to increase the percentage of monolayer graphene. Similarly, we coated the graphene/Cu surface with the same PMMA bilayer (MicroChem). Each PMMA layer was spin coated at 3000 RPM for 30 s and cured at 200 °C for 2 min. The graphene

on Cu backside was removed by an O_2 plasma in a RIE. The Cu foil was then etched by commercial Cu etchant, CE-100 ($FeCl_3$ base, Transene Co.) overnight. Using a cleaned glass slide, the remaining graphene film was transferred to a DI water bath for ~15 min. The PMMA/graphene film was cleaned in a room-temperature, modified RCA clean. In this clean, SC-2 (20:1:1 H_2O:H_2O_2:HCl, concentrated) was followed by SC-1 (20:1:1 H_2O:H_2O_2:NH_4OH, concentrated) for 15 min each to eliminate metal and organic contaminants underneath the graphene. We transferred the film to another DI bath, in which we transferred the film to the mica surface with CNTs on it. The PMMA was stripped with an acetone bath for 20 min, followed by annealing at 400 °C in Ar/H_2 for 1.5 hr.

Dry transferred samples were made by growing graphene on 1 mil Cu (Alfa Aesar, 99.8% purity) using 75 sccm of CH_4 and 50 sccm of H_2 at 1000 °C for 25 min. The operating pressure during growth was ~0.5 torr. The resulting substrates were cooled to room temperature at ~20 °C/min under the same gas flow. PMMA was coated on the graphene on Cu and the backside and Cu were etched following the above procedure. The PMMA film was cleaned with 3 DI water baths, ~15 min each. A piece of cured PDMS was cleaned using methanol, acetone, and IPA, and it was dried with N_2. This PMMA-fluid meniscus was inverted onto the PDMS so that the PMMA was flipped onto the PDMS. Thus, the stack had the following order from the top: graphene, PMMA, and PDMS. The exposed graphene top side was carefully dried with N_2 and placed in a Fluoroware container. It was then placed on top of hot (~150 °C), freshly cleaved mica (on a hot plate), and a heavy weight forced the PDMS/PMMA/graphene stack into contact with the mica. The system was kept at that temperature for ~18 hrs to make the PMMA glassy and bring about good graphene adhesion. The PDMS stamp was then removed rapidly, leaving some PMMA residue on the dry transferred graphene on mica.

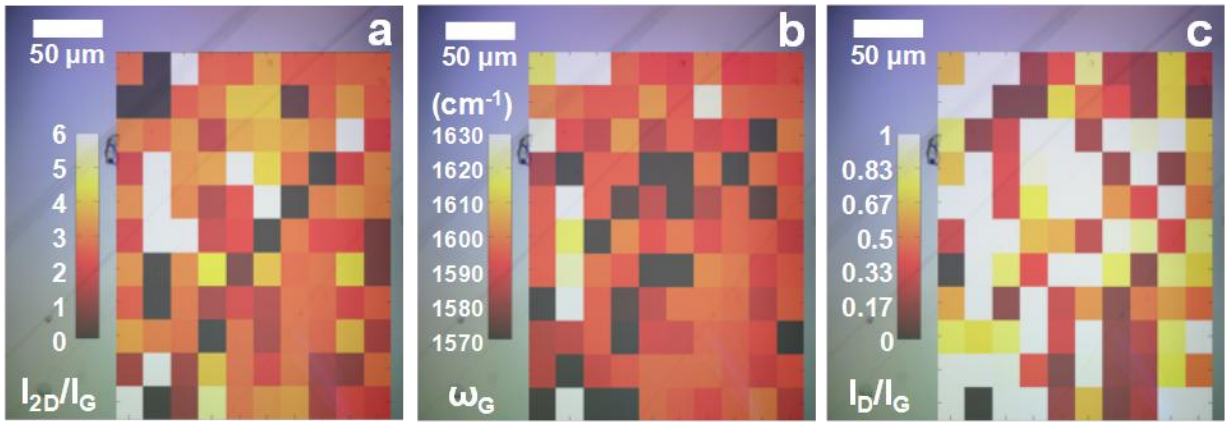

Figure 5.7. Spatial Raman mapping at λ_{exc} = 633 nm and 20X objective for RCA cleaned graphene transferred to mica in water. **(a)** Monolayer peak height I_{2D}/I_G map, showing evidence of monolayer or turbostratic graphene. **(b)** G band position map of the same area in (a), giving a high value for the G band position due to adsorbed PMMA and residual dopants. The histogram in Fig. 1d is derived from this figure. **(c)** Defect density I_D/I_G (peak intensity from fitted Lorentzians) map of the same area in (a). There are minor defects induced by the transfer as well as contributions from residual PMMA.

5.7.2. Scanning Tunneling Microscopy (STM)

A 270 nm gold contact was sputtered onto the samples using a shadow mask. We used a homebuilt, room-temperature UHV system with a base pressure of ~5×10^{-11} torr for scanning tunneling microscopy measurements. The sample was degassed in the UHV-STM system by direct-current heating through a n+ Si backing at a temperature of ~650-700 °C for several hours. We acquired STS data using standard lock-in techniques. Our STM tips are made of etched tungsten wire and sharpened using field directed sputtering [77].

5.7.3. Raman Spectroscopy

Raman spectroscopy was taken using a Renishaw Raman microsope (inVia and WiRE 3.2 software) with 20x and 50x objectives, 1800 lines/mm grating, 30 s acquisition time, ~1.8-9 mW power, and 633 nm laser excitation, unless otherwise noted. Raman maps were analyzed by fitting single Lorentzians around the 2D (also called G'), G, and D bands, centered at 2690 cm^{-1}, 1580 cm^{-1}, and 1350 cm^{-1}, respectively. A six-point polynomial background was subtracted before Lorentzian fitting. G peak position data values were considered physical if they were

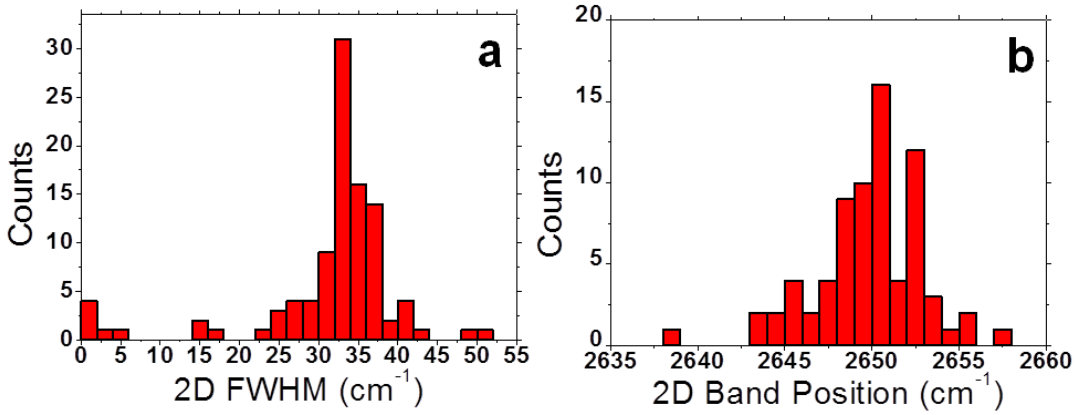

Figure 5.8. Evidence of monolayer CVD graphene on mica. **(a)** Histogram of the 2D band's full width at half maximum (FWHM) for the region mapped in Fig. 5.7. Distribution is centered around ~32 cm^{-1}, consistent with monolayer CVD graphene. **(b)** Histogram of the 2D band's position (Lorentzian fitted), centered at ~2650 cm^{-1}. This is also representative of monolayer graphene.

greater than 1570 cm^{-1} and less than 1630 cm^{-1}. 2D band full width at half maxima (FWHM) were considered physical if their values were greater than 0 cm^{-1} and less than 60 cm^{-1}.

To assess both graphene and trapped water coverage, we used Raman spectroscopy. In Figs. 5.7a and 5.7b, we give spatial Raman spectra maps for transferred CVD graphene on mica. These maps are overlaid on the optical image in which they were taken. We then took a ratio of the Lorentzian peak intensity under the 2D (G') and G Lorentzian curves for Fig. 5.7a and the Lorentzian G band position for Fig. 5.7b. Most of the points in Fig. 5.7a are above 2 (peak height), indicative of monolayer graphene [48] or turbostratically stacked graphene. The G band positions within Fig. 5.7b are greater than 1590 cm^{-1} (see Fig. 5.1d), showing that there is doping on the graphene film from residual PMMA. We note that there is probably remaining PMMA after the acetone liftoff, as these samples did not undergo an Ar/H_2 anneal to remove PMMA. Within Fig. 5.7c, we show a spatial map of I(D)/I(G) (peak not area ratio), giving graphene defect density and sp^3 character. Raman spectra taken on the Cu foil after growth did not show an appreciable D band, so we attribute its presence in the map to the graphene transfer.

Furthermore, residual PMMA has been shown to contribute to the D band's intensity by increasing the amount of sp^3 carbon present [78].

To determine whether the graphene is not turbostratically stacked from growth, one must look at the 2D band's FWHM. For Raman taken with λ_{exc} = 633 nm, it is known that turbostratically stacked CVD graphene increases the 2D FWHM from its expected value of ~30-35 cm^{-1} to ~45-55 cm^{-1} [49]. Further, turbostratically stacked graphite has been shown to blue-shift the 2D band from its known position at ~2655 cm^{-1} for λ_{exc} = 633 nm to ~2663 cm^{-1}. Within Fig. 5.8a, we see that the 2D FWHM is γ_{2D} = 31.4 ± 9.5 cm^{-1} (n = 100), close to the value expected for monolayer and not turbostratic graphene. In Fig. 5.8b, the 2D peak position is ω_{2D} = 2650.6 ± 7.2 cm^{-1} (n = 74), red-shifted from its known position. Within the error, there is not an appreciable up-shift expected for a turbostratic sample. This discussion, combined with the fact that the peak height (from Lorentzian fits) I(2D)/I(G) is greater than 2 for most of the sample within Fig. 5.7 (and Fig. 5.1d), makes us conclude that our samples are predominantly monolayer graphene.

During the 650 °C degas, the mica should expand and the graphene should contract, possibly becoming a source of uniaxial, biaxial, or inhomogeneous strain [50, 51]. This strain can consequently cause the positions of the 2D and G band to shift. Moreover, the strain softens the G phonons, increasing the G band FWHM; this could lead to the doping shifts (G band downshift) and the increase in G band FWHM that we observe in our Raman data after the degas. Figure 5.9 gives a schematic diagram of the shifts that would occur for the simultaneous removal of doping and addition of strain for the 2D and G bands. Within Fig. 5.9a, we estimate the sample's doping shift due to the evaporation of PMMA, using recent reports for annealed CVD graphene [79]. Starting from $\langle\omega_{2D}\rangle$ = 2651 cm^{-1} (n = 99), this loss of PMMA ($\Delta p \sim 10^{12}$

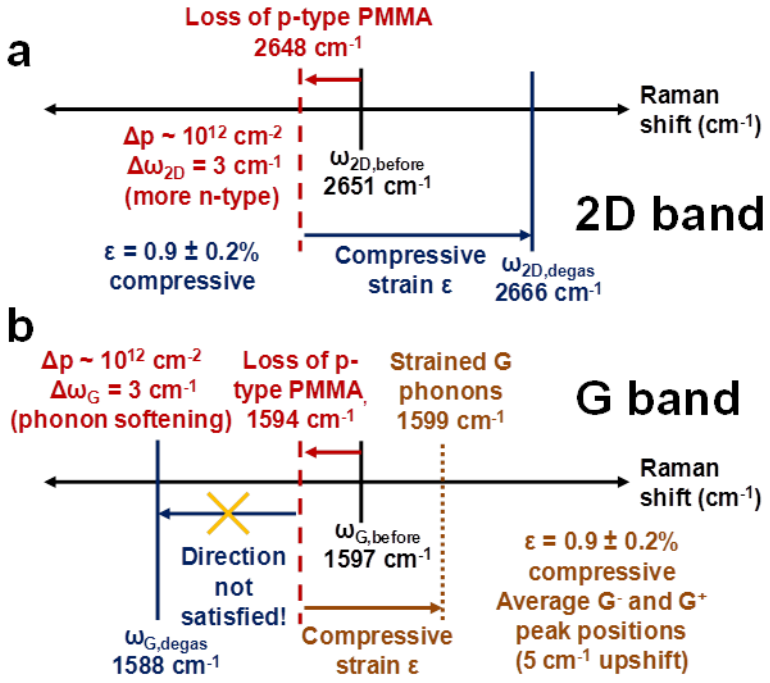

Figure 5.9. Elucidating the 2D and G band position shifts for the graphene on mica system before and after the degas. **(a)** 2D band position diagram, showing how the loss of PMMA (decreased doping) and onset of compressive strain from the degas gives the final band position. **(b)** G band position diagram, which also highlighting the combination of doping and strain within the CVD graphene. The final G band position observed – at ~1588 cm^{-1} – cannot be achieved by using doping and strain working in concert, as is the case in (a). Thus, the band's shift and increase in FWHM must be due to doping and another factor. We hold that it is doping and band structure modification [54].

cm^{-2}) should downshift the 2D band by 3 cm^{-1}, giving $\omega_{2D,PMMA}$ = 2648 cm^{-1}. The final position of the band is at $\langle\omega_{2D,degas}\rangle$ = 2666 cm^{-1} (n = 73). To arrive at this final band position, one must

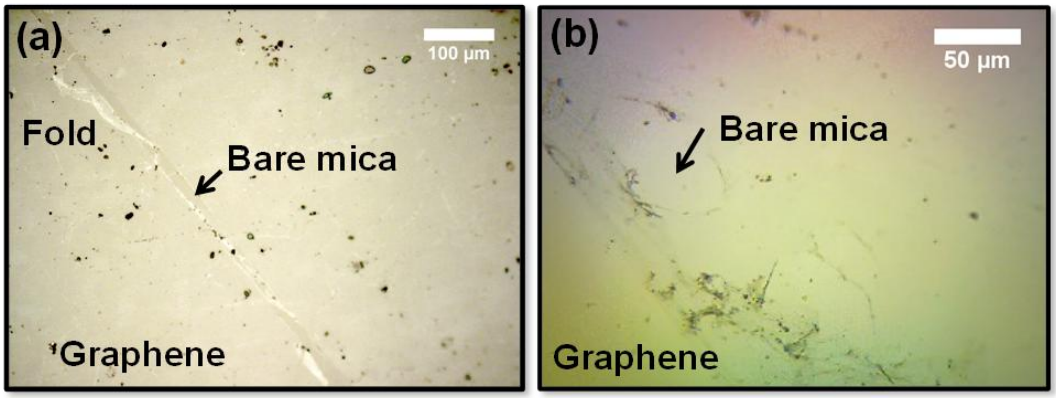

Figure 5.10. (a) Optical microscope image of DI water transferred graphene on mica. Folds, tears, and PMMA residue apparent in the image. **(b)** Optical microscope image of D_2O transferred graphene on mica. Similar tears and PMMA residue are present.

uniaxially apply a compressive shift [51] to the graphene of $\varepsilon = 0.9 \pm 0.2\%$. We then use this compressive shift when analyzing the G band in Fig. 5.9b, initially at $\langle\omega_G\rangle = 1597$ cm^{-1} (n = 71). The compressive strain will upshift the G band after removing the contribution due to PMMA doping (a downshift). Strain will also split the G band into separate G^- and G^+ (with respect to energy) bands, whose splitting is best observed by polarized Raman spectroscopy; the value of strain from Fig. 5.9a will give upshifts of 4.8 cm^{-1} and 2.1 cm^{-1}, respectively. Averaging these shifts gives an overall upshift of 3.5 cm^{-1} for the unsplit G band. This is the incorrect direction for the observed final G band position at $\langle\omega_G\rangle = 1588$ cm^{-1} (n = 20). Thus, we must conclude that data cannot be explained by a compressive shift and decreased doping.

An alternative approach to explaining the data considers the effect of the degas on the residual PMMA. Lin et al. [55] showed that PMMA which is adsorbed at defects (i.e., wrinkles and grain boundaries) is difficult to remove with temperature processing. Their work also argued that temperature processed PMMA can modulate the linear band structure of graphene. All of their Raman data—both on SiO_2 and suspended—showed an anomalous blue-shift for the 2D band; they claimed that these blue-shifts were not attributable to strain and that they originated from an approximately parabolic PMMA/graphene dispersion under the Raman spot. For a parabolic dispersion ($E = \hbar^2k^2/(2m^*)$) the Fermi velocity v_F scales as k ($v_F \sim k$), which at low energy gives velocities two orders of magnitude less than the Fermi velocity in pristine graphene ($v_F = 1 \times 10^6$ m/s). The 2D band shift can be approximated at double-resonance as $\Delta\omega_{2D} \approx [E_L - \hbar\omega_{2D}D_{2D}/2]\Delta v_F/(\hbar v_F^2)$, where E_L is the laser energy (eV), and D_{2D} is the electron-phonon coupling at the K (K') point (eV·Å) [56]. Though most of the PMMA is removed by the degas, it is likely that some PMMA still exists at grain boundaries and defects in our CVD films. Our STM images do not show strongly adsorbed PMMA on graphene, but the large size of the

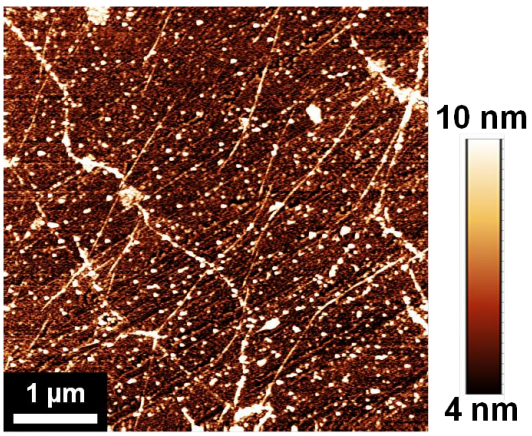

Figure 5.11. AFM (5 µm x 5 µm) image of graphene wet transferred to mica. The image shows wrinkles, holes, and PMMA residues from the transfer. The high roughness of these features makes observing fine water features difficult, even at smaller length scales (less than 5 µm).

Raman spot relative to the area sampled by STM makes observing these larger-scale effects possible. This annealed PMMA/graphene, with its quasi-parabolic dispersion, should lower the Fermi velocity and blue-shift the 2D band relative to the pre-degas 2D band position. We also note that the blue-shift in the 2D band from this PMMA interaction ($\Delta\omega_{2D}$ = 18 cm^{-1}) is close to previously observed value for annealed PMMA on suspended graphene ($\Delta\omega_{2D}$ = 13±6 cm^{-1}) [55]. It was formerly noted that the G band's position did not substantially change with a modification of the Fermi velocity [56, 80]. Thus, we attribute the G band downshift and broadened FWHM in our data to decreased PMMA doping, and the 2D band upshift to band structure modification.

5.7.4. Fourier Transform Infrared (FTIR) Spectroscopy

Fourier transform infrared (FTIR) spectroscopy was performed with a Thermo Scientific Nicolet 6700 FTIR. Data was spaced with two wavenumber resolution, and 64 scans were taken for both the background mica and the graphene-water-mica samples.

5.7.5. Optical Microscopy

We determined the amount of CVD graphene coverage on our transparent mica substrates using optical microscopy, shown in Fig. 5.10. For Fig. 5.10, we transferred PMMA-coated graphene into a final DI H_2O bath. Figure 5.10a shows tears and folds in the film, which can give

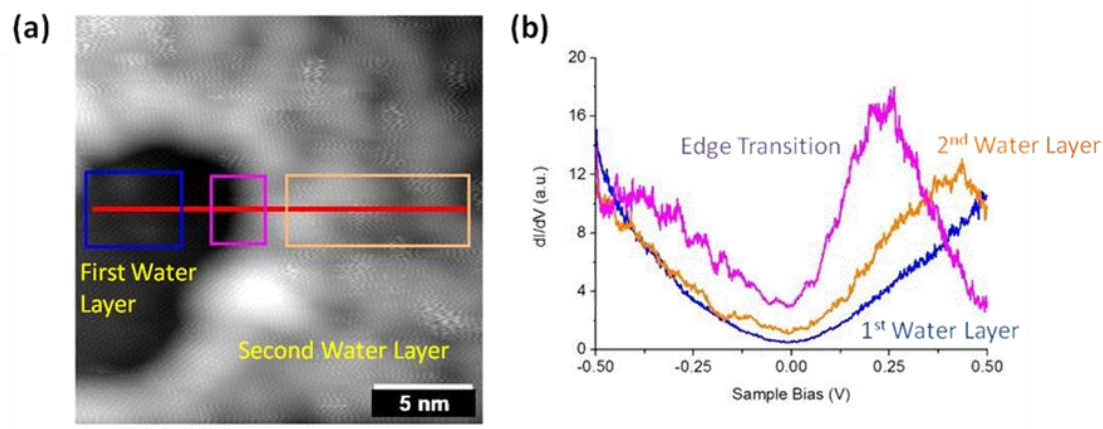

Figure 5.12. STS characterization of graphene on mica. **(a)** STM topograph with spectroscopy taken along the red line. **(b)** Averaged dI/dV data from the colored boxes in (a), showing a surface state at ~0.25 V at the edge of the transition between the first and second water layers. The Dirac points are all centered at zero bias, indicating the lack of graphene doping. The spectra were taken with standard lock-in techniques and 1 nA setpoint current. STM image taken at –0.35 V sample bias, 1 nA tunneling current.

some the turbostratic bilayer regions seen by STM. Moreover, the film has noticeable PMMA residue from the transfer. In Fig. 5.10b, we transferred PMMA-coated graphene into a final D_2O (99.9% pure) water bath. Films were in both baths for ~1 min before transfer onto the final mica substrate. The film of Fig. 5.10a looks similar to the DI water transferred film in Fig. 5.10b.

5.7.6. Atomic Force Microscopy (AFM)

With a Bruker Dimension IV AFM, we performed tapping mode AFM using 300 kHz resonant frequency Si cantilevers on our wet transferred graphene on mica. We show a representative AFM image in Fig. 5.11. The image has considerable PMMA residue present, and there are wrinkles and tears in the graphene film. With these large features, we cannot use AFM to discern the finer water features that were visible in STM. Additionally, our tips had large radii of curvature (we estimate ~40 nm or more), making these fine water features hard to see, even in clean regions.

5.7.7. Scanning Tunneling Spectroscopy (STS)

In Fig. 5.12, STS shows that there is little difference in the location of the Dirac point when comparing graphene on one layer of water and graphene on two layers of water. It also

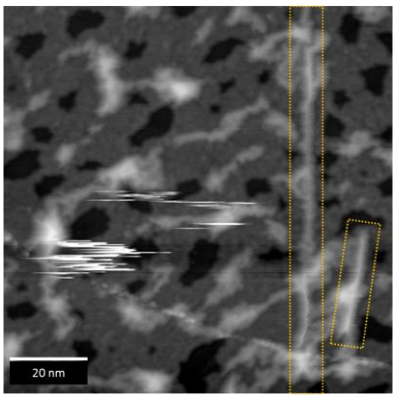

Figure 5.13. Large area STM topographic scan of two SWNTs encased in few-layered water between a graphene coating and mica substrate. The SWNTs are marked with the dotted orange boxes. All the other linear strand-like features are water structures. Scanning conditions are –0.35 V sample bias at 1 nA tunneling current.

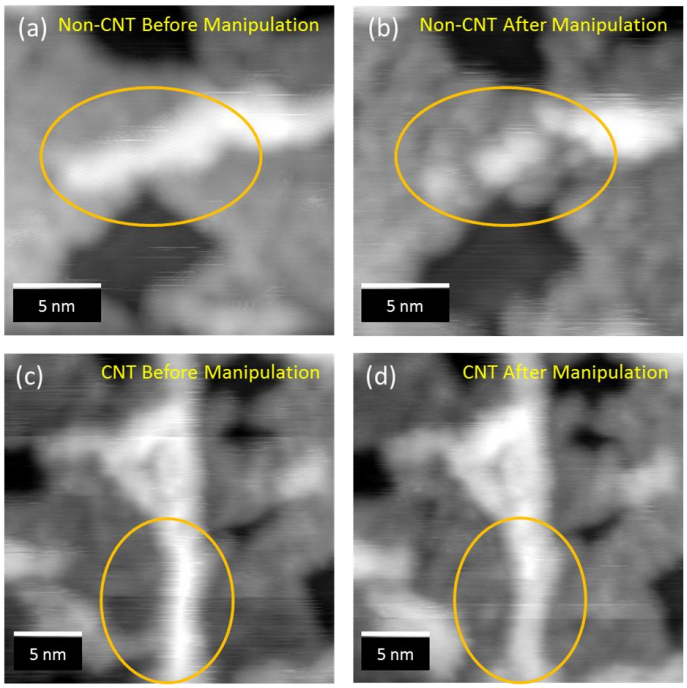

Figure 5.14. A STM topographic image of a linear water structure **(a)** before and **(b)** after manipulation using the STM tip. The water structure is clearly damaged and no longer holds its shape. A SWNT **(c)** before and **(d)** after manipulation. The structure holds its shape, despite the surrounding water being moved. Scanning conditions are –0.35 V sample bias and 1 nA tunneling current.

shows that there is no p-doping of the graphene (indicated by the lack of a Dirac point offset from zero bias), which has been demonstrated to occur for graphene on bare mica [7]. This is consistent with previous Raman and scanning Kelvin probe microscopy measurements

demonstrating that few-layered water screens graphene from the doping effects of the mica substrate [7].

5.7.8. Differentiating SWNTs from Water Structures

Along with SWNTs, there are also many water structures that populate our surface, as shown in Fig. 5.13. In order to differentiate the SWNTs from the water structures, we perturb them with the STM tip [3]. The non-SWNT water structures are easily damaged by the STM tip, but the SWNTs maintain their shape. This can be seen in Fig. 5.13.

In Figs. 5.14c and 5.14d, we notice that although the shape of the SWNT does not change, there appears to be a reduction in the CNT height after manipulation. The manipulated region is ~2.5 Å shorter than the non-manipulated region. We believe that this height change is due to a monolayer layer of water trapped between the SWNT and graphene coating being removed, as a water monolayer is approximately 2.5 Å tall. All of our SWNT height measurements are performed with the water layer removed.

5.8. References

[1] P. A. Thiel and T. E. Madey, "The interaction of water with solid surfaces: Fundamental aspects," *Surface Science Reports,* vol. 7, no. 6-8, pp. 211-385, 1987.

[2] A. Verdaguer, G. M. Sacha, H. Bluhm, and M. Salmeron, "Molecular structure of water at interfaces: Wetting at the nanometer scale," *Chemical Reviews,* vol. 106, no. 4, pp. 1478-510, 2006.

[3] K. T. He, J. D. Wood, G. P. Doidge, E. Pop, and J. W. Lyding, "Scanning tunneling microscopy study and nanomanipulation of graphene-coated water on mica," *Nano Letters,* vol. 12, no. 6, pp. 2665-2672, 2012.

[4] G. E. Brown, "How minerals react with water," *Science,* vol. 294, no. 5540, pp. 67-69, 2001.

[5] R. Guckenberger, M. Heim, G. Cevc, H. F. Knapp, W. Wiegräbe, and A. Hillebrand, "Scanning tunneling microscopy of insulators and biological specimens based on lateral conductivity of ultrathin water films," *Science,* vol. 266, no. 5190, pp. 1538-1540, 1994.

[6] C. Jang, S. Adam, J. H. Chen, E. D. Williams, S. Das Sarma, and M. S. Fuhrer, "Tuning the effective fine structure constant in graphene: Opposing effects of dielectric screening on short- and long-range potential scattering," *Physical Review Letters,* vol. 101, no. 14, pp. 146805-146805-4, 2008.

[7] J. Shim, C. H. Lui, T. Y. Ko, Y. J. Yu, P. Kim, T. F. Heinz, and S. Ryu, "Water-gated charge doping of graphene induced by mica substrates," *Nano Letters,* vol. 12, no. 2, pp. 648-654, 2012.

[8] J. N. Israelachvili and R. M. Pashley, "The hydrophobic interaction is long range, decaying exponentially with distance," *Nature,* vol. 300, no. 25, pp. 341-342, 1982.

[9] J. N. Israelachvili and R. M. Pashley, "Molecular layering of water at surfaces and origin of repulsive hydration forces," *Nature,* vol. 306, no. 17, pp. 249-250, 1983.

[10] J. N. Israelachvili and H. Wennerström, "Role of hydration and water structure in biological and colloidal interactions," *Nature,* vol. 379, no. 18, pp. 219-255, 1996.

[11] U. Raviv and J. Klein, "Fluidity of bound hydration layers," *Science,* vol. 297, no. 5586, pp. 1540-1543, 2002.

[12] S. Granick, S. Bae, S. Kumar, and C. Yu, "Confined liquid controversies near closure?," *Physics,* vol. 3, no. 73, p. 1, 2010.

[13] S. Khan, G. Matei, S. Patil, and P. Hoffmann, "Dynamic solidification in nanoconfined water films," *Physical Review Letters,* vol. 105, no. 10, pp. 106101-106101-4, 2010.

[14] N. Severin, M. Dorn, A. Kalachev, and J. P. Rabe, "Replication of single macromolecules with graphene," *Nano Letters,* vol. 11, no. 6, pp. 2436-2439, 2011.

[15] K. Xu, P. G. Cao, and J. R. Heath, "Graphene visualizes the first water adlayers on mica at ambient conditions," *Science,* vol. 329, no. 5996, pp. 1188-1191, 2010.

[16] K. I. Bolotin, K. J. Sikes, Z. Jiang, M. Klima, G. Fudenberg, J. Hone, P. Kim, and H. L. Stormer, "Ultrahigh electron mobility in suspended graphene," *Solid State Communications,* vol. 146, no. 9-10, pp. 351-355, 2008.

[17] A. K. Geim, "Graphene: Status and prospects," *Science,* vol. 324, no. 5934, pp. 1530-15344, 2009.

[18] A. K. Geim and K. S. Novoselov, "The rise of graphene," *Nature Materials,* vol. 6, no. 3, pp. 183-191, 2007.

[19] K. S. Novoselov, A. K. Geim, S. V. Morozov, D. Jiang, M. I. Katsnelson, I. V. Grigorieva, S. V. Dubonos, and A. A. Firsov, "Two-dimensional gas of massless Dirac fermions in graphene," *Nature,* vol. 438, no. 7065, pp. 197-200, 2005.

[20] K. S. Novoselov, A. K. Geim, S. V. Morozov, D. Jiang, Y. Zhang, S. V. Dubonos, I. V. Grigorieva, and A. A. Firsov, "Electric field effect in atomically thin carbon films," *Science,* vol. 306, no. 5696, pp. 666-669, 2004.

[21] X. Du, I. Skachko, A. Barker, and E. Y. Andrei, "Approaching ballistic transport in suspended graphene," *Nature Nanotechnology,* vol. 3, no. 8, pp. 491-495, 2008.

[22] K. T. He, J. C. Koepke, S. Barraza-Lopez, and J. W. Lyding, "Separation-dependent electronic transparency of monolayer graphene membranes on III-V semiconductor substrates," *Nano Letters,* vol. 10, no. 9, pp. 3446-3452, 2010.

[23] M. Ishigami, J. H. Chen, W. G. Cullen, M. S. Fuhrer, and E. D. Williams, "Atomic structure of graphene on SiO_2," *Nano Letters,* vol. 7, no. 6, pp. 1643-1648, 2007.

[24] K. A. Ritter and J. W. Lyding, "The influence of edge structure on the electronic properties of graphene quantum dots and nanoribbons," *Nature Materials,* vol. 8, no. 3, pp. 235-242, 2009.

[25] G. M. Rutter, N. P. Guisinger, J. N. Crain, E. A. A. Jarvis, M. D. Stiles, T. Li, P. N. First, and J. A. Stroscio, "Imaging the interface of epitaxial graphene with silicon carbide via scanning tunneling microscopy," *Physical Review B,* vol. 76, no. 23, pp. 235416-235416-6, 2007.

[26] F. Schedin, A. K. Geim, S. V. Morozov, E. W. Hill, P. Blake, M. I. Katsnelson, and K. S. Novoselov, "Detection of individual gas molecules adsorbed on graphene," *Nature Materials,* vol. 6, no. 9, pp. 652-655, 2007.

[27] P. Cao, K. Xu, J. O. Varghese, and J. R. Heath, "Atomic force microscopy characterization of room-temperature adlayers of small organic molecules through graphene templating," *Journal of the American Chemical Society,* vol. 133, no. 8, pp. 2334-2337, 2011.

[28] N. Mohanty, M. Fahrenholtz, A. Nagaraja, D. Boyle, and V. Berry, "Impermeable graphenic encasement of bacteria," *Nano Letters,* vol. 11, no. 3, pp. 1270-1275, 2011.

[29] P. Cao, K. Xu, J. O. Varghese, and J. R. Heath, "The microscopic structure of adsorbed water on hydrophobic surfaces under ambient conditions," *Nano Letters,* vol. 11, no. 12, pp. 5581-5586, 2011.

[30] J. S. Bunch, S. S. Verbridge, J. S. Alden, A. M. van der Zande, J. M. Parpia, H. G. Craighead, and P. L. McEuen, "Impermeable atomic membranes from graphene sheets," *Nano Letters,* vol. 8, no. 8, pp. 2458-2462, 2008.

[31] C. H. Lui, L. Liu, K. F. Mak, G. W. Flynn, and T. F. Heinz, "Ultraflat graphene," *Nature,* vol. 462, no. 7271, pp. 339-341, 2009.

[32] C. Lee, Q. Li, W. Kalb, X.-Z. Liu, H. Berger, R. W. Carpick, and J. Hone, "Frictional characteristics of atomically thin sheets," *Science,* vol. 328, no. 5974, pp. 76-80, 2010.

[33] X. Li, W. Cai, J. An, S. Kim, J. Nah, D. Yang, R. Piner, A. Velamakanni, I. Jung, E. Tutuc, S. K. Banerjee, L. Colombo, and R. S. Ruoff, "Large-area synthesis of high-quality and uniform graphene films on copper foils," *Science,* vol. 324, no. 5932, pp. 1312-1314, 2009.

[34] X. Li, W. Cai, L. Colombo, and R. S. Ruoff, "Evolution of graphene growth on Ni and Cu by carbon isotope labeling," *Nano Letters,* vol. 9, no. 12, pp. 4268-4272, 2009.

[35] J. D. Wood, S. W. Schmucker, A. S. Lyons, E. Pop, and J. W. Lyding, "Effects of polycrystalline Cu substrate on graphene growth by chemical vapor deposition," *Nano Letters,* vol. 11, no. 11, pp. 4547-4554, 2011.

[36] S. Bhaviripudi, X. Jia, M. S. Dresselhaus, and J. Kong, "Role of kinetic factors in chemical vapor deposition synthesis of uniform large area graphene using copper catalyst," *Nano Letters,* vol. 10, no. 10, pp. 4128-4133, 2010.

[37] W. Zhang, P. Wu, Z. Li, and J. Yang, "First-principles thermodynamics of graphene growth on Cu surfaces," *The Journal of Physical Chemistry C,* vol. 115, no. 36, pp. 17782-17787, 2011.

[38] X. Li, Y. Zhu, W. Cai, M. Borysiak, B. Han, D. Chen, R. D. Piner, L. Colombo, and R. S. Ruoff, "Transfer of large-area graphene films for high-performance transparent conductive electrodes," *Nano Letters,* vol. 9, no. 12, pp. 4359-4363, 2009.

[39] Z. Wu, Z. Chen, X. Du, J. M. Logan, J. Sippel, M. Nikolou, K. Kamaras, J. R. Reynolds, D. B. Tanner, A. F. Hebard, and A. G. Rinzler, "Transparent, conductive carbon nanotube films," *Science,* vol. 305, no. 5688, pp. 1273-1276, 2004.

[40] R. R. Nair, P. Blake, A. N. Grigorenko, K. S. Novoselov, T. J. Booth, T. Stauber, N. M. R. Peres, and A. K. Geim, "Fine structure constant defines visual transparency of graphene," *Science,* vol. 320, no. 5881, p. 1308, 2008.

[41] M. D. Ellison, A. P. Good, C. S. Kinnaman, and N. E. Padgett, "Interaction of water with single-walled carbon nanotubes: Reaction and adsorption," *The Journal of Physical Chemistry B,* vol. 109, no. 21, pp. 10640-10646, 2005.

[42] W. Vedder and R. S. McDonald, "Vibrations of the OH ions in muscovite," *The Journal of Chemical Physics,* vol. 38, no. 7, pp. 1583-1590, 1963.

[43] P. Miranda, L. Xu, Y. Shen, and M. Salmeron, "Icelike water monolayer adsorbed on mica at room temperature," *Physical Review Letters,* vol. 81, no. 26, pp. 5876-5879, 1998.

[44] G. A. Kimmel, J. Matthiesen, M. Baer, C. J. Mundy, N. G. Petrik, R. S. Smith, Z. Dohnalek, and B. D. Kay, "No confinement needed: Observation of a metastable hydrophobic wetting two-layer ice on graphene," *Journal of the American Chemical Society,* vol. 131, no. 35, pp. 12838-12844, 2009.

[45] D. Donadio, G. Cicero, E. Schwegler, M. Sharma, and G. Galli, "Electronic effects in the IR spectrum of water under confinement," *The Journal of Physical Chemistry B,* vol. 113, no. 13, pp. 4170-4175, 2009.

[46] V. Crupi, S. Interdonato, F. Longo, D. Majolino, P. Migliardo, and V. Venuti, "A new insight on the hydrogen bonding structures of nanoconfined water: A Raman study," *Journal of Raman Spectroscopy,* vol. 39, no. 2, pp. 244-249, 2008.

[47] J. W. Suk, A. Kitt, C. W. Magnuson, Y. Hao, S. Ahmed, J. An, A. K. Swan, B. B. Goldberg, and R. S. Ruoff, "Transfer of CVD-grown monolayer graphene onto arbitrary substrates," *ACS Nano,* vol. 5, no. 9, pp. 6916-6924, 2011.

[48] A. Ferrari, "Raman spectroscopy of graphene and graphite: Disorder, electron-phonon coupling, doping and nonadiabatic effects," *Solid State Communications,* vol. 143, no. 1-2, pp. 47-57, 2007.

[49] D. R. Lenski and M. S. Fuhrer, "Raman and optical characterization of multilayer turbostratic graphene grown via chemical vapor deposition," *Journal of Applied Physics,* vol. 110, no. 1, pp. 013720-013720-4, 2011.

[50] S. Berciaud, S. Ryu, L. E. Brus, and T. F. Heinz, "Probing the intrinsic properties of exfoliated graphene: Raman spectroscopy of free-standing monolayers," *Nano Letters,* vol. 9, no. 1, pp. 346-352, 2008.

[51] M. Huang, H. Yan, C. Chen, D. Song, T. F. Heinz, and J. Hone, "Phonon softening and crystallographic orientation of strained graphene studied by Raman spectroscopy," *Proceedings of the National Academy of Sciences,* vol. 106, no. 18, pp. 7304-7308, 2009.

[52] X. Liang, B. A. Sperling, I. Calizo, G. Cheng, C. A. Hacker, Q. Zhang, Y. Obeng, K. Yan, H. Peng, Q. Li, X. Zhu, H. Yuan, A. R. Hight Walker, Z. Liu, L. Peng, and C. A. Richter, "Toward clean and crackless transfer of graphene," *ACS Nano,* vol. 5, no. 11, pp. 9144-9153, 2012.

[53] A. Das, S. Pisana, B. Chakraborty, S. Piscanec, S. K. Saha, U. V. Waghmare, K. S. Novoselov, H. R. Krishnamurthy, A. K. Geim, A. C. Ferrari, and A. K. Sood, "Monitoring dopants by Raman scattering in an electrochemically top-gated graphene transistor," *Nature Nanotechnology,* vol. 3, no. 4, pp. 210-215, 2008.

[54] L. M. Malard, M. A. Pimenta, G. Dresselhaus, and M. S. Dresselhaus, "Raman spectroscopy in graphene," *Physics Reports,* vol. 473, no. 5-6, pp. 51-87, 2009.

[55] Y. C. Lin, C. C. Lu, C. H. Yeh, C. H. Jin, K. Suenaga, and P. W. Chiu, "Graphene annealing: How clean can it be?," *Nano Letters,* vol. 12, no. 1, pp. 414-419, 2012.

[56] Z. Ni, Y. Wang, T. Yu, Y. You, and Z. Shen, "Reduction of Fermi velocity in folded graphene observed by resonance Raman spectroscopy," *Physical Review B,* vol. 77, no. 23, pp. 113407-113407-5, 2008.

[57] L. Cheng, P. Fenter, K. Nagy, M. Schlegel, and N. Sturchio, "Molecular-scale density oscillations in water adjacent to a mica surface," *Physical Review Letters,* vol. 87, no. 15, pp. 156103-156103-4, 2001.

[58] A. Pirkle, J. Chan, A. Venugopal, D. Hinojos, C. W. Magnuson, S. McDonnell, L. Colombo, E. M. Vogel, R. S. Ruoff, and R. M. Wallace, "The effect of chemical residues on the physical and electrical properties of chemical vapor deposited graphene transferred to SiO_2," *Applied Physics Letters,* vol. 99, no. 12, pp. 122108-122108-3, 2011.

[59] C.-C. Chen, W. Bao, J. Theiss, C. Dames, C. N. Lau, and S. B. Cronin, "Raman spectroscopy of ripple formation in suspended graphene," *Nano Letters,* vol. 9, no. 12, pp. 4172-4176, 2009.

[60] P. Y. Huang, C. S. Ruiz-Vargas, A. M. van der Zande, W. S. Whitney, M. P. Levendorf, J. W. Kevek, S. Garg, J. S. Alden, C. J. Hustedt, Y. Zhu, J. Park, P. L. McEuen, and D. A. Muller, "Grains and grain boundaries in single-layer graphene atomic patchwork quilts," *Nature,* vol. 469, no. 7330, pp. 389-392, 2010.

[61] J. C. Koepke, J. D. Wood, D. Estrada, Z.-Y. Ong, K. T. He, E. Pop, and J. W. Lyding, "Atomic-scale evidence for potential barriers and strong carrier scattering at graphene grain boundaries: A scanning tunneling microscopy study," *ACS Nano,* vol. 7, no. 1, pp. 75-86, 2013.

[62] N. Levy, S. A. Burke, K. L. Meaker, M. Panlasigui, A. Zettl, F. Guinea, A. H. Castro Neto, and M. F. Crommie, "Strain-induced pseudo-magnetic fields greater than 300 tesla in graphene nanobubbles," *Science,* vol. 329, no. 5991, pp. 544-547, 2010.

[63] P. Sutter, J. T. Sadowski, and E. Sutter, "Graphene on Pt(111): Growth and substrate interaction," *Physical Review B,* vol. 80, no. 24, pp. 245411-245411-10, 2009.

[64] R. Grantab, V. B. Shenoy, and R. S. Ruoff, "Anomalous strength characteristics of tilt grain boundaries in graphene," *Science,* vol. 330, no. 6006, pp. 946-948, 2010.

[65] S.-H. Park and G. Sposito, "Structure of water adsorbed on a mica surface," *Physical Review Letters,* vol. 89, no. 8, pp. 085501-085501-4, 2002.

[66] P. M. Albrecht and J. W. Lyding, "Ultrahigh-vacuum scanning tunneling microscopy and spectroscopy of single-walled carbon nanotubes on hydrogen-passivated Si(100) surfaces," *Applied Physics Letters,* vol. 83, no. 24, pp. 5029-5031, 2003.

[67] Information regarding HiPco single walled carbon nanotubes (Feb 15, 2012). [Online]. Available: http://www.nanointegris.com/en/hipco

[68] J. Xue, J. Sanchez-Yamagishi, D. Bulmash, P. Jacquod, A. Deshpande, K. Watanabe, T. Taniguchi, P. Jarillo-Herrero, and B. J. LeRoy, "Scanning tunnelling microscopy and spectroscopy of ultra-flat graphene on hexagonal boron nitride," *Nature Materials,* vol. 10, no. 4, pp. 282-285, 2011.

[69] Y. Zhang, V. W. Brar, C. Girit, A. Zettl, and M. F. Crommie, "Origin of spatial charge inhomogeneity in graphene," *Nature Physics,* vol. 5, no. 10, pp. 722-726, 2009.

[70] T. Bakos, S. N. Rashkeev, and S. T. Pantelides, "Reactions and diffusion of water and oxygen molecules in amorphous SiO_2," *Physical Review Letters,* vol. 88, no. 5, pp. 055508-055508-4, 2002.

[71] J. Rafiee, X. Mi, H. Gullapalli, A. V. Thomas, F. Yavari, Y. Shi, P. M. Ajayan, and N. A. Koratkar, "Wetting transparency of graphene," *Nature Materials,* vol. 11, no. pp. 217-222, 2012.

[72] T. Ohta, T. E. Beechem, J. T. Robinson, and G. L. Kellogg, "Long-range atomic ordering and variable interlayer interactions in two overlapping graphene lattices with stacking misorientations," *Physical Review B,* vol. 85, no. 7, pp. 075415-075415-7, 2012.

[73] J. T. Robinson, S. W. Schmucker, C. B. Diaconescu, J. P. Long, J. C. Culbertson, T. Ohta, A. L. Friedman, and T. E. Beechem, "Electronic hybridization of large-area stacked graphene films," *ACS Nano,* vol. 7, no. 1, pp. 637-644, 2013.

[74] Z. Li, Y. Wang, A. Kozbial, G. Shenoy, F. Zhou, R. McGinley, P. Ireland, B. Morganstein, A. Kunkel, S. P. Surwade, L. Li, and H. Liu, "Effect of airborne contaminants on the wettability of supported graphene and graphite," *Nature Materials,* vol. 12, no. pp. 925-931, 2013.

[75] M. Odelius, M. Bernasconi, and M. Parrinello, "Two dimensional ice adsorbed on mica surface," *Physical Review Letters,* vol. 78, no. 14, pp. 2855-2858-4, 1997.

[76] K. A. Ritter and J. W. Lyding, "Characterization of nanometer-sized, mechanically exfoliated graphene on the H-passivated Si(100) surface using scanning tunneling microscopy," *Nanotechnology,* vol. 19, no. 1, pp. 015704-015704-9, 2008.

[77] S. W. Schmucker, N. Kumar, J. R. Abelson, S. R. Daly, G. S. Girolami, M. R. Bischof, D. L. Jaeger, R. F. Reidy, B. P. Gorman, J. Alexander, J. B. Ballard, J. N. Randall, and J. W. Lyding, "Field-directed sputter sharpening for tailored probe materials and atomic-scale lithography," *Nature Communications,* vol. 3, no. 935, pp. 1-8, 2012.

[78] Y. C. Lin, C. H. Jin, J. C. Lee, S. F. Jen, K. Suenaga, and P. W. Chiu, "Clean transfer of graphene for isolation and suspension," *ACS Nano,* vol. 5, no. 3, pp. 2362-2368, 2011.

[79] J. Chan, A. Venugopal, A. Pirkle, S. McDonnell, D. Hinojos, C. W. Magnuson, R. S. Ruoff, L. Colombo, R. M. Wallace, and E. M. Vogel, "Reducing extrinsic performance-limiting factors in graphene grown by chemical vapor deposition," *ACS Nano,* vol. 6, no. 4, pp. 3224-3229, 2012.

[80] J. Yan, Y. B. Zhang, P. Kim, and A. Pinczuk, "Electric field effect tuning of electron-phonon coupling in graphene," *Physical Review Letters*, vol. 98, no. 16, pp. 116802-116802-4, 2007.

CHAPTER 6. HYDRATION AND INTERACTIONS IN GRAPHENE-BIOMOLECULE NANOSANDWICHES

6.1. Introduction to Biomolecule Hydration

The water around proteins, DNA, viruses, and other biomolecules ultimately determines their mobility [1]. This bound interfacial—or vicinal [2]—water has been shown to template protein surfaces [3] or even enter their hydrophobic cores [4, 5]. To date, researchers have examined vicinal water at protein surfaces by nuclear magnetic resonance (NMR) [5] and neutron and X-ray crystallography [6, 7]. NMR-based methods of vicinal water detection around proteins require small proteins, bulk solutions, and are inherently transient [4]. Conversely, X-ray crystallography measurements insist that the proteins to be non-perturbatively fixed. Further, those measurements need the H_2O to be well bound to the protein and thereby appear in electron density maps. H_2O positions in these maps often are smeared [8], making vicinal water identification challenging.

When confined between two hydrophilic surfaces, vicinal water can have orders of magnitude higher viscosity [9], but this phenomenon can change dramatically if the surfaces differ in hydrophobic character [10-13]. This suggests that confined vicinal water is still an area of hot debate [2]. Graphene, an atomically thin, two-dimensional sheet of carbon atoms [14], is allegedly hydrophobic [15] like graphite [16]. However, there have been recent reports that claim that graphene possesses wetting transparency, where the substrate's wetting character shows through the graphene [17, 18]. The controversy surrounding water and graphene makes studying that system worthwhile.

Additionally, graphene is a perfectly conformal membrane [19-21], allowing it to "shrink wrap" water [22] and encapsulate biomolecules. These shrink wrapped structures make

previously inaccessible ultrahigh vacuum (UHV) techniques like scanning tunneling microscopy (STM) and transmission electron microscopy (TEM) straightforward. Compared to NMR and X-ray crystallography, STM and TEM are direct ways to view vicinal water around and next to biomolecules. Further, STM opens the possibility of performing spectroscopy on the biomolecules and learn about their electronic band structures. Throughout the rest of this chapter, we transfer graphene under and on top of biomolecules. Our goal is to image vicinal water at the nanoscale with STM. We note that the experimental data and conclusions outlined in this chapter are still preliminary. Further clarifying experiments are currently underway.

6.2. Confirming Biomolecule Deposition and Water Entrapment

We first grow graphene using previous procedures (see Chapter 2 and references [22-26]) and transfer it with PMMA or PC (Chapter 4) on to SiO_2/Si and mica. It is imperative to get extremely clean graphene surfaces (see Chapter 4) to decouple the effects of growth- and transfer-related contaminants within our encapsulated structures. All of our transfers are wet, employing H_2O as a cleaning solvent and an adhesion promoter [27]. Through the remaining discussion, we use the term "nanosandwiches" in the following cases: for graphene on top of a biomolecule; for graphene on top a liquid on top of graphene; or, for graphene on top of a liquid with biomolecules on top of graphene. The liquid introduced in the nanosandwiches is predominantly H_2O, as will be evident shortly.

Figure 6.1 provides a general physical and chemical characterization of our graphene-biomolecule nanosandwiches. We employ viruses, proteins, and DNA in our nanosandwiches. In Fig. 6.1a, we show a schematic of the tobacco mosaic virus (TMV) [25], a rod-shaped virion that is 18 nm in diameter and 300 nm long [28, 29]. Our TMV samples have a rigid protein capsid and are filled with a single strand of viral RNA. Figures 6.1b and 6.1c reveal cartoons for the two

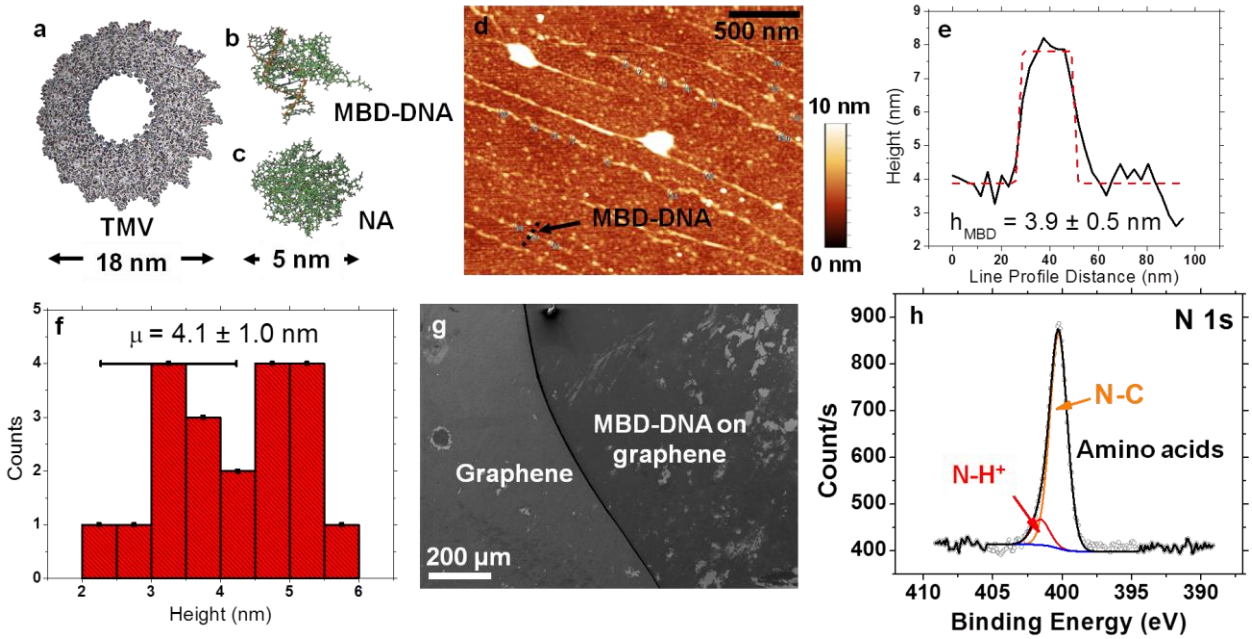

Figure 6.1. Biomolecule deposition on graphene. Cartoon schematics of the **(a)** 18 x 300 nm tobacco mosaic virus (TMV), the **(b)** 5 nm diameter methyl-binding domain (MBD1) protein complex methylated to CpG sites on 827 bp double-stranded DNA (MBD-DNA), and the **(c)** 5 nm diameter NeutrAvidin (NA) protein. **(d)** Atomic force microscopy (AFM) height image of 30:1 MBD-DNA deposited on monolayer graphene. **(e)** Height profile for a ~4 nm tall, individual MBD-DNA complex on graphene. **(f)** Height distribution for an array of MBD-DNA complexes on graphene. **(g)** Scanning electron microscopy (SEM) image of the MBD-DNA deposition dry-down area. **(h)** X-ray photoelectron spectroscopy (XPS) N 1s core level spectrum for the MBD-DNA area in (g), revealing N–C and N–H^+ bonding characteristic of the residues within MBD-DNA.

proteins we use in our experiments, the methyl-binded domain (MBD) protein [30, 31] and the NeutrAvidin (NA) protein [32], respectively. In their default folded states, both proteins are about 5 nm in diameter. The MBD protein can be covalently attached by CpG methylation [31] to 827 bp double-stranded DNA (see Section 6.6.3), giving us a MBD-DNA complex. Herein, we work with bare MBD (i.e., no DNA attachment) proteins, MBD-DNA complexes, and bare NA proteins.

We use atomic force microscopy (AFM) to confirm our biomolecule deposition on graphene, as shown for MBD-DNA complexes on graphene in Fig. 6.1d. The MBD-DNA complexes are ~4 nm in height on graphene (Figs. 6.1e and 6.1f), close to expected dimensions (ca. 4.2 nm × 4.3 nm × 5.2 nm). Further, the MBD-DNA deposition area on graphene is easily

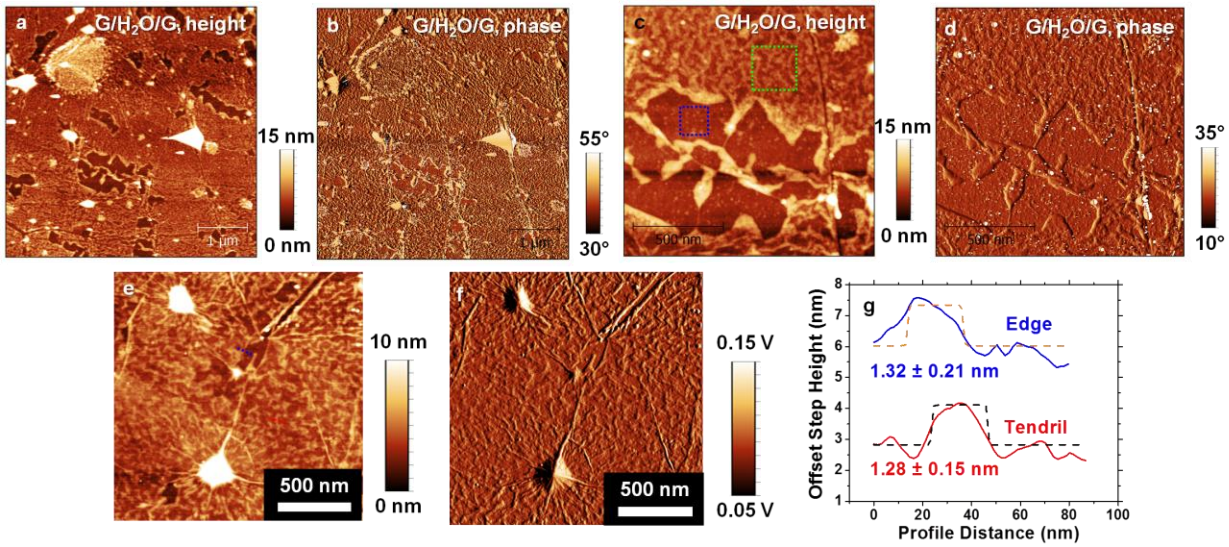

Figure 6.2. AFM images of graphene/H_2O/graphene (G/H_2O/G) nanosandwiches on SiO_2/Si. **(a)** Height image of a G/H_2O/G nanosandwich, showing smooth dark regions and filamentary structures. **(b)** Phase image for (a). The smooth (dark brown) and filamentary (lighter brown) structures are either different materials or in different states. **(c)** Zoom-in height image, demonstrating the difference between the smooth and filamentary areas. RMS roughnesses are 0.54 nm for the dark brown area (blue box) and 0.92 nm for the filamentary area (green box). **(d)** Phase image for (b). **(e)** Height image of another G/H_2O/G area, with obvious H_2O filaments and trapped, bulk H_2O (large protrusions). **(f)** Amplitude image for (e). Protrusions do not have sharp edges in the image, implying graphene encapsulation. **(g)** Height profiles for the lines in (f). The filaments and the transition regions to the smooth, dark brown areas share same height.

discerned from bare graphene, as seen in the higher contrast region of the scanning electron microscopy (SEM) image of Fig. 6.1g. Figure 6.1h gives an N 1s X-ray photoelectron spectroscopy (XPS) core level spectrum for the as-deposited MBD-DNA complex in Fig. 6.1g. These N–C and N–H^+ subpeaks at 400.3 eV and 401.6 eV, respectively, confirm the presence of amino acids and ionized buffer on the graphene [33, 34].

Our wet transfers introduce water under the graphene surface (see Chapter 5). Before we consider the effects of a wet-transferred graphene overlayer on TMV, MBD-DNA, and NA, we must look at graphene nanosandwiches with only H_2O in them. Figure 6.2 gives AFM images of graphene/H_2O/graphene (G/H_2O/G) nanosandwiches at a variety of length scales. There are filamentary and smooth morphologies apparent in Figs. 6.2a and 6.2b, respectively. The small-area scans of Figs. 6.2c and 6.2d make these morphologies more obvious. The "dark" regions in

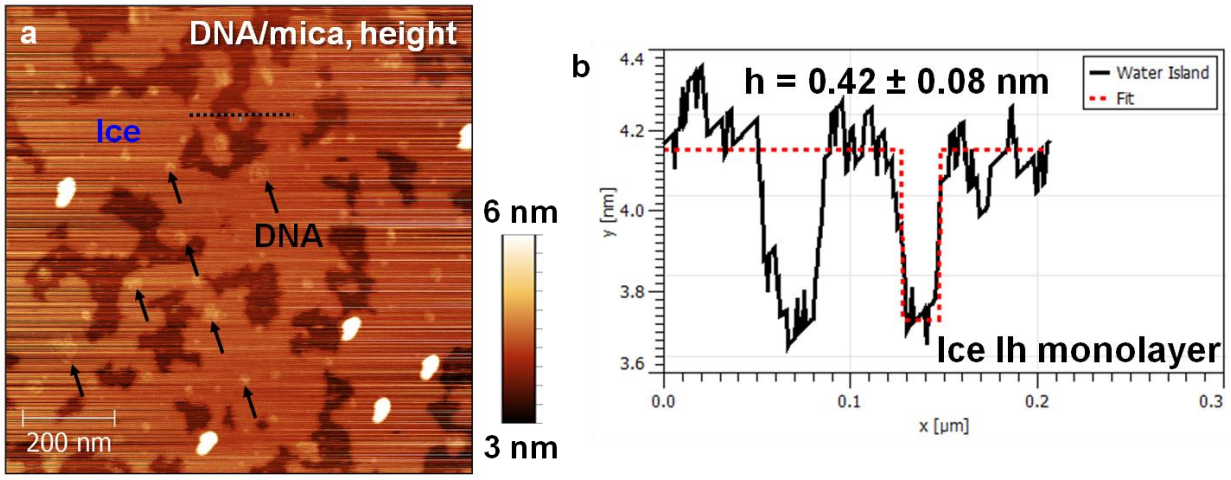

Figure 6.3. (a) AFM image of water templated by 827 bp, dsDNA. 20 µL of 2 nM dsDNA was adsorbed onto mica immediately after cleaving the mica thrice. Water forms ice Ih monolayers, and depressions in the ice monolayers originate near DNA strands. Multiple mica cleaves make the sample mechanically unstable. **(b)** Step height of the depression (black) in (a), showing the characteristic 4 Å height [36].

Figs. 6.2a and 6.2c possess a lower RMS roughness than the filamentary regions, suggesting a different trapped material there. Phase contrast (Figs. 6.2b and 6.2d) in AFM is indicative of different materials or phases [35, 36]. The images are clearly split into a dichotomy of filaments and smooth areas with no correlation to surface features. If there were two different trapped materials, we would expect point-like defects and not homogeneous layering as seen in Figs. 6.2a-d. Thus, it is likely that a single compound of differing phases is trapped in the G/H_2O/G nanosandwich. Figures 6.2e-f give a close-up height and amplitude image of the filaments in the G/H_2O/G nanosandwich. As made clear by the amplitude image, the filaments are trapped under the graphene, but they are unstructured and amorphous. The height profiles in Fig. 6.2g show that the structures are ~1.3 nm tall, corresponding to more than four ice Ih monolayers [36]. If the filaments are H_2O, then their tall, amorphous character is well-described by liquid H_2O [22].

On the other hand, ice Ih forms ordered, layered structures that are ~0.4 nm tall [22, 36]. In Figs. 6.3a, we show layered structures on a mica sample previously impregnated with 827 bp dsDNA. Dendritic depressions appear in these monolayers around the dsDNA macromolecules,

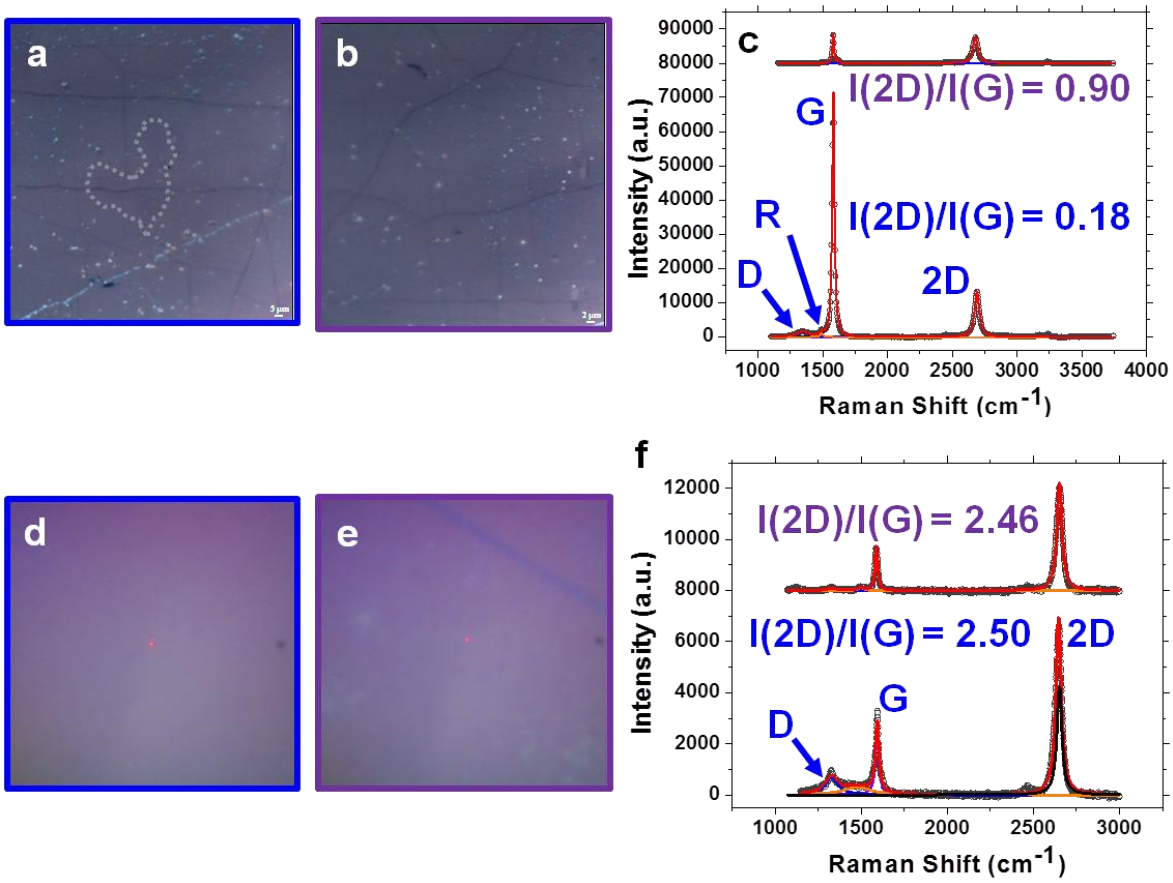

Figure 6.4. Twisted graphene bilayer nanosandwiches on SiO_2/Si. **(a)** Optical image of a G/G nanosandwich on 100 nm SiO_2/Si. Optical enhancement via van Hove singularities occurs in the dotted gray region. **(b)** Optical image of same sample as (a), except in a region without optical enhancement. **(c)** Point Raman spectra for the center of (a) (blue) and the center of (b) (purple). Raman G band is higher for (a) compared to (b) from an on-resonance bilayer electronic interaction. **(d-e)** Optical images of G/H_2O/G nanosandwiches on 90 nm SiO_2/Si. No optical enhancement evident. **(f)** Point Raman spectra for (d) and (e), following the procedure in (c). No increases in the G band occur for either spectrum. Thus, the G/G electronic interaction is suppressed by a mediating agent (H_2O).

and their heights (Fig. 6.3b) agree well with previous results [22, 36] for ice Ih monolayers. Therefore, it is possible that the dsDNA strands crystallize ice formation on mica. Our deposition process for Fig. 6.3 only introduces DNA with a buffer solution and water to the mica surface. Those types of solvents further support the conclusion that Fig. 6.3 reveals solid H_2O.

Nevertheless, we have not provided rigorous chemical or vibrational grounds to demonstrate that the G/H_2O/G nanosandwiches contain trapped H_2O. Figure 6.4 shows optical and Raman spectroscopy data on G/G nanosandwiches made with two different SiO_2 substrates

and growth recipes. For the samples in Figs. 6.4a-c, we grow the graphene by an enclosure method [37, 38], resulting in large grains (~50 to ~100 μm in dimension). Further, we use an 100 nm SiO_2/Si substrate. We use our medium grain growth recipes (Chapters 2, 4, and elsewhere [22, 23, 26]) and more hydrophilic 90 nm SiO_2/Si for the samples in Fig. 6.4d-f. Figure 6.4a shows increased optical absorbance in the region indicated by the dotted line. This increase in absorbance does not occur from a thicker graphene region (e.g. trilayer graphene) but rather by electronic interaction between the two graphene layers [38, 39]. However, a different twist angle [38, 39] between the two graphene layers in Fig. 6.4b does not produce the correct electronic interaction to result in optical absorbance enhancement. These electronic enhancements affect the Raman spectra of Fig. 6.4c, whereby the region of Fig. 6.4a shows a pronounced increase in G band [40] versus the region of Fig. 6.4b. Such enhancements are only possible if the bilayer's twist angle gives an optical enhancement [38] and if the bilayer interfaces are van der Waals bonded and uncontaminated [39, 41]. An additional R peak occurs in the spectrum from the twisted graphene superlattice [42].

Conversely, no such optical enhancements are prominent in Figs. 6.4d-e. Furthermore, the Raman spectra of Fig. 6.4f appear like turbostratic graphene [43-45], with no electronic structure enhancements [40]. Combined with the AFM data of Figs. 6.2 and 6.3, Figs. 6.4d-f imply that there is a trapped interfacial layer [41] that is preventing electronic interaction between the graphene layers. To isolate grain size as a contributing factor, we transfer large grain graphene grown in the same way [37, 38] as Figs. 6.4a-c on to our 90 nm SiO_2/Si wafers. We discover no optical or Raman enhancement, despite clean transfers (see Chapter 4). Hence, the only remaining variable is the 90 nm SiO_2/Si substrate versus the 100 nm SiO_2/Si used in Figs. 6.4a-c. We hold that our 90 nm SiO_2/Si substrate is more hydrophilic than the 100 nm SiO_2/Si,

but we have yet to produce a contact angle measurement to bear that out. A more hydrophilic SiO_2/Si surface will give trapped, interfacial H_2O in the G/H_2O/G nanosandwich via graphene wetting transparency [17, 18, 46].

We confirm the chemical identity of the trapped H_2O in Figure 6.5 by Fourier transform infrared (FTIR) spectroscopy. H_2O strongly absorbs in the IR, having fundamental OH stretching (~3400 cm^{-1}) [47-51], OH bending (~1640 cm^{-1}) [49, 50], librational (~700 cm^{-1}) [49], and

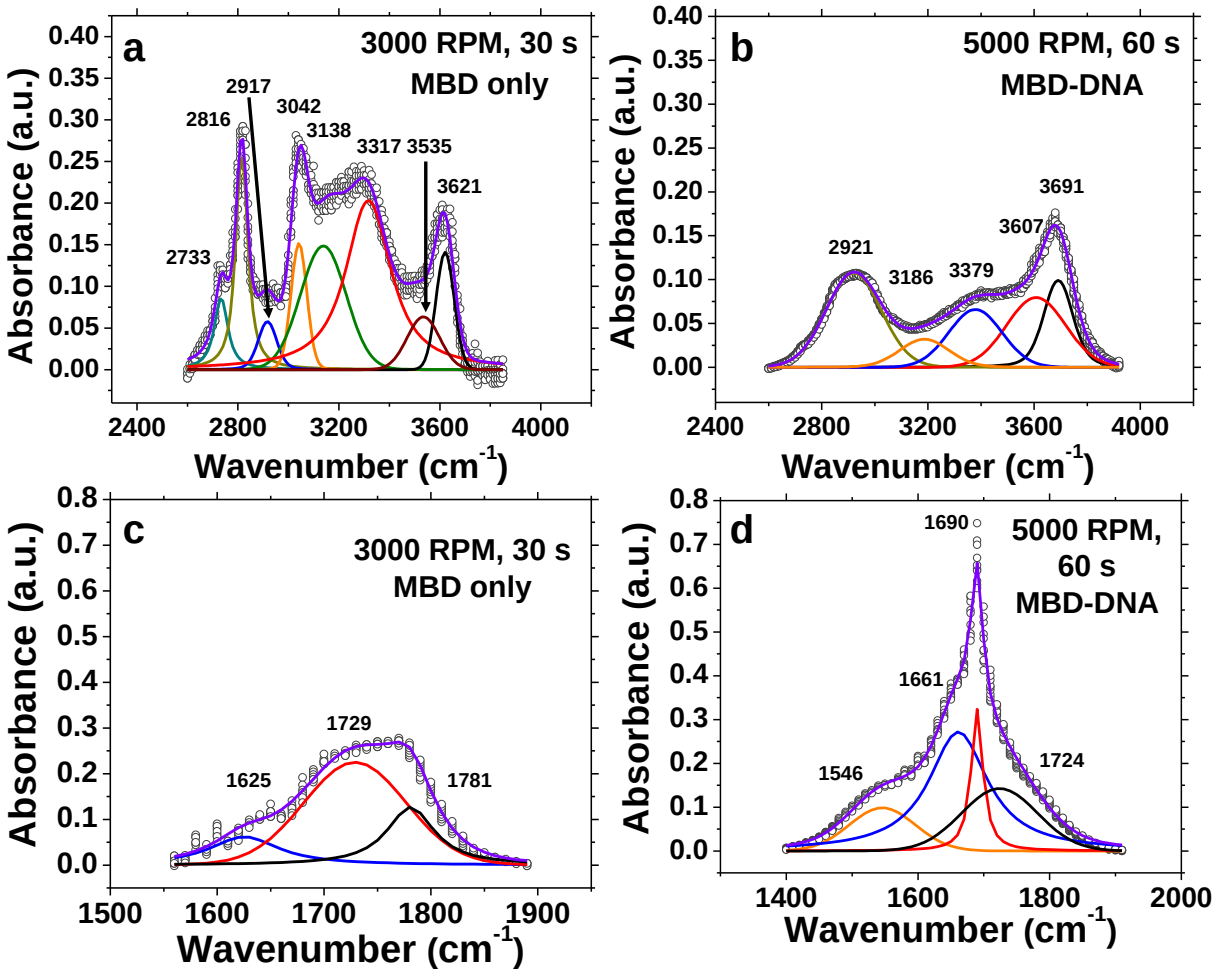

Figure 6.5. Fourier transform infrared (FTIR) spectroscopy data on G/MBD+H_2O/G and G/MBD-DNA+H_2O/G nanosandwiches on Ge. **(a)** OH stretching (ν_{OH}) spectrum for MBD proteins with H_2O encapsulated by two G sheets. Excess H_2O removed from the nanosandwich at 3000 RPM for 30 s. **(b)** ν_{OH} spectrum for MBD-DNA complexes with H_2O nanosandwiched by two G sheets. Excess H_2O removed at 5000 RPM for 60 s. **(c)** In-plane OH bending (δ_{OH}) spectrum for the sample of (a). **(d)** δ_{OH} spectrum for the sample of (d). All samples show both trapped water and amide-based vibrational modes.

OH…O connectivity (~100 cm^{-1}) [49] modes. We fit all of our spectra in Fig. 6.5 with Voigt functions under a linear baseline, following a previous report [52]; these Voigt lineshapes give lower residuals than merely Gaussian or Lorentzian subpeaks. The OH stretching band (ν_{OH}) about ~3400 cm^{-1} can be decomposed into four Voigt subbands. The two high wavenumber subbands at ~3650 cm^{-1} and ~3580 cm^{-1}, respectively, correspond to unassociated H_2O monomers (e.g. liquid H_2O) and poorly connected, H-bonded H_2O networks [47, 49, 50]. Conversely, the two low wavenumber subbands at ~3400 cm^{-1} and ~3200 cm^{-1}, respectively, correspond to more strongly H-bonded H_2O networks, with the ~3200 cm^{-1} band having the highest degree of H-bonding coordination, like ice [47, 49, 50]. The OH in-plane bending band (δ_{OH}) can similarly be decomposed into subbands based on phase. For δ_{OH}, ice has a band at ~1655 cm^{-1}, whereas liquid and vapor H_2O are at ~1630 cm^{-1} and ~1595 cm^{-1} [53].

With the preceding information, we can analyze the H_2O structures assessed in Fig. 6.5. Both Figs. 6.5a and 6.5b show liquid H_2O, with strong unassociated H_2O subbands at ~3621 cm^{-1} and 3691 cm^{-1}, respectively. The separation between these subbands could be caused by graphene-induced confinement [54] or a by a superposition of the OH and protein-based N–H stretching bands [55, 56]. IR measurements of G/H_2O/G nanosandwiches without biomolecules will clarify this point. Regardless, further analysis of the remaining subbands in Figs. 6.5a and 6.5b prove that the biomolecule nanosandwiches have co-existing domains of liquid and strongly H-bonded H_2O [50]. We then examine the H_2O association band at ~2125 cm^{-1} [57] for the G/MBD-DNA+H_2O/G and G/MBD+H_2O/G nanosandwiches. This band is characteristic of only liquid H_2O and does not overlap with protein vibrational signatures [56]. We take a ratio of the H_2O association band's area to adjacent CO_2-related bands to get a quantitative estimate of the amount of liquid H_2O present in each nanosandwich. From this, we find that the G/MBD+H_2O/G

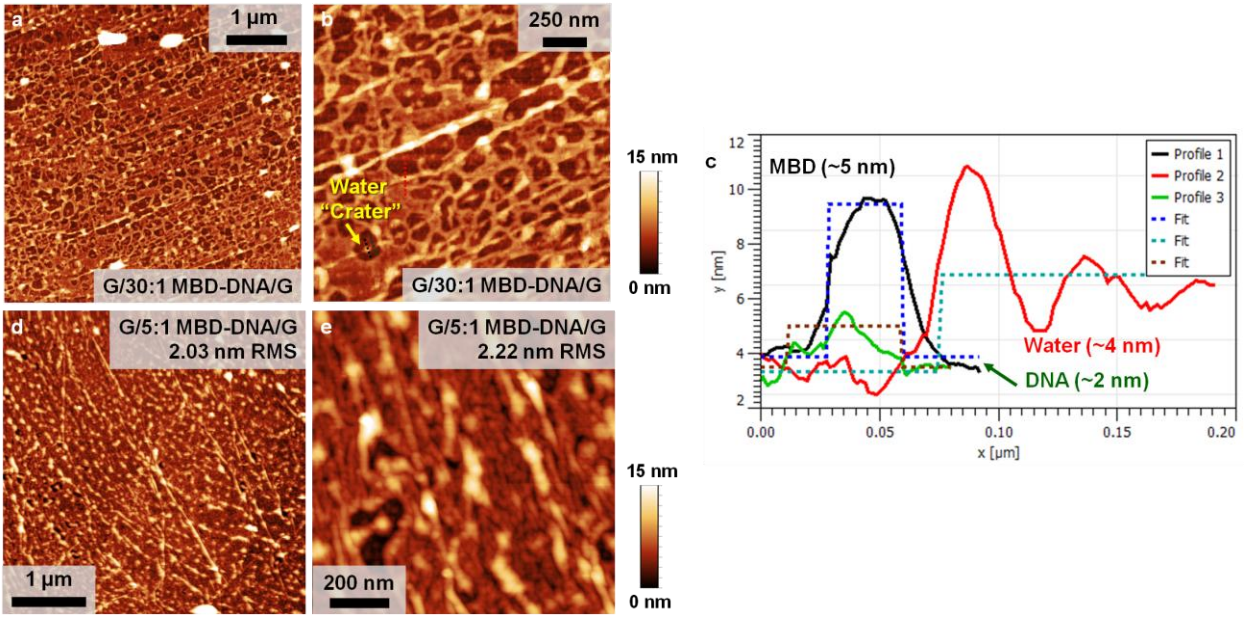

Figure 6.6. AFM imaging of G/MBD-DNA/G nanosandwiches on 90 nm SiO_2/Si. Large-area **(a)** and small-area **(b)** height images of 30:1 MBD-DNA complexes deposited between two graphene sheets. Liquid H_2O is present, and H_2O depressions ("craters") exist with bumps in them. **(c)** Height profiles corresponding to the lines in (b). The 5 nm height of the bumps in the craters suggest that they are MBD proteins. Large-area **(d)** and small-area **(e)** height image of 5:1 MBD-DNA complexes deposited within two graphene sheets. H_2O depressions are not present, implying that there is critical DNA concentration to achieve them.

nanosandwich has 3.6× more liquid H_2O than the G/MBD-DNA+H_2O/G nanosandwich. Thus, the increased H-bonding in the G/MBD-DNA+H_2O/G nanosandwich is consistent with DNA-induced water crystallization (Fig. 6.3).

In Figs. 6.5a and 6.5b, all of the subbands below 3100 cm^{-1} are related to the amide bands [56] from the trapped MBD or MBD-DNA biomolecules. Figures 6.5c and 6.5d give the in-plane bending mode δ_{OH} for the samples in Figs. 6.5a and 6.5b. Both figures have a band about ~1720 cm^{-1} that is related to carbonyl (C=O) stretching [50]. Figure 6.5c has a weak liquid H_2O band at ~1620 cm^{-1}, but this band is superimposed by protein vibrations in Fig. 6.5d. Neither spectrum shows a band for other H_2O phases [53]. The subband at ~1546 cm^{-1} in Fig. 6.5d is unequivocally a protein-based amide II vibration [56]. Also, the absorptions at 1661 cm^{-1} and 1690 cm^{-1} in Fig. 6.5d are likely amide I MBD1 vibrations, but it is challenging to decouple them

from the ubiquitous H_2O [56]. That notwithstanding, Fig. 6.5 makes evident the graphene encapsulation of both H_2O and biomolecules.

6.3. Biomolecule Hydration and Pressure Denaturation

Figure 6.6 gives AFM height information on our G/MBD-DNA/G nanosandwiches on SiO_2/Si, using a 30:1 (see Section 6.6.3) and a 5:1 MBD-DNA solution for deposition. These nanosandwiches also have trapped H_2O in them (Fig. 6.5). In Figs. 6.6a and 6.6b, there are regions where the trapped H_2O is screened by the presence of the 30:1 MBD-DNA complex. This results in H_2O "craters," each of which has a central protrusion. The central protrusion is ~5 nm in height, as apparent in Fig. 6.6c; the MBD1 protein is ~4 to ~5 nm in diameter, so we identify this protrusion as a MBD1 protein methylated to dsDNA. Across the entire image of Fig. 6.6b, we find MBD heights of $\langle h \rangle = 3.9 \pm 0.8$ nm. In addition, the accompanying dsDNA and liquid H_2O regions in Fig. 6.6c are in agreement with their expected heights. The phase images for Figs. 6.6a and 6.6b show that the depressions are qualitatively similar to Figs. 6.2b and 6.2d, respectively. Thus, it is possible that the H_2O craters are G/ice/G or G/G nanosandwiches. By finding a moiré superstructure within the H_2O craters by scanning tunneling microscopy (STM), one could conclude whether there was trapped ice or not.

Based on the CpG methylation process [31], a 30:1 MBD-DNA complex can have up to 22 MBD1 proteins attached to 827 bp dsDNA. A 5:1 MBD-DNA complex, on the other hand, can have up to 3 MBD1 proteins on 827 bp dsDNA. The MBD1 protein (PDB ID: 1IG4) has an estimated adsorption energy of ~0.56 eV/molecule on graphene [58], large enough to promote good MBD1 adhesion (Fig. 6.1). Still, to get the H_2O craters, the DNA strands need to be present, as they crystallize the local water (Figs. 6.3 and 6.5). Thus, one must successfully attach the MBD to the DNA to produce water depressions, and this process is quite sensitive to the

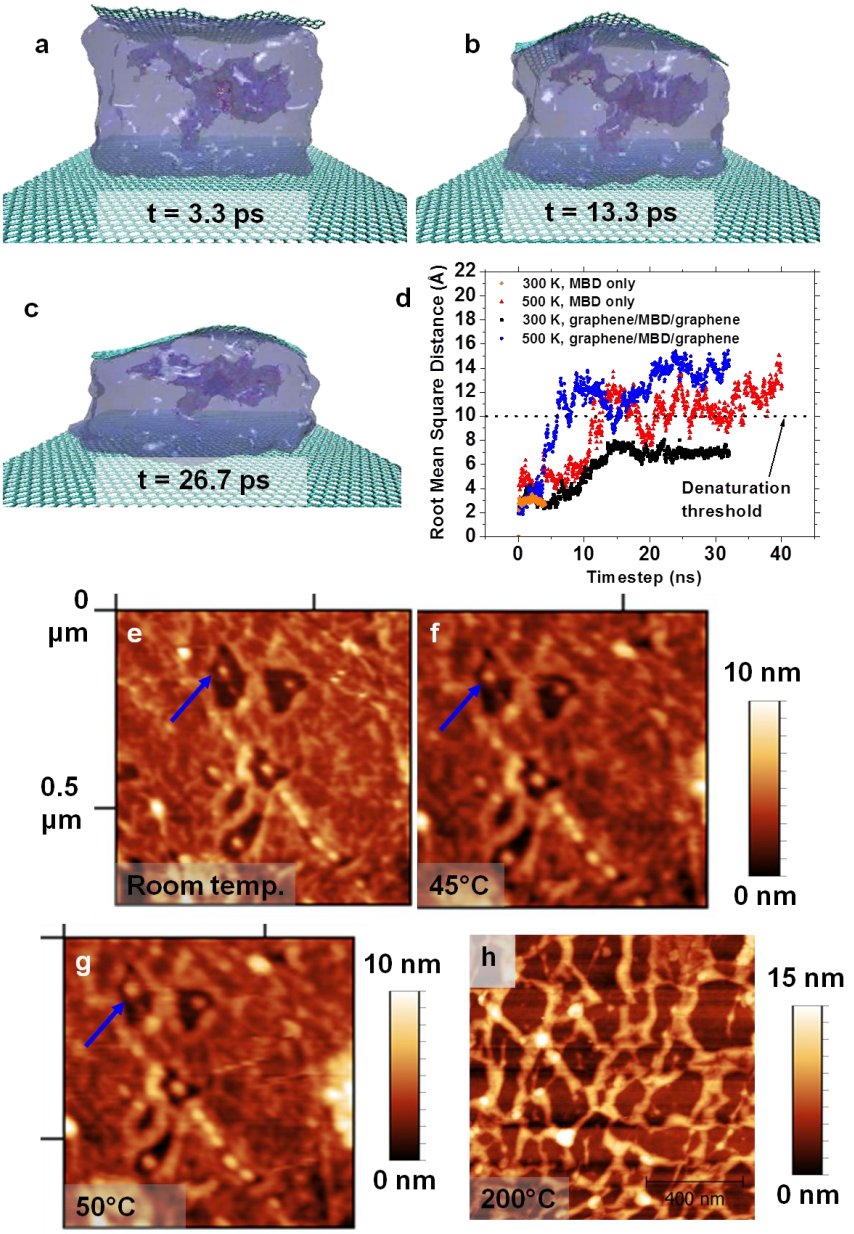

Figure 6.7. Pressure denaturation in G/MBD/G nanosandwiches. Molecular dynamics (MD) simulation of a G/MBD/G nanosandwich at **(a)** t = 3.3 ps, **(b)** t = 13.3 ps, and **(c)** t = 26.7 ps. The MBD protein undergoes extreme hydrostatic pressure as the top graphene sheet collapses. **(d)** Root-mean-square displacement (RMSD) for bare MBD proteins and G/MBD/G nanosandwiches. 300 K and 500 K simulated for both systems. Graphene encapsulation causes partial, pressure-induced denaturation, and both systems denature at 500 K. AFM height images of the same G/MBD-DNA/G area at **(e)** room-temperature, **(f)** 45 °C, and **(g)** 50 °C. The feature in question does not change, suggesting that it had already denatured prior to measurement. **(h)** A similar G/MBD-DNA/G region after 200 °C annealing, with the protein-related protrusions still evident.

starting MBD to DNA concentrations. Therefore, an entrapped 5:1 MBD-DNA complex will likely give fewer H_2O depressions in a G/MBD-DNA/G nanosandwich. This is indeed the case,

as made evident in Figs. 6.6d and 6.6e, respectively; no water depressions are obvious, and the MBD1 proteins tend to agglomerate (~8 nm in height).

Figures 6.7a-d reveal molecular dynamics (MD) simulations of the MBD1 protein nanosandwiched between two graphene sheets. In the simulations, we fix the bottom graphene sheet, let the top sheet be free to move (see Section 6.6.6 and following), and apply periodic boundary conditions elsewhere. As the simulation advances (Figs. 6.7a-c), the graphene overlayer collapses on the MBD1 protein, applying a ~2 GPa hydrostatic pressure (Section 6.6.8) to the protein. Such pressures were recently reported in a synthetic graphene-diamond cell [59]. Moreover, this hydrostatic pressure is far in excess of any other reported pressure applied to proteins [60-62]. Thus, the proteins likely undergo pressure denaturation [61], whereby the water in Figs. 6.7a-c is forced into the MBD1 hydrophobic core. Figure 6.7d bears this conclusion out; we plot the root-mean-squared-displacement (RMSD) as a function of time for both the bare MBD protein and for the G/MBD/G nanosandwich. A protein with a RMSD value exceeding 10 Å is considered denatured (either by temperature or by pressure) [63]. From Fig. 6.7d, the MBD proteins within the G/MBD/G nanosandwich are almost completely pressure denatured at room temperature (300 K). Not surprisingly, both the bare and nanosandwiched MBD denature when the temperature is elevated to 500 K.

If the proteins were already denatured by the graphene-induced, 2 GPa hydrostatic pressure, then we would not expect them to morphologically change as we approached their melting temperature [64]. In Figs. 6.7e-g, we give temperature-dependent AFM height data for a single MBD-DNA complex nanosandwiched between two graphene layers. The images show no change in the MBD-DNA protrusion as the temperature goes from 45 °C to 80 °C (80 °C data not shown), supporting the idea that the complexes are already denatured. The protein

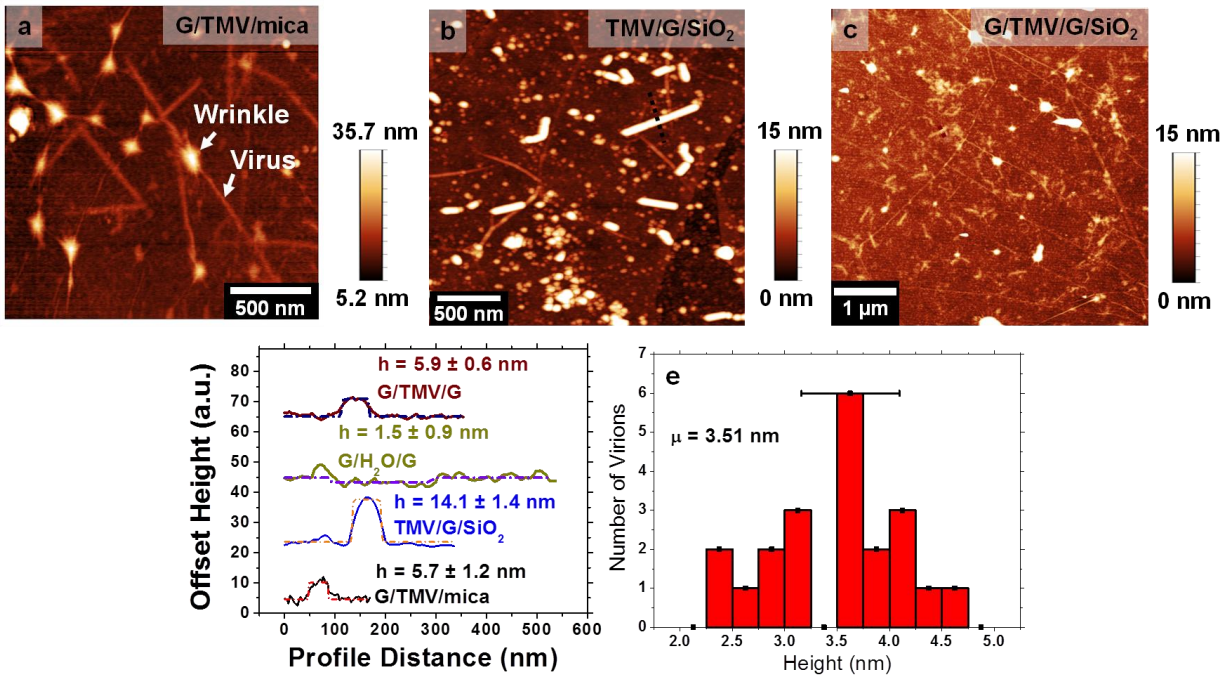

Figure 6.8. AFM imaging of TMV-based nanosandwiches on mica and 90 nm SiO_2/Si. **(a)** Graphene-encapsulated TMV on mica. **(b)** TMV on top of a graphene sheet on SiO_2/Si. **(c)** G/TMV/G nanosandwich on SiO_2/Si. **(d)** Height profiles for the features in (a-c). Note that the TMV height is the same whether the underlying substrate is graphene or mica. **(e)** Height distribution for the virions in (c), with an average encapsulated TMV height of ~3.5 nm.

protrusions remain even after high temperature treatment. Figure 6.7h shows a height image for a different region in the sample of Figs. 6.7e-g after 200 °C annealing. Therefore, the MBD-DNA complexes are pressure denatured by the graphene overlayer.

To further our understanding of pressure denaturation in the graphene-biomolecule nanosandwiches, we encapsulate the TMV under and between graphene layers. Figure 6.8a shows a height image of TMV virions encapsulated by a graphene sheet on mica. Unlike MBD-DNA, no unusual hydration patterns are present for the encapsulated TMV. Figures 6.8b and 6.8c give images of TMV on graphene/SiO_2/Si before and after graphene nanosandwiching, respectively. The TMV are ~14 nm (Fig. 6.8d) before graphene nanosandwiching, shorter than the expected ~18 nm (Fig. 6.1a) from strong graphene adsorption forces. Still, all of the graphene encapsulated TMV (Figs. 6.8a and 6.8c) have heights about ~3.5 nm (Fig. 6.8d), a fourfold height decrease. Using the discussion of Arkhipov et al. [28], we find that a fourfold decrease in

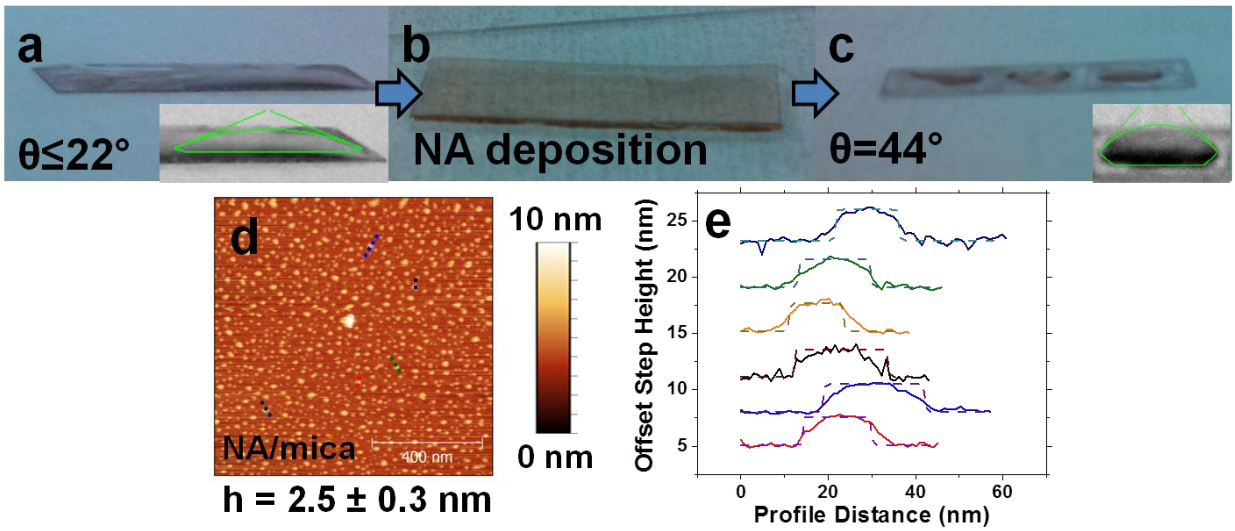

Figure 6.9. Characteristics of NA protein deposition on mica. **(a)** Photograph of a water droplet on freshly cleaved mica surface. Contact angle θ is 22° based on the best fit of the image. **(b)** Photograph of the sample in (a) after NA deposition (wetting). **(c)** Photograph of water on the NA-deposited sample in (b). The NA is incubated for 5 min, N_2 dried, and then rinsed in DI H_2O five times. Contact angle θ is 44°, and thus the sample is more hydrophobic than (a). **(d)** AFM height image of NA on mica, giving a height of 2.5 ± 0.3 nm from strong NA adsorption. **(e)** Height profiles for (d).

TMV height corresponds to a hydrostatic pressure of ~0.8 GPa. Such a large pressure would certainly denature the TMV. Thus, the TMV deformation is consistent with our pressure denaturation predictions for MBD-DNA under a graphene sheet (Fig. 6.7). Using Raman spectroscopy (not shown), we can also calculate the hydrostatic pressure in our G/MBD/G nanosandwiches. Hydrostatic pressure induces strain splitting [65] in the nanosandwich's two graphene layers. From the separation of each graphene sheet's G band, we find a hydrostatic pressure of P = 1.4 ± 0.6 GPa. This is also consistent with our theoretical and experimental findings surrounding pressure denaturation.

6.4. Nanoscale Vicinal Water

We also use another protein, NA, to examine hydration within graphene-biomolecule nanosandwiches. Figure 6.9 shows our deposition process for putting NA on mica samples. The NA deposition makes the surface more hydrophobic (Fig. 6.9c). The NA proteins strongly adsorb on the charged mica surface [66], lowering their expected height to 2.5 ± 0.3 nm (Figs. 6.9d and

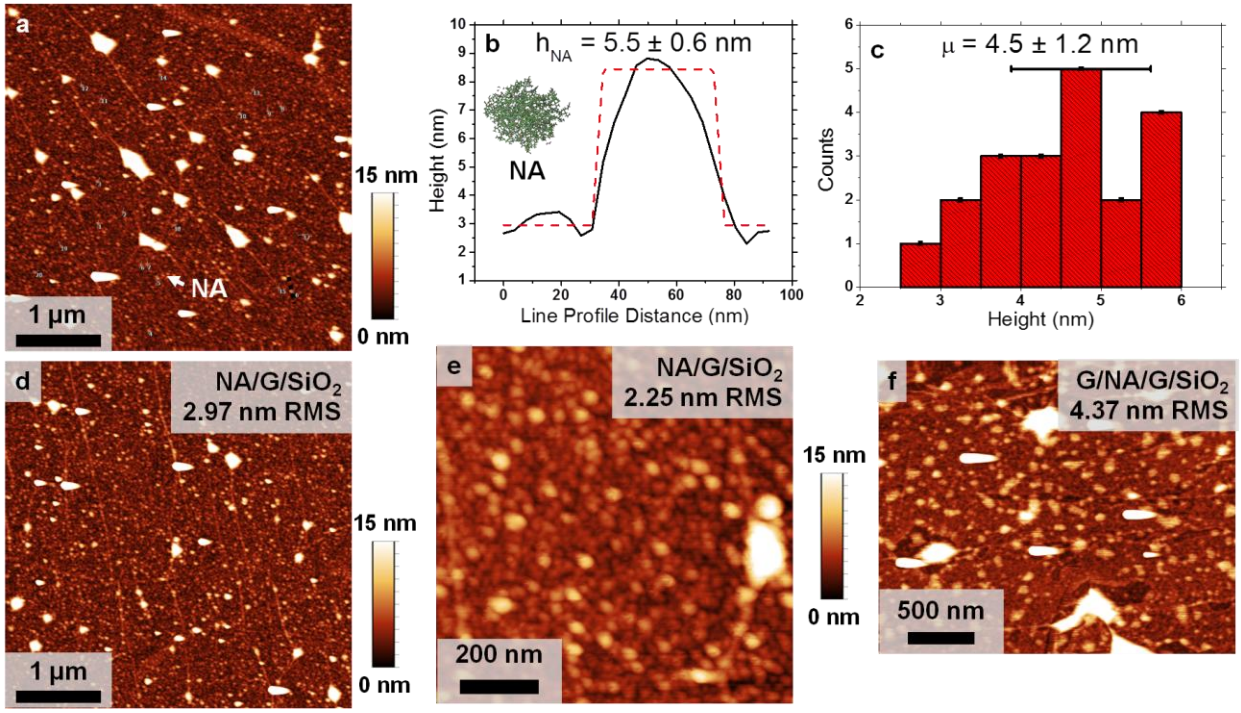

Figure 6.10. Graphene/NA/graphene nanosandwiches on 90 nm SiO_2/Si. **(a)** AFM height image of NA as as deposited on G/SiO_2/Si. Surface is rough by nearly complete NA coverage. **(b)** Height profile of an individual NA protein, with secondary structure shown inset. **(c)** Height distribution for NA proteins, centered about 4.5 ± 1.2 nm. Dimensions are similar to MBD. Large-area **(d)** and small-area **(e)** AFM images of NA on G/SiO_2 before nanosandwiching. Both surfaces are fully impregnated by NA proteins, as confirmed by the high RMS roughness values. **(f)** G/NA/G nanosandwich, showing predominantly liquid H_2O some small H_2O craters.

6.9e). The NA/mica surface contact angle of ~44° is markedly similar to graphene on Cu [17]. This suggests that graphene encapsulation of NA will potentially have similar wetting characteristics to the G/MBD-DNA/G nanosandwiches.

We briefly examine G/NA/G nanosandwiches on SiO_2/Si in Fig. 6.10. Figures 6.10a,d,e all show a high degree of NA adsorption on a graphene sheet on SiO_2. NA (PDB ID: 1VYO) also has an estimated adsorption energy of 0.56 eV per molecule [58]. The NA proteins on graphene are not as strongly adsorbed as on mica (Fig. 6.9d), resulting in an overall ~4.5 nm height (Figs. 6.10b,c) closer to the expected, as-folded dimensions (Fig. 6.1c). Figure 6.10f reveals a G/NA/G nanosandwich. The graphene overlayer is perfectly conformal and, for the most part, there are no H_2O "craters" are present. This implies that a majority of the sample has entrapped liquid H_2O,

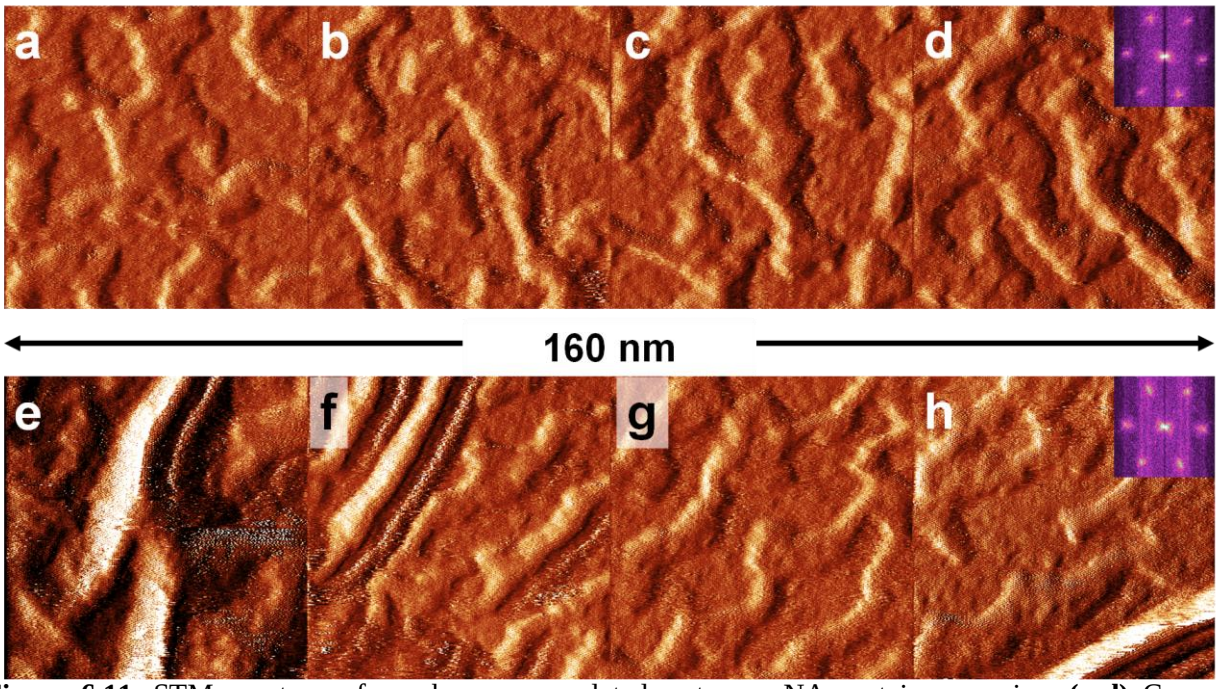

Figure 6.11. STM montage of graphene-encapsulated water on NA proteins on mica. **(a-d)** Current images showing the protein-induced hydration patterns. Images correspond to their actual spatial locations. *Inset, (d)*: FFT of (d), showing the hexagonal reciprocal lattice for graphene. **(e-h)** Additional montage images, horizontally continued from (d). Graphene wrinkles evident in (e) and (h). *Inset, (h)*: FFT of (h), again showing the graphene reciprocal lattice. Images (d) and (h) have the same FFT pattern, implying that the graphene is monocrystalline over those regions.

but we will need to do FTIR measurements to confirm this. We will note that NA samples with DNA (not shown) do exhibit H_2O craters, again supporting the notion the local DNA strands crystallize H_2O (Figs. 6.3 and 6.5) in the graphene-biomolecule nanosandwiches.

We then return to the quasi-hydrophobic NA/graphene surface on mica (Fig. 6.9). We deposit ~1 μM of NA proteins (see Section 6.6.4) on freshly cleaved mica, giving a densely populated (Fig. 6.10) mica surface. Avidin and streptavidin have previously formed tetramers on ultraflat graphite [67], and the concentrated deposition conditions used here likely give isolated NA tetramers or even a complete NA monolayer [68]. We will also note that tetrameric proteins can produce dewetting, hydrophobic exclusion regions [69] for vicinal water. After encapsulating with a graphene overlayer, we produce G/NA+H_2O/mica nanosandwiches, and we

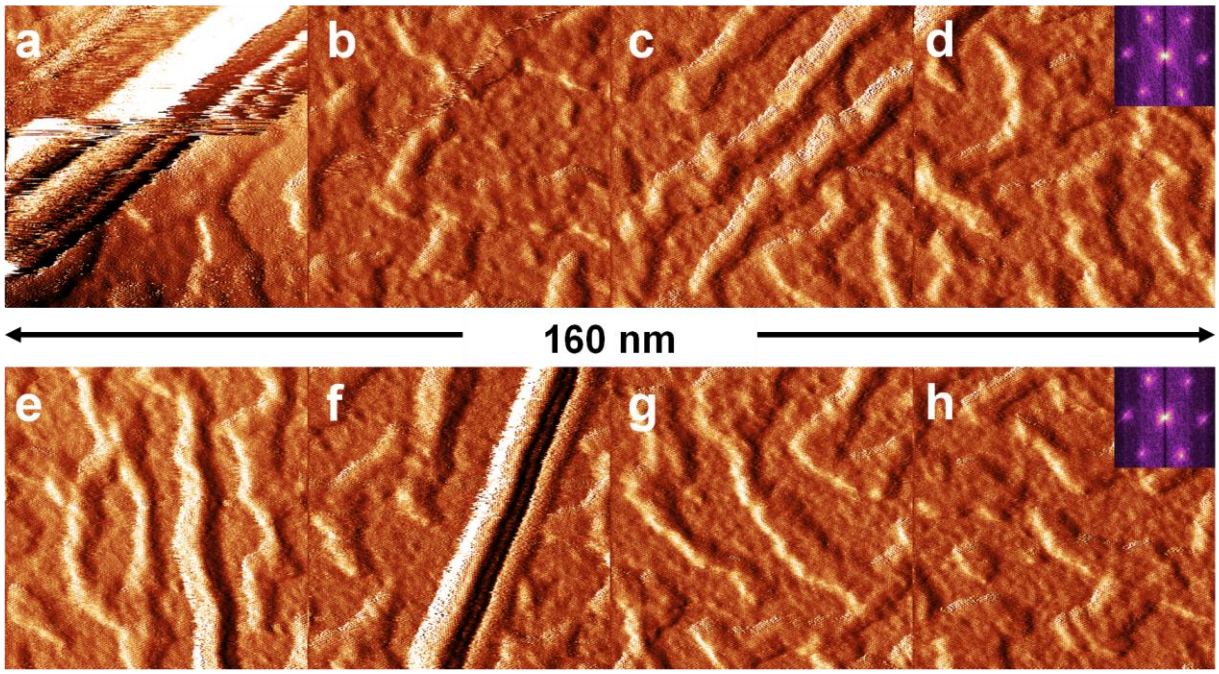

Figure 6.12. Second STM montage of graphene-encapsulated water on NA proteins on mica. **(a-d)** Current images showing the hydration patterns induced by the NA proteins. Images correspond to their actual spatial locations. *Inset, (d)*: FFT of (d), showing the hexagonal reciprocal lattice for graphene. **(e-h)** Additional montage images, horizontally continued from (d). Wrinkles and protein-related bumps apparent. *Inset, (h)*: FFT of (h), again showing the graphene reciprocal lattice.

then image them with UHV-STM after an in situ 130 °C degas. NA proteins have a melting temperature well above 100 °C [70], making temperature denaturation by the degas less likely.

Figure 6.11 shows a series of STM current images for the G/NA+H_2O/mica nanosandwich, all collected at 0.5 nA and –0.5 V (391.41 Å × 391.41 Å image size). Figures 6.11a-h are all taken in spatial succession, that is, each image is spatially located to the next. We give a fast Fourier transform (FFT) in the insets on Figs. 6.11d,h; we observe graphene's hexagonal reciprocal lattice in those FFT images. We do not show FFT images for every subplot in Fig. 6.11, but they all show graphene's reciprocal lattice. Two distinct wetting patterns are present in Fig. 6.11; STM topograph images show that they differ in height by 4 Å, consistent with water layers on mica (Chapter 5 and reference [22]). Nevertheless, these patterns are not as continuous as the water patterns seen for graphene on water on mica [22], implying that the NA

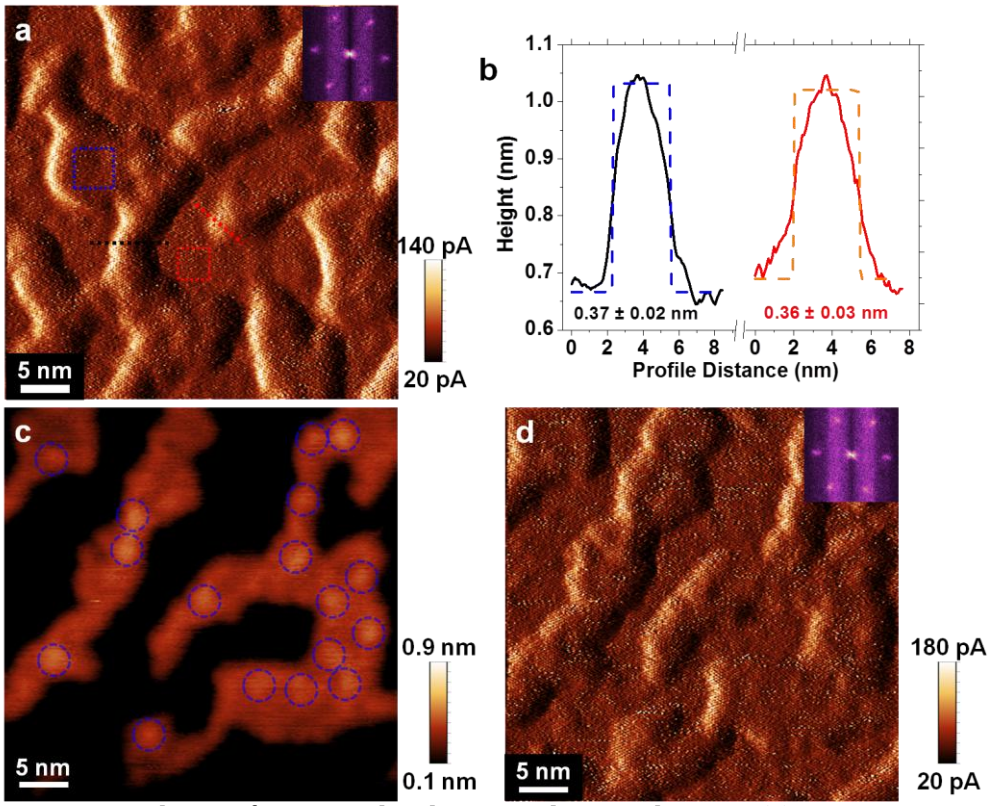

Figure 6.13. STM evidence of NA-templated, nanoscale vicinal water. **(a)** STM current image of the G/NA+H_2O/mica nanosandwich, showing complex water patterns. Root-mean-square roughness is 0.33 Å and 0.27 Å for the second (blue box) and first (red box) H_2O layers. **Inset:** FFT of the image, showing the hexagonal reciprocal lattice for graphene. **(b)** Height profiles for the red and blue lines in (a), showing the expected ~4 Å for H_2O. **(c)** STM height image of the same sample, revealing hydration patterns mediated by the NA proteins (blue circles). **(d)** STM current image of (c), confirming the conformal nature of the graphene shrink wrap. **Inset:** FFT of the image, again giving graphene structure.

proteins are mediating the nanoscale hydration. In fact, the patterns are well described as two phases separated via spinodal dewetting [71]. By using the step height for a H_2O monolayer (4 Å), we can fit the nanoscale water heights through the established Cahn-Hilliard equation [72], corroborating the conclusion that spinodal dewetting is occurring in the G/NA+H_2O/mica nanosandwich. We also find that the surface tension of the H_2O is 9× that of the bulk [71] .

Further, the patterns are stable, not changing after nanomanipulation or successive scans [22]. We also do not observe any moiré superstructures between the graphene and H_2O layers, implying that the H_2O layers are not hydrogen-bonded. If the layers had any crystalline character, then moiré patterns would be obvious in the graphene. The observed phenomena can

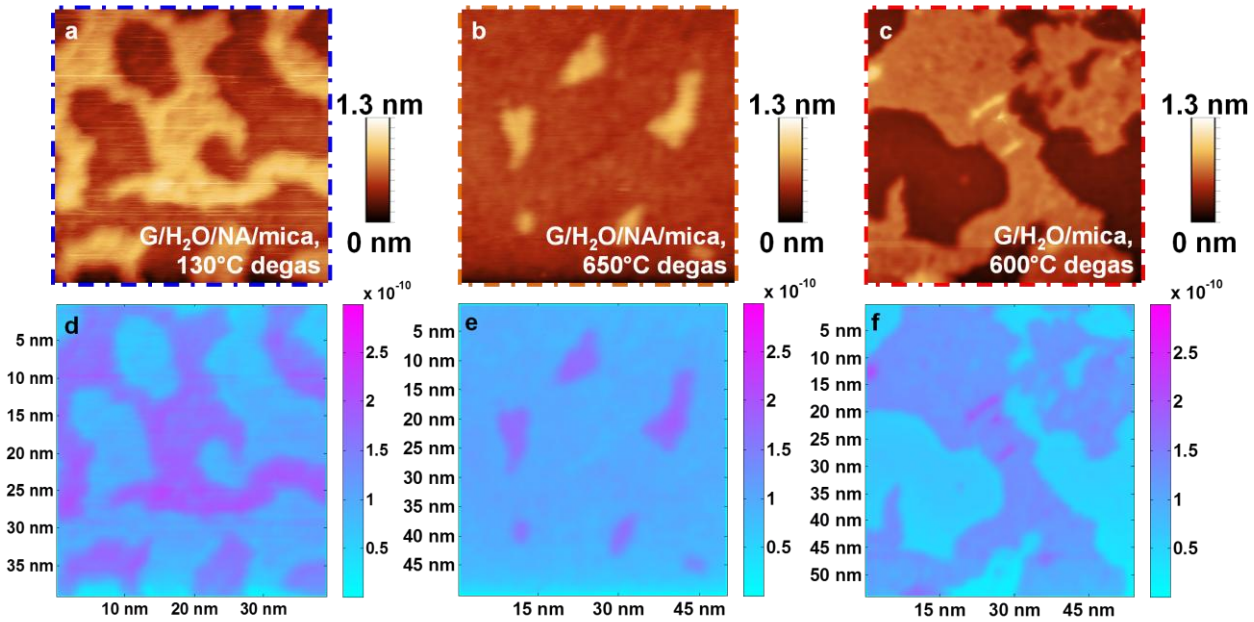

Figure 6.14. Nanoscale roughness measurements for G/NA+H_2O/mica and G/H_2O/mica nanosandwiches. **(a)** STM topograph of the G/NA+H_2O/mica nanosandwich in Figs. 6.11-13, showing NA-templated, vicinal water. **(b)** STM topograph of the nanosandwich in (a) after a 650 °C in situ degas. H_2O islands have predominantly disappeared. **(c)** STM topograph of a G/H_2O/mica nanosandwich from reference [22]. **(d-f)** Nearest neighbor root-mean-square (RMS) roughness measurements for the topographs in (a-c), respectively. H_2O water layers are smoother on the G/H_2O/mica nanosandwiches versus the G/NA+H_2O/mica nanosandwiches.

be explained if the H_2O is liquid but highly viscous [9] from the hydrostatically pressured environment. For spinodal dewetting [71], the pattern's growth rate R_M is inversely proportional to the viscosity, which is 0.001 Pa·s for bulk, liquid H_2O at 20 °C. Thus, the only way the growth rate would be near zero (i.e., stable) is if the vicinal water's viscosity was orders of magnitude higher [9] than bulk H_2O. Figure 6.12 shows a different area in the G/NA+H_2O/mica nanosandwich; the montage shows similar vicinal water dewetting.

We give evidence of the NA proteins templating the vicinal water in Fig. 6.13. Figure 6.13a reveals an atomic-resolution current image of the G/NA+H_2O/mica nanosandwich (0.5 nA, –0.5 V, 391.41 Å × 391.41 Å image size). The atomic-scale H_2O patterns are again similar to the larger area scans of Figs. 6.11 and 6.12, and the step heights of the H_2O layers are ~3.7 Å (Fig. 6.13b). In the STM topograph of Fig. 6.13c, we can see that the second H_2O layer is templated

by 17 bright protrusions (blue circles). Additional protrusions also occur in the first H_2O layer, as evident in the topograph of Fig. 6.12b. If a ~5 nm diameter NA protein (Fig. 6.1c) were to be fully pressure denatured by graphene-induced hydrostatic pressure, a ~12 nm^2 NA residue "sheet" would result. Since avidin proteins are known to be tetrameric [67], one would expect the surface area of a denatured set of tetrameric NA proteins to be between ~12 and ~48 nm^2. Notably, the surface area of the second water layer in Fig. 6.13c is ~792 nm^2, which gives 47 nm^2 per circular protrusion (17 total). This area of influence is in good agreement with what we expect for denatured, tetrameric NA proteins. The STM current image of Fig. 6.13d confirms successful graphene encapsulation.

Figure 6.14 reveals nanoscale roughness calculations for G/NA+H_2O/mica and G/H_2O/mica (from reference [22]) nanosandwiches. Figures 6.14a-c give STM topographs for the different nanosandwiches and in situ degas conditions. We calculate the root-mean-squared (RMS) roughness from the STM topographs using two nearest-neighbor height pixels. The number of H_2O layers decreases considerably from the 130 °C (Fig. 6.14a) to the 650 °C degas case (Fig. 6.14b). During the 650 °C degas, the extra nanosandwiched H_2O likely escapes through the edges [73] or through the mica bulk by supercriticality [59]. All of H_2O layers in the G/NA+H_2O/mica nanosandwiches are rougher (Figs. 6.14d,e) than entrapped H_2O in the water-only nanosandwiches (Fig. 6.14f). We collected the data for Figs. 6.14a and 6.14b on different STM systems and with different tips [74], thereby ruling out spurious system and tip effects in the data collection. Figures 6.14b and 6.14c were degassed under similar conditions, but they have distinctly different RMS roughnesses (Fig. 6.15). Therefore, we conclude that the larger RMS roughness in the G/NA+H_2O/mica nanosandwiches results from a trapped, interfacial protein layer.

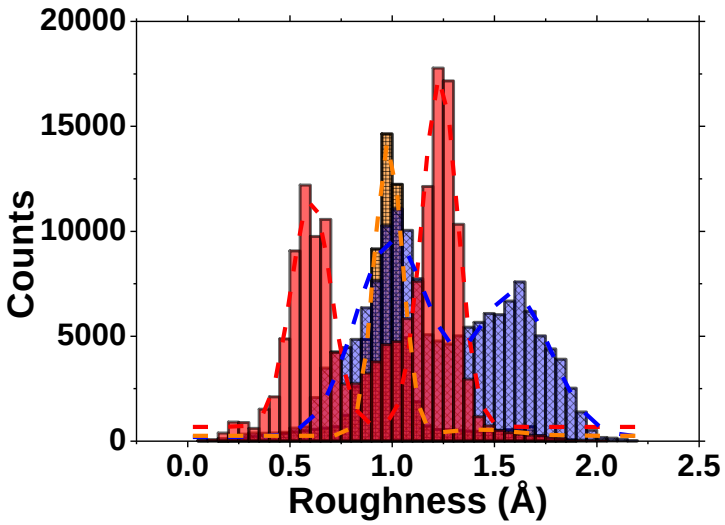

Figure 6.15. RMS roughness distribution for the 130 °C degassed G/NA+H_2O/mica nanosandwich (blue), the 650 °C degassed G/NA+H_2O/mica nanosandwich (orange), and the 600 °C degassed G/H_2O/mica nanosandwich (red) from reference [22]. The bipartite distributions result from the two entrapped H_2O layers. NA nanosandwiches have higher RMS roughness, and both degas conditions converge on the same RMS roughness value for layer 1 H_2O ($\sigma = 1.0 \pm 0.4$ Å).

6.5. Conclusions

Nanoscale vicinal water is critical for DNA sequencing [75], water desalination [76], and protein folding [3], but its characterization has been the source of great controversy [2]. We examined these controversies by imaging vicinal water between two seemingly hydrophobic [17, 18, 46] graphene layers. We shrink-wrapped water and TMV, MBD-DNA complexes, and NA proteins under a cleanly transferred (Chapter 4) graphene overlayer, producing vicinal, highly viscous [9] water at graphene-biomolecule interfaces. FTIR data revealed coexisting domains of liquid and clustered, hydrogen-bonded water in the graphene-biomolecule nanosandwiches. The graphene shrink wrap exerted up to 2 GPa hydrostatic pressures at these interfaces, as evident from detailed MD simulations deformations in the TMV capsid [28]. Such hydrostatic pressures denature the biomolecules [61, 62], inserting water into their hydrophobic cores. With AFM and UHV-STM, we produced observation of vicinal water in graphene-biomolecule nanosandwiches. This highly viscous water is stable and cannot be manipulated with the STM probe, unlike

graphene-encapsulated water on mica [22]. The water crystallizes near MBD-DNA complexes and spinodally dewets [71] around pressure-denatured NA proteins. Our platform allowed us to explore fundamental aspects of the hydrophobic effect around the biomolecules and elucidated protein hydration at the atomic level. Using graphene as a conformal, shrink wrapping membrane for biomolecules had not been examined previously. Therefore, this study will have broad implications in both the graphene and biophysical communities.

6.6. Materials and Methods

6.6.1. Graphene Growth and Transfer

Graphene was grown using chemical vapor deposition (CVD) following previously established procedures and the details outlined in Chapters 2, 4, and 5. We transferred most of our graphene layers using poly(bisphenol A carbonate) (PC), which gives atomically clean graphene surfaces. When we used poly(methyl methacrylate) (PMMA) for graphene transfer, we made sure to anneal the samples in Ar/H_2 forming gas for 90 min at 400 °C (Chapter 4).

6.6.2. Tobacco Mosaic Viruses (TMV)

Tobacco mosaic viruses (TMV) were kindly provided by Sadia Bekal in the Department of Agricultural and Biological Engineering at the University of Illinois at Urbana-Champaign. Briefly, the TMV were extracted from infected tobacco leaves via centrifugation. The murky white supernatant was drawn out after centrifugation. We deposited 10 to 40 μL of this concentrated TMV solution on to our graphene sheets on SiO_2/Si or on freshly cleaved, bare mica. The droplets of TMV solution were incubated for 5 min before being blown off by dry N_2. Then, we rinsed the sample five times in DI water. We then either imaged the sample or transferred a graphene layer over the deposited TMV.

6.6.3. Methyl-Binded Domain Protein with DNA (MBD-DNA)

We used the MBD1 protein (PDB ID: 1IG4, 75 residue sequence: M-A-E-D-W-L-D-C-P-A-L-G-P-G-W-K-R-R-E-V-F-R-K-S-G-A-T-C-G-R-S-D-T-Y-Y-Q-S-P-T-G-D-R-I-R-S-K-V-E-L-T-R-Y-L-G-P-A-C-D-L-T-L-F-D-F-K-Q-G-I-L-C-Y-P-A-P-K) in the methyl-binded domain (MBD) protein family for all the MBD experiments (ca. 4.2 nm × 4.3 nm × 5.2 nm, total weight 17 kDa). We employed ds-DNA that was 827 base pairs (bp) long (ca. 280 nm, total weight 511.586 kDa). We stabilized our pre-methylated MBD complexes in glycerol until they were diluted and mixed with DNA. We prepared MBD-DNA complexes in two different concentrations, 5:1 and 30:1 MBD:DNA. The base DNA concentration was 1 nM, giving 5 nM and 30 nM MBD concentrations for the 5:1 and 30:1 MBD-DNA solutions, respectively. The DNA solution buffer was 10 mM Tris–HCl with 1 mM EDTA at pH = 7.4 (the TE solution). For the 30:1 and 5:1 solutions, 15 μL was deposited on cleaned graphene and incubated for 10 min. Then, we blew the excess fluid off with dry N_2 and rinsed the sample five times in DI water.

6.6.4. NeutrAvidin (NA) Proteins

We also used the NeutrAvidin (NA) protein (Thermo Scientific, Inc.), which is a deglycosylated version of avidin (PDB ID: 1VYO, 128 residue sequence: A-R-K-C-S-L-T-G-K-W-T-N-D-L-G-S-N-M-T-I-G-A-V-N-S-R-G-E-F-T-G-T-Y-I-T-A-V-T-A-T-S-N-E-I-K-E-S-P-L-H-G-T-Q-N-T-I-N-K-R-T-Q-P-T-F-G-F-T-V-N-W-K-F-S-E-S-T-T-V-F-T-G-Q-C-F-I-D-R-N-G-K-E-V-L-K-T-M-W-L-L-R-S-S-V-N-D-I-G-D-D-W-K-A-T-R-V-G-I-N-I-F-T-R-L-R-T-Q-K-E) with a nearly neutral isoelectric point (pH ~ 6.3). The NA protein possessed similar dimensions (ca. 5.5 nm × 5.5 nm × 4.8 nm, total weight 60 kDa) to the MBD protein. The base NA concentration was 1 μM for the AFM and STM samples in Figs. 6.10 to 6.14. The NA solution buffer was 10 mM Tris–HCl at pH = 7.4 (the TE solution). For the sample in Fig. 6.9,

the NA concentration was 2 nM. All NA solutions were deposited on cleaned graphene on SiO_2/Si or freshly cleaved, bare mica and incubated for 5 min. Then, the excess fluid was blown off with dry N_2; any buffer residues were further removed by rinsing the samples five times in DI water.

6.6.5. Scanning Tunneling Microscopy (STM)

Au contacts were evaporated onto the samples using a shadow mask. We used a homebuilt, room-temperature UHV system with a base pressure of $\sim 5\times10^{-11}$ torr for STM measurements. Mica samples were degassed in the UHV-STM system by direct-current heating through a n^{++} Si backing at the temperatures previously listed for several hours. We acquired STS data with standard lock-in techniques and found only graphene-related electronic band structure. Our STM tips were made of etched W and PtIr wire and were sharpened [74].

6.6.6. Molecular Dynamics (MD) Simulation

Molecular dynamics (MD) simulation was performed using LAMMPS software [77]. Temperature was maintained at 300 K by using a Nose-Hoover thermostat with a time constant of 0.1 ps. Periodic boundary condition were applied in all three directions. A TIP3P model [78] was used for H_2O. Lennard-Jones parameters for C atoms were $\sigma = 0.339$ nm and $\varepsilon = 0.2897$ kJ/mol [79]. The CHARMM (charmm27) force field was used to describe the protein [80]. The total number of atoms was from 21002 to 24218 atoms, depending on whether or not the graphene sheets were included. C atoms were frozen to their lattice position to prevent out-of-plane displacement. The simulation was ran with NVT ensemble for 1 ns to attain equilibrium. The equilibrium density of bulk water reservoir was around 1 g/cm^3. After equilibration, the simulation was run for an additional 30-40 ns.

6.6.7. Root-Mean-Squared-Displacement (RMSD) Calculations

One of the ways used to determine whether or not a protein is denatured is by measuring the root-mean-squared-displacement (RMSD) of the alpha-carbon atoms of the protein. Usually, an RMSD value of about 2 Å or fewer is indicative of a protein that is stable and has not denatured. A value of 10 Å or more is indicative of a protein that has denatured [63].

The first case we ran was of the protein placed in a water bath at room temperature (300 K). The RMSD was then measured and, as shown earlier, the value was about 2 Å, which is expected of the protein at room temperature. The second case we tried was trapping the protein between two graphene sheets at 300 K. We determined that the RMSD was much higher than 2 Å, almost reaching the 10 Å cut-off point. This implies that the MBD protein was almost fully denatured just by being trapped between the graphene sheets.

To further our study, we decided to make the top graphene sheet flexible/free by using the AIREBO potential [81]. This time, we calculated the pressure the protein was experiencing just due to the graphene and the highest recorded pressure we observed was about 1.97 GPa. Details about how the pressure was calculated are available in the next section. These pressures are well in excess of the highest pressures examined in prior pressure denaturation reports [60-62]. Thus, the induced pressure denatures the MBD1 proteins.

6.6.8. Pressure Calculation

The pressure that we calculated in our MD simulations was the atomistic pressure, which we obtained by calculating the per-atom stress tensor and dividing its components by the volume of our protein. The stress tensor was calculated by:

$$S_{ab} = -\left[\begin{array}{l} mv_a v_b + \frac{1}{2}\sum_{n=1}^{Np}\left(r_{1a}F_{1b} + r_{2a}F_{2b}\right) + \frac{1}{2}\sum_{n=1}^{Nb}\left(r_{1a}F_{1b} + r_{2a}F_{2b}\right) + \\ \frac{1}{3}\sum_{n=1}^{Na}\left(r_{1a}F_{1b} + r_{2a}F_{2b} + r_{3a}F_{3b}\right) + \frac{1}{4}\sum_{n=1}^{Nd}\left(r_{1a}F_{1b} + r_{2a}F_{2b} + r_{3a}F_{3b} + r_{4a}F_{4b}\right) + \\ \frac{1}{4}\sum_{n=1}^{Ni}\left(r_{1a}F_{1b} + r_{2a}F_{2b} + r_{3a}F_{3b} + r_{4a}F_{4b}\right) + Kspace\left(r_{ia}, F_{ib}\right) + \sum_{n=1}^{Nf} r_{ia}F_{ib} \end{array}\right] \quad (6.1)$$

where the first term is the kinetic energy contribution, the second term is the pairwise energy contribution, and the third term is a bond contribution. Further, there is a term for the KSpace contribution from long-range Coulombic interactions and a term for the internal constraint forces onto the atom [82].

6.7. References

[1] W. Saenger, "Structure and dynamics of water surrounding biomolecules," *Annual Review of Biophysics and Biophysical Chemistry,* vol. 16, no. 1, pp. 93-114, 1987.

[2] P. Ball, "Chemical physics: How to keep dry in water," *Nature,* vol. 423, no. 6935, pp. 25-26, 2003.

[3] A. E. Eriksson, W. A. Baase, X. J. Zhang, D. W. Heinz, M. Blaber, E. P. Baldwin, and B. W. Matthews, "Response of a protein structure to cavity-creating mutations and its relation to the hydrophobic effect," *Science,* vol. 255, no. 5041, pp. 178-183, 1992.

[4] G. Otting, E. Liepinsh, and K. Wuthrich, "Protein hydration in aqueous solution," *Science,* vol. 254, no. 5034, pp. 974-980, 1991.

[5] J. A. Ernst, R. T. Clubb, H. X. Zhou, A. M. Gronenborn, and G. M. Clore, "Demonstration of positionally disordered water within a protein hydrophobic cavity by NMR," *Science,* vol. 267, no. 5205, pp. 1813-1817, 1995.

[6] T. L. Blundell and L. N. Johnson, *Protein Crystallography*. Philadelphia, PA: Academic Press, 1976.

[7] M. Levitt and B. H. Park, "Water: Now you see it, now you don't," *Structure,* vol. 1, no. pp. 223-226, 1993.

[8] M. M. Teeter, "Water-protein interactions: Theory and experiment," *Annual Review of Biophysics and Biophysical Chemistry,* vol. 20, no. 1, pp. 577-600, 1991.

[9] Y. Zhu and S. Granick, "Viscosity of interfacial water," *Physical Review Letters,* vol. 87, no. 9, pp. 096104-096104-4, 2001.

[10] N. Giovambattista, P. J. Rossky, and P. G. Debenedetti, "Effect of pressure on the phase behavior and structure of water confined between nanoscale hydrophobic and hydrophilic plates," *Physical Review E,* vol. 73, no. 4, pp. 041604-041604-14, 2006.

[11] G. Hummer, J. C. Rasaiah, and J. P. Noworyta, "Water conduction through the hydrophobic channel of a carbon nanotube," *Nature,* vol. 414, no. 6860, pp. 188-190, 2001.

[12] A. Kalra, S. Garde, and G. Hummer, "Osmotic water transport through carbon nanotube membranes," *Proceedings of the National Academy of Sciences,* vol. 100, no. 18, pp. 10175-10180, 2003.

[13] X. Zhang, Y. Zhu, and S. Granick, "Hydrophobicity at a Janus interface," *Science,* vol. 295, no. 5555, pp. 663-666, 2002.

[14] K. S. Novoselov, A. K. Geim, S. V. Morozov, D. Jiang, M. I. Katsnelson, I. V. Grigorieva, S. V. Dubonos, and A. A. Firsov, "Two-dimensional gas of massless Dirac fermions in graphene," *Nature,* vol. 438, no. 7065, pp. 197-200, 2005.

[15] Q. H. Wang, Z. Jin, K. K. Kim, A. J. Hilmer, G. L. C. Paulus, C.-J. Shih, M.-H. Ham, J. D. Sanchez-Yamagishi, K. Watanabe, T. Taniguchi, J. Kong, P. Jarillo-Herrero, and M. S. Strano, "Understanding and controlling the substrate effect on graphene electron-transfer chemistry via reactivity imprint lithography," *Nature Chemistry,* vol. 4, no. 9, pp. 724-732, 2012.

[16] F. M. Fowkes, "Dispersion force contributions to surface and interfacial tensions, Contact angles, and heats of immersion," in *Contact Angle, Wettability, and Adhesion,* vol. 43, Washington, DC: American Chemical Society, 1964, pp. 99-111.

[17] Z. Li, Y. Wang, A. Kozbial, G. Shenoy, F. Zhou, R. McGinley, P. Ireland, B. Morganstein, A. Kunkel, S. P. Surwade, L. Li, and H. Liu, "Effect of airborne contaminants on the wettability of supported graphene and graphite," *Nature Materials,* vol. 12, no. pp. 925-931, 2013.

[18] J. Rafiee, X. Mi, H. Gullapalli, A. V. Thomas, F. Yavari, Y. Shi, P. M. Ajayan, and N. A. Koratkar, "Wetting transparency of graphene," *Nature Materials,* vol. 11, no. pp. 217-222, 2012.

[19] J. S. Bunch, S. S. Verbridge, J. S. Alden, A. M. van der Zande, J. M. Parpia, H. G. Craighead, and P. L. McEuen, "Impermeable atomic membranes from graphene sheets," *Nano Letters,* vol. 8, no. 8, pp. 2458-2462, 2008.

[20] J. M. Yuk, K. Kim, B. Alemán, W. Regan, J. H. Ryu, J. Park, P. Ercius, H. M. Lee, A. P. Alivisatos, M. F. Crommie, J. Y. Lee, and A. Zettl, "Graphene veils and sandwiches," *Nano Letters,* vol. 11, no. 8, pp. 3290-3294, 2011.

[21] J. M. Yuk, J. Park, P. Ercius, K. Kim, D. J. Hellebusch, M. F. Crommie, J. Y. Lee, A. Zettl, and A. P. Alivisatos, "High-resolution EM of colloidal nanocrystal growth using graphene liquid cells," *Science,* vol. 336, no. 6077, pp. 61-64, 2012.

[22] K. T. He, J. D. Wood, G. P. Doidge, E. Pop, and J. W. Lyding, "Scanning tunneling microscopy study and nanomanipulation of graphene-coated water on mica," *Nano Letters,* vol. 12, no. 6, pp. 2665-2672, 2012.

[23] J. C. Koepke, J. D. Wood, D. Estrada, Z.-Y. Ong, K. T. He, E. Pop, and J. W. Lyding, "Atomic-scale evidence for potential barriers and strong carrier scattering at graphene grain boundaries: A scanning tunneling microscopy study," *ACS Nano,* vol. 7, no. 1, pp. 75-86, 2013.

[24] P. K. Mohseni, A. Behnam, J. D. Wood, C. D. English, J. W. Lyding, E. Pop, and X. Li, "$In_xGa_{1-x}As$ nanowire growth on graphene: Van der Waals epitaxy induced phase segregation," *Nano Letters,* vol. 13, no. 3, pp. 1153-1161, 2013.

[25] J. D. Wood, S. W. Schmucker, R. T. Haasch, G. P. Doidge, L. Nienhaus, G. L. Damhorst, A. S. Lyons, M. Gruebele, R. Bashir, E. Pop, and J. W. Lyding, "Improved graphene growth and fluorination on Cu with clean transfer to surfaces," in *IEEE Conference on Nanotechnology,* 2012, pp. 1-4.

[26] J. D. Wood, S. W. Schmucker, A. S. Lyons, E. Pop, and J. W. Lyding, "Effects of polycrystalline Cu substrate on graphene growth by chemical vapor deposition," *Nano Letters,* vol. 11, no. 11, pp. 4547-4554, 2011.

[27] Z. Wu, Z. Chen, X. Du, J. M. Logan, J. Sippel, M. Nikolou, K. Kamaras, J. R. Reynolds, D. B. Tanner, A. F. Hebard, and A. G. Rinzler, "Transparent, conductive carbon nanotube films," *Science,* vol. 305, no. 5688, pp. 1273-1276, 2004.

[28] A. Arkhipov, W. H. Roos, G. J. L. Wuite, and K. Schulten, "Elucidating the mechanism behind irreversible deformation of viral capsids," *Biophysical Journal,* vol. 97, no. 7, pp. 2061-2069, 2009.

[29] R. R. Nair, P. Blake, J. R. Blake, R. Zan, S. Anissimova, U. Bangert, A. P. Golovanov, S. V. Morozov, A. K. Geim, K. S. Novoselov, and T. Latychevskaia, "Graphene as a transparent conductive support for studying biological molecules by transmission electron microscopy," *Applied Physics Letters,* vol. 97, no. 15, pp. 153102-153102-3, 2010.

[30] I. Ohki, N. Shimotake, N. Fujita, J.-G. Jee, T. Ikegami, M. Nakao, and M. Shirakawa, "Solution structure of the methyl-CpG binding domain of human MBD1 in complex with methylated DNA," *Cell,* vol. 105, no. 4, pp. 487-497, 2001.

[31] J. Shim, G. I. Humphreys, B. M. Venkatesan, J. M. Munz, X. Zou, C. Sathe, K. Schulten, F. Kosari, A. M. Nardulli, G. Vasmatzis, and R. Bashir, "Detection and quantification of methylation in DNA using solid-state nanopores," *Scientific Reports,* vol. 3, no. 2013.

[32] M. Moro, M. Pelagi, G. Fulci, G. Paganelli, P. Dellabona, G. Casorati, A. G. Siccardi, and A. Corti, "Tumor cell targeting with antibody-avidin complexes and biotinylated tumor necrosis factor α," *Cancer Research,* vol. 57, no. 10, pp. 1922-1928, 1997.

[33] O. Olivares, N. V. Likhanova, B. Gómez, J. Navarrete, M. E. Llanos-Serrano, E. Arce, and J. M. Hallen, "Electrochemical and XPS studies of decylamides of α-amino acids adsorption on carbon steel in acidic environment," *Applied Surface Science,* vol. 252, no. 8, pp. 2894-2909, 2006.

[34] A. Sadough Vanini, J. P. Audouard, and P. Marcus, "The role of nitrogen in the passivity of austenitic stainless steels," *Corrosion Science,* vol. 36, no. 11, pp. 1825-1834, 1994.

[35] R. García and R. Pérez, "Dynamic atomic force microscopy methods," *Surface Science Reports,* vol. 47, no. 6-8, pp. 197-301, 2002.

[36] K. Xu, P. G. Cao, and J. R. Heath, "Graphene visualizes the first water adlayers on mica at ambient conditions," *Science,* vol. 329, no. 5996, pp. 1188-1191, 2010.

[37] X. Li, C. W. Magnuson, A. Venugopal, R. M. Tromp, J. B. Hannon, E. M. Vogel, L. Colombo, and R. S. Ruoff, "Large-area graphene single crystals grown by low-pressure chemical vapor deposition of methane on copper," *Journal of the American Chemical Society,* vol. 133, no. 9, pp. 2816-2819, 2011.

[38] J. T. Robinson, S. W. Schmucker, C. B. Diaconescu, J. P. Long, J. C. Culbertson, T. Ohta, A. L. Friedman, and T. E. Beechem, "Electronic hybridization of large-area stacked graphene films," *ACS Nano,* vol. 7, no. 1, pp. 637-644, 2013.

[39] T. Ohta, T. E. Beechem, J. T. Robinson, and G. L. Kellogg, "Long-range atomic ordering and variable interlayer interactions in two overlapping graphene lattices with stacking misorientations," *Physical Review B,* vol. 85, no. 7, pp. 075415-075415-7, 2012.

[40] K. Kim, S. Coh, L. Z. Tan, W. Regan, J. M. Yuk, E. Chatterjee, M. F. Crommie, M. L. Cohen, S. G. Louie, and A. Zettl, "Raman spectroscopy study of rotated double-layer graphene: Misorientation-angle dependence of electronic structure," *Physical Review Letters,* vol. 108, no. 24, pp. 246103-246103-4, 2012.

[41] S. J. Haigh, A. Gholinia, R. Jalil, S. Romani, L. Britnell, D. C. Elias, K. S. Novoselov, L. A. Ponomarenko, A. K. Geim, and R. Gorbachev, "Cross-sectional imaging of individual

layers and buried interfaces of graphene-based heterostructures and superlattices," *Nature Materials,* vol. 11, no. 9, pp. 764-767, 2012.

[42] V. Carozo, C. M. Almeida, E. H. M. Ferreira, L. G. Cançado, C. A. Achete, and A. Jorio, "Raman signature of graphene superlattices," *Nano Letters,* vol. 11, no. 11, pp. 4527-4534, 2011.

[43] A. Jorio, M. Dresselhaus, R. Saito, and G. Dresselhaus, *Raman Spectroscopy in Graphene Related Systems*. Weinheim, Germany: Wiley-VCH, 2011, pp. 288-289.

[44] D. R. Lenski and M. S. Fuhrer, "Raman and optical characterization of multilayer turbostratic graphene grown via chemical vapor deposition," *Journal of Applied Physics,* vol. 110, no. 1, pp. 013720-013720-4, 2011.

[45] L. M. Malard, M. A. Pimenta, G. Dresselhaus, and M. S. Dresselhaus, "Raman spectroscopy in graphene," *Physics Reports,* vol. 473, no. 5-6, pp. 51-87, 2009.

[46] C.-J. Shih, Q. H. Wang, S. Lin, K.-C. Park, Z. Jin, M. S. Strano, and D. Blankschtein, "Breakdown in the wetting transparency of graphene," *Physical Review Letters,* vol. 109, no. 17, pp. 176101-176101-4, 2012.

[47] S. Cotugno, D. Larobina, G. Mensitieri, P. Musto, and G. Ragosta, "A novel spectroscopic approach to investigate transport processes in polymers: The case of water-epoxy system," *Polymer,* vol. 42, no. 15, pp. 6431-6438, 2001.

[48] Y. Jin and S.-I. Ikawa, "Near-infrared spectroscopic study of water at high temperatures and pressures," *The Journal of Chemical Physics,* vol. 119, no. 23, pp. 12432-12438, 2003.

[49] J. B. Brubach, A. Mermet, A. Filabozzi, A. Gerschel, and P. Roy, "Signatures of the hydrogen bonding in the infrared bands of water," *The Journal of Chemical Physics,* vol. 122, no. 18, pp. 184509-184509-7, 2005.

[50] A. Lasagabaster, M. a. J. Abad, L. Barral, and A. Ares, "FTIR study on the nature of water sorbed in polypropylene (PP)/ethylene alcohol vinyl (EVOH) films," *European Polymer Journal,* vol. 42, no. 11, pp. 3121-3132, 2006.

[51] T. Tassaing, P. A. Garrain, D. Begue, and I. Baraille, "On the cluster composition of supercritical water combining molecular modeling and vibrational spectroscopic data," *The Journal of Chemical Physics,* vol. 133, no. 3, pp. 034103-034103-9, 2010.

[52] J. L. Dashnau, N. V. Nucci, K. A. Sharp, and J. M. Vanderkooi, "Hydrogen bonding and the cryoprotective properties of glycerol/water mixtures," *The Journal of Physical Chemistry B,* vol. 110, no. 27, pp. 13670-13677, 2006.

[53] M. Laporta, M. Pegoraro, and L. Zanderighi, "Perfluorosulfonated membrane (Nafion): FT-IR study of the state of water with increasing humidity," *Physical Chemistry Chemical Physics,* vol. 1, no. 19, pp. 4619-4628, 1999.

[54] J. B. Brubach, A. Mermet, A. Filabozzi, A. Gerschel, D. Lairez, M. P. Krafft, and P. Roy, "Dependence of water dynamics upon confinement size," *The Journal of Physical Chemistry B,* vol. 105, no. 2, pp. 430-435, 2000.

[55] B. W. Caughey, A. Dong, K. S. Bhat, D. Ernst, S. F. Hayes, and W. S. Caughey, "Secondary structure analysis of the scrapie-associated protein PrP 27-30 in water by infrared spectroscopy," *Biochemistry,* vol. 30, no. 31, pp. 7672-7680, 1991.

[56] M. Jackson and H. H. Mantsch, "The use and misuse of FTIR spectroscopy in the determination of protein structure," *Critical Reviews in Biochemistry and Molecular Biology,* vol. 30, no. 2, pp. 95-120, 1995.

[57] F. Dousseau, M. Therrien, and M. Pézolet, "On the spectral subtraction of water from the FT-IR spectra of aqueous solutions of proteins," *Applied Spectroscopy,* vol. 43, no. 3, pp. 538-542, 1989.

[58] R. B. Pandey, Z. Kuang, B. L. Farmer, S. S. Kim, and R. R. Naik, "Stability of peptide (P1 and P2) binding to a graphene sheet via an all-atom to all-residue coarse-grained approach," *Soft Matter,* vol. 8, no. 35, pp. 9101-9109, 2012.

[59] C. H. Y. Xuan Lim, A. Sorkin, Q. Bao, A. Li, K. Zhang, M. Nesladek, and K. P. Loh, "A hydrothermal anvil made of graphene nanobubbles on diamond," *Nature Communications,* vol. 4, no. p. 1556, 2013.

[60] K. Heremans and L. Smeller, "Protein structure and dynamics at high pressure," *Biochimica et Biophysica Acta (BBA) - Protein Structure and Molecular Enzymology,* vol. 1386, no. 2, pp. 353-370, 1998.

[61] G. Hummer, S. Garde, A. E. García, M. E. Paulaitis, and L. R. Pratt, "The pressure dependence of hydrophobic interactions is consistent with the observed pressure denaturation of proteins," *Proceedings of the National Academy of Sciences,* vol. 95, no. 4, pp. 1552-1555, 1998.

[62] L. Smeller, "Pressure-temperature phase diagrams of biomolecules," *Biochimica et Biophysica Acta (BBA) - Protein Structure and Molecular Enzymology,* vol. 1595, no. 1-2, pp. 11-29, 2002.

[63] M. Eleftheriou, R. S. Germain, A. K. Royyuru, and R. Zhou, "Thermal denaturing of mutant lysozyme with both the OPLSAA and the CHARMM force fields," *Journal of the American Chemical Society,* vol. 128, no. 41, pp. 13388-13395, 2006.

[64] Melting temperature specification for MBD1 (July 31, 2013). Temperature about 87 °C. [Online]. Available: http://genecopoeia.com/product/search/detail.php?prt=19&cid=&key=HQP011073

[65] M. Huang, H. Yan, C. Chen, D. Song, T. F. Heinz, and J. Hone, "Phonon softening and crystallographic orientation of strained graphene studied by Raman spectroscopy," *Proceedings of the National Academy of Sciences,* vol. 106, no. 18, pp. 7304-7308, 2009.

[66] J. Shim, C. H. Lui, T. Y. Ko, Y. J. Yu, P. Kim, T. F. Heinz, and S. Ryu, "Water-gated charge doping of graphene induced by mica substrates," *Nano Letters,* vol. 12, no. 2, pp. 648-654, 2012.

[67] J. M. Cooper, J. Shen, F. M. Young, P. Connolly, J. R. Barker, and G. Moores, "The imaging of streptavidin and avidin using scanning tunnelling microscopy," *Journal of Materials Science: Materials in Electronics,* vol. 5, no. 2, pp. 106-110, 1994.

[68] C. Lamprecht, J. Danzberger, P. Lukanov, C. M. Tîlmaciu, A. M. Galibert, B. Soula, E. Flahaut, H. J. Gruber, P. Hinterdorfer, A. Ebner, and F. Kienberger, "AFM imaging of functionalized double-walled carbon nanotubes," *Ultramicroscopy,* vol. 109, no. 8, pp. 899-906, 2009.

[69] P. Liu, X. Huang, R. Zhou, and B. J. Berne, "Observation of a dewetting transition in the collapse of the melittin tetramer," *Nature,* vol. 437, no. 7055, pp. 159-162, 2005.

[70] E. Salm, private communication, Aug. 6, 2013.

[71] R. Xie, A. Karim, J. F. Douglas, C. C. Han, and R. A. Weiss, "Spinodal dewetting of thin polymer films," *Physical Review Letters,* vol. 81, no. 6, pp. 1251-1254, 1998.

[72] J. W. Cahn and J. E. Hilliard, "Free energy of a nonuniform system. I. Interfacial free energy," *The Journal of Chemical Physics,* vol. 28, no. 2, pp. 258-267, 1958.

[73] N. Severin, P. Lange, I. M. Sokolov, and J. P. Rabe, "Reversible dewetting of a molecularly thin fluid water film in a soft graphene mica slit pore," *Nano Letters,* vol. 12, no. 2, pp. 774-779, 2012.

[74] S. W. Schmucker, N. Kumar, J. R. Abelson, S. R. Daly, G. S. Girolami, M. R. Bischof, D. L. Jaeger, R. F. Reidy, B. P. Gorman, J. Alexander, J. B. Ballard, J. N. Randall, and J. W. Lyding, "Field-directed sputter sharpening for tailored probe materials and atomic-scale lithography," *Nature Communications,* vol. 3, no. 935, pp. 1-8, 2012.

[75] B. M. Venkatesan, D. Estrada, S. Banerjee, X. Jin, V. E. Dorgan, M.-H. Bae, N. R. Aluru, E. Pop, and R. Bashir, "Stacked graphene-Al_2O_3 nanopore sensors for sensitive detection of DNA and DNA-protein complexes," *ACS Nano,* vol. 6, no. 1, pp. 441-450, 2012.

[76] D. Cohen-Tanugi and J. C. Grossman, "Water desalination across nanoporous graphene," *Nano Letters,* vol. 12, no. 7, pp. 3602-3608, 2012.

[77] S. Plimpton, "Fast parallel algorithms for short-range molecular dynamics," *Journal of Computational Physics,* vol. 117, no. 1, pp. 1-19, 1995.

[78] D. J. Price and C. L. Brooks III, "A modified TIP3P water potential for simulation with Ewald summation," *The Journal of Chemical Physics,* vol. 121, no. 20, pp. 10096-10103, 2004.

[79] G. Chen, Y. Guo, N. Karasawa, and W. A. Goddard, III, "Electron-phonon interactions and superconductivity in K_3C_{60}," *Physical Review B,* vol. 48, no. 18, pp. 13959-13970, 1993.

[80] N. Foloppe and J. A. D. MacKerell, "All-atom empirical force field for nucleic acids: I. Parameter optimization based on small molecule and condensed phase macromolecular target data," *Journal of Computational Chemistry,* vol. 21, no. 2, pp. 86-104, 2000.

[81] S. J. Stuart, A. B. Tutein, and J. A. Harrison, "A reactive potential for hydrocarbons with intermolecular interactions," *The Journal of Chemical Physics,* vol. 112, no. 14, pp. 6472-6486, 2000.

[82] T. W. Sirk, S. Moore, and E. F. Brown, "Characteristics of thermal conductivity in classical water models," *The Journal of Chemical Physics,* vol. 138, no. 6, pp. 064505-064505-11, 2013.

CHAPTER 7. PRESSURE AND CRYSTALLOGRAPHIC EFFECTS FOR HEXAGONAL BORON NITRIDE GROWTH

7.1. Introduction to Hexagonal Boron Nitride Chemical Vapor Deposition on Cu

Hexagonal boron nitride (h-BN) is an insulating, two-dimensional equivalent of graphene. There has been recent interest in isolating h-BN layers for use as insulating spacers [1], as encapsulatory structures [2], or as high-performance substrates for graphene-based electronics [3, 4]. Regardless, most of these structures employ small-area (~100 μm^2) exfoliated h-BN pieces from sintered h-BN crystals [5]. Just like graphene, groups have sought to overcome these area issues by growing h-BN by chemical vapor deposition (CVD) [6-17]. Historical h-BN CVD growths used a borazine precursor ($B_3N_3H_6$, isoelectronic with benzene). There are decades of work studying the pyrolysis and dehydrogenation of borazine [18-21], both necessary steps in the growth of h-BN by borazine [9, 15, 22]. Still, there are burgeoning results growing h-BN with diborane (B_2H_6) and ammonia (NH_3) [10] and by ammonia–borane ($H_3N–BH_3$) [6, 11, 12, 23]. While borazine can give controlled h-BN growths, it is expensive to isolate and difficult to work with in an ex-situ CVD system. Furthermore, growths using B_2H_6 with NH_3, though also controlled [10], require dangerous amounts of toxic, pyrophoric diborane. By contrast, $H_3N–BH_3$ is inexpensive, inert, and can be sublimed and controlled in a h-BN CVD growth furnace.

While ammonia–borane has advantages as a h-BN growth precursor, h-BN growths with it have proven inconsistent [7, 8, 11, 12, 14]. A careful understanding of the growth dynamics that affect h-BN growth with ammonia–borane remains elusive. We can establish a baseline understanding using comparisons between h-BN and graphene growth. For example, it is known that growth pressure [24] and hydrogen partial pressure [25, 26] both determine whether graphene is defective, multilayered, or both. Further, ammonia–borane CVD growths typically

occur on Cu or Ni substrates. Cu and Ni differ dramatically in their growth mechanisms for graphene (i.e., surface catalysis versus predominantly bulk dissolution and precipitation) [27]. It has been speculated that ammonia–borane h-BN growths on Cu proceeds by surface catalysis [11], but there has not been conclusive evidence to back that claim. Finally, no consideration has been given to the polycrystalline nature of the growth substrate itself, which is known to affect graphene [28].

Herein, we study how the growth pressure, hydrogen partial pressure, and the polycrystalline Cu substrate affect h-BN growth via ammonia–borane. Furthermore, we grow heterostructured graphene on h-BN (G/h-BN) and determine that the h-BN film quality ultimately controls the graphene quality. We find that low pressure CVD (LPCVD) growths give high-quality, large grain h-BN films, as ascertained by optical microscopy, scanning electron microscopy (SEM), atomic force microscopy (AFM), X-ray photoelectron spectroscopy (XPS), Raman spectroscopy, device transport, and scanning tunneling microscopy (STM) and spectroscopy (STS). As the growths proceed toward atmospheric pressure CVD (APCVD), the films become more sp^3 like, having rough regions with a polymeric amino/iminoborane (PAB/PIB) chemical nature [23]. Also, these APCVD films are thicker and are more nanocrystalline. We note that nanocrystalline h-BN films have worsened electrical properties versus planar h-BN films. Finally, we observe that high-index Cu surfaces give lower-quality h-BN and G/h-BN films, compared to the low-index Cu(100) surface.

7.2. h-BN Film Morphology at Different Growth Pressures

Figure 7.1 manifests bright-field optical microscopy images of our transferred h-BN and heterostructured G/h-BN films grown at different pressure regimes. The growth in Fig. 7.1a is a LPCVD growth, with a total pressure of 2 torr and a hydrogen partial pressure (P_{H2}) of 0.4 torr.

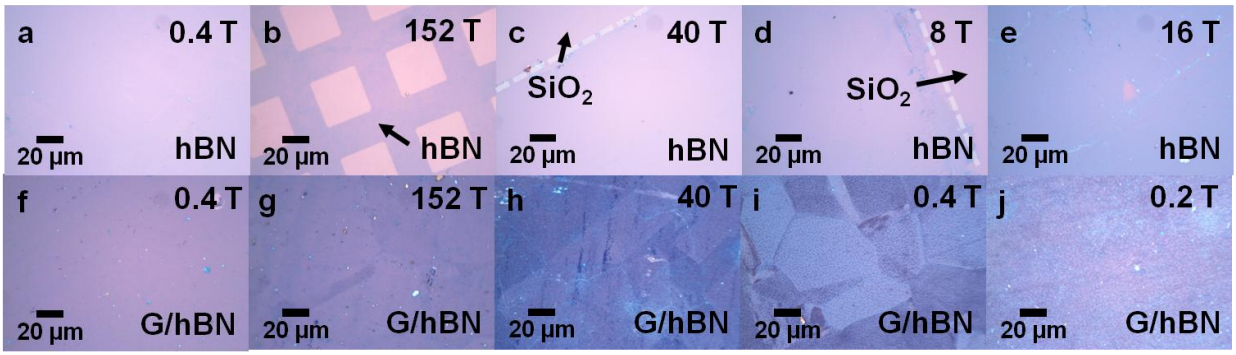

Figure 7.1. Optical images of CVD hexagonal boron nitride (h-BN) and graphene/h-BN (G/h-BN) heterostructures grown at different pressure setpoints, transferred to 90 nm SiO_2/Si. Transferred h-BN films grown at 2 torr **(a)**, 760 torr **(b)**, 200 torr **(c)**, 40 torr **(d)**, and 80 torr **(e)**. Pressures listed inset are the H_2 partial pressures, and (b) has been lithographically patterned after transfer. Higher pressures give thicker h-BN films with rougher morphology. Transferred G/h-BN heterostructures on SiO_2/Si, for bottom h-BN layers grown at 2 torr **(f)**, 760 torr **(g)**, 200 torr **(h)**, 2 torr with high H_3N–BH_3 flow rate **(i)**, and 1 torr with lowered Ar carrier gas flow rate **(j)**. Graphene quality degrades with worsened h-BN morphology.

We contrast enhance this image, and even with this enhancement, the 0.4 torr h-BN film is difficult to visualize [12, 16], with an optical contrast of ~4.0% to the SiO_2. In white light, h-BN monolayers show ~1.5% and ~2.5% contrast on 300 nm and 80 ± 10 nm SiO_2, respectively [29]. Thus, the sample in Fig. 7.1a is likely 1 to 2 layers thin. Conversely, Fig. 1b shows an APCVD h-BN growth (P_{H2} = 152 torr) that has been lithographically patterned down to the SiO_2. There are subtle changes in the film's contrast (dark purple), suggesting differences in h-BN layer number or morphology. The sample exhibits a ~16.1% contrast to the substrate, implying that the APCVD film is fourfold thicker (8+ layers) than the LPCVD film. Nonetheless, this contrast argument assumes pristine h-BN layers, which is not the case for our APCVD films, as will be evident later.

Figures 7.1c-e give optical images for h-BN grown at a variety of pressure setpoints between LPCVD and APCVD. Figure 7.1c is a film grown at 200 torr (P_{H2} = 40 torr), which has a negative contrast of ~4.3%. Since all of the films share the same 90 nm SiO_2 substrate, the negative contrast is at odds with the positive ~2.5% contrast argument per layer [29], implying

that the 40 torr film has a different quality and morphology. We note that the stronger contrast shown in Figs. 7.1d-e has nothing to do with the growth pressure setpoints but is rather due to carbon contamination within our growth chamber; this contamination gives serendipitous graphene layers on top of the h-BN (Raman spectra confirmed, but not shown). Hence, caution must be taken within the growth chamber to eliminate possible carbon sources, otherwise h-BNC [6] or defective G/h-BN heterostructures will result.

We reveal purposefully heterostructured versions of some of the samples in Figs. 7.1a-e in Figs. 7.1f-j. By thermolysis of C_2H_4 (see Section 7.7) [11], we grow graphene on the same LPCVD h-BN growth of Fig. 7.1a, shown in Fig. 7.1f. It is of a uniform and increased contrast, denoting a homogeneous, layer-by-layer graphene growth. Comparatively, the higher pressure samples of Figs. 7.1g and 7.1h, respectively, show mottled contrast and linear features that resemble the former Cu morphology (e.g. grain boundaries and annealing twins) [28]. While graphene grows on both of these samples, the inhomogeneous contrast makes it evident that the films are of a different quality than Fig. 7.1f. Thus, the h-BN morphology, via the different growth pressure setpoints, appears to affect the graphene growth during heterostructure formation. Finally, Figs. 7.1i and 7.1j show optical images for two additional LPCVD h-BN growths with graphene grown on them. While these growths occurred at H_2 pressures of 0.4 torr and 0.2 torr, respectively, the samples resemble Figs. 7.1g,h. The different h-BN morphology occurs from a higher $H_3N–BH_3$ flow rate for the 0.4 torr growth and from a lower H_2 flow rate relative to the $H_3N–BH_3$ flow rate for the 0.2 torr growth. Therefore, the h-BN morphology can dramatically change with respect to the ratio of the $H_3N–BH_3$ flow rate to the H_2 flow rate (or partial pressure). This was previously observed for the carbon feedstock in LPCVD surface catalysis for graphene growth [24, 26].

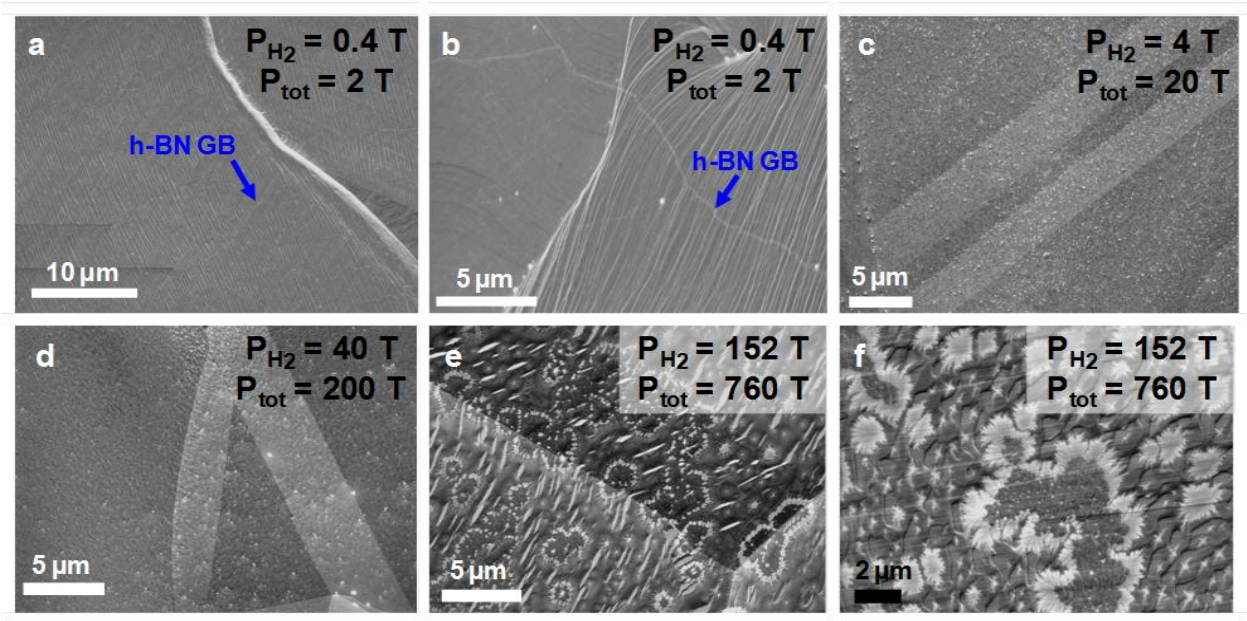

Figure 7.2. Scanning electron microscopy (SEM) imaging of h-BN on Cu at different pressure setpoints. Pressure setpoints shown inset. Low-pressure h-BN growth at a large-scale **(a)** and a small-scale **(b)**, revealing a planar h-BN film that produces Cu hillocks and h-BN grain boundaries. **(c)** Higher pressure growth, showing a loss of the Cu hillock morphology and an increase in charging. **(d)** Medium-pressure growth, with similar morphology and charged nanoparticles as (c). Atmospheric pressure h-BN growth at a large-scale **(e)** and a small-scale **(f)**, with polymeric features plainly evident. These features result from a breakdown in Cu-mediated catalysis.

We now turn to observing the h-BN morphology directly on the growth surface by means of SEM. Figure 7.2a shows a large-area SEM image of high-quality, large grain (~5 µm) h-BN on Cu, grown at 0.4 torr H_2 partial pressure. An h-BN grain boundary (GB) [13] is present, and it traverses the Cu step flow direction. The Cu is stepped and forms hillocks [30] from the coefficient of thermal expansion mismatch between h-BN and Cu. We note that these features will only result if the h-BN were planar and of high quality. Figure 7.2b is a small-area SEM image of another h-BN region on the 0.4 torr H_2 grown sample. Here, we observe a h-BN GB crossing a Cu GB, similar to graphene [31], though we see that h-BN often nucleates at rough Cu morphologies like GBs [28, 32]. Traversing topographically large Cu GBs could only result if the growth proceeds by surface diffusion. Surface diffusion is intimately tied to surface catalysis [28, 31] and growth temperature, suggesting further variables for controlling the h-BN growth.

Figure 7.2c manifests a 4 torr (P_{H2}) h-BN growth on Cu; this growth does not have obvious h-BN GBs and appears morphologically rough. There is also a high density of charged nanoparticles in the image. While the morphology of the Cu is obvious, the former hillocks and step flow features of Figs. 7.2a,b are absent, implying the loss of surface-mediated growth and potentially a thicker film. Note that all the other growth parameters—substrate temperature, precursor temperature, flow rates, surface preparation, etc.—have been held constant as we vary the pressure from LPCVD to APCVD. Figure 7.2d gives a SEM image of h-BN on Cu at a higher h-BN pressure setpoint, 40 torr (P_{H2}). Similar to Fig. 7.2c, the image lacks Cu hillocks, possesses charged nanoparticles, and has a diverse morphology. The morphological features become more drastically apparent as we proceed to APCVD (P_{H2} = 152 torr) in Figs. 7.2e and 7.2f. In both the large-area (Fig. 7.2e) and small-area (Fig. 7.2f) a non-planar h-BN film with dendritic, charged features is apparent. Again, there are no obvious h-BN GBs or Cu hillocks, a breakdown of surface-mediated growth.

The dendritic features evident in Figs. 7.2e and 7.2f can be explained in terms of Cu surface-mediated catalysis and the pyrolysis adducts resulting from ammonia–borane. Ammonia–borane produces polyaminoborane ($–(H_2N–BH_2)_n–$, PAB), borazine, and H_2 upon heating past ~110 °C [23, 33]. Further heating past ~110 °C to >130 °C decomposes PAB into polyiminoborane ($–(HN=BH)_n–$, PIB) and evolves more H_2, and temperatures >1170 °C are required to produce h-BN [23, 33]. Our growth temperatures are ~1000 °C, insufficient to completely breakdown PIB and give crystalline h-BN. However, the temperature requirement for ammonia–borane can be lessened in the presence of catalytic metals [34, 35], but this in turn necessitates surface-mediated catalysis for the h-BN growth. We note that the borazine byproduct could produce h-BN at these temperatures [9, 20, 21], but it is lower in concentration

than the main PIB pyrolysis byproduct, especially at the growth temperatures used. If the growth switched from surface dominated to mass-transport dominated [24], then the surface catalysis of PIB (and residual borazine) would be mitigated. Consequently, the PIB would not breakdown, giving a polymeric deposit, as confirmed in Figs. 7.2e and 7.2f, respectively.

In Fig. 7.3, we determine even more unequivocal evidence about the h-BN film morphologies by transferring the films to SiO_2 and performing AFM. Figures 7.3a and 7.3b show LPCVD-grown h-BN films (P_{H2} = 0.4 torr) under a high ammonia–borane mass (HM, high mass) flow condition. From the high root-mean-square (RMS) roughness and the black line profiles, it is apparent that the films are morphologically rough, despite the low pressure used for growth. The roughness results from the HM condition; at LPCVD, the growth is especially

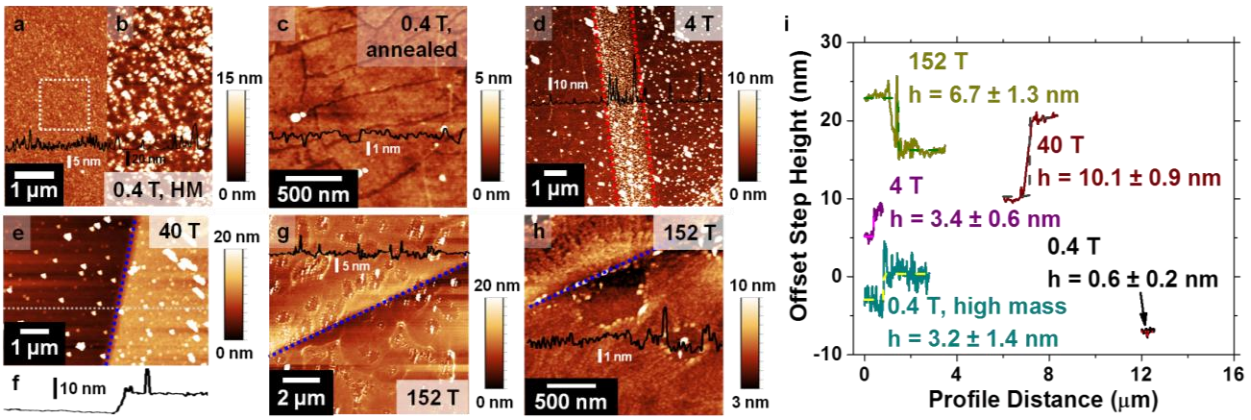

Figure 7.3. Changes in h-BN film morphology due to precursor mass flow and growth pressure. **(a,b)** Atomic force microscopy (AFM) images of transferred h-BN on SiO_2 grown at low pressure but with a high mass (HM) flow of $H_3N–BH_3$ (P_{H2} = 0.4 torr). The HM condition gives a more nanocrystalline h-BN film, as seen in the overlaid black line profile. Root-mean-square (RMS) roughness in the white box is 1.64 nm. **(c)** Low pressure h-BN growth with improved precursor mass flow control (P_{H2} = 0.4 torr). Film is smoother and approaches intrinsic h-BN. Sample was annealed in Ar/H_2 at 400 °C, giving the depressions within the image. Those depressions were h-BN grain boundaries that were catalytically etched by H_2. **(d)** Medium pressure h-BN growth showing heightened $H_3N–BH_3$ catalysis on a former Cu annealing twin (P_{H2} = 4 torr). AFM image **(e)** and height profile **(f)** for lithographically patterned (blue line) h-BN grown at medium pressure (P_{H2} = 40 torr). Film shows some small crystallites induced by the higher growth pressure. Patterned large-area **(g)** and small-area **(h)** AFM images for h-BN grown at atmospheric pressure (P_{H2} = 152 torr). Films are greatly inhomogeneous and rough, with polymeric depressions corresponding to the features seen in SEM. **(i)** Height profiles for all of the growths. Low pressure, mass-controlled h-BN films are the thinnest, with the thickness increasing as a function of growth pressure and sublimed precursor.

sensitive to the ratio between the H_2 flow rate and the ammonia–borane feedstock [26]. For LPCVD graphene, it was shown that the ratio between the carbon feedstock and H_2 needed to be $J_{H2}/J_{CH4} \sim 2$ for high-quality, monolayer graphene growth [26]. By extension, the HM ammonia–borane condition lowers $J_{H2}/J_{H3N–BH3}$ and thereby results in nanocrystalline, multilayered h-BN.

Controlling the HM condition to a more reasonable flow rate at LPCVD gives the h-BN film shown in Fig. 7.3c (P_{H2} = 0.4 torr). We annealed this LPCVD h-BN film in Ar/H_2 (90 min, 400 °C) before AFM imaging. The H_2 in this annealing process catalytically etches [9] the h-BN GBs [13, 14], which are evidently more reactive than the surrounding h-BN (see Fig. 7.4). While destructive, we note that this could be a way to estimate h-BN grain size, like graphene [36]. These depressions conveniently allow us to measure the h-BN film's thickness. Besides the topographic features, the high-quality h-BN surface is smooth and clean [37], as expected [3]. We increase the h-BN growth pressure to 20 torr (P_{H2} = 4 torr) in Fig. 3d. Large protrusions are scattered about the image, but they are unusually concentrated in a linear feature in the AFM image center. We deem this feature to be a reactive annealing twin (red lines) from the former

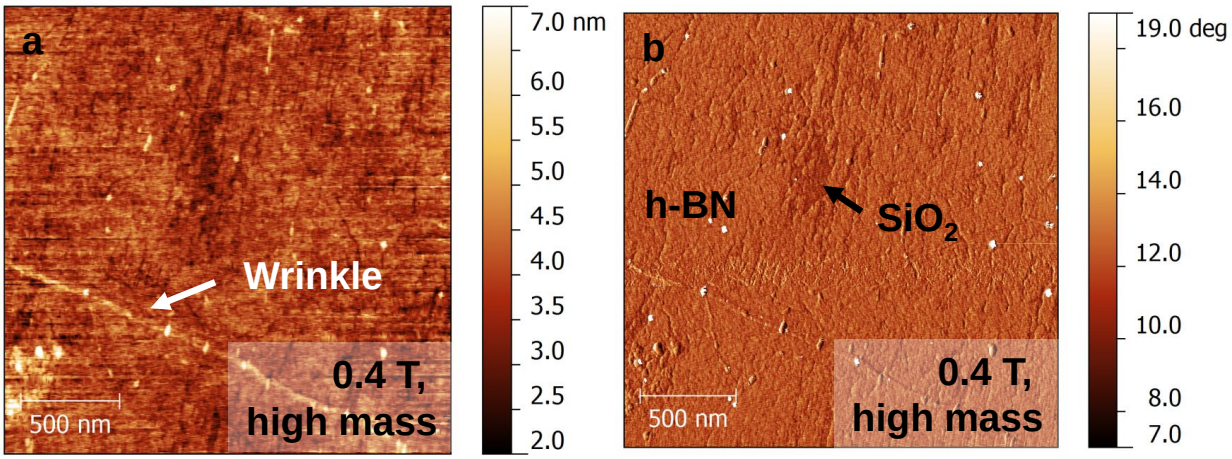

Figure 7.4. Etch pits in transferred h-BN on SiO_2/Si (P_{H2} = 4 torr). **(a)** AFM height image of h-BN on SiO_2 after Ar/H_2 annealing at 400 °C for 4 hrs. **(b)** AFM phase image for (a), showing contrast between the h-BN film and the underlying SiO_2 substrate. This shows that more reactive sites (grain boundaries) on the h-BN are prone to etching [9].

Cu morphology (see Fig. 7.2). Such high-index Cu surfaces are known to affect graphene growth [28], so increased h-BN growth on a reactive high-index Cu twin is not especially surprising.

Figures 7.3e-h show AFM images for h-BN films at different pressure setpoints after lithographic patterning (see Section 7.7). The h-BN growth at 200 torr (P_{H2} = 4 torr) possesses a step height of ~10 nm (Fig. 7.3f) and is relatively smooth. Still, there are some topographic protrusions which look akin to Fig. 7.3d, suggesting a common chemical origin. Figures 7.3g-h give AFM large- and small-scale images for h-BN films grown at APCVD (P_{H2} = 152 torr). Both images possess high RMS roughness and have inhomogeneous depressions with contours that correspond to the features seen in Figs. 7.2e,f. Furthermore, the sample in Figs. 7.3g,h was lithographically processed and exposed to O_2 plasma concurrently with the sample in Fig. 7.3e. Despite this, the step height (dividing blue line) is much lower on Figs. 7.3g,h than on Fig. 7.3e. This intimates that the APCVD h-BN growth is in a different, possibly polymeric, chemical state than the 4 torr h-BN growth. It also stands to reason that the depressions in the film were former PAB or PIB polymeric protrusions extricated by the transfer process. Figure 7.3i summarizes the step heights of the different h-BN films, with the h-BN thicknesses approximately increasing with respect to the growth pressure. LPCVD films under mass control appear to give one to two layer thick h-BN.

7.3. Chemical and Vibrational Changes in the h-BN Growth Quality

Up to this point, we speculated on the chemical states of the h-BN films grown between LPCVD and APCVD. Figure 7.5 elucidates the chemical identity of our h-BN samples, as well as grown heterostructures of G/h-BN. Figures 7.5a and 7.5b give XPS photoelectron (PE) data for the B 1s and N 1s core levels for the differing h-BN growth pressures. We have additional PE and analysis shown in Figs. 7.6–7.8. In the B 1s PE data of Fig. 7.5a, all of the growths possess

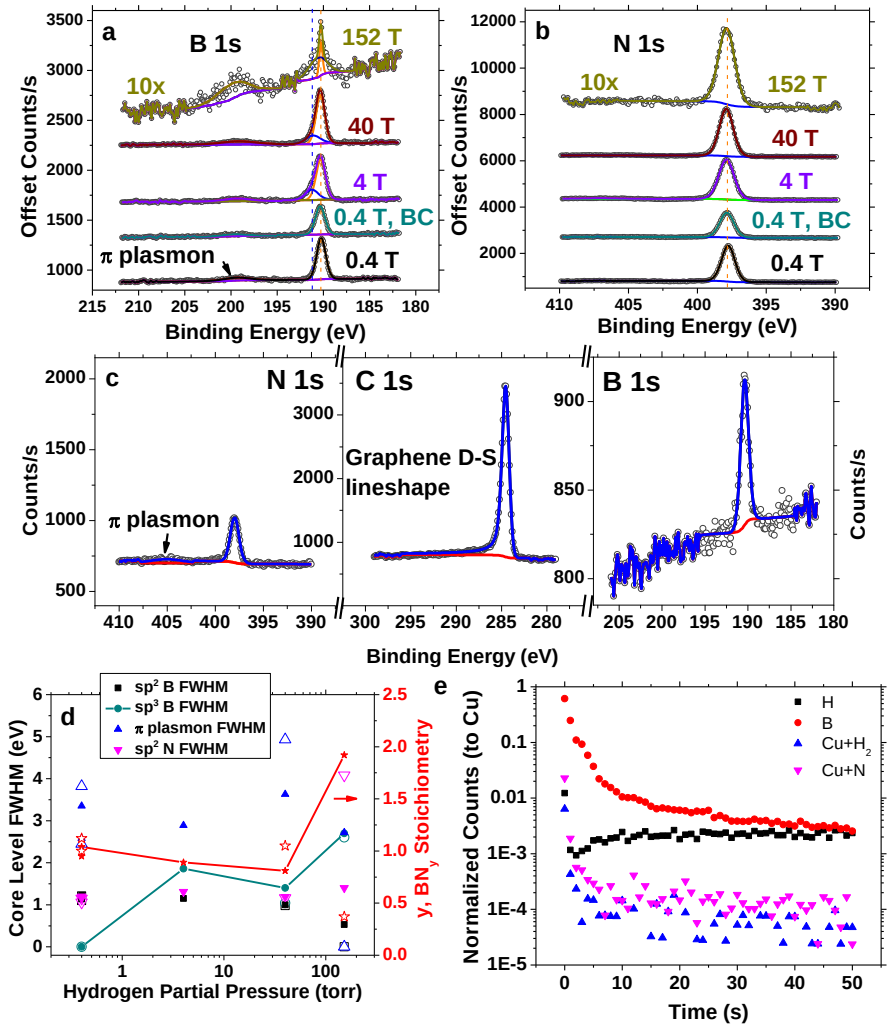

Figure 7.5. Chemical information for different h-BN and G/h-BN growth pressure setpoints. X-ray photoelectron spectroscopy (XPS) core level data with respect to growth pressure for the B 1s **(a)** and N 1s **(b)** photoelectron (PE) lines. All growths give hexagonally structured BN, as confirmed by the main B sp^2 peak (orange) and the π plasmon in the B 1s PE line. For B 1s, a secondary sp^3 B peak (blue) appears and widens with increasing hydrogen partial pressure, indicative of polymerized iminoborane (PIB) species. The atmospheric pressure (P_{H2} = 152 torr) grown B 1s and N 1s PE data both are noisy and disordered. **(c)** N 1s, C 1s, and B 1s PE spectra for graphene grown on high-quality h-BN (P_{H2} = 0.4 torr), revealing pristine graphene via the asymmetric Doniach-Sunjic (D-S) lineshape. **(d)** h-BN (solid) and G/h-BN (hollow) core level FWHM and stoichiometry values *versus* the H_2 pressure. Overall, the FWHM increase with pressure, revealing a more disordered h-BN film at APCVD. The stoichiometries of the h-BN and G/h-BN films show a strong PIB contribution. **(e)** Time-of-flight secondary ion mass spectroscopy (TOF-SIMS) depth profiling for low-pressure h-BN (P_{H2} = 0.4 torr), demonstrating sub-surface B diffusion in the Cu.

the π plasmon loss [38] indicative of hexagonal (resonant) and not sp^3 cubic ordering in the BN films. All of the films have one major sp^2 B sub-peak about ~190 eV binding energy (BE). There are two LPCVD growths (P_{H2} = 0.4 torr) on Alfa Aesar and Basic Copper (BC) [28] Cu

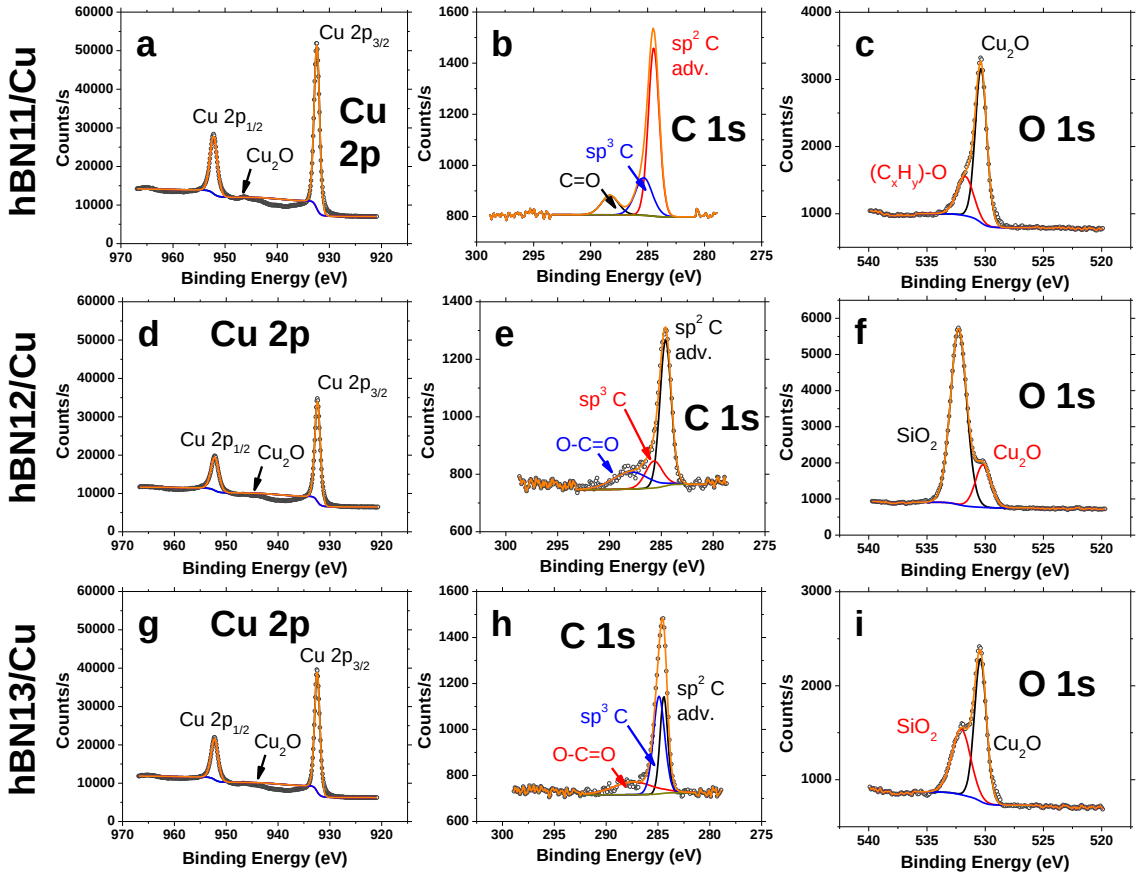

Figure 7.6. X-ray photoelectron spectroscopy (XPS) core level data for different h-BN growths. Cu 2p **(a)**¸ adventitious (adv.) C 1s **(b)**, and O 1s **(c)** core level spectra for h-BN grown at 0.4 torr (hBN#11) hydrogen partial pressure (2 torr total). Oxidized copper and spurious oxygenated hydrocarbons are present, with no obvious Cu–B or oxygenated borides in the spectra. Cu 2p **(d)**¸ adventitious (adv.) C 1s **(e)**, and O 1s **(f)** core level spectra for h-BN grown at 152 torr (hBN#12) hydrogen partial pressure (760 torr total). Oxidized copper and SiO_2 nanoparticles evident, with no obvious Cu–B or oxygenated borides in the spectra. Note that the Cu $2p_{3/2}$ and $2p_{1/2}$ peak intensities are lower than (a) due to a thicker h-BN film. Further, broader O–C=O and sp^3 C peaks suggest possible carbon doping and polymerization in the h-BN film. Cu 2p **(g)**¸ adventitious (adv.) C 1s **(h)**, and O 1s **(i)** core level spectra for h-BN grown at 40 torr (hBN#13) hydrogen partial pressure (200 torr total). Oxidized copper and SiO_2 nanoparticles apparent. Note that the Cu $2p_{3/2}$ and $2p_{1/2}$ peak intensities are lower than (a) but greater than (d), implying an intermediary thickness for h-BN#13 (compared to the 2 torr and 760 torr growths).

substrates, and both growths are markedly similar in BE and lineshape (see Tables 7.1-7.3). In Fig. 7.5a, a secondary sub-peak occurs at ~191 eV BE past the 0.4 torr (P_{H2}) setpoint. This sub-peak was not typically considered in previous analyses of CVD h-BN data [6-8, 10, 32], but it is characteristic of sp^3 B bonding, seen previously for sp^3 c-BN [39] and for PAB (BE ~191.1 eV) [40]. The sp^3 B sub-peak broadens with growth pressure (see Tables 7.4-7.6), and it is the largest

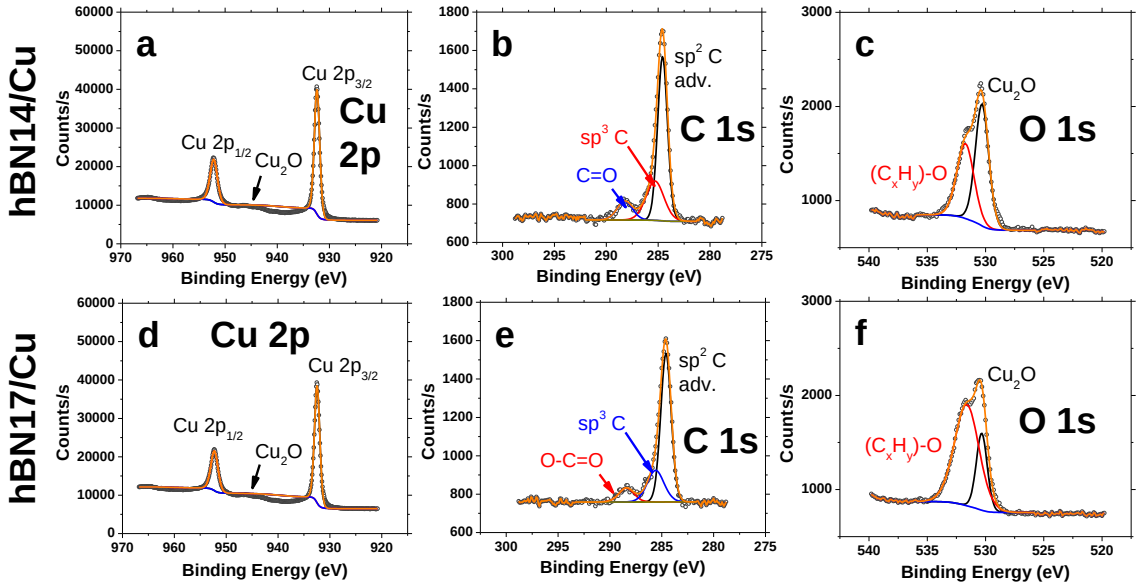

Figure 7.7. Additional XPS core level data for different h-BN growths. Cu 2p **(a)**, adventitious (adv.) C 1s **(b)**, and O 1s **(c)** core level spectra for h-BN grown at 0.4 torr (hBN#14) hydrogen partial pressure (2 torr total) on a Cu substrate from a different Cu vendor [28]. Oxidized copper and spurious oxygenated hydrocarbons are present, with no obvious oxygenated borides or Cu–B evident in the spectra. Cu 2p **(d)** adventitious (adv.) C 1s **(e)**, and O 1s **(f)** core level spectra for h-BN grown at 4 torr (hBN#17) hydrogen partial pressure (20 torr total). Spectra look similar to (a-c), with the exception that the oxygenated hydrocarbon contribution is larger. This suggests that some amorphous carbons and/or graphene grew on top of the h-BN during growth.

for APCVD grown h-BN. Hence, as the growths proceed towards APCVD, they are heterogeneously mixed between h-BN domains and polymeric (e.g. PAB, PIB) domains. Also, the signal for the APCVD films is noisier, showing a lack of crystalline order and typical for a charged polymer.

Similarly, the main sp^2 N peak for the N 1s core level in Fig. 7.5b broadens with growth pressure (see Tables 7.2–7.6). The APCVD data again is noisy, bolstering the notion that the APCVD h-BN film is more like PAB or PIB than like h-BN. Figure 7.5c gives N 1s, C 1s, and B 1s PE spectra for a G/h-BN heterostructure, grown on LPCVD (P_{H2} = 0.4 torr) h-BN on Cu (see Section 7.7). The h-BN maintains its π plasmon loss peak [38], though here it appears under the N 1s core level from graphene-based intensity attenuation of the B 1s signal. The C 1s PE spectrum is fit remarkably well by a single asymmetric Doniach-Sunjic (D-S) lineshape [41, 42],

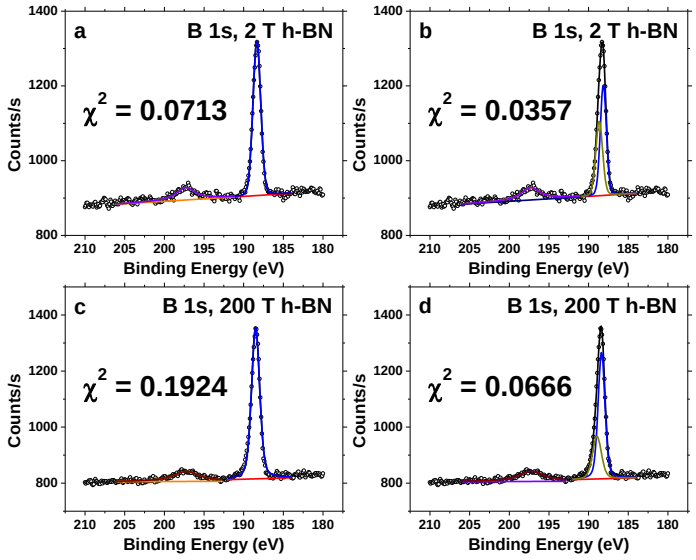

Figure 7.8. Fitting comparisons for XPS B 1s core level data. **(a)** Core level data for CVD h-BN grown at 2 torr, fitted with one Gaussian-Lorentzian (GL) lineshape about the main sp^2 B 1s peak. Spectrum shows the characteristic h-BN π plasmon loss [43] sub-peak at ~8 eV higher than the main sp^2 B 1s peak. We hold that accurate fits are achieved when the residual value, given by χ^2, is less than 0.1, as is the case for (a). **(b)** The same core level data as (a), fitted with two GL lineshapes under the main sp^2 B 1s peak. A sub-peak at higher binding energy (BE) under the main sp^2 B 1s peak can correspond to sp^3-like B domains within the film [39] similar to graphene C 1s XPS spectra. The χ^2 value for (b) is less than (a), but since both are less than 0.1, the second GL sub-peak at higher BE is redundant. Thus, the number of sp^3 domains in the 2 torr h-BN growth (h-BN#11) is minimal. **(c)** Core level data for CVD h-BN grown at 200 torr (h-BN#13). Like (a) and (b), the characteristic π plasmon is present. However, a single GL fit about the sp^2 B 1s peak gives a high χ^2 value, implying that some sp^3 domains might be present. **(d)** The same core level data as (c), fitted with two GL lineshapes under the main sp^2 B peak. Compared to (c), the lower χ^2 value asserts that two sub-peaks are necessary. Therefore, the 200 torr h-BN has some sp^3 domains. Nevertheless, the presence of the π plasmon loss peak and the missing c-BN bulk plasmon peak [43] both show that the sp^3 domains are not in a c-BN configuration. The sp^3 domains likely originate from partially dehydrogenated $H_3N–BH_3$ species.

showing a pristine graphene surface. The lack of B 1s or N 1s full-width at half-maximum (FWHM) broadening also point to minimal h-BN etching during the graphene growth, despite H_2 being present [9]. We then include such extracted h-BN (solid points) and G/h-BN heterostructure (hollow points, same color) FWHM sub-peak data with respect to H_2 partial pressure in Fig. 7.5d. Generally, the sub-peak FWHM increase with the growth pressure, revealing the switch from crystalline h-BN at LPCVD to polymeric, amorphous h-BN at APCVD. The films' stoichiometries become more N-rich (Tables 7.2–7.6) as the pressure increases. At APCVD, the stoichiometry reaches ~BN_2, whereby sub-surface B diffusion is

lowered and polymeric branching is increased. We reveal evidence of B diffusion into the Cu sub-surface with time-of-flight secondary ion mass spectroscopy (TOF-SIMS) depth profiling data in Fig. 7.5e (P_{H2} = 0.4 torr). The sub-surface B diffusion does not necessarily imply bulk precipitation based growth, like graphene on Ni [31], but it warrants further study. Still, this sub-surface B can explain our B-rich stoichiometries (Fig. 7.5d) at low growth pressure.

In Figure 7.9, we complement the chemical identities of our h-BN ascertained by XPS with vibrational information determined by Raman spectroscopy. We take Raman spectra at 532 nm for transferred h-BN films on SiO_2. Compared to graphene, the Raman cross-section of h-BN is very low, especially off resonance at 532 nm [44], requiring high acquisition times, moderate power (~10 mW), and high NA optics (see Section 7.7). These conditions could introduce anharmonic effects [45], but these effects should be consistent across all of our growths. Figure 7.9a shows an optical image for h-BN Raman mapping data given in Fig. 7.9b. We map about the E_{2g} band position (~ 1370 cm^{-1}) [29], the h-BN equivalent of graphene's G band. The average position for the growth (P_{H2} = 0.4 torr) in Fig. 7.9b suggests monolayer character [29] for the film, but such an assignment is inaccurate, as the position shifts with inhomogeneous strain [46, 47]. While we report the E_{2g} band position, we focus on the E_{2g} band FWHM, which is less sensitive to strain and more representative of h-BN crystallite size [48].

Figure 7.9c manifests an overlaid Raman FWHM map for a higher pressure h-BN growth (P_{H2} = 40 torr); a wrinkle (white lines) is apparent in the image. The FWHM is slightly wider about the wrinkle but is essentially homogeneous at ~25 cm^{-1}. We extract these Raman statistics for the 40 torr and other h-BN growth pressures in Fig. 7.9d (point spectra given in Fig. 7.10). Using the model extracted by Nemanich et al., we determine an approximate h-BN crystallite (defect separation) size of L_a ~ 18.4 nm, 9.2 nm, and 12.8 nm for the 4 torr, 40 torr, and 152 torr

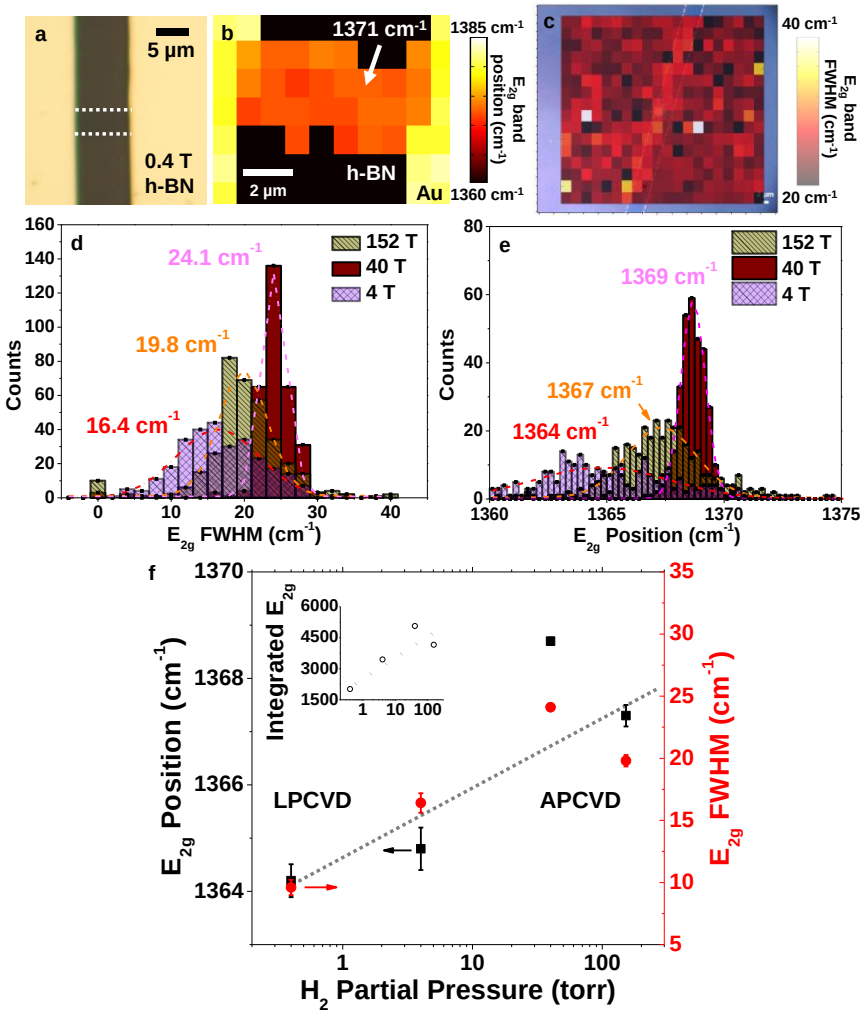

Figure 7.9. Raman spectroscopy of transferred h-BN grown at different pressures. **(a)** Optical image of CVD h-BN after lithographic device patterning (P_{H2} = 0.4 torr). h-BN denoted by the dotted lines. **(b)** Raman map of the device in (a), showing the characteristic ~1371 cm^{-1} E_{2g} band position for h-BN. **(c)** E_{2g} band full-width at half-maximum (FWHM) Raman map overlaid on an optical image for transferred h-BN on SiO_2/Si (P_{H2} = 40 torr). A wrinkle in the film (dotted line) gives a higher FWHM from strain and nanocrystalline h-BN within the laser spot. E_{2g} FWHM **(d)** and band position **(e)** for h-BN H_2 pressures of 4 torr, 40 torr, and 152 torr, respectively. Distributions are broader for thinner (4 torr) and less crystalline (152 torr) films. **(f)** Summary of Raman populations (standard error given) with respect to the H_2 partial pressure. Higher FWHM values correlate to more nanocrystalline h-BN, suggesting that APCVD growths give lower quality h-BN. Integrated E_{2g} band area shown inset, whose increasing value implies thicker h-BN films for higher growth pressure.

h-BN growths, respectively. We recognize that this crystallite size is a conservative underestimate of the true defect separation, a subject of future study. The APCVD (P_{H2} = 152 torr) h-BN film's larger FWHM relative to the 40 torr data likely occurs from a lower signal-to-noise ratio in the polymeric APCVD film and spurious polymeric-induced doping in the film's

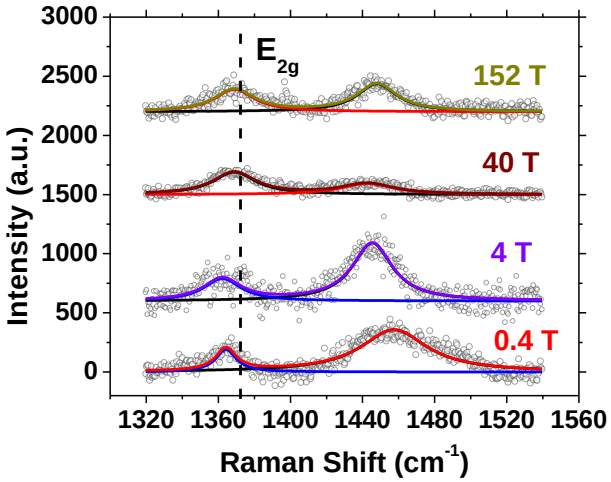

Figure 7.10. Point Raman spectra for different h-BN growth pressures. The E_{2g} full-width at half-maximum (FWHM) increases with respect to pressure, indicative of more nanocrystalline h-BN [48].

PAB/PIB-surrounded h-BN regions. The E_{2g} band position data points in Fig. 7.9e suggest more bulk-like (multilayer) h-BN characteristics for both the 40 torr and 152 torr samples [29]; however, the broad distribution of the 4 torr sample could only occur if it were thinner and thereby strongly affected by strain [46]. We then plot the Raman metrics with respect to the growth pressure in Fig. 7.9f. The apparent linear trend with growth pressure implies that the h-BN film quality degrades as the growths progress from LPCVD to APCVD. In the inset, we show the E_{2g} peak area versus the growth pressure, which indicates film thickness [29]. Thus, the films become thicker and more nanocrystalline at higher growth pressure.

7.4. Polycrystalline Cu Growth Substrate Effects

Even though we can easily control the h-BN growth pressure, we have less control over the polycrystalline Cu substrate typically used for growth. To that end, we must understand the limiting h-BN growth factors that innately occur from the Cu substrate. Figure 7.11a shows an optical image of thick h-BN (HM condition) transferred to SiO_2. Artifacts of Cu-based features—like annealing twins (red) and grain boundaries (white)—abound in the image, giving darker contrast. This increased contrast suggests heightened h-BN nucleation [28, 32] on these

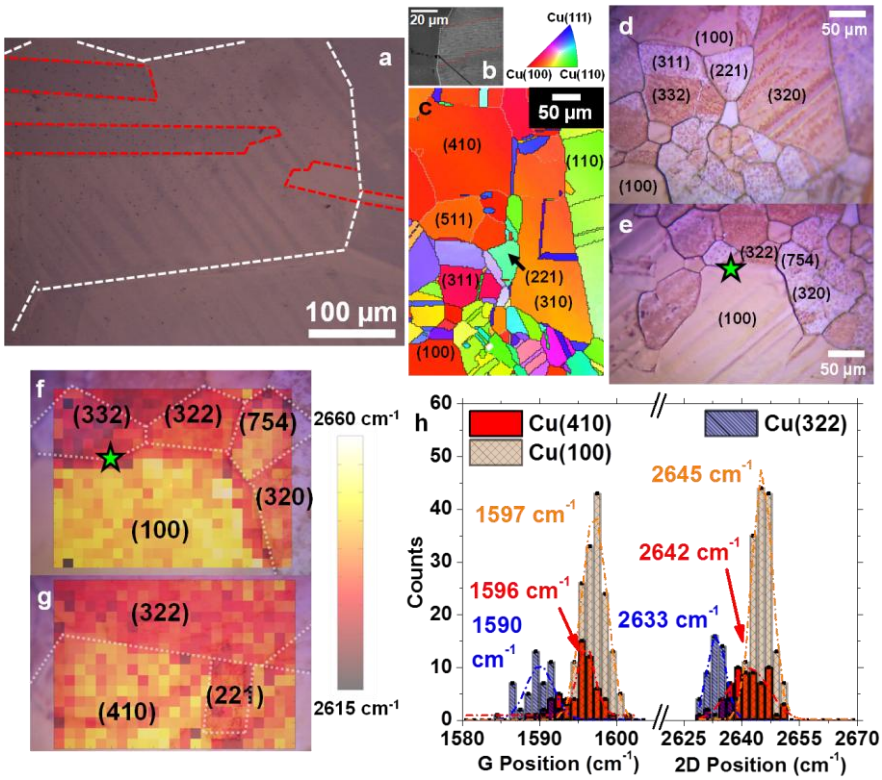

Figure 7.11. Crystallographic effects on heterostructured h-BN growth on Cu. **(a)** Optical image of thick h-BN transferred to SiO_2, showing the former Cu grain boundaries (white) and annealing twins (red) within the h-BN film. **(b)** SEM image of a thick transferred h-BN on SiO_2, again showing former Cu morphology. **(c)** Electron-backscattered diffraction (EBSD) mosaic of Cu, taken on graphene grown on low pressure (0.4 torr H_2) h-BN/Cu. Surface possesses diverse low- and high-index facets. Optical images of partially oxidized high-index **(d)** and low-index **(e)** Cu facets with G/h-BN on them after a 6 month ambient exposure. Low-index **(f)** and high-index Cu (**g**) Raman maps of graphene's 2D band for G/h-BN/Cu after the 6 month ambient exposure. High-index facets oxidize readily, giving tensile strain in the graphene. **(h)** Raman histograms for G and 2D band populations for high-index Cu(410) and Cu(322) and low-index Cu(100). Concurrent shifts in the 2D and G bands for high-index Cu point to tensile strain. Oxygen diffuses through lower-quality h-BN on high-index facets, promoting Cu oxidation. Cu(100) possesses intrinsic band positions, suggesting the existence of high-quality h-BN on that facet.

Cu features. Similar features are apparent in the SEM image (h-BN grown with HM condition, P_{H2} = 0.4 torr) of Fig. 7.11b. To correlate these h-BN regions with the actual Cu crystallography, we grow graphene on h-BN/Cu (LPCVD, P_{H2} = 0.4 torr) and perform electron-backscattered diffraction (EBSD) on the as-grown G/h-BN heterostructure (see Section 7.7). From the EBSD inverse pole figure in Fig. 7.11c, we observe a crystallographically diverse Cu surface, with varied high-index and low-index Cu facets [28]. The Alfa Aesar Cu surface is predominantly (100) in character, as previously observed [49].

We then permit our G/h-BN (LPCVD) samples to oxidize in air for ~6 months. The local graphene growth quality is assuredly dependent on how the carbon-containing feedstock adsorbs on the h-BN/Cu surface. These adsorption dynamics are thus dependent on the h-BN morphology and local energy landscape. Consequently, we can use the graphene quality as an indicator of the h-BN growth quality. Oxygen is known to oxidize Cu by diffusing through graphene GBs [50], so similar behavior would not be unexpected for defective h-BN [13, 51]. In Figs. 7.11d and 7.11e, respectively, we show optical images for different oxidized high- and low-index Cu facets with G/h-BN on them. High-index facets like Cu(320) and Cu(332) are highly oxidized (Cu_2O) [28], whereas low-index Cu(100) appears not oxidized. Taking the green star in Fig. 7.11e as a spatial reference, we gather Raman mapping data for the graphene's 2D (also termed G') band [52] position versus the different Cu facets, as shown in Figs. 7.11f and 7.11g, respectively. The 2D band position for low index Cu(100) is at ~2645 cm^{-1}, consistent with pristine graphene (Fig. 7.5c) on Cu at 633 nm (the laser excitation used here, see Section 7.7). Conversely, graphene on all of the high-index facets are all redshifted by ~10 cm^{-1} from a tensile strain [46] induced by the expanded Cu_2O [50]. We reveal the graphene Raman band positions for Cu(100), Cu(322), and approximately low-index Cu(410) in Fig. 7.11h. This allows us to deduce whether the observed 2D band redshift is strain-related, doping-related, or both [37, 52]. Based on graphene's Grüneisen parameters [46, 52], we find that the shift is indeed from strain. Thus, the heightened Cu oxidation on the high-index facets, combined with the morphological images of Figs. 7.11a,b, point to lower-quality h-BN on the high-index facets. On the other hand, h-BN appears to be higher-quality on low-index Cu(100), similar to graphene on low-index Cu(111) [28].

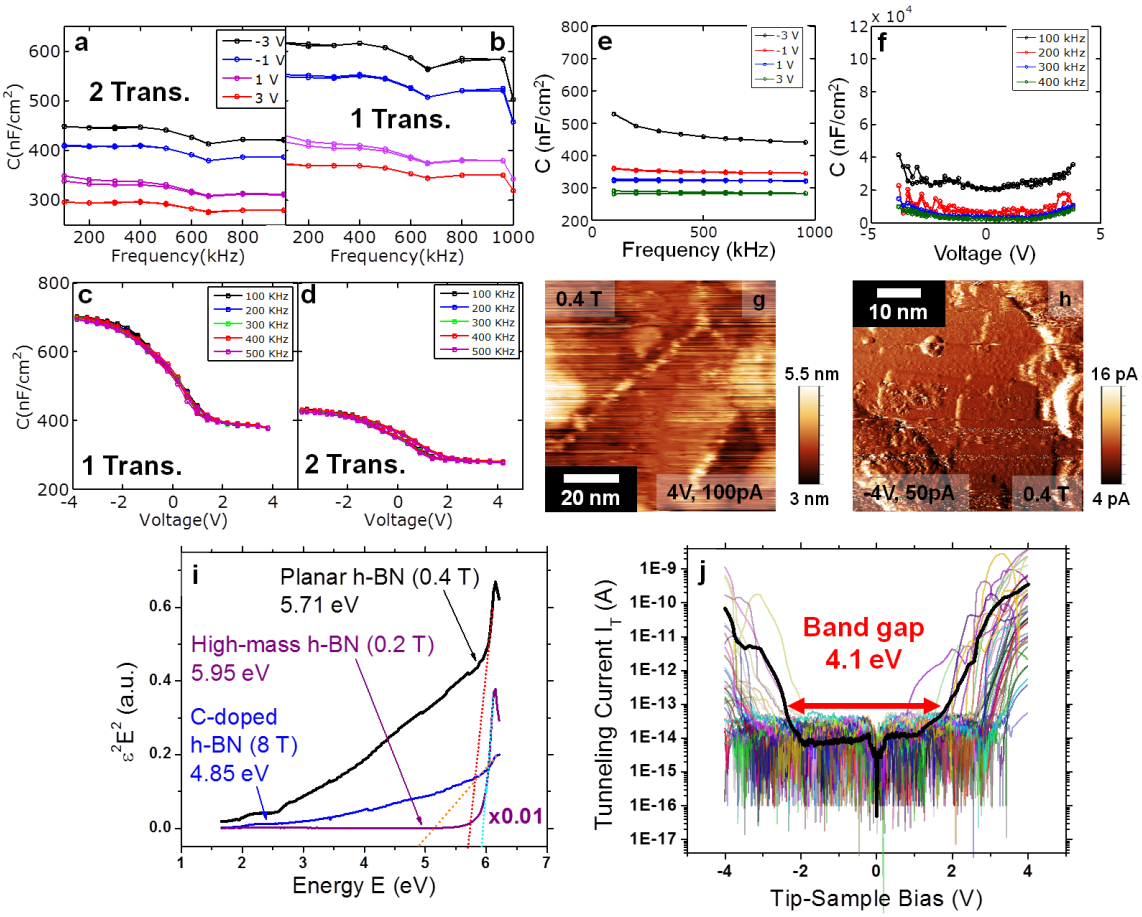

Figure 7.12. Electrical, optical, and spectroscopic data for h-BN films of differing quality. Capacitance–frequency (*C–F*) measurements for two layers **(a)** and one layer **(b)** of transferred nanocrystalline h-BN on n^{++}-Si, showing no obvious frequency dependence. Capacitance–voltage (*C–V*) measurements for one **(c)** and two layers **(d)** of transferred nanocrystalline h-BN on n^{++}-Si, showing depletion from trapped impurities within the h-BN film. Capacitance decreases with the two transfers, as expected. *C–F* **(e)** and *C–V* **(f)** measurements for h-BN grown at lower pressure (P_{H2} = 40 torr). The higher quality CVD h-BN film does not produce depletion, unlike the nanocrystalline film in (a-d). Scanning tunneling microscopy (STM) topograph **(g)** and current image **(h)** for thin, low pressure h-BN (P_{H2} = 0.4 torr) on Cu. The large band gap necessitates high bias conditions for imaging. **(i)** Optical band gap extraction from low pressure (P_{H2} = 0.2 and 0.4 torr) and higher pressure (P_{H2} = 2 torr) CVD h-BN films. Adventitious C-doping lowers the optical band gap in h-BN. **(j)** Scanning tunneling spectroscopy (STS) data on the same low-pressure sample in (g,h), showing a wide electronic band gap characteristic of pristine h-BN.

7.5. Electrical and Optical Signatures of h-BN Growth Morphologies

Finally, we look at the electrical, optical, and spectroscopic nature of our CVD h-BN films grown at different pressures and flow rate conditions. Figures 7.12a-b show capacitance–frequency (*C–F*) device data for LPCVD, nanocrystalline h-BN (HM condition, P_{H2} = 0.4 torr) films, transferred to H–passivated n^{++}–Si (see Section 7.7). Figure 7.12a gives *C–F* data for two

transferred h-BN layers, whereas Fig. 7.12b is for one transferred h-BN layer. We note that trapped H_2O [37] between the h-BN layers is a minor concern for hysteresis in the capacitance measurement. The capacitance in the h-BN films is invariant to frequency, characteristic of an insulator. We extract a dielectric constant of $\varepsilon_r \sim 3.9$ for our films, consistent with previous reports [3, 47]. Nevertheless, the capacitance–voltage (*C–V*) data points of Figs. 7.12c,d show that these h-BN films do not electrically behave as perfect h-BN, depleting at positive biases. Hysteresis in Figs. 7.12c,d is minimal. The depletion likely occurs from static charging (trapped charges) within the nanocrystalline h-BN. Conversely, we give *C–F* and *C–V* measurements from capacitors made from a less nanocrystalline, medium pressure (P_{H2} = 40 torr) h-BN growth in Figs. 7.12e and 7.12f, respectively. These films again show frequency invariance, and they do not deplete, thereby purporting their higher electrical quality. We can also concurrently assess electronic and topographic information by using STM. Figures 7.12g and 7.12h show a STM topograph and current image for LPCVD, thin h-BN (P_{H2} = 0.4 torr) on Cu. Both images are relatively streaky and require high bias conditions for imaging. These bias conditions would only be necessary if the film were thin (one to two layers) and possessed a wide band gap.

To determine the optical and electrical band gaps of our h-BN films, we perform absorption spectroscopy and STS. Figure 7.12i gives Tauc-extracted [6-8, 12, 14] optical band gaps for LPCVD h-BN (P_{H2} = 0.4 torr), LPCVD h-BN under a HM growth condition (P_{H2} = 0.4 torr), and higher pressure h-BN (P_{H2} = 8 torr), all transferred to UV-transparent quartz. Residual C-doping lowers [53] the optical band gap of the higher pressure h-BN, but the other two films have an expected 5.7 to 6 eV band gap [5, 6]. Thus, the LPCVD films are of a high optical quality. Figure 7.12j manifests our STS data that confirms a wide electronic band gap in the LPCVD (P_{H2} = 0.4 torr) films on Cu, with values well in excess of 4 eV.

7.6. Discussion

We now further discuss why our CVD h-BN films vary dramatically in terms of quality based on the growth pressure and the Cu substrate crystallography. For graphene growth on Cu, it is known that the growth regime competes between surface catalysis and mass transport [24]. During APCVD, the reaction rate constant is dominated by mass transport through a gas boundary; conversely, LPCVD growth reactions are dominated by the availability of catalytic Cu. To grow h-BN with ammonia–borane, the $H_3N–BH_3$ precursor must thermally decompose through PAB, borazine, and PIB intermediaries [23]. The final decomposition step requires temperatures in excess of 1170 °C. Therefore, to dehydrogenate and thermolyze the PAB and PIB to give h-BN, a catalytically active surface is necessary, as was demonstrated for Ru dehydrogenation of $H_3N–BH_3$ [34]. In the mass transport regime, catalytically active regions are determined by local protrusions in the gas boundary layer, which ultimately is more turbulent over rough morphological features (e.g. Cu GBs). Hence, the mass-transport regime gives an inhomogeneous mixture of catalytically active and quenched Cu regions. Under APCVD, the resultant CVD h-BN film can thus have some catalytically decomposed PAB and PIB areas which will indeed be h-BN [54]. Still, these growth conditions increase the likelihood of thicker films that will rapidly quench catalysis, giving the branched PAB and PIB evident in our aforementioned analysis. Exiting the mass-transport regime and entering the surface-catalysis regime in LPCVD is the only way to ensure effective Cu-based catalysis of ammonia–borane's thermolyzed byproducts.

While LPCVD-based growths can result in high-quality, planar h-BN films, it is possible to get decent h-BN quality at APCVD if the H_2 flow rate is well in excess [55] of the ammonia–borane flow rate. In all growth regimes, the H_2 serves to etch spurious h-BN nucleation [9],

remove polymeric PAB and PIB species [56], and co-catalyze [25] h-BN formation. This thereby suggests that the ratio of H_2 to ammonia–borane feedstock [25, 26] is critically important in h-BN growth. While Cu-based catalysis allows that ratio to be lower for LPCVD vis-à-vis APCVD, the h-BN growth thickness is still sensitive to it, as made apparent by our high ammonia–borane mass flow data. Higher ratios will etch back more h-BN growth at the expense of a slower growth rate [25, 31]. For our high-quality h-BN films at LPCVD, we estimate the ratio to be $J_{H2}/J_{H3N–BH3} \sim 50$.

In light of the rich literature surrounding h-BN growth with borazine [13, 15, 18, 20-22], our choice of ammonia–borane as a growth precursor is up for debate. While borazine can give well-controlled h-BN growths on transition metal surfaces [9, 16, 17, 22], h-BN growth with it often proceeds by magic clusters [15]. Furthermore, borazine, like benzene, does not provide the monomeric B–N or B=N necessary to precisely attach to edges and prevent aperiodic h-BN GBs [13, 57]. This borazine-induced cluster attachment to the growing h-BN film will result in smaller grain size and meandering [57], unstitched h-BN GBs. Ammonia–borane, like the dual source ammonia and diborane-based h-BN growth, provides the B–N and B=N monomers required for improved growth attachment [58].

Finally, we comment on why the high-index Cu surfaces produce lower-quality h-BN. High-index Cu facets are known to be more reactive than their low-index counterparts [28], resulting from increased vicinality, higher roughness, and a modified workfunction [59]. This heightened reactivity would result in increased nucleation, giving the thicker, more defective h-BN films we see on high-index Cu. Additionally, it is known that the adsorption probability for H_2 on high-index Cu facets is higher than low-index Cu(100) or Cu(111) [60, 61]. The increased

H_2 adsorption could very well drive ammonia–borane catalysis of equilibrium (via Le Chatelier's principle) or etch back the h-BN growth front.

In conclusion, we find that the growth of large-area h-BN on Cu by CVD depends critically on the growth pressure and the Cu substrate's innate crystallography. High-quality, thin h-BN grows under LPCVD conditions, and APCVD growth conditions give thick films with a mixture of h-BN and polymeric PIB/PAB domains. The drastic change in film quality results from the growth switching from surface-catalysis to mass-transport. Moreover, graphene grown on h-BN will be more defective and multilayer if the underlying h-BN is thick, polymeric, defective, or all of the aforementioned. High-index Cu facets also give lower quality h-BN films, as evidenced by graphene grown on the h-BN. Low-index Cu(100) gives pristine, one to two layer thick h-BN films. Our fundamental insights into the CVD growth of h-BN on Cu builds onto the well-established methodologies that exist for graphene on Cu. Knowledge of these growth mechanisms will therefore help enable the fabrication of large-area, high-quality electronic and encapsulatory heterostructures with h-BN.

7.7. Materials and Methods

7.7.1. CVD h-BN Growth Setup and Transfer

We grew our h-BN films in a retrofitted Atomate CVD furnace, as shown in Fig. 7.13, on 1 mil Alfa Aesar, 99.8% purity Cu foils. These foils were first pre-cleaned with a 10:1 H_2O:HCl clean, according to procedures previously discussed [37, 62, 63]. In a N_2 dry environment, we packed a stainless steel precursor ampoule with $H_3N–BH_3$ (Sigma Aldrich, #682098) and sealed it, preventing the hygroscopic ammonia–borane from H_2O exposure. The Cu foils were annealed for 2 hrs under Ar/H_2 (500 sccm Ar / 100 sccm H_2) at 1000 °C, which increased the Cu grain size and lowered the number of h-BN nucleation sites [32]. After annealing, we grew h-BN in an

Ar/H_2 background for 25 min at different pressure setpoints (discussed in Sections 7.2-7.5), subliming the precursor at ~95–96 °C. We took care to keep the temperature stable about ~95 °C, as higher temperatures increased the mass flow and therefore the growth regime, often resulting in nanocrystalline h-BN (termed high mass, HM, in Sections 7.2-7.5). The as-grown h-BN/Cu foils were cooled at the growth pressure and flow conditions using Ar/H_2 at a rate of ~20 °C/min. We then transferred some of the h-BN/Cu foils to piranha-cleaned 90 nm SiO_2/Si (SiO_2) using poly(methyl methacrylate) (PMMA) and poly(bisphenol A carbonate) (PC) using methodologies detailed in Chapter 4 and elsewhere [63]. Additionally, we grew heterostructures of graphene on h-BN (G/h-BN) by two methods.

The first method placed two pieces of cleaned Cu upstream and downstream of the h-BN/Cu foil. Then, we annealed all three Cu pieces in an Ar/H_2 mixture for 1 hr at 1000 °C. Afterward, we placed C_2H_4 into the furnace (1000 °C) for 25 min. The exposed Cu pieces

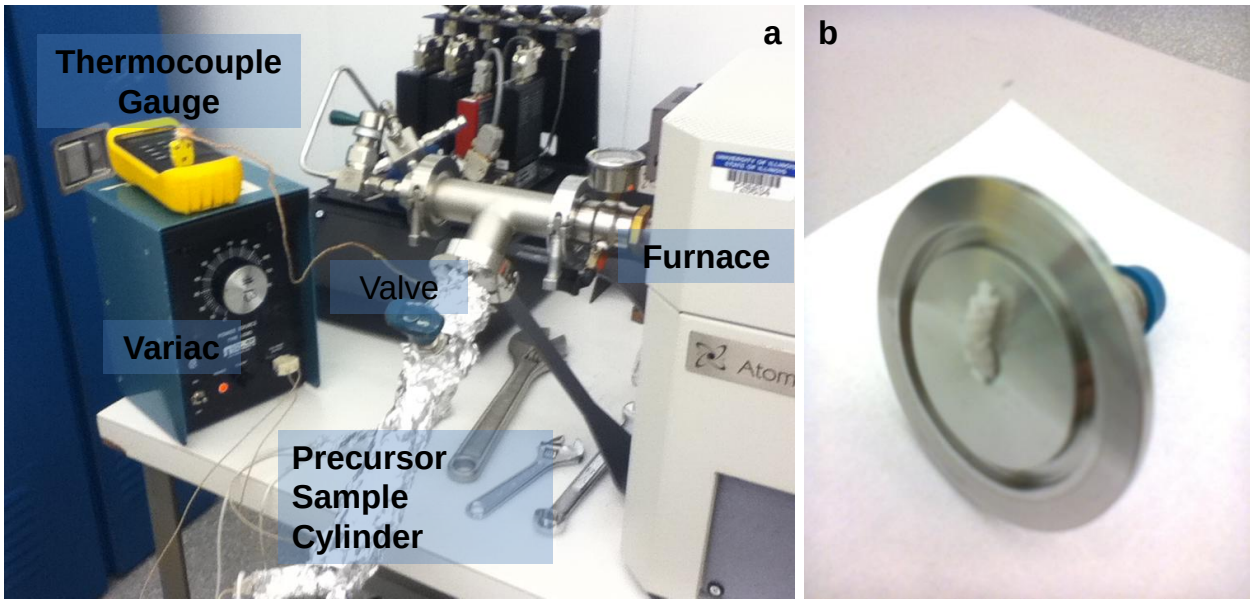

Figure 7.13. Experimental setup for CVD h-BN growth. **(a)** NH_3-BH_3 precursor cylinder and variac used to modulate the ammonia borane sublimation temperature. **(b)** Polymerized $H_3N–BH_3$ on a stainless steel flange after CVD h-BN growth. Growth run was at 2 torr, growth time was 25 min, and the precursor temperature was 95 °C. Polymerization occurs in the presence of high $H_3N–BH_3$ mass flow (high sublimation), and thus care must be taken to control the sublimation rate carefully.

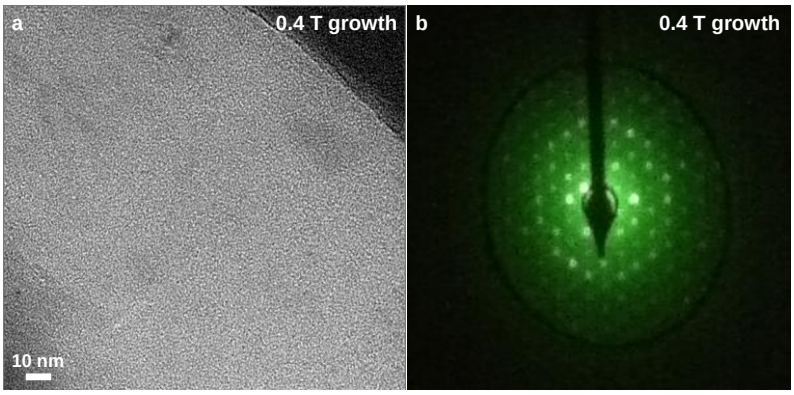

Figure 7.14. Transmission electron microscopy (TEM) imaging of h-BN grown at low pressure. **(a)** Bright-field TEM image of PMMA-transferred, 2 torr (0.4 torr H_2 partial pressure) grown h-BN. **(b)** Photograph of selected-area electron diffraction (SAED) of the area in (a), showing hexagonal, single-domain CVD h-BN. The single set of diffraction spots suggests that we have AA' stacked h-BN and not turbostratic BN (t-BN), as t-BN possesses multiple h-BN layers rotationally misoriented out of the basal plane.

generated hydrocarbon radicals that landed on the h-BN/Cu. After the graphene completed its growth on both the upstream and downstream Cu pieces, no more hydrocarbon radicals were generated. The second method simply used thermolysis of CH_4 at 1000 °C for 25 min. No Cu radical sources were used, and the resulting G/h-BN heterostructures were thicker.

We transferred these G/h-BN heterostructures using the aforementioned PMMA and PC support scaffolds. In Fig. 7.14, we confirmed the hexagonal character of our films by transmission electron microscopy (TEM) and selected area electron diffraction.

7.7.2. Scanning Electron Microscopy (SEM)

We used a FEI environmental SEM at 5 kV on graphene. All images were taken using a ultra high-definition mode, which increases the dwell time and the beam current. We maintained similar values for the brightness and contrast during image collection, so that the images in Fig. 7.2 can be adequately compared.

7.7.3. X-Ray Photoelectron Spectroscopy (XPS)

A Kratos ULTRA XPS with a monochromatic Kα-Al X-ray line was used to collect data. We fitted all sub-peaks (Figs. 7.5–7.8) with Shirley backgrounds and Gaussian-Lorentzian (GL)

mixing. The amount of GL character was optimized (i.e., not fixed) in our fits, so as to lower the chi-squared value (vide infra) and be representative of the true chemical state of the sub-peak in question. Charging effects on the sub-peak binding energy were corrected by offsetting to the Cu $2p^{3/2}$ peak at 932.4 eV (Cu_2O). For the C 1s photoelectron, we employed the asymmetric Doniach-Sunjic (D-S) lineshape for the sp^2 carbon sub-peak [64]. All other sub-peaks were fitted using the aforementioned GL mixing procedure.

7.7.4. Raman Spectroscopy

We took most Raman spectra using a Horiba Raman spectrometer at 532 nm, and the power was kept below ~10 mW to avoid local heating. The acquisition time was at least 180 s, often spaced in 30 s increments (six acquisitions). For one to two layer samples, longer acquisitions (~ 300 s) were necessary. We used a 1800 lines/mm grating centered about ~1370 cm^{-1} and a 100X (~0.8 NA) objective. Mapping data for the E_{2g} mode was fit with by a single Lorentzian; a second Lorentzian was used for the higher order (~1450 cm^{-1}) Si 3TO intrinsic to the SiO_2/Si. For the data in Fig. 7.11 a Renishaw Raman spectrometer at 633 nm excitation (~1-10 mW, ~2 μm spot) and inVia software. The acquisition time was 30 s, and the grating was 1800 lines/mm. During Renishaw mapping, a backscattering 50X objective (~0.7 NA) was used, and the pixel-to-pixel distance was much larger than the spot size (~5 μm).

For our graphene on h-BN mapping data (Fig. 7.11), we used a Lorentzian fitting procedure for the D, G, and 2D bands, as discussed elsewhere [28]. The point spectra in this document were fitted with Lorentzians using a Levenburg-Marquardt fitting procedure in Fityk.

7.7.5. Atomic Force Microscopy (AFM)

We performed atomic force microscopy (AFM) measurements in tapping mode with ~300 kHz Si cantilevers on a Bruker AFM with a Dimension IV controller. Scan rates were

slower than 2 Hz, and sampling is at least 512 samples per line by 512 lines. Most images were sampled at 1024 samples per line by 1024 lines. Images without substantial noise and stable phase imaging were selected for analysis. RMS roughness values were determined by Gwyddion. Images were de-streaked, plane fit, and analyzed using Gwyddion. Some AFM images given in this document were taken on an Asylum Research MFP-3D AFM. On that system, tapping mode AFM was performed with ~300 kHz Si cantilevers (NSG30 AFM, NT-MDT).

7.7.6. Capacitor Measurements

h-BN was transferred onto H-passivated n^{++}-Si, and no annealing was performed. Top capacitor contact electrodes (Ti/Au) were defined using a PMGI/PR stack and UV lithography. PMGI (MicroChem) was spun at 3500 RPM for 30 s and cured at 165 °C for 5 min. Shipley 1813 PR (MicroChem) was spun on top of the cured PMGI at 5000 RPM for 30 s. The PR was soft baked at 110 °C for 70 s, exposed to UV for 4 s on a Karl-Suss aligner (i-line) and developed for 50 s in MF-319 (MicroChem). In the case of electrodes, Ti (0.7 nm) and Au (40 nm) were e-beam evaporated followed by lift-off in hot n-methyl pyrrolidone (Remover PG, MicroChem). Non-desired h-BN regions were removed by an O_2 plasma RIE. All measurements were performed in air at room temperature with a Keithley 4200.

For the lithographically patterned h-BN samples in Figs. 7.1 and 7.3, we follow the same PMGI/PR and UV lithography procedure listed above, using a conventional TEM grid as a mask. However, instead of metal deposition, we use an O_2 plasma through the exposed regions in the mask to leave a resultant TEM grid pattern in the transferred h-BN.

7.7.7. Scanning Tunneling Microscopy (STM)

Our experiments employed a homebuilt, room-temperature ultrahigh vacuum scanning tunneling microscope (UHV-STM) with a base pressure of $\sim 3\times10^{-11}$ Torr [65] and

electrochemically etched W and PtIr tips [66]. We scanned the samples in constant-current mode to get topographic data. In this procedure, the tip height was feedback-controlled, maintaining a current set point while rastering the tip across the surface. We grounded the STM tip through a current amplifier, and we applied the tunneling bias to the sample.

7.8. Tables

Table 7.1. XPS Cu $2p^{3/2}$ peak intensity versus growth pressure. With a relatively homogeneous h-BN overlayer on the Cu, the Cu $2p^{3/2}$ peak intensity should decrease with increasing thickness. Thus, the grown films are thickest at APCVD, which is qualitatively supported by the AFM step height data.

Identifier	Pressure (torr)	AFM Thickness (nm)	Intensity, Cu $2p^{3/2}$ (cps)
h-BN #3	0.4 (high mass)	3.2 ± 1.4	–
h-BN #10	0.4	0.6 ± 0.2	–
h-BN #11	0.4	–	51897.9
h-BN #14	0.4 (different foil)	–	40690.9
h-BN #17	4	3.4 ± 0.6	39312.3

Table 7.2. XPS sub-peak parameters for h-BN grown with LPCVD at 2 torr growth pressure. More insulating films have a Gaussian-Lorentzian mixing of 0. Stoichiometry BN_x, x = 0.95 (survey BN_x, x = 1.22).

Peak	Binding Energy (eV)	FWHM Γ (eV)	Gaussian-Lorentzian Mixing (0%=Gaussian, 100%=Lorentz)	Area (cps·eV)
sp^2 B	190.2	1.14	12	532.9
sp^3 B	–	–	–	–
π plasmon	199.2	2.58	100	136.3
sp^2 N	397.8	1.15	0	1866.7

Table 7.3. XPS sub-peak parameters for h-BN grown with LPCVD at 2 torr growth pressure on a different Cu substrate [28]. More insulating films have a Gaussian-Lorentzian mixing of 0. Stoichiometry BN_x, x = 1.04 (survey BN_x, x = 1.03).

Peak	Binding Energy (eV)	FWHM Γ (eV)	Gaussian-Lorentzian Mixing (0%=Gaussian, 100%=Lorentz)	Area (cps·eV)
sp^2 B	190.4	1.22	1	368.4
sp^3 B	–	–	–	–
π plasmon	199.5	3.35	3	76.4
sp^2 N	397.5	1.20	7	1400.6

Table 7.4. XPS sub-peak parameters for h-BN grown with LPCVD at 4 torr growth pressure. More insulating films have a Gaussian-Lorentzian mixing of 0. The onset of the sp^3 B sub-peak [39] confirms a larger polymeric aminoborane [23] contribution in the CVD film. Stoichiometry BN_x, x = 0.89 (survey BN_x, x = 1.07).

Peak	Binding Energy (eV)	FWHM Γ (eV)	Gaussian-Lorentzian Mixing (0%=Gaussian, 100%=Lorentz)	Area (cps·eV)
sp^2 B	190.3	1.15	30	532.5
sp^3 B	191.0	1.86	0	227.3
π plasmon	199.3	2.89	69	117.6
sp^2 N	397.9	1.31	10	2498.2

Table 7.5. XPS sub-peak parameters for h-BN grown at 200 torr growth pressure. More insulating films have a Gaussian-Lorentzian mixing of 0. The onset of the sp^3 B sub-peak [39] confirms a larger polymeric iminoborane [23] contribution in the CVD film. Stoichiometry BN_x, x = 0.81 (survey BN_x, x = 0.92).

Peak	Binding Energy (eV)	FWHM Γ (eV)	Gaussian-Lorentzian Mixing (0%=Gaussian, 100%=Lorentz)	Area (cps·eV)
sp^2 B	190.3	1.00	23	490.1
sp^3 B	190.8	1.40	34	309.7
π plasmon	199.2	3.63	77	176.7
sp^2 N	397.9	1.19	11	2712.1

Table 7.6. XPS sub-peak parameters for h-BN grown with APCVD at 760 torr growth pressure. More insulating films have a Gaussian-Lorentzian mixing of 0. The onset of the sp^3 B sub-peak [39] confirms a larger polymeric iminoborane [23] contribution in the CVD film. Stoichiometry BN_x, x = 1.92 (cannot determine from survey).

Peak	Binding Energy (eV)	FWHM Γ (eV)	Gaussian-Lorentzian Mixing (0%=Gaussian, 100%=Lorentz)	Area (cps·eV)
sp^2 B	190.3	0.53	100	34.1
sp^3 B	190.8	2.70	0	35.6
π plasmon	199.4	2.72	100	81.9
sp^2 N	397.9	1.40	6	496.4

7.9. References

[1] L. Britnell, R. V. Gorbachev, R. Jalil, B. D. Belle, F. Schedin, M. I. Katsnelson, L. Eaves, S. V. Morozov, A. S. Mayorov, N. M. R. Peres, A. H. Castro Neto, J. Leist, A. K. Geim, L. A. Ponomarenko, and K. S. Novoselov, "Electron tunneling through ultrathin boron nitride crystalline barriers," *Nano Letters,* vol. 12, no. 3, pp. 1707-1710, 2012.

[2] A. S. Mayorov, R. V. Gorbachev, S. V. Morozov, L. Britnell, R. Jalil, L. A. Ponomarenko, P. Blake, K. S. Novoselov, K. Watanabe, T. Taniguchi, and A. K. Geim, "Micrometer-scale ballistic transport in encapsulated graphene at room temperature," *Nano Letters,* vol. 11, no. 6, pp. 2396-2399, 2011.

[3] C. R. Dean, A. F. Young, I. Meric, C. Lee, L. Wang, S. Sorgenfrei, K. Watanabe, T. Taniguchi, P. Kim, K. L. Shepard, and J. Hone, "Boron nitride substrates for high-quality graphene electronics," *Nature Nanotechnology,* vol. 5, no. 10, pp. 722-726, 2010.

[4] P. J. Zomer, S. P. Dash, N. Tombros, and B. J. van Wees, "A transfer technique for high mobility graphene devices on commercially available hexagonal boron nitride," *Applied Physics Letters,* vol. 99, no. 23, pp. 232104-232104-3, 2011.

[5] K. Watanabe, T. Taniguchi, and H. Kanda, "Direct-bandgap properties and evidence for ultraviolet lasing of hexagonal boron nitride single crystal," *Nature Materials,* vol. 3, no. 6, pp. 404-409, 2004.

[6] L. Ci, L. Song, C. Jin, D. Jariwala, D. Wu, Y. Li, A. Srivastava, Z. F. Wang, K. Storr, L. Balicas, F. Liu, and P. M. Ajayan, "Atomic layers of hybridized boron nitride and graphene domains," *Nature Materials,* vol. 9, no. 5, pp. 430-435, 2010.

[7] Y. Shi, C. Hamsen, X. Jia, K. K. Kim, A. Reina, M. Hofmann, A. L. Hsu, K. Zhang, H. Li, Z.-Y. Juang, M. S. Dresselhaus, L.-J. Li, and J. Kong, "Synthesis of few-layer hexagonal boron nitride thin film by chemical vapor deposition," *Nano Letters,* vol. 10, no. 10, pp. 4134-4139, 2010.

[8] L. Song, L. Ci, H. Lu, P. B. Sorokin, C. Jin, J. Ni, A. G. Kvashnin, D. G. Kvashnin, J. Lou, B. I. Yakobson, and P. M. Ajayan, "Large scale growth and characterization of atomic hexagonal boron nitride layers," *Nano Letters,* vol. 10, no. 8, pp. 3209-3215, 2010.

[9] P. Sutter, J. Lahiri, P. Albrecht, and E. Sutter, "Chemical vapor deposition and etching of high-quality monolayer hexagonal boron nitride films," *ACS Nano,* vol. 5, no. 9, pp. 7303-7309, 2011.

[10] A. Ismach, H. Chou, D. A. Ferrer, Y. Wu, S. McDonnell, H. C. Floresca, A. Covacevich, C. Pope, R. Piner, M. J. Kim, R. M. Wallace, L. Colombo, and R. S. Ruoff, "Toward the controlled synthesis of hexagonal boron nitride films," *ACS Nano,* vol. 6, no. 7, pp. 6378-6385, 2012.

[11] K. K. Kim, A. Hsu, X. Jia, S. M. Kim, Y. Shi, M. Hofmann, D. Nezich, J. F. Rodriguez-Nieva, M. Dresselhaus, T. Palacios, and J. Kong, "Synthesis of monolayer hexagonal boron nitride on Cu foil using chemical vapor deposition," *Nano Letters,* vol. 12, no. 1, pp. 161-166, 2012.

[12] Y. Gao, W. Ren, T. Ma, Z. Liu, Y. Zhang, W.-B. Liu, L.-P. Ma, X. Ma, and H.-M. Cheng, "Repeated and controlled growth of monolayer, bilayer and few-layer hexagonal boron nitride on Pt foils," *ACS Nano,* vol. 7, no. 6, pp. 5199-5206, 2013.

[13] A. L. Gibb, N. Alem, J.-H. Chen, K. J. Erickson, J. Ciston, A. Gautam, M. Linck, and A. Zettl, "Atomic resolution imaging of grain boundary defects in monolayer chemical vapor deposition-grown hexagonal boron nitride," *Journal of the American Chemical Society,* vol. 135, no. 18, pp. 6758-6761, 2013.

[14] G. Kim, A. R. Jang, H. Y. Jeong, Z. Lee, D. J. Kang, and H. S. Shin, "Growth of high-crystalline, single-layer hexagonal boron nitride on recyclable platinum foil," *Nano Letters,* vol. 13, no. 4, pp. 1834-1839, 2013.

[15] J. Lu, P. S. E. Yeo, Y. Zheng, H. Xu, C. K. Gan, M. B. Sullivan, A. H. Castro Neto, and K. P. Loh, "Step flow versus mosaic film growth in hexagonal boron nitride," *Journal of the American Chemical Society,* vol. 135, no. 6, pp. 2368-2373, 2013.

[16] C. Orofeo, S. Suzuki, H. Kageshima, and H. Hibino, "Growth and low-energy electron microscopy characterization of monolayer hexagonal boron nitride on epitaxial cobalt," *Nano Research,* vol. 6, no. 5, pp. 335-347, 2013.

[17] S. Roth, F. Matsui, T. Greber, and J. Osterwalder, "Chemical vapor deposition and characterization of aligned and incommensurate graphene/hexagonal boron nitride heterostack on Cu(111)," *Nano Letters,* vol. 13, no. 6, pp. 2668-2675, 2013.

[18] A. W. Laubengayer, P. C. Moews, and R. F. Porter, "The condensation of borazine to polycyclic boron-nitrogen frameworks by pyrolytic dehydrogenation," *Journal of the American Chemical Society,* vol. 83, no. 6, pp. 1337-1342, 1961.

[19] S.-I. Hirano, T. Yogo, S. Asada, and S. Naka, "Synthesis of amorphous boron nitride by pressure pyrolysis of borazine," *Journal of the American Ceramic Society,* vol. 72, no. 1, pp. 66-70, 1989.

[20] M. T. Paffett, R. J. Simonson, P. Papin, and R. T. Paine, "Borazine adsorption and decomposition at Pt(111) and Ru(001) surfaces," *Surface Science,* vol. 232, no. 3, pp. 286-296, 1990.

[21] A. B. Preobrajenski, A. S. Vinogradov, and N. MÃ¥rtensson, "Monolayer of h-BN chemisorbed on Cu(111) and Ni(111): The role of the transition metal 3d states," *Surface Science,* vol. 582, no. 1-3, pp. 21-30, 2005.

[22] S. Joshi, D. Ecija, R. Koitz, M. Iannuzzi, A. P. Seitsonen, J. Hutter, H. Sachdev, S. Vijayaraghavan, F. Bischoff, K. Seufert, J. V. Barth, and W. Auwärter, "Boron nitride on Cu(111): An electronically corrugated monolayer," *Nano Letters,* vol. 12, no. 11, pp. 5821-5828, 2012.

[23] S. Frueh, R. Kellett, C. Mallery, T. Molter, W. S. Willis, C. King'ondu, and S. L. Suib, "Pyrolytic decomposition of ammonia borane to boron nitride," *Inorganic Chemistry,* vol. 50, no. 3, pp. 783-792, 2011.

[24] S. Bhaviripudi, X. Jia, M. S. Dresselhaus, and J. Kong, "Role of kinetic factors in chemical vapor deposition synthesis of uniform large area graphene using copper catalyst," *Nano Letters,* vol. 10, no. 10, pp. 4128-4133, 2010.

[25] I. Vlassiouk, M. Regmi, P. Fulvio, S. Dai, P. Datskos, G. Eres, and S. Smirnov, "Role of hydrogen in chemical vapor deposition growth of large single-crystal graphene," *ACS Nano,* vol. 5, no. 7, pp. 6069-6076, 2011.

[26] W. Zhang, P. Wu, Z. Li, and J. Yang, "First-principles thermodynamics of graphene growth on Cu surfaces," *The Journal of Physical Chemistry C,* vol. 115, no. 36, pp. 17782-17787, 2011.

[27] X. Li, W. Cai, L. Colombo, and R. S. Ruoff, "Evolution of graphene growth on Ni and Cu by carbon isotope labeling," *Nano Letters,* vol. 9, no. 12, pp. 4268-4272, 2009.

[28] J. D. Wood, S. W. Schmucker, A. S. Lyons, E. Pop, and J. W. Lyding, "Effects of polycrystalline Cu substrate on graphene growth by chemical vapor deposition," *Nano Letters,* vol. 11, no. 11, pp. 4547-4554, 2011.

[29] R. V. Gorbachev, I. Riaz, R. R. Nair, R. Jalil, L. Britnell, B. D. Belle, E. W. Hill, K. S. Novoselov, K. Watanabe, T. Taniguchi, A. K. Geim, and P. Blake, "Hunting for monolayer boron nitride: Optical and Raman signatures," *Small,* vol. 7, no. 4, pp. 465-468, 2011.

[30] J. M. Wofford, S. Nie, K. F. McCarty, N. C. Bartelt, and O. D. Dubon, "Graphene islands on Cu foils: The interplay between shape, orientation, and defects," *Nano Letters,* vol. 10, no. 12, pp. 4890-4896, 2010.

[31] X. Li, W. Cai, J. An, S. Kim, J. Nah, D. Yang, R. Piner, A. Velamakanni, I. Jung, E. Tutuc, S. K. Banerjee, L. Colombo, and R. S. Ruoff, "Large-area synthesis of high-quality and uniform graphene films on copper foils," *Science,* vol. 324, no. 5932, pp. 1312-1314, 2009.

[32] K. H. Lee, H.-J. Shin, J. Lee, I.-Y. Lee, G.-H. Kim, J.-Y. Choi, and S.-W. Kim, "Large-scale synthesis of high-quality hexagonal boron nitride nanosheets for large-area graphene electronics," *Nano Letters,* vol. 12, no. 2, pp. 714-718, 2012.

[33] F. Baitalow, J. Baumann, G. Wolf, K. Jaenicke-Rößler, and G. Leitner, "Thermal decomposition of B-N-H compounds investigated by using combined thermoanalytical methods," *Thermochimica Acta,* vol. 391, no. 1-2, pp. 159-168, 2002.

[34] N. Blaquiere, S. Diallo-Garcia, S. I. Gorelsky, D. A. Black, and K. Fagnou, "Ruthenium-catalyzed dehydrogenation of ammonia boranes," *Journal of the American Chemical Society,* vol. 130, no. 43, pp. 14034-14035, 2008.

[35] M. C. Denney, V. Pons, T. J. Hebden, D. M. Heinekey, and K. I. Goldberg, "Efficient catalysis of ammonia borane dehydrogenation," *Journal of the American Chemical Society,* vol. 128, no. 37, pp. 12048-12049, 2006.

[36] P. Nemes-Incze, K. J. Yoo, L. Tapaszto, G. Dobrik, J. Labar, Z. E. Horvath, C. Hwang, and L. P. Biro, "Revealing the grain structure of graphene grown by chemical vapor deposition," *Applied Physics Letters,* vol. 99, no. 2, pp. 023104-023104-3, 2011.

[37] K. T. He, J. D. Wood, G. P. Doidge, E. Pop, and J. W. Lyding, "Scanning tunneling microscopy study and nanomanipulation of graphene-coated water on mica," *Nano Letters,* vol. 12, no. 6, pp. 2665-2672, 2012.

[38] R. Trehan, Y. Lifshitz, and J. W. Rabalais, "Auger and x-ray electron spectroscopy studies of hBN, cBN, and N_2^+ ion irradiation of boron and boron nitride," *Journal of Vacuum Science & Technology A: Vacuum, Surfaces, and Films,* vol. 8, no. 6, pp. 4026-4032, 1990.

[39] Y. Panayiotatos, S. Logothetidis, M. Handrea, and W. Kautek, "Homogeneous and amorphous sputtered sp^3-bonded BN films at RT: A stress, spectroscopic ellipsometry and XPS study," *Diamond and Related Materials,* vol. 12, no. 3-7, pp. 1151-1156, 2003.

[40] R. A. Geanangel and J. W. Rabalais, "Evidence from mass spectra and X-ray photoelectron spectra concerning the structure of poly(aminoborane)," *Inorganica Chimica Acta,* vol. 97, no. 1, pp. 59-64, 1985.

[41] F. Sette, G. K. Wertheim, Y. Ma, G. Meigs, S. Modesti, and C. T. Chen, "Lifetime and screening of the C 1s photoemission in graphite," *Physical Review B,* vol. 41, no. 14, pp. 9766-9770, 1990.

[42] S. Unarunotai, J. C. Koepke, C.-L. Tsai, F. Du, C. E. Chialvo, Y. Murata, R. Haasch, I. Petrov, N. Mason, M. Shim, J. Lyding, and J. A. Rogers, "Layer-by-layer transfer of multiple, large area sheets of graphene grown in multilayer stacks on a single SiC wafer," *ACS Nano,* vol. 4, no. 10, pp. 5591-5598, 2010.

[43] D. H. Berns and M. A. Cappelli, "Cubic boron nitride synthesis in low-density supersonic plasma flows," *Applied Physics Letters,* vol. 68, no. 19, pp. 2711-2713, 1996.

[44] S. Reich, A. C. Ferrari, R. Arenal, A. Loiseau, I. Bello, and J. Robertson, "Resonant Raman scattering in cubic and hexagonal boron nitride," *Physical Review B,* vol. 71, no. 20, pp. 205201-205201-12, 2005.

[45] G. J. Exarhos and J. W. Schaaf, "Raman scattering from boron nitride coatings at high temperatures," *Journal of Applied Physics,* vol. 69, no. 4, pp. 2543-2548, 1991.

[46] M. Huang, H. Yan, C. Chen, D. Song, T. F. Heinz, and J. Hone, "Phonon softening and crystallographic orientation of strained graphene studied by Raman spectroscopy," *Proceedings of the National Academy of Sciences,* vol. 106, no. 18, pp. 7304-7308, 2009.

[47] M. S. Bresnehan, M. J. Hollander, M. Wetherington, M. LaBella, K. A. Trumbull, R. Cavalero, D. W. Snyder, and J. A. Robinson, "Integration of hexagonal boron nitride with quasi-freestanding epitaxial graphene: Toward wafer-scale, high-performance devices," *ACS Nano,* vol. 6, no. 6, pp. 5234-5241, 2012.

[48] R. J. Nemanich, S. A. Solin, and R. M. Martin, "Light scattering study of boron nitride microcrystals," *Physical Review B,* vol. 23, no. 12, pp. 6348-6356, 1981.

[49] L. Tao, J. Lee, H. Chou, M. Holt, R. S. Ruoff, and D. Akinwande, "Synthesis of high quality monolayer graphene at reduced temperature on hydrogen-enriched evaporated copper (111) films," *ACS Nano,* vol. 6, no. 3, pp. 2319-2325, 2012.

[50] D. L. Duong, G. H. Han, S. M. Lee, F. Gunes, E. S. Kim, S. T. Kim, H. Kim, Q. H. Ta, K. P. So, S. J. Yoon, S. J. Chae, Y. W. Jo, M. H. Park, S. H. Chae, S. C. Lim, J. Y. Choi, and Y. H. Lee, "Probing graphene grain boundaries with optical microscopy," *Nature*, vol. 490, no. 7419, pp. 235-239, 2012.

[51] N. G. Coles, D. R. Glasson, and S. A. A. Jayaweera, "Formation and reactivity of nitrides. III. Boron, aluminium and silicon nitrides," *Journal of Applied Chemistry,* vol. 19, no. 6, pp. 178-181, 1969.

[52] L. M. Malard, M. A. Pimenta, G. Dresselhaus, and M. S. Dresselhaus, "Raman spectroscopy in graphene," *Physics Reports,* vol. 473, no. 5-6, pp. 51-87, 2009.

[53] C.-K. Chang, S. Kataria, C.-C. Kuo, A. Ganguly, B.-Y. Wang, J.-Y. Hwang, K.-J. Huang, W.-H. Yang, S.-B. Wang, C.-H. Chuang, M. Chen, C.-I. Huang, W.-F. Pong, K.-J. Song, S.-J. Chang, J.-H. Guo, Y. Tai, M. Tsujimoto, S. Isoda, C.-W. Chen, L.-C. Chen, and K.-H. Chen, "Band gap engineering of chemical vapor deposited graphene by in situ BN doping," *ACS Nano,* vol. 7, no. 2, pp. 1333-1341, 2013.

[54] M. Wang, S. K. Jang, W.-J. Jang, M. Kim, S.-Y. Park, S.-W. Kim, S.-J. Kahng, J.-Y. Choi, R. S. Ruoff, Y. J. Song, and S. Lee, "A platform for large-scale graphene electronics – CVD growth of single-layer graphene on CVD-grown hexagonal boron nitride," *Advanced Materials,* vol. 25, no. 19, pp. 2746-2752, 2013.

[55] Q. Yu, L. A. Jauregui, W. Wu, R. Colby, J. Tian, Z. Su, H. Cao, Z. Liu, D. Pandey, D. Wei, T. F. Chung, P. Peng, N. P. Guisinger, E. A. Stach, J. Bao, S.-S. Pei, and Y. P. Chen, "Control and characterization of individual grains and grain boundaries in

graphene grown by chemical vapour deposition," *Nature Materials,* vol. 10, no. 6, pp. 443-449, 2010.

[56] R. S. Chellappa, T. Autrey, M. Somayazulu, V. V. Struzhkin, and R. J. Hemley, "High-pressure hydrogen interactions with polyaminoborane and polyiminoborane," *ChemPhysChem,* vol. 11, no. 1, pp. 93-96, 2009.

[57] J. C. Koepke, J. D. Wood, D. Estrada, Z.-Y. Ong, K. T. He, E. Pop, and J. W. Lyding, "Atomic-scale evidence for potential barriers and strong carrier scattering at graphene grain boundaries: A scanning tunneling microscopy study," *ACS Nano,* vol. 7, no. 1, pp. 75-86, 2013.

[58] Z. Luo, S. Kim, N. Kawamoto, A. M. Rappe, and A. T. C. Johnson, "Growth mechanism of hexagonal-shape graphene flakes with zigzag edges," *ACS Nano,* vol. 5, no. 11, pp. 9154-9160, 2011.

[59] R. Smoluchowski, "Anisotropy of the electronic work function of metals," *Physical Review,* vol. 60, no. 9, pp. 661-674, 1941.

[60] A. Gelb and M. J. Cardillo, "Classical trajectory study of the dissociation of hydrogen on copper single crystals: II. Cu(100) and Cu(110)," *Surface Science,* vol. 64, no. 1, pp. 197-208, 1977.

[61] J. Tabatabaei, B. H. Sakakini, M. J. Watson, and K. C. Waugh, "The detailed kinetics of the adsorption of hydrogen on polycrystalline copper studied by reactive frontal chromatography," *Catalysis Letters,* vol. 59, no. 2-4, pp. 151-155, 1999.

[62] P. K. Mohseni, A. Behnam, J. D. Wood, C. D. English, J. W. Lyding, E. Pop, and X. Li, "$In_xGa_{1-x}As$ nanowire growth on graphene: Van der Waals epitaxy induced phase segregation," *Nano Letters,* vol. 13, no. 3, pp. 1153-1161, 2013.

[63] A. Salehi-Khojin, D. Estrada, K. Y. Lin, M. H. Bae, F. Xiong, E. Pop, and R. I. Masel, "Polycrystalline graphene ribbons as chemiresistors," *Advanced Materials,* vol. 24, no. 1, pp. 53-57, 2012.

[64] S. Unarunotai, Y. Murata, C. E. Chialvo, H.-S. Kim, S. MacLaren, N. Mason, I. Petrov, and J. A. Rogers, "Transfer of graphene layers grown on SiC wafers to other substrates and their integration into field effect transistors," *Applied Physics Letters,* vol. 95, no. 20, pp. 202101-202101-3, 2009.

[65] J. W. Lyding, S. Skala, J. S. Hubacek, R. Brockenbrough, and G. Gammie, "Variable-temperature scanning tunneling microscope," *Review of Scientific Instruments,* vol. 59, no. 9, pp. 1897-1902, 1988.

[66] S. W. Schmucker, N. Kumar, J. R. Abelson, S. R. Daly, G. S. Girolami, M. R. Bischof, D. L. Jaeger, R. F. Reidy, B. P. Gorman, J. Alexander, J. B. Ballard, J. N. Randall, and J.

W. Lyding, "Field-directed sputter sharpening for tailored probe materials and atomic-scale lithography," *Nature Communications*, vol. 3, no. 935, pp. 1-8, 2012.

CHAPTER 8. SUMMARY AND FUTURE WORK

8.1. Summary

We demonstrated methods to improve the large-area growth, transfer, fluorination, and layering of graphene, h-BN, water, and biomaterials. We found that the hexagonal Cu(111) surface produces monolayer graphene with a low defect density. Additionally, we ascertained that Cu(100), Cu(110), and high-index Cu surfaces give defective, multilayer graphene. We modified the electronic band structure of the CVD graphene films by fluorination through XeF_2. This fluorination produced a fluorinated graphene (FG) material with a ~3 eV band gap and single-sided (C_4F) and dual-sided (CF) stoichiometries. We used FG films to seed high-κ HfO_2 dielectrics; the fluorinated derivatives gave uniform, ultra-thin dielectrics, as compared to pristine graphene.

We showed an atomically clean nanomaterial transfer method using poly(bisphenol A carbonate) (PC) and elaborated the polymer chemistries which made it a clean process. With a suite of characterization methods, we compared the cleanliness of the PC transfer method against PMMA, PLA, PPA, and other transfer scaffolds. We entrapped one to three nanoscale water layers on mica and characterized them by Raman spectroscopy and STM. The trapped water was robust and highly viscous, but it could be nanomanipulated.

We then used the PC transfer process to shrink wrap combinations of graphene and TMV, proteins (MBD and NA), and DNA. We observed that graphene nanosandwiched biomolecules experienced pressure denaturation, which then changed the entrapped, viscous, vicinal water. We noted that the vicinal water spinodally dewetted at pressure-denatured NA proteins on mica and crystallized at MBD-DNA complexes between graphene sheets. Finally, we clarified the growth mechanisms for large-area CVD h-BN films. We determined that CVD h-

BN growth proceeded from large-grain, planar films to polymeric, amorphous films as the growth pressure was increased. Like graphene CVD on Cu, the CVD h-BN film thickness and defect density depended on the underlying Cu substrate; the h-BN films were thicker and more defective on high-index Cu facets over and against low-index Cu(100).

8.2. Future Work

Si-based switches are not running out of gas anytime soon, and it is currently premature to say whether the Silicon Age's successor is the Carbon Age. This is mostly because of the concerns levied in this document. Graphene's future success will likely be determined with how well it plays with others. To that end, the world of graphene is looking "up," that is, in the out-of-plane direction. Designer layered nanomaterials—the so-called van der Waals heterostructures—promise unique electrical, optical, mechanical, and chemical combinations that could not be realized by the nanomaterials by themselves.

The next generation of novel nanomaterials are denoted the "post-graphene" materials. These post-graphene materials include the transition metal dichalcogenides (e.g. MoS_2 [1, 2], WS_2 [3], etc.), silicene [4], and germanene [5]. Regardless, post-graphene material applications will be subject to the concerns brought up in this document. Therefore, one can use many of the techniques outlined herein to guide the synthesis, manipulation, and chemical modification of those post-graphene materials, with a focus on heterogeneous applications.

Finally, the encapsulation of biomolecules by graphene or other layered nanomaterials is still an untapped area of research. One could envision performing experiments on entrapped biomolecules without any solvent in the nanosandwich. In addition, one could switch the top nanosandwiching layer from monolayer CVD graphene to monolayer CVD h-BN. In turn, this thin top layer would be a "tunnel window," allowing the electronic properties of the encapsulated

biomolecule to be assessed by scanning tunneling spectroscopy (STS). Further, the techniques solicited in the biomolecule nanosandwiches could generally apply to other bio-inspired materials. Graphene could nanosandwich energy harvesting complexes like chlorophyllin A [6] to make cheap, atomically thin photovoltaics [7].

8.3. References

[1] S. Najmaei, Z. Liu, W. Zhou, X. Zou, G. Shi, S. Lei, B. I. Yakobson, J.-C. Idrobo, P. M. Ajayan, and J. Lou, "Vapour phase growth and grain boundary structure of molybdenum disulphide atomic layers," *Nature Materials*, vol. 12, no. 8, pp. 754-759, 2013.

[2] B. Radisavljevic, A. Radenovic, J. Brivio, V. Giacometti, and A. Kis, "Single-layer MoS_2 transistors," *Nature Nanotechnology*, vol. 6, no. 3, pp. 147-150, 2011.

[3] A. L. Elías, N. Perea-López, A. Castro-Beltrán, A. Berkdemir, R. Lv, S. Feng, A. D. Long, T. Hayashi, Y. A. Kim, M. Endo, H. R. Gutiérrez, N. R. Pradhan, L. Balicas, T. E. Mallouk, F. López-Urías, H. Terrones, and M. Terrones, "Controlled synthesis and transfer of large-area WS_2 Sheets: From single layer to few layers," *ACS Nano*, vol. 7, no. 6, pp. 5235-5242, 2013.

[4] B. Lalmi, H. Oughaddou, H. Enriquez, A. Kara, S. Vizzini, B. Ealet, and B. Aufray, "Epitaxial growth of a silicene sheet," *Applied Physics Letters*, vol. 97, no. 22, pp. 223109-223109-3, 2010.

[5] E. Bianco, S. Butler, S. Jiang, O. D. Restrepo, W. Windl, and J. E. Goldberger, "Stability and exfoliation of germanane: A germanium graphane analogue," *ACS Nano*, vol. 7, no. 5, pp. 4414-4421, 2013.

[6] S.-Y. Chen, Y.-Y. Lu, F.-Y. Shih, P.-H. Ho, Y.-F. Chen, C.-W. Chen, Y.-T. Chen, and W.-H. Wang, "Biologically inspired graphene-chlorophyll phototransistors with high gain," *Carbon*, vol. 63, pp. 23-29, 2013.

[7] L. Britnell, R. M. Ribeiro, A. Eckmann, R. Jalil, B. D. Belle, A. Mishchenko, Y. J. Kim, R. V. Gorbachev, T. Georgiou, S. V. Morozov, A. N. Grigorenko, A. K. Geim, C. Casiraghi, A. H. C. Neto, and K. S. Novoselov, "Strong light-matter interactions in heterostructures of atomically thin films," *Science*, vol. 340, no. 6138, pp. 1311-1314, 2013.